POLITECNICO DI TORINO

DEPARTMENT OF ENERGY

PhD in Electrical Engineering

Power Electronics, Electrical Machines and Drives

Self-Commissioning of AC Motor Drives

PhD Dissertation

by

Shafiq Ahmed Odhano

PhD Advisor:

Prof. Iustin Radu Bojoi

April 2014

This page was intentionally left blank

Dedication

I dedicate my doctorate degree to my sisters **Fareeda**, **Rabia**, and **Maria** who could not attend even the high school due to cultural backwardness of our society. Given a chance I am sure they would have done far better than what I have managed. Their deprivation of higher education was solely due to their being girls. I was promoted over them only for being a male child and this fact will haunt me throughout my life.

This page was intentionally left blank

Acknowledgements

The PhD research and this dissertation are a fruit of extensive cooperation of so many people whom I owe a sincere gratitude. It is opportune to give due credit here.

It is my foremost duty to thank the Higher Education Commission (HEC) and the Government of Pakistan for providing the necessary financial means for my PhD. The support rendered by the HEC throughout the course of my studies in Italy has undoubtedly been invaluable.

The untiring help and support of my PhD advisor, Professor Iustin Radu Bojoi, has been of utmost importance to carry forward this research theme. His patience with a young researcher like me at the early stages of my PhD had been remarkable.

I feel highly indebted to Professor Alberto Tenconi for his assistance that was vital in helping me sail smoothly on course to completing my PhD. His elderly advice, professorial experience and affectionate behaviour always inspired me in marching forward towards the final goal.

I am thankful to Professor Aldo Boglietti, Professor Giovanni Griva and Professor Andrea Cavagnino whose help and support have always proven useful in helping me comprehend stuff in more detail and from various vantage points.

I sincerely appreciate the support of Professor Mario Chiampi (the PhD Coordinator) and the efforts of Professor Federico Piglione that helped resolve some of the important issues at the beginning of my PhD course.

The worth of the kind and generous cooperation of Dr. Eric Armando cannot be stated in my humble words. He acted both as my senior colleague and a mentor for my work in the laboratory. The support and appreciation of Professor Gianmario Pellegrino always pushed me one step ahead for which I am grateful to him. I highly appreciate Professor Paolo Guglielmi and Dr. Davide Ronchetto for they always lent me a helping hand in the time of need.

Ms. Mariapia Martino (the PhD secretary) deserves a special mention here not only for the professionalism with which she handled my official matters but also for her friendly attitude.

A special thank-you to Professor Gianfranco Chicco, Professor Roberto Napoli, Professor Filippo Spertino, and Professor Angela Russo for their cooperation during my MS courses when I had difficulty in understanding lectures due to lack of the knowledge of Italian language.

Besides the people in the Department of Energy, I would also like to thank the staff of the Office of International Affairs of Politecnico di Torino for they have always been supportive in helping me resolve issues beyond Politecnico's jurisdiction.

At the University of Nottingham (United Kingdom) I had the opportunity to benefit from the experience and kindness of Professor Christopher Gerada and Dr. Paolo Giangrande. I thank them for their collaboration during my stay at Nottingham as visiting PhD student.

I would like to thank my affectionate senior Engr. Abdul Rashid Sangi in the Kingdom of Saudi Arabia for all his support that was pivotal in helping me continue my studies with least to worry about everything else.

Finally, I extend my sincere thanks to my family and friends in Pakistan and to my friends in Italy, Saudi Arabia, United Kingdom, and everywhere else in the world. It is the appreciation and encouragement of these people that maintained my confidence and helped me approach the finish line.

This page was intentionally left blank

Abstract

In modern motion control and power conversion applications, the use of inverter-fed electrical machines is fast growing with continuous development in the field of power electronics and drives. The Variable Voltage Variable Frequency (VVVF) supply for electrical machines gives superior performance in terms of speed control, efficiency and dynamics compared to the machines operated directly from the mains. In one of the most basic configurations, a drive system consists of a closed loop speed control that has a current controller inside the loop. For effective and stable current control, the controller gains need to be set according to the parameters of the machine at hand. Besides, accurate parameter information is helpful in ensuring better machine exploitation as well as maintaining higher efficiency in various operating modes and conditions.

The traditional methods of determining machine parameters consist of extensive machine testing under prescribed supply and ambient conditions. These methods become impracticable when the machine cannot be isolated from its load or the test equipment cannot be made available. Under such conditions, the alternatives are needed that use only the available hardware included in a standard drive to completely define the machine parameters. Self-commissioning thus comes into play in such situations. The *automatic* determination of machine electrical parameters before the drive is put in continuous operation is called *self-commissioning* of the drive system. In this thesis, self-commissioning of AC electric motors is studied, analyzed and results are presented for the implementation of different self-commissioning methods either proposed in the literature or developed in the course of this research.

By far the commonest control strategy of AC machines is the *vector control* that allows dc-machine like decoupled control of machine flux and torque. The separation of flux and torque producing current components depends heavily on the parameters of the machine at hand. In case the parameters fed to the controller do not match the actual machine parameters, the control performance deteriorates both in terms of accuracy and efficiency. For synchronous machines using permanent magnets, the magnetic model of the machine is important both for flux estimation accuracy at low speeds and for deriving maximum torque out of machine per ampere of input stator current. The identification of the magnetic model of permanent magnet synchronous machines requires special tests in a laboratory environment by loading the machine.

A number of machine parameter identification methods have been studied in the past and proposed in the literature. As the power amplifier implied is almost always an inverter, the estimation of machine parameters at start-up by generating special test signals through the inverter have been researched in depth and are investigated in this thesis. These techniques are termed as *offline parameter identification strategies*. Other methods that focus on parameter updating during routine machine operation are called *online parameter estimation methods*. In this thesis, only the offline identification schemes are studied and explored further.

With continuous improvements in power semiconductor devices' switching speeds and more powerful microprocessors being used for the control of electric drives, generating a host of test signals has been made possible. Analysing the machine response to the injected test signals using enhanced computational power onboard is relatively easier. These conditions favour the use of even more complex test strategies and algorithms for self-commissioning and to reduce the time required for conducting these tests. Moreover, the universal design of electric drives renders the self-commissioning algorithms easily adaptable for different machine types used in industry.

Among a number of AC machines available on the market, the most widely used in industrial drives are considered for study here. These include AC induction and permanent magnet synchronous machines. Induction machines still play a major part in industrial processes due, largely, to their ruggedness and maintenance-freeness; however, the permanent magnet machines are fast replacing them as competitive alternatives because of their low volume-to-power, weight-

to-power ratios and higher efficiency. Their relatively light weight makes these machines a preferred choice in traction and propeller applications over their asynchronous counterparts.

Contents

List of figures

Nomenclature

This section defines various symbols, characters and acronyms used in this thesis.

Reference frame symbols:

123 or abc	stator three-phase frame
$\alpha\beta$	stationary reference frame
dq	rotor flux oriented reference frame
$d^{m}q^{m}$	rotor mechanical reference frame
$d^{s}q^{s}$	stator flux oriented reference frame

Special mathematical symbols:

$\times$	scalar product
$\wedge$	vector product
$\lvert x \rvert$	modulus or absolute value of x (x may be a variable or a vector)
$\angle \bar{x}$	angle of vector x
$\dfrac{d}{dt}$	time derivative
$\dfrac{\partial}{\partial x}$	partial derivative with respect to variable x

Superscripts:

$x^{\alpha\beta}$	variable x in $\alpha\beta$ frame of reference (applicable to all other reference frames)
x^{*}	reference value for variable x
$\hat{x}$	estimated value of variable x
$\widehat{x}$	peak value of variable x
$\bar{x}$	over-bar on x means x is a vector or a phasor

Subscripts:

char	characteristic
e	electromagnetic
elec	electrical
err	error
est	estimated
L	load
L-L	line to line
lim	limit value
m	motor, mechanical or magnetizing (depending on the context)
mag	magnetizing
max	maximum value
meas	measured
mech	mechanical
out	output value

s	stator
sl	slip
r	rotor
ref	reference
rel	reluctance
tot	total
x_{dq}	vector x in *dq* reference frame (applicable also to other reference frames)

Multiples:

μ	micro- (10^{-6})
m	milli- (10^{-3})
k	kilo- (10^{3})

Greek alphabet (small):

α	first axis of stationary reference frame
β	second axis of stationary reference frame
γ	current vector angle from positive *q*-axis for PM machines
δ	load angle or torque angle for all ac machines
ε	error between estimated and actual quantity
ζ	(zeta) damping factor
η	efficiency
ϑ or θ	angle between αβ and *dq* frame
ι	(iota) not used
κ	not used
λ	magnetic flux linkages
μ	as prefix micro- (10^{-6}) and as subscript stands for magnetizing
ν	(nu) not used
ξ	(xi) not used
o	(omicron) not used
π	a constant with value 3.14159265358
ρ	not used
σ	induction machine's total leakage factor
τ	time constant
υ	(upsilon) not used
φ	phase angle between ac voltage and current
χ	(chi) not used
ψ	(psi) not used
ω	angular speed (in radians per second)

Greek letters (capital):

Γ	used in naming some of induction machine equivalent circuits
Δ	winding connection type
Δ*x*	change in variable *x*

Δ_a	duty cycle for phase a of the inverter
Σ	summation
Ω	symbol for Ohm (the unit of resistance)

Other constants and variables:

A	area (unless otherwise defined)
$cos\varphi$	power factor
D_x	duty cycle for inverter switch x
e	base of natural logarithm (≈ 2.71828)
E	emf
f	frequency
g	flux observer transition gain
i	current (variable or vector)
I	current (constant or phasor)
J	moment of inertia
k_f	filter gain
k_i	integral gain
k_p	proportional gain
k_r	induction motor rotor coupling factor
L	inductance
L_{lr}	induction motor rotor leakage inductance
L_{ls}	induction motor stator leakage inductance
m	modulation index
p	pole-pairs
P	power
$R(\vartheta)$	rotational transformation matrix
R	resistance
R_{Fe}	equivalent iron loss resistance
s	induction motor slip or frequency domain operator (depends on the context)
t	time
T	torque
v	voltage (variable or vector)
V	voltage (constant or phasor)
ω_{bw}	bandwidth frequency (in radians per second)
X	reactance
Z	impedance

Abbreviations and Acronyms:

μP	Microprocessor
A/D	Analog to Digital (conversion)
AC/ac	Alternating Current
D/A	Digital to Analog (conversion)
DC/dc	Direct Current

DFT/FFT	Discrete/Fast Fourier Transform
DTC	Direct Torque Control
emf	electromotive force
FEA/FEM	Finite Elements Analysis/Method
FOC	Field Oriented Control
HEV	Hybrid Electric Vehicle
ICE	Internal Combustion Engine
IM	Induction Motor
IPM/IPMSM	Interior Permanent Magnet Synchronous Motor
LUT	Look-up Table
MTPA	Maximum Torque Per Ampere
MTPV	Maximum Torque Per Volt
MUT	Machine Under Test
PC	Personal Computer
PI	Proportional Integral
PM	Permanent Magnet
PMSM	Permanent Magnet Synchronous Machine
PPC	Power PC
p.u.	per unit
PWM	Pulse Width Modulation
rad	radians
RFOC	Rotor Field Oriented Control
rpm	revolutions per minute
SFOC	Stator Field Oriented Control
SPM/SPMSM	Surface-mounted Permanent Magnet Synchronous Motor
UDFVC	Unified Direct Flux Vector Control

Note: The units used throughout this thesis are SI (Système International) units.

Chapter – 1

INTRODUCTION

1.1.   Definition and importance of self commissioning

Self-commissioning of an electric drive refers to the accurate estimation of machine electrical parameters without the necessity of any additional test equipment and/or commissioning personnel. It can be considered the ability of the control algorithm to identify the machine connected to it without requiring any intervention from the user. It is useful in situations when the drive and the machine are separate entities at the time of construction i.e. the two are supplied by different manufacturers, which is usually the case in industrial applications especially when a faulty machine is to be replaced keeping the same drive. It is to be underlined that self-commissioning is needed for the universal design of drive regardless of the candidate machine being connected to, and controlled by, it. The need for self-commissioning can also be understood from the necessity of knowing a machine before being able to control it efficiently. Besides control, the information about actual machine parameters is required for fault diagnosis schemes to quickly and correctly detect any abnormal condition during operation. For instance, a broken rotor bar in a squirrel cage induction motor changes its rotor resistance. All the control algorithms and schemes depend on the knowledge of machine parameters and characteristics for their proper functioning.

From the physics of machines and industrial experience, it is a well established fact that the electrical parameters of a particular machine depend on the ambient and working conditions it operates in, so the parameters need to be known in the specific conditions the operation is meant for. For a given production line of machines, the manufacturing spread causes the parameters to vary a great deal between machines of the same category even. One of the requirements on self-commissioning algorithm is to individuate changing parameters in machines with similar nameplate data. In some practical applications, the same inverter and control algorithm may be used for two to three (even many) different machines in which case the algorithm must be able to identify the connected machine and use the parameters already fed to it or to run the entire self-commissioning routine to define the parameters. The machine parameters measured at the time of manufacture or commissioning with traditional tests are valid only in the specific test and supply conditions, however, when the machine operates in different conditions, for instance, from a different power source (e.g. an inverter instead of a purely sinusoidal supply), the electrical and magnetic parameters are destined to vary. Additionally, machine loading, ageing and temperature play an important role in the variation of parameters. Keeping track of these changing parameters is in the best interest of control performance.

To be able to identify a machine accurately in a given environment, onsite tests are indispensable. However, onsite traditional tests mean a waste of resources and time along with added inconveniences. These inconveniences can be circumvented if the drive is intelligent enough to identify the machine that is connected at its terminals by performing different tests automatically, that is to say, the drive is able to do self-commissioning; besides identifying a new machine, self-commissioning routine incorporated in the control algorithm ensures continuous tracking of machine parameters in the midst of changing loading and ambient conditions. The subject of self-commissioning thus studies various methodologies by which an electric drive can be rendered independent of user intervention as far as machine parameter identification is concerned.

For the sake of clarity, it is necessary to distinguish between self-commissioning and online parameter updating. Self-commissioning is concerned with *offline* parameter identification of the machine that means the machine parameters are estimated from tests that are performed while the

machine is at standstill and there is no power flow from supply to load, whereas *online* parameter update refers to the techniques that give an estimate of motor parameters in continuous operation. The definition of self-commissioning followed here is in accordance with the technical terminology used for 'commissioning'; that is the pre-operation verification procedures required to ensure proper subsequent operation. As commissioning takes place before continuous use of an equipment or system, similarly the process of self-commissioning precedes the continuous operation. The prefix 'self' highlights the automaticity of this process, i.e. least or no user intervention. An ideal self-commissioning algorithm does not impose any prerequisites on the drive configuration with regards to available sensors and connection configurations. The algorithm needs to be safe and intelligent enough to adapt to different machine sizes being tested/identified, for that matter it is useful to avoid open-loop current or voltage imposition i.e. the available feedback signals are fully used and monitored.

Among the drive control strategies most widely found in industry are: torque control, speed control and position control. Although all three suffer performance deterioration due to parameter mismatch, the application of high bandwidth proportional-integral controllers, further assisted with position sensors, in speed and position drives makes them less dependent on parameter information. The most sensitive control scheme to parameter errors is the torque control (used mostly in all-electric or hybrid vehicles) for the torque-sensors are rarely used in standard drive hardware. Therefore, accurate parameter information is essential especially in torque drive. The advantages of self-commissioning enabled drive systems can be realised in terms of savings in personnel and equipment requirements, least interruption in production, continuous high performance operation due to accurate parameters used by the control algorithm and operator-error-free parameter identification and settings.

1.2.   Machine types under focus

Among the electric motor types in use throughout the industry, the most widespread AC motor types are selected for study in this thesis. Motors used for high power applications such as machine tools, traction, milling, rolling and manufacturing processes attract greater attention due to their impact on energy consumption and economy of the overall process. The efficiency and performance of these motors need constant review and improvement and that is what provokes more interest in their design and performance evolution. A brief introduction is given below about the machines considered for self-commissioning forming the basis of this dissertation.

1.2.1. Induction Motor (IM)

About 60% of the industrial electric energy is converted into mechanical energy by means of pumps, fans, adjustable speed drives and machine tools equipped with induction motors [1]. The induction motor has been the workhorse of industry due to its simpler design, robustness, over-loadability and ability to operate in harsh environments. It has been the fastest evolving electrical equipment in the 20th century to become ever more compact and versatile along with giving maximum reliability [2]. It successfully outweighed and outnumbered its dc machine counterpart right at the outset of AC power systems due to its favourable design and operation characteristics. A high starting torque makes it a perfect choice for inertial loads that demand more torque to start from rest than continuous steady state torque. The ability of induction motor to start directly from mains is another advantage its use brings for applications such as fans that operate at constant load at constant speed without the necessity of special starting equipment. In modern drive systems where inverter-fed, controlled operation is ubiquitous, the IM has kept in step with the changing technology and still holds the larger portion of the market for variable frequency drives (VFD) even in the presence of strong competitors such as permanent magnet machines.

Induction motor as a part of Variable Voltage Variable Frequency (VVVF) drive holds the key in efficient performance of the entire drive system since the current and flux in the machine can

be precisely controlled to trace optimum point of operation. For traction drives, this feature translates to direct gains in terms of efficient use of available battery power and, at the same time, desired dynamic performance. In machine tool applications where the load torque keeps varying, the precise control of point of operation enables maximum exploitation of machine and inverter ratings. Furthermore, in high speed operations, the flux-weakening capability is indispensable and the induction machine possesses this to a fair degree (if constructed appropriately for enabling field-weakening operation).

The inclusion of induction motor for self-commissioning analysis in this thesis has a logical backing in that being the widely used machine and having a relatively higher number of unknowns to be determined for acceptable control performance, the induction machine still remains a challenge due to its elevated number of parameters whose accuracy determines the efficiency and dynamics of control. It is due to this reason that the methods of IM self-commissioning that had been proposed way back in the late 80s are included for analysis in this thesis and they are yet to be accepted across the industry as a viable alternative for offline testing and commissioning. Besides control performance, the accuracy of parameters incorporated in control algorithm determines the precision with which the induced torque is estimated. Torque estimation is required by intelligent traction drives particularly when the feature of stability in the curve is needed, which is an essential requirement in modern vehicles.

1.2.2. Permanent Magnet Synchronous Machines (PMSMs)

The permanent magnet synchronous machines are known for their high efficiency performance and high power density compared to their magnet-less synchronous counterparts or asynchronous machines. They are the fast growing motive elements in industry. They are widely used in electric/hybrid electric vehicle applications because of lower on-board power losses and heat generation thus imposing less stringent geometrical restrictions. In the absence of rotor losses, that are present in induction machine rotors, PM machines are particularly preferred for their 'cold rotor' operation. Additionally, with no magnetizing current required, more torque is obtained per ampere of stator current and the converters supplying the machine are more efficient. Since the PMs have high flux density and lower weight per volume compared to iron cores, the PM machines offer higher torque densities and better dynamic performance due to low rotor moment of inertia. The design and construction flexibility allows for higher number of poles, larger radius, axial and transverse flux machines and concentrated wound stators.

Among the drawbacks of their use are their greater costs (due to the cost of permanent magnets), the difficulty in flux weakening at high speeds, and perilous behaviour under faults caused by uncontrolled field. These motors are ideal for small to medium power ranges (up to 30kW) beyond which induction machines take the lead both in cost and in performance. The PM machines are not suitable for extreme environments such as high temperature operation as the magnets lose magnetism, either partially or entirely, at above 150 to 200 °C. As opposed to induction machines, they cannot be operated directly from the mains i.e. an inverter is always required. Therefore, there is always a trade-off between performance, cost and convenience and the design takes into consideration the optimization of all these factors. Depending on the radial position of permanent magnets on the rotor, these machines are classified in two main categories: interior permanent magnet synchronous machines and surface mounted permanent magnet synchronous machines.

1.2.2.1. Interior Permanent Magnet Synchronous Motor (IPMSM)

Interior Permanent Magnet Synchronous Motors (IPMSMs) have stator windings identical to induction machine or any other three-phase ac motor that produce revolving magnetic field around rotor periphery. The permanent magnets in the rotor and rotor design are what make an IPMSM different from other ac machine types. The rotor is constructed with magnets buried inside the ferromagnetic core Fig. 1.1(b), thus the name 'interior permanent magnet'. This special rotor

makes them be classified as anisotropic or salient pole machines. The anisotropy is due to varying reluctance path provided by the rotor to magnetic field surrounding it. The anisotropy or saliency plays a key role in determining the field-weakening operability of the motor. Another advantage of salient-pole rotor is the ease with which encoder-less (sensorless) control can be implemented. The sensorless control algorithm exploits rotor saliency to determine its position in space.

The IPMSMs are finding ever increasing number of applications in industry for their high power to weight, torque to volume density, high efficiency, wide constant-power speed range, improved power factor, little noise [3, 4] compared to their other counterparts like the induction motors. They are particularly suitable for high dynamic performance and precise position control at low speeds. Their increasing use in more electric aircraft (MEA) is due to their compact size and less cooling requirements. They are also fast becoming the preferred motor technology for traction applications due to their high power density and less stringent cooling requirements.

These machines are usually tailor-made for specific application at hand; therefore each machine has its distinct characteristics based on specific design. Various designs differ only in their rotor structures with different levels of anisotropy while the stator remains effectively the same. Rotor geometry depends on the requirements of the application at hand and is often a result of designer's imagination.

Regardless of the rotor structure, the machine needs to be identified for efficient control. Rotor anisotropy in IPMSMs gives additional torque component called the reluctance torque that supplements the magnet alignment torque due to permanent magnets. The proportions in which these two torque components contribute to total torque at a given phase current magnitude must be such that the efficiency is a maximum. This condition known as Maximum Torque Per Ampere (MTPA) is highly dependent on the machine's parameters that must be known beforehand.

The parameter identification of IPMSMs is among the topics of interest in industry and academia alike because of increasing demands and restrictions on control performance and efficiency, especially in traction applications. It is still a challenge to completely determine the machine's electrical/magnetic characteristics at standstill; this is the reason why it is undertaken in this thesis along with being inline with the general theme of the topic at hand i.e. self-commissioning of ac machines.

1.2.2.2.   *Surface Mounted Permanent Magnet Synchronous Motor (SPMSM)*

A surface mounted permanent magnet synchronous motor is a direct descendent of permanent magnet dc motors as their 'inside out'. Although it resembles an IPMSM with regards to construction, it exhibits markedly different characteristics in operation. The stators of the two PM ac machines are identical in that they contain balanced three-phase windings; the difference lies on the rotor side. Whereas in an IPMSM the magnets are buried inside the rotor core, in an SPMSM they are mounted on its surface Fig. 1.1(a).

(a)   (b)

Fig. 1.1: Rotor construction (a) SPMSM, (b) IPMSM

Depending on the wave-shape of the mmf the permanent magnets produce in the airgap, these motors are further divided in two categories: square wave and sine wave. The stator is then supplied with either square wave or sinusoidal voltages through the power amplifier i.e. the

inverter. The spread of magnets over almost entire circumference of rotor, as depicted in Fig. 1.1(a), renders the SPMSM isotropic as far as inductance is concerned, that is to say, the rotor presents uniform reluctance path to the magnetic flux all around its circumference. While the isotropic rotor brings the advantages such as less torque ripple, reduced cogging torque, it also entails poor field-weakening capability along with difficulties in sensorless control.

As the knowledge of machine's electrical parameters is of paramount importance for high performance control of any motor type supplied by a drive, the same is true for SPM machines. The self-commissioning of an SPMSM drive requires accurate identification of the machine at standstill which is studied in this thesis.

1.3.   <u>Review of previous research</u>

Ever since the electric drives imparting mechanical power to loads in controlled fashion became widely used, the efforts for improving both performance and efficiency of this control took off. A major factor affecting the machine control is the accuracy with which its electrical parameters are known. More significant is the effect of deviation of parameters in operating conditions from test conditions in which they are pre-determined. This deviation led to concentrated efforts in measuring/estimating and tracking parameters onsite. However, due to limitations posed by site conditions such as unavailability of test equipment, inaccessible machine position or extreme environment, and expertise required to carry out onsite tests, the alternatives are needed. Furthermore, since an electrical machine is almost always 'embedded' in the drive-load system, independent tests requiring total isolation from its environment are mostly avoided for economic and operational reasons. In the event of a motor failure when the motor is to be replaced, the drive and thus the control are usually retained and they need to adapt to new machine automatically. In such situations, self-commissioning proves advantageous in sparing time and manpower and for fast resumption of production. The parameter estimation thus becomes a challenging task with all these restrictions and exigencies.

The most commonly used high performance control of ac machines is the vector control or the so-called field oriented control first conceived by [5]. The basic prerequisite for this control is that the machine parameters be known in all operating conditions including their variation with time (ageing) and temperature. The field orientation is lost if the actual machine parameters deviate from those fed to control and thus the performance obtained is inferior than expected of the control. Optimization of this field oriented control had been one of the reasons that invoked interest in self-commissioning and draw attention of researchers around the world.

In the following sections, a detailed literature review is presented for the self-commissioning of the machines covered in the scope of this thesis. In the subsequent chapters, the effects of parameter deviation on control performance are discussed and some of the most promising methods are studied in detail for the specific machine types.

1.3.1. Induction motor identification

In the early 80s when the induction motor's vector control was maturing to become a preferred control method for the machine, the need for machine parameters identification and tracking was felt as the vector control's performance depended on real-time knowledge of machine parameters. The '90s saw a greater interest in parameter identification and tracking mostly because of more powerful processors found their way into drives applications and requirements on control increased with advancement of technology. Faster and improved power electronics further helped and a number of identification schemes were developed. The methods for electrical parameter identification fall in two categories: the ones giving parameter estimates for an idle machine and the others estimating parameters during normal operation. These are discussed in detail below.

1.3.1.1.   *Offline parameter identification*

The offline parameter identification covers a wide range of test methods that also include the traditional no-load and short-circuit tests as described in the IEEE's (Institute of Electrical and Electronic Engineers) recommended practices on testing of polyphase induction machines [6]. Following the guidelines of this standard procedure, the machine parameters are established with fair accuracy; however, these parameters are valid only in the conditions the test is conducted under. The identification techniques that excite the machine with special test signals, prior to continuous operation, also fall in the category of offline methods. The only exception is when the parameters are calculated from nameplate and design data in which case even the test signals are not required. However, the nameplate data is not always sufficient to calculate all the parameters necessary for vector control, the simplest example being the absence of stator resistance value on the nameplate. As far as geometrical dimensions and other design data are concerned, they are hardly available and even if they are, they suffer from manufacturing tolerance and spreads. The computation of parameters from available data is dealt with in detail in chapter 3.

The earliest works [7] on offline parameter identification through machine excitation with test signals at standstill, that we call self-commissioning, were those of Schierling [8, 9]. In these papers the author put forward the idea of using only the inverter as test signal generator and observing machine response to various test signals through available current sensors to estimate parameters of interest. The objective of the work was to eliminate the need for any special test equipment for establishing machine parameters and without mounting additional sensors except those already present in a standard drive configuration. This contribution acted as the stimulus for further research in the area, though it gave very few details on the technicalities of the procedure. Other works concentrating on parameter estimation at standstill are grouped in various categories below.

i)   Parameter identification schemes that give parameter estimates at standstill and do not require rotor locking and isolation from load are described by [8], [9], [10], [11], [12], [13], [14], [15], [16], [17], [18], [19], [20], [21], [22], [23], [24], [25], [26], [27], [28], [29], [30], [31], [32], [33], [34], [35], [36], [37], [38], [39], [40].

Of these, the methods based on time-domain standstill data are computationally intensive such as [15], [22], [38], [31], [23], [37] for they employ system identification theory. While some of the above methods estimate all the required equivalent circuit parameter, others give only some of them [26], [19], [34], [24], [29], [35], [27], [40], [36], [39], [33]. Whereas the rest of the schemes do not require additional equipment, the single-phase testing procedure of [28] envisages the use of a wattmeter and [40] employs a special frequency generator. Methods based on standstill frequency response are [20], [34], [29], [40].

ii)   Offline identification techniques that entail rotor rotation and therefore mechanical decoupling from load are [41], [42]. [43], [44], [45], [46], [47], [48], [49], [50], [51], [52].

Although most of the methods of self-commissioning need machine nameplate data, the techniques that use nameplate data along with some no-load measurements are [43-45].

Some special methods which do not fit in any of the two categories above are grouped here. For instance, [53] propose that induction motor parameters to be used in control be averaged for a certain class of industrial machines through statistical data. The work in [54] proposes fuzzy logic based gain setting of current and speed controller parameters without determining actual numerical values of machine parameters. Similarly, [55] uses self-tuning of current and speed controllers for drives not equipped with shaft encoders without estimating motor parameters. Speed controller's integral part is used in [56] to determine detuning in rotor time constant. Induction motor drive's health assessment is performed in [57] based on parameters identified through self-commissioning procedures.

1.3.1.2.   Online parameter estimation

Keeping track of induction motor parameters during operation is the main purpose of online parameter identification techniques. The online parameter updating is particularly useful in S1, i.e. continuous, duty machines when the machine operates under rated conditions for longer periods. The machine parameters that are most likely to change are the stator and rotor resistances due to temperature rise in continuous operation. Whereas the stator resistance has least effect on rotor field alignment in a rotor field oriented control system, the rotor resistance variations affect the alignment and hence the control performance. For a given rotor inductance, any change in rotor resistance alters rotor time constant which is an important parameter used by indirect field oriented control systems to determine slip speed. An error in slip speed means no decoupled flux and torque control which is a hallmark of field oriented control. The relationship between demanded torque and realized torque is not linear when the slip speed used by the controller does not match the actual one. Apart from rotor resistance, the rotor time constant is also affected by the saturation of main flux path that alters machine magnetizing inductance. While saturation effects can be taken into account by means of look-up tables obtained prior to machine taking on the load, the rotor resistance is hard to predict unless temperature sensors are used.

Therefore, much of the effort is devoted to rotor time constant updating in online parameter identification techniques. The online identification methods are sub-divided in two broad categories here: the schemes monitoring rotor quantities and the ones including the rest of the machine parameters as well. They are given below.

i)   The methods focusing on rotor side parameters' online update are [58], [59], [60], [61], [62], [63], [64], [65], [66], [67], [68], [69], [70], [71]

Some of these methods [61, 63, 66] are based on model reference adapted system (MRAS) that is an indirect approach of parameter estimation consisting in comparing measured signals, such as voltages and currents, with those computed from the 'reference' analytical model of the motor [45]. The deviations of the estimated values from the measured ones are minimized by adjusting the parameter estimates. Of the rest, [59] proposes injection of Pseudo-Random Binary Sequence (PRBS) signals. [58] necessitates dc-link power measurement and [64] does not address saturation phenomenon.

ii)   Other parameters along with rotor time constant are dealt with in [72], [73], [74], [75], [76], [77], [78], [79], [80], [81].

Various schemes of online parameter tracking are described in [76] such as reactive power compensation, air-gap power feedback. Other works like [69, 71, 77, 78] are based on spectral analysis.

1.3.2. Permanent Magnet Synchronous motor identification methods

As mentioned in section 1.2.2, the permanent magnet synchronous machines' lossless rotor adds to their efficiency improvement. The absence of rotor currents also simplifies the equivalent circuits of these machines and there is relatively less number of parameters to be determined for complete description of the machine. However, the difficulty in accurately estimating permanent magnet flux and the phenomenon of saturation and cross-saturation makes their identification a challenging task even with dedicated testing. Furthermore, similar to the rotor resistance in a squirrel-cage induction motor, the permanent magnet flux also varies with temperature, but with a negative slope; so following the changing PM flux during operation is as important for control as knowing it beforehand. In the flux-weakening region of operation, the parameters play important role in determining optimum control.

Similar to induction motor parameter identification techniques, the permanent magnet motors' parameter estimation methods can be divided in two categories: offline estimation and

online parameter updating. Offline methods can further be divided into those at standstill and the ones that require rotor rotation. Online tracking of machine electrical parameters is useful for ensuring optimal control with varying parameters. Since the state-of-the-art control of PM machines is sensorless, the parameter identification for sensorless control schemes has also received much interest from the researchers around the world.

i)   Offline parameter identification methods are discussed in [82], [83], [84], [85], [86], [87], [88], [89], [90], [91], [92], [93], [94], [95]

The workds presented in [82, 83] give parameters from analytical model for which machine's geometry and design data are required. While [85] necessitates the use of a load test drive along with power analayzer, [86-90] require laboratory testing of the machine and [92-94] work with free-to-rotate and/or locked rotor, hence they do not fit the definition of self-commissioning as does [91] which needs a speed-controlled prime-mover.

ii)   Online identification is taken up by [96], [97], [98], [99], [100], [101], [102], [103], [104], [105], [106], [107], [108], [109], [110]

Parameters identification using system identification theory is reported in [96, 105] while [97] implements predictive control for parameter identification. In [98] the authors describe a consolidated scheme for sensorless control of all synchronous machines with online parameter identification. Works presented in [100-104, 106] are again sensorless schemes while [107] requires temperature sensors at end-windings for tracing machine parameters' variations. The focus of [109, 110] is the permanent magnet flux-linkage estimation.

1.4.   Thesis structure and goals

This doctorate thesis is composed of seven chapters discussing parameter identification of each machine type selected for study in this thesis. The machine types are assigned dedicated chapters for their detailed analysis. A brief overview of the contents of each chapter is given below.

Chapter 2 describes the basic structure of an electric drive. The main components are briefly described. The mechanical load types commonly found in industrial processes are enumerated and the drive operating modes are described. Commonly used control strategies of ac machines are presented through block diagrams.

Chapter 3 gives an insight into induction motor drive and machine parameter identification techniques found in literature. The methods promising accurate parameters are implemented on the laboratory test rigs for verification along with proposing improvements. A state-of-the-art control strategy of Unified Direct Flux Vector Control (UDFVC) is applied for ascertaining the benefits of self-commissioning at start-up.

Chapter 4 takes up the case of interior permanent magnet synchronous machine. Machine model is constructed for simulation. The peculiarities of this machine are highlighted besides discussing the MTPA characteristics. Machine identification techniques presented in the past (cf. 1.3.2) are studied. A new method for determining machine parameters based on high-frequency injection is proposed and its results are given. The results are compared with finite element analysis (FEA) and with machine magnetic characterization data. Finally, a technique for obtaining an estimate of permanent magnet flux is presented.

Chapter 5 focuses on the 'surface mounted' version of permanent magnet machines. The isotropic nature of the machine is discussed and difficulty in flux-weakening is commented. The same parameter estimation technique proposed in chapter 4 is adapted for this machine and results are presented.

Chapter 6 discusses the importance of torque estimation accuracy in special applications. Its dependence on machine parameters' information is highlighted and estimation accuracy improvement strategies are explored. The results are compared with torque-sensor readings.

Chapter 7 enlists the conclusions drawn through this work and makes recommendations for future work. The appendices at the end enlist the software and hardware tools used in the research along with some pictures of the hardware equipment and test machines. Excerpts from software programmes developed in the course of this work are also given for reference.

1.5.   <u>Software and hardware tools used in the research</u>

Fig. 1.2 gives a simplified system block diagram showing essential components used in this work on self-commissioning. Only the machine under test (MUT) is changed for various machine types studied, the rest of the system i.e. the inverter, acquisition and command system and the personal computer (PC), remains the same all throughout. The control algorithm is executed with Matlab Simulink on a dSpace PPC (Power PC) controller board that generates pulse width modulation (PWM) commands for the inverter and acquires physical variables from the current and voltage sensors and from the encoder for rotor position.
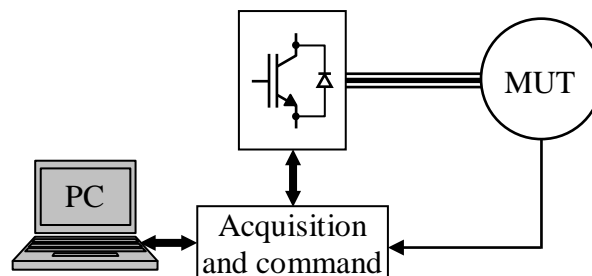
Fig. 1.2: Basic system block diagram

The self-commissioning and machine control algorithms are devised and written using two different strategies. In the first, the programme code is written in C language and compiled using Matlab's compiler for C and carried to the dSpace PPC controller board through Simulink. The second uses only Simulink blocks to perform various computations and to generate the commands. The commands generated for the physical system through both these strategies are transported on a data bus through the acquisition and command system to the inverter that generates desired voltage on the motor terminals.

The principal software used are Matlab, with Simulink and dSpace library, ControlDesk interface programme for dSpace containing virtual instruments and data acquisition facility. Finite element analysis software MagNet was used for IPMSM experimental results' comparison. Among others are some dedicated software for equipments and instruments used as an aid to verification process such as: Siemens' DC drive controller and ABB's Selicom for synchronous drive employed as prime-mover.

The hardware parts depend predominantly on the power amplifier i.e. the inverter used with different machines. The inverters were chosen according to machine ratings. The associated hardware with the inverter included the gate drivers, current and voltage sensors, signal conditioning circuits, and protection modules. In all, three different inverters were used: a 27 kVA SITRA converter, a 45 kVA Eurotherm drive, and a 22 kVA inverter controlled through an FPGA (Field Programmable Gate Array) board.

This page was intentionally left blank

Chapter – 2

FUNDAMENTALS OF ELECTRIC DRIVES

2.1.   The electric drive structure

An adjustable speed electric drive is the first choice when it comes to electromechanical energy conversion in an efficient and controlled manner. The ease and flexibility of control offered by electric drive make it a favourable alternative of mechanical drives. The efficiency improvements obtained outweigh the investments made. The essential parts of an electric drive, as shown in Fig. 2.1, are:

a) Power converter

b) Control system

c) Electrical machine

d) Load or process
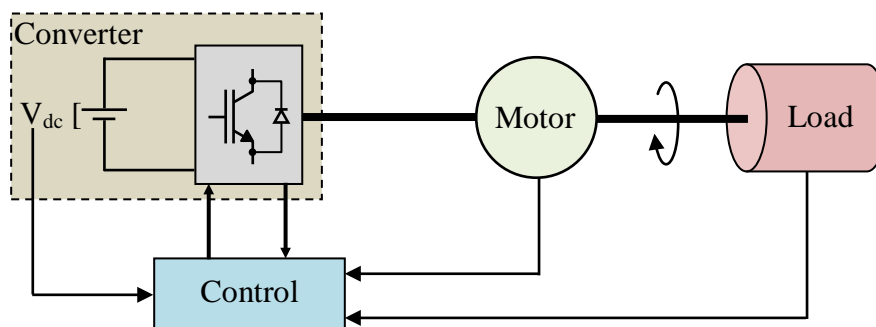
Fig. 2.1: Drive structure

2.1.1. Power converter

The power converter supplies the machine with desired three-phase voltage vectors determined by the control system. A number of converter configurations and command techniques exist which are chosen based on various system constraints and requirements. Some typical types are: voltage/current fed two-level three-phase bridge inverters, multi-level bridge inverters, cycloconverters, and matrix converters. The most widely used configuration is the voltage-fed two-level bridge converter and its control techniques are: square wave or six-step, pulse width modulation (PWM) and its variants.

Fig. 2.2 shows the construction of a two-level three-phase bridge inverter. $D_1 - D_6$ are duty cycles of opening and closing of each switch. The duty cycles give the time of persistence of closing of the switches that in turn determines the average voltage supplied to each of the phases of a three phase load. The duty cycles are generated depending on load requirements i.e. the average voltage required at load terminals. The most ubiquitous way is to use PWM technique in which a required reference signal (a sinusoid for instance) is compared against a high-frequency triangular wave called the carrier wave. The amplitude of the reference signals modulates the width of the switching pulses hence the name pulse width modulation. At each intersection of the two waves, a switching command is generated. This technique automatically takes care of the time of persistence

for each switch. Fig. 2.3 illustrates switching signals generation by a pulse width modulator for supplying sinusoidal voltage to one phase.
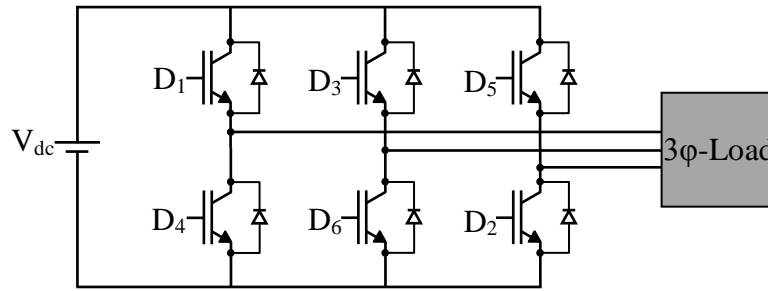
Fig. 2.2: Two-level three phase bridge inverter

Eq. (2.1) defines the carrier triangular wave.

$$
v_{tr} = \begin{cases} At & 0 < t < \dfrac{T}{2} \\ -At & \dfrac{T}{2} < t < T \end{cases} \tag{2.1}
$$

where A is the slope of the carrier and T is the period.

The modulation index, m, is defined as the ratio of required reference voltage (normalized) to the peak of triangular wave, i.e.

$$
m = \frac{v*}{\widehat{v}_{tr}} \tag{2.2}
$$

For maintaining a linear range of regulation between commanded and obtained voltages, it is necessary that $v* \leq \widehat{v}_{tr}$ or $m \leq 1$.
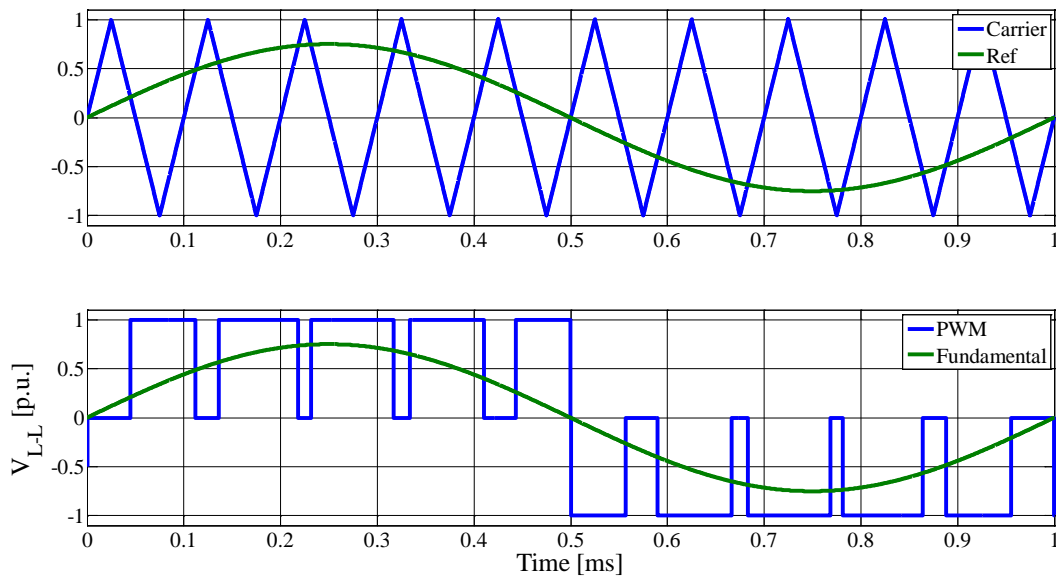
Fig. 2.3: PWM generation for one phase with $m = 0.75$

It can be seen in Fig. 2.3 (lower plot) that the phase voltage supplied to the load terminals is not sinusoidal but a train of pulses of varying widths, however, the fundamental wave obtained with

Fourier transform of these pulses shows a sinusoidal voltage of amplitude as required by the reference signal (upper plot). Usually, the frequency of the carrier wave is much higher than the reference, in Fig. 2.3 the ratio between reference voltage frequency and carrier is kept 1:10 for the sake of visualization clarity.

2.1.2. *Control system*

The main function of the control system block is to ensure that the command is executed and demand is met within certain set limits. This block hosts all the hardware and software related to control algorithms, system start-up information, data acquisition routines, signal processing, system protection checks, and command generation code. The core of the control system is a powerful microcontroller/microprocessor that executes all the routines, acquires external system variables, synchronizes the software and hardware operations, and outputs variables for visualization (if required). Fig. 2.4 shows important blocks of the control system.
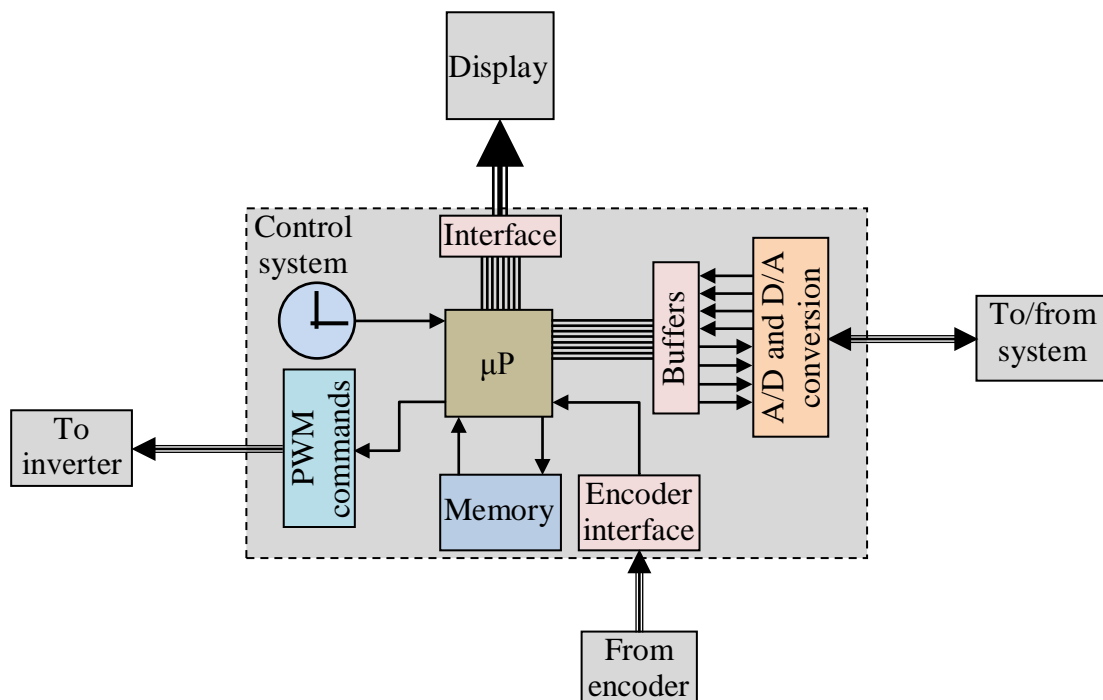
Fig. 2.4: Control system

Apart from the signals shown in Fig. 2.4, some auxiliary inputs and outputs such as hardware protection statuses, auxiliary supply alarms, temperature sensing signals and drive status commands are usually included.

2.1.3. *Electrical machine*

The electric machine is the motive element of the drive system. The machine is chosen based on various system considerations and application requirements. It can be a dc, a single-phase ac, or a three- or multi-phase ac motor. A three-phase ac machine is most widely used and various such machines will be discussed in detail in this and following chapters.

The machine produces mechanical torque demanded by the control system to be imparted to the load. The position sensing devices, such as absolute/incremental encoders, resolvers, tachometers/tacho-generators, are mounted on the shaft. They provide shaft position information to control which is indispensable for feedback controlled speed and position drives besides serving for vector control. Additionally, the machine usually hosts temperature sensors that measure temperature of critical spots inside the machine. The control uses this information to take decisions to ensure safe operation.

2.1.4. *Load or process*

Load is an equipment, machine, device or process that does useful work given the mechanical power input. In a drive system, the mechanism driven by the actuator i.e. the electric machine is what can be termed as the load. Usually, it is of rotary type in mechanical systems connected through rotating shafts, belts, pulleys, and/or gears. The type of load can be any of the myriad of applications found in daily life and in the industry such as binders, blowers, carousels, centrifuges, chippers, churners, coilers, compressors, conveyors, cranes, crushers, diggers, drills, dryers, engine starters/generators, escalators, extractors, extruders, fans, gas turbine starters, grinders, harvesters, hoists, lathes, lifts, locomotives, looms, machine tools, mixers, paper mills, piledrivers, propellers, pulverisers, pumps, reels, robots, rollers, refiners, saws/sawmills, spindles, textile mills, threshers, thrusters, tumblers, vehicles, washers, winders.

The electric motor is required to generate torque necessary to turn the shaft at the other end of which is the load. The load torque tends to oppose the motor torque which is the most primary requirement for energy conversion from one form to other i.e. there must be a resistant force. Fig. 2.5 shows the motor and load connected through a flexible shaft.
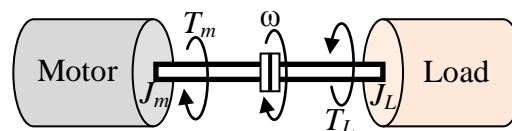
Fig. 2.5: Motor-load system

The mechanical equation of this system can be written as in (2.3).

$$T_m = J_m \frac{d\omega}{dt} + T_L + J_L \frac{d\omega}{dt} \qquad (2.3)$$

here ω is shaft speed in rad/s, J_m and J_L are motor and load moments of inertia in kg-m^2, respectively. T_L is the load torque in Nm referred to the motor shaft independently of the internal parts of the load block. During acceleration and deceleration the motor torque must also provide the inertial torque along with load torque. In steady state, however, the motor torque equals the load torque except for mechanical losses such as friction and windage losses.

Based on the direction of rotation and that of torque, the motor operation can be identified as: forward motoring, forward generation, reverse motoring, and braking. These four regions of operation are marked on a torque-speed plane (Fig. 2.6) and termed quadrants of operation. In the second and fourth quadrant when the direction of torque is opposite to that of the shaft speed, the motor works in generation mode and thus the direction of power flow is towards the power converter. For active front end converters that allow power flow in both directions (i.e. from source to load and vice versa), this generation mode of operation does not pose any problem. However, when the power converter allows one-way flow of energy, the generated power charges the dc-link capacitances to excessive levels; a braking chopper is needed to discharge the excessive dc-link voltage to a braking resistor.

2.2. The electric drive control

The drive's control system (of Fig. 2.4) receives the command from the user or supervisory control logic in a process. This command is processed based on the programmed algorithm to carry out the commanded operation. Usually, the command is in terms of position/displacement, speed or torque demand.
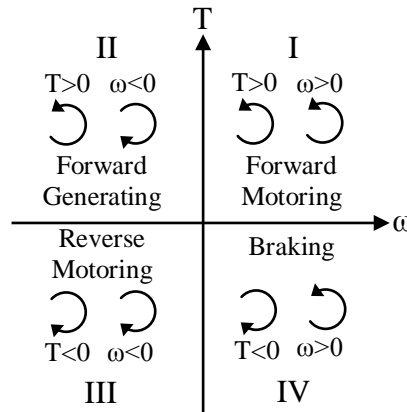
Fig. 2.6: Four quadrants of drive operation

Depending on whether a position, a speed or a torque control is needed, appropriate feedback is needed to carry out the commanded task. The mechanical position sensors are usually employed in electric drives' applications to obtain the necessary feedback for position and speed drives. In case of torque drives, however, the torque sensors are rarely used due to cost constraints; therefore the shaft torque is estimated from other measured quantities for control feedback.

Comparing the demand against the feedback, the control issues appropriate commands to the inverter to meet the demand. Since the motive element in an electric drive is an electric motor, the plant of the basic control system is the motor itself. The overall drive operation is fundamentally dependent on how efficiently the control of the electric motor works. Various motor control strategies are in use in industry that continuously evolve to respond to increasingly challenging performance and efficiency requirements.

Regardless of whether a position, speed or torque reference signal is to be tracked by the control, the electric motor always works as a generator of mechanical torque. For this reason, the control block of Fig. 2.4 must ensure that necessary torque is produced to carry out the desired control action. The electromagnetic torque of any electrical machine is a vector product of magnetic flux and current as given by (2.4) where k is a constant depending on machine data and λ and i are flux and current vectors, respectively. This expression is derived in the next chapter for an induction machine and is used throughout the rest of the chapters for other machines.

$$T_e = k\left(\overline{\lambda} \wedge \overline{i}\right)$$
(2.4)

The motor control has to make sure that the angle between current and flux vectors is maintained such that the torque obtained is at its maximum. Maintaining an optimum angle necessitates that one of these vectors is taken as a reference and the other's direction is varied to obtain the desired angle. From this basic requirement for maximizing electromagnetic torque comes the concept of vector control. The vector control has now become the most widely used control strategy. It originated as the field oriented control (FOC) of ac machines. It was first discovered by Blaschke [5] for induction machines. It is briefly described below.

Vector control finds its basis in the theory of dc machines. The dc machines had been widely used in industry in the past for their ability to give high performance torque control with fast response, reduced harmonics, low audible noise and minimal torque ripple. The secret of this performance was the ability to control machine flux and torque independently of each other. The reason for this is that in dc machines, the field circuit is always independent of the armature (torque producing) circuit, especially when separately excited dc machines are considered (Fig. 2.7). However, in the ac machines such as the induction machine, the flux and torque producing current components are hard to separate when the machine is supplied directly from the mains. The development of solid state power converters did away with this limitation and permitted

independent control of the two current components. Closed-loop current control allows application of a certain current space phasor in a given direction with respect to machine flux. Fig. 2.7 defines the analogy between dc machine and vector controlled ac machine torque production phenomenon.
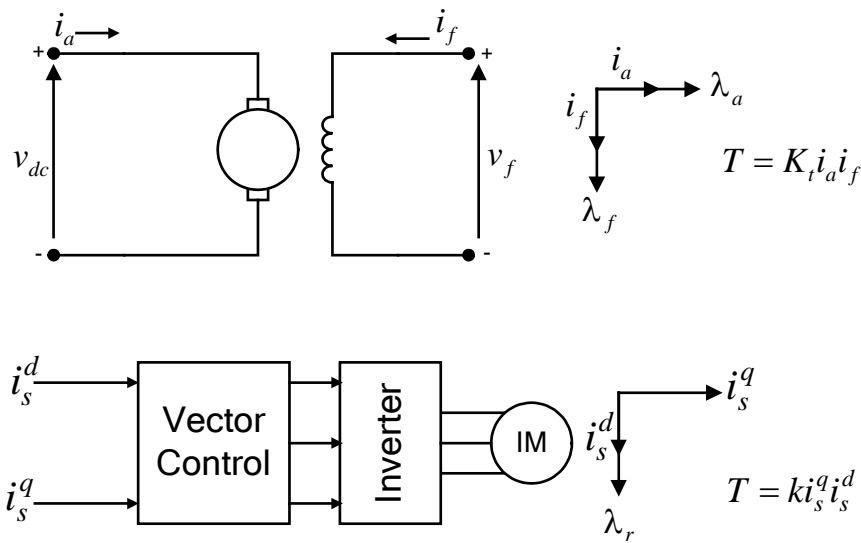
Fig. 2.7: Analogy between (separately excited) dc machine and vector controlled ac (induction) machine [111]

The vector control requires the application of a current vector in a direction fixed in space with respect to the flux vector. This is achieved only when the direction of the flux vector is known. In this situation, the '*dq*' rotating reference frame comes in handy in that once the two vectors (current and flux) are referenced to the *dq*-frame, their exact position with respect to each other is always ensured provided the *dq*-frame is accurately identified. As shown in Fig. 2.8, the flux and current vectors, after being referenced to *dq*-frame are at a certain angle (θ) and this angle remains fixed in steady state conditions when the torque demand is constant. The determination of this angle is possible when the flux vector's angle with respect to the

Fig. 2.8: Current and flux vectors in *dq*-frame

stationary axis (α) is known. The power converter discussed earlier in this chapter allows application of voltage vectors in space at any angle by commanding appropriately its power switches, what is more important is that the angle of these vectors can be changed almost instantaneously thanks to the fast switching capability of power switches. This is helpful in coping with fast torque transients. For a high dynamic response, the current vector is controlled instead of the flux vector since the current control loop can be designed with high bandwidth whereas the flux loop usually involves inherent delays, such as the rotor time constant in case of an ac induction machine.

In the following sections, a brief overview of the variants of vector control is given.

2.2.1. Rotor Field Oriented Control

When the *d*-axis of the rotating *dq* reference frame of Fig. 2.8 is tied to the rotor flux vector of the machine, the new vector diagram of Fig. 2.9 can be drawn. The control of the machine under this new vector diagram becomes the rotor field oriented control. This convention simplifies the control and allows decoupled control of flux and torque by appropriately controlling the respective current components. Depending on the type of ac machine used, the rotor field can either be that

produced by the permanent magnets (in PM machines) or through the induced currents in the rotor circuit due to transformer action of stator alternating currents (in ac induction machine).

The block diagram of Fig. 2.10 shows the rotor field oriented control of a generic speed controlled ac machine. The proportional-integral (PI) speed controller outputs torque command based on the speed error between reference and feedback inputs. The demanded torque signal is translated to d- and q-axis current demands which are then fed to two separate PI current controllers as shown. The function correlating dq currents with torque depend on the parameters of the particular machine in use. The blocks

Fig. 2.9: Rotor Field Oriented d-axis

named αβ/abc, abc/αβ, $R(\vartheta)$ and $R^{-1}(\vartheta)$ are required for transforming three-phase measured quantities to two-phase equivalent and vice versa, these are discussed in more details in the next chapter. Based on the voltage command for each phase the switching signals for the inverter switches are issued using the PWM strategy of Fig. 2.3.

The PI current controllers give appropriate d- and q-axis voltages to ensure that the desired current vector is maintained in space with respect to the rotor flux vector to generate the demanded torque as per (2.4). The position of rotor flux vector is obtained from the rotor position feedback obtained through a shaft mounted position sensor or by using a position estimation algorithm (sensorless applications). This position information is highly important for a completely decoupled flux and torque control, especially for ac induction machines. In case the rotor flux vector position contains errors, the relation between demanded torque and realized torque is no longer linear.
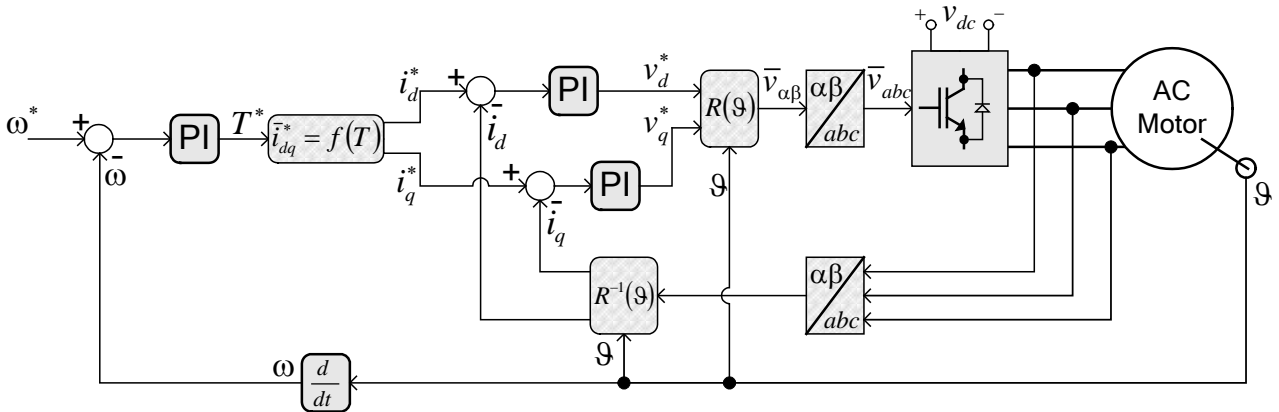
Fig. 2.10: Rotor field oriented vector control block diagram

A logical variant of rotor field oriented control is the *stator field oriented control* in which the d-axis of the dq reference frame of Fig. 2.9 coincides with the stator flux vector. The control scheme is similar to the one shown in Fig. 2.10 with minute changes.

More detailed description of rotor field oriented vector control for each ac machine considered in this thesis is given in the following chapters where the electromagnetic equations and models are discussed for each machine type.

2.2.2. *Direct Torque Control (DTC)*

Commanding the inverter switches *directly* based on the required torque demand is what is known as direct torque control. It is also called direct flux and torque control, however, since only

the mechanical torque is what matters the most in electromechanical conversion, the name is usually shortened to direct torque control only.

The direct selection of inverter switching states excludes the need for current controllers [112], as those of Fig. 2.10, and thus gives higher dynamic performance. The need for high resolution position sensor (e.g. an encoder) is also excluded as only six sectors of the complete electrical revolution are to be identified.

Individual control of the six inverter switches of Fig. 2.2 allows producing any of the six *static* voltage vectors as shown in Fig. 2.11 relative to the phases of the load. In case the load is a three-phase ac electrical machine, the phases are uniformly distributed along stator assembly thus resembling the phases *a*, *b*, and *c* of Fig. 2.11. For instance, to produce voltage vector v_4 along phase *a* of the machine, the inverter switches 1, 3, 5 are respectively controlled as 1, 0, 0 (with corresponding lower switches 6, 4, 2 commanded to 0, 1, 1, respectively). The six vectors shown in Fig. 2.11 are the *active vectors*. The numbers in the parenthesis indicate the state of the switches 1, 3, and 5. The states of the corresponding lower switches (2, 4, and 6) are simply the binary conjugates of the above switches, so they are not shown in Fig. 2.11 for simplicity. It is evident that consecutive active vectors are 60° apart that divides the entire circle in six equal sections called *sectors*. For the convenience of explaining the direct torque and flux control principle, the sectors are not named or numbered for the moment.

$$v_2(0,1,0) \qquad v_6(1,1,0)$$

$$b$$

$$v_3(0,1,1) \longleftrightarrow v_4(1,0,0)$$

$$a$$

$$c$$

$$v_1(0,0,1) \qquad v_5(1,0,1)$$
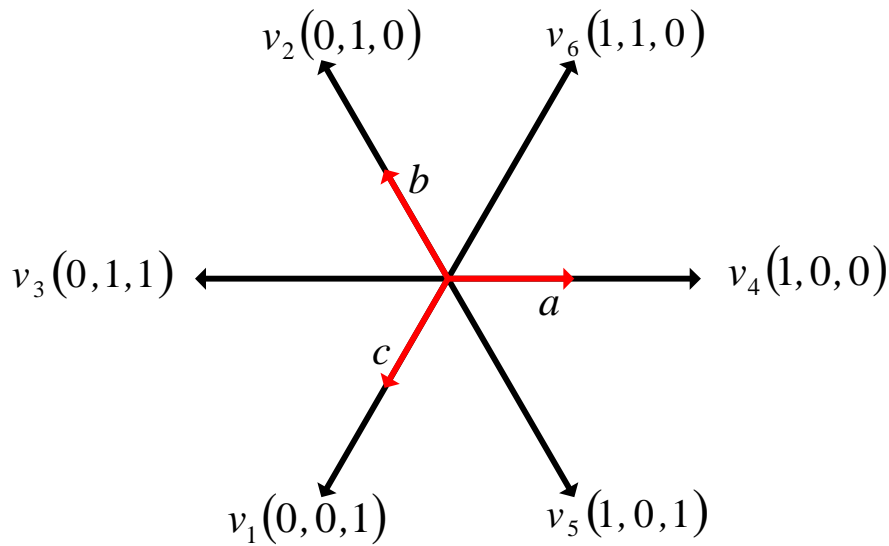
Fig. 2.11: Six possible voltage vectors for static control of inverter switches

Renaming the voltage vectors of Fig. 2.11 in increasing sequence starting from vector v_4 as $v_4 = v_I$, $v_6 = v_{II}$, $v_2 = v_{III}$, $v_3 = v_{IV}$, $v_1 = v_V$, $v_5 = v_{VI}$, the new vectors are shown in Fig. 2.12. Apart from the inverter switching states shown in Fig. 2.11, there exist two other states when all the upper or all the lower switches of Fig. 2.2 are conducting simultaneously i.e. the states (1, 1, 1) or (0, 0, 0). The voltage vectors corresponding to these states are called *null vectors*. The bisector of the two consecutive active vectors forms the sector boundary as shown by dotted line in Fig. 2.12. The sectors are numbered according to the vector they host e.g. sector-I is where the vector v_I lies.

Since the DTC requires direct control of stator flux, the torque expression (2.4) must also be modified to express the torque in terms of flux-linkages only. The expression (2.5) can be derived from (2.4) with a different constant k_2 based on ac machine at hand.

$$T_e = k_2\left(\overline{\lambda}_s \wedge \overline{\lambda}_r\right) \qquad (2.5)$$

Expanding the vector product $\qquad\qquad T_e = k_2 \lambda_s \lambda_r \sin(\delta) \qquad\qquad\qquad (2.6)$

here δ is the angle between stator and rotor flux vectors and is also called the load angle or torque angle. The expression (2.6) suggests that for a greater electromagnetic torque the angle between stator and rotor flux vectors must be increased up to a maximum of 90°. Besides, the magnitudes of the flux vectors must also be controlled in shortest possible time to give the fastest torque response to abrupt load changes.
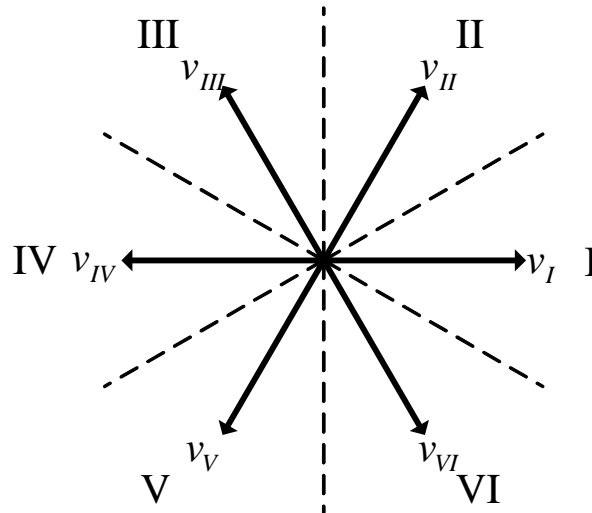
Fig. 2.12: Renaming voltage vectors of Fig. 2.11 and numbering of sectors

Depending on the sector (cf. Fig. 2.12) in which the stator flux vector lies and the direction of rotation, the next switching sequence is determined based on increase/decrease in flux and/or torque demand. Fig. 2.13 shows the impact of voltage on the stator flux vector when the flux is in sector-I of Fig. 2.12 with anticlockwise rotation and vector v_{II} of voltage is applied for a time interval Δt. After time Δt, the stator flux magnitude as well as angle with respect to rotor flux vector has changed. The rotor flux has been shown unchanged between time t and $t + \Delta t$ because for a small time interval Δt the variations in rotor flux are negligible. This is true for both induction machine as well as PM synchronous machines. The large rotor time constant in induction machines prevents instantaneous change in rotor flux vector. In PM synchronous machines, the flux magnitude is fixed by permanent magnets' flux while an abrupt change in the rotor flux angle is prevented by the mechanical inertia of the rotor (and the load, if any). Thus the application of voltage vector v_{II} increases the magnitude of the stator flux as well as accelerates it with respect to the rotor flux vector so that the net torque increases as per (2.6). The impact of other vectors can be intuited similarly through their direction with respect to stator and rotor flux vectors as shown by the vector position key in Fig. 2.13. For instance the application of vector v_{VI} would increase the magnitude of stator flux vector while decreasing its relative angle with respect to rotor flux vector thus causing a decrease in electromagnetic torque. In general, the active vectors whose angle with respect to the stator flux vector is more than 90° will decrease the magnitude of stator flux while those making acute angle with it increase its magnitude.

While the active vectors either increase or decrease the magnitude of stator flux vector, the null vectors simply retard the stator flux vector so that the rotor flux catches up and the angle δ (and hence developed torque) decreases.

Now the question arises: "When to switch from one state to the other?" The direct torque and flux control occurs through a continuous comparison between reference flux and torque and the corresponding estimated values. Since the inverter switches of Fig. 2.2 can either be fully 'ON' (conducting) or fully 'OFF' (inhibiting current through them), an intermediate or 'partial conduction' regime does not exist. In order to generate command signals compatible with the behaviour of inverter switches, a *hysteresis control* is required. This control is invariably referred to as on/off control or bang-bang control.
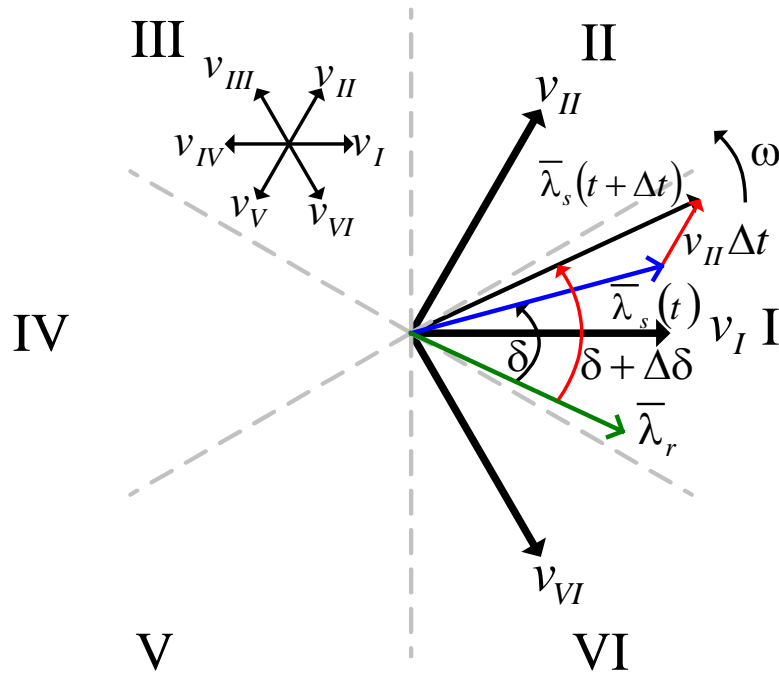
Fig. 2.13: Impact of voltage on stator flux magnitude and angle with respect to rotor flux for anticlockwise rotation

The control logic in a hysteresis controller is rather simple and can be easily implemented using basic comparators. The controller *compares* the reference signal with the measured feedback and if the difference is higher than a set tolerance level, the controller gives its maximum output as shown in Fig. 2.14 for two different strategies. On the left, the controller's output remains between 0 and 1 while in the figure on right the output varies between +1 and -1 while also passing through 0. The one-sided logic on the left is usually preferred for flux controller since the flux variation demands do not require high dynamics. However, for torque the two-sided scheme on the right must be used to meet requirements of a servo drive. Moreover, the sign of torque can be abruptly changed from positive to negative, while that of flux undergoes a delay governed by total inductance and available dc-link voltage.

Fig. 2.15 shows a basic direct torque and flux control scheme using the hysteresis controllers of Fig. 2.14. The feedback for flux and torque controllers is estimated using the machine's electrical variables. While the current is measured through current sensors, the voltage vector is reconstructed using the inverter duty cycles and the measured dc link voltage. The sector is determined using only the position of flux vector based on which the next switching state is selected. For this reason, the rotor position sensor is not strictly required. However, at extremely low speeds, the flux estimation is not as reliable that calls for rotor position sensing.
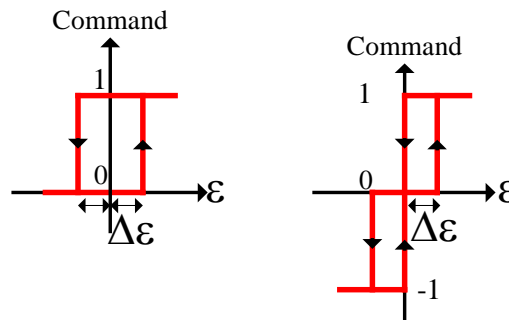
Fig. 2.14: Two different implementations of a hysteresis controller
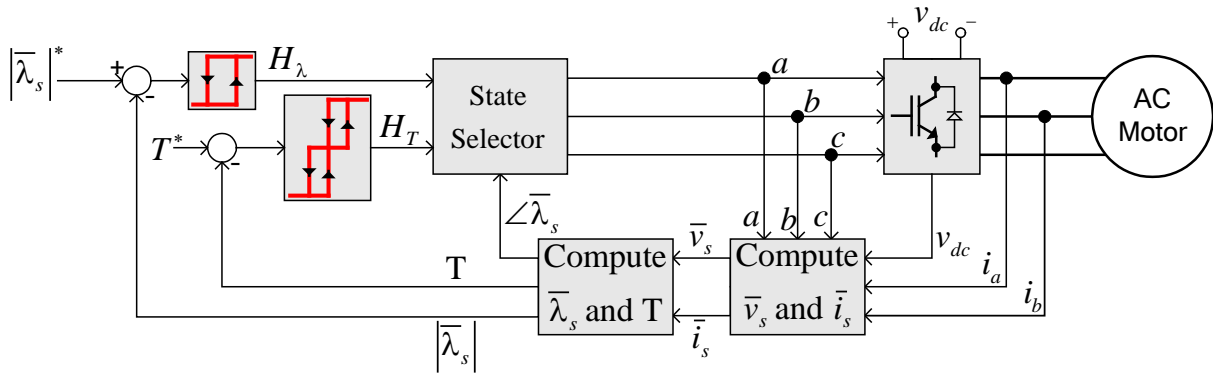
Fig. 2.15: Direct torque and flux control scheme

The switching state selection takes place based on the outputs of the flux and torque hysteresis controllers. It is also dependent on the direction of rotation of the machine. Referring to the impact of stator voltage on flux and torque (cf. Fig. 2.13), the switching sequence of Table I can be constructed. The first row gives the output of flux controller (H_λ) while the second contains the torque controller's output (H_T). Based on the sector in which the flux vector lies, the next switching state is given in terms of the voltage vector to be applied according to Fig. 2.11. Although the null vectors v_0 and v_7 have the same effect of slowing down the stator flux vector (thus momentarily reducing the torque), they are selected in order to make minimum switch transitions. For instance, after the application of vector v_1 $(0, 0, 1)$ of Fig. 2.11 if a null vector is required, the vector v_0 $(0, 0, 0)$ is a more efficient choice than v_7 $(1, 1, 1)$. This condition is taken care of in Table I.

Table I: Switching state selection

Rotation: **anticlockwise**

H_λ	0			1		
H_T	-1	0	1	1	0	-1
Flux in						
sector-I	v_1	v_0	v_2	v_6	v_7	v_5
sector-II	v_5	v_7	v_3	v_2	v_0	v_4
sector-III	v_4	v_0	v_1	v_3	v_7	v_6
sector-IV	v_6	v_7	v_5	v_1	v_0	v_2
sector-V	v_2	v_0	v_4	v_5	v_7	v_3
sector-VI	v_3	v_7	v_6	v_4	v_0	v_1

Rotation: **clockwise**

H_λ	0			1		
H_T	-1	0	1	1	0	-1
Flux in						
sector-I	v_2	v_0	v_1	v_5	v_7	v_6
sector-II	v_3	v_7	v_5	v_4	v_0	v_2
sector-III	v_1	v_0	v_4	v_6	v_7	v_3
sector-IV	v_5	v_7	v_6	v_2	v_0	v_1
sector-V	v_4	v_0	v_2	v_3	v_7	v_5
sector-VI	v_6	v_7	v_3	v_1	v_0	v_4

Some properties of Table I must be highlighted here which inherently ensure that the commutation losses occurring in the semiconductor switches during operation are a minimum. Adjacent columns and rows differ from one another by only one switching state. For instance, in the anticlockwise direction of rotation with flux located in sector-I and the flux controller's output

remaining 0, when the torque controller changes its output from -1 to 0, the switching from vector v_1 to v_0 occurs causing only the change in state of one switch (that of phase *c*) i.e. from (0, 0, 1) to (0, 0, 0). Similarly, when the torque hysteresis controller has 1 at its output and the flux controller also goes from 0 to 1, the change is between active vectors v_2 and v_6 i.e. from (0, 1, 0) to (1, 1, 0). The same condition can be verified when a change of sector occurs. However, there is only one exception here i.e. the alternate switching between the two null vectors v_0 to v_7 and vice versa when the torque controller's output latches to 0 and the machine keeps rotating (i.e. the sectors keep changing). This condition usually occurs at no-load only because when the machine is loaded, the torque controller's output keeps alternating between -1 and 1 passing through 0 to satisfy the load demand continuously. At no-load, the current through the semiconductor switches is at its minimum and hence the commutation losses are also low. For approaching ideality in terms of efficiency, the switching state selector algorithm can be programmed to avoid frequent switching between the two null vectors to keep the commutation losses to absolute minimum.

Fig. 2.16 shows stator flux trajectory during a typical direct torque control cycle. The hysteresis band for flux control is shown with red circles; the control must keep the flux inside this band. The direction of rotation is shown as anticlockwise and it is assumed that the torque controller's output is latched to 1, i.e. the demanded torque is greater than the torque generated by the machine. It can be seen that as the flux vector changes sector, the switching state also changes even though the flux remains within the hysteresis band. As soon as the flux vector hits the upper or lower boundary the hysteresis flux controller changes state and the state selector of Fig. 2.15 changes the voltage vector to be applied in accordance with Table I. It is evident that if the hysteresis band is too narrow, the number of switching states per cycle is higher thus causing more commutation losses in the semiconductor switches. On the other hand, an excessively wide band would deteriorate the drive performance. Thus, the band selection should take into account both of these aspects.
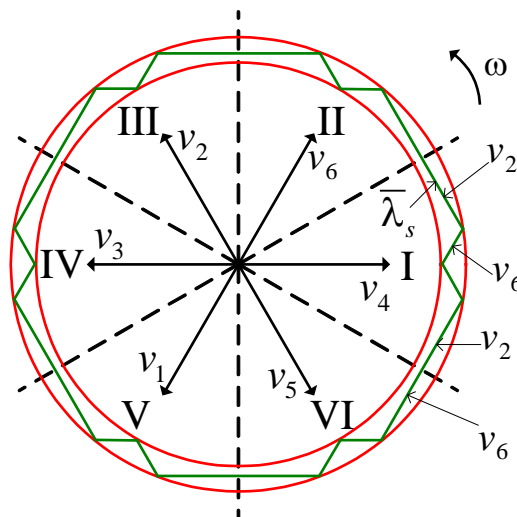
Fig. 2.16: Stator flux vector trajectory during direct torque control with $H_T = 1$

2.2.3.   *Unified Direct Flux Vector Control (UDFVC)*

In the previous two sections, two commonly used control techniques are discussed. While the field oriented current control strategy gives less torque ripple but also has inferior dynamic response especially for flux regulation, the direct torque control has better dynamic performance but it comes with more torque ripple that causes noise and mechanical wear. The Unified Direct Flux Vector Control (UDFVC) is a hybrid of these two and combines the advantages of both. Although the direct control of inverter switches (as in DTC) does not take place, the higher dynamics in flux control are achieved anyway. The torque control is through current control loop similar to the ones shown in Fig. 2.10.

The UDFVC operates in stator flux-oriented frame in which the *d*-axis of the reference frame is tied to the stator flux magnitude instead of rotor flux (cf. Fig. 2.9). In the stator flux frame, the generic voltage equation of an ac machine can be written as in (2.7). When resolved into *dq* components while assuming that all the stator flux remains along the *d*-axis, the *d*-axis equation simplifies to (2.8).

$$\overline{v}_s = R_s \overline{i}_s + \frac{d\overline{\lambda}_s}{dt} \tag{2.7}$$

In the *d*-axis
$$v_{sd} = R_s i_{sd} + \frac{d\lambda_s}{dt} \tag{2.8}$$

It can be observed in (2.8) that the stator flux can be controlled by acting on the *d*-axis voltage directly without passing through any current controllers, thus the name 'direct flux control'. In UDFVC scheme, the stator flux is controlled through a high bandwidth PI controller using (2.8). The PI controller takes in the command in terms of flux magnitude and outputs *d*-axis voltage command to establish commanded stator flux magnitude.

With the stator flux established by the flux controller as above, the mechanical torque produced by the machine can be controlled by maintaining an appropriate current vector with respect to the flux vector (cf. Fig. 2.7 in section 2.2). Referring again to Fig. 2.9, the position and magnitude of current vector with respect to flux vector depends on the magnitude of the *q*-axis current component. Thus a PI current controller is all that is needed in the *q*-axis to control the torque produced as can be deduced from (2.4).

Fig. 2.17 shows a generic UDFVC scheme for all ac machines. Comparing with the DTC scheme of Fig. 2.15, it can be observed that the flux and torque are both controlled through PI regulators. The use of PWM for generating switching commands in accordance with Fig. 2.3 is another difference between this control scheme and the DTC. More detailed equations for implementing this control strategy for all the machines considered in this thesis are derived in the following chapters.
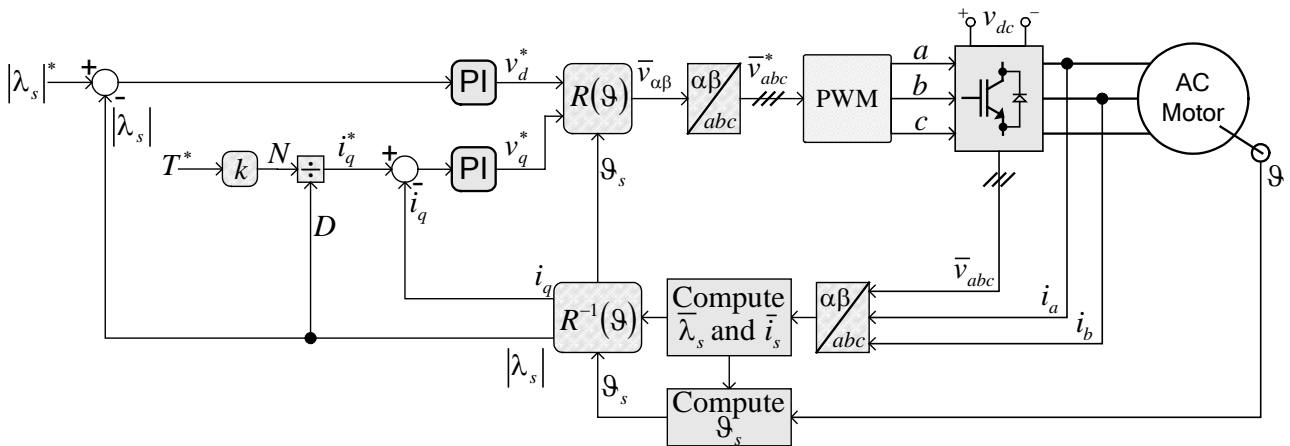
Fig. 2.17: Unified Direct Flux Vector Control scheme

2.3.   Measured quantities in a standard drive

Accurate measurement of essential physical variables of the drive is important for proper operation and control. In a standard drive supplying a three-phase machine through a power converter of Fig. 2.2, at least two of the three phase currents must be measured to properly implement the control techniques discussed in section 2.2. The third phase current is usually not

measured and it is computed from the other two exploiting the zero-sum definition of isolated neutral systems. In the laboratory environment, however, all three currents are measured for allowing operation for machines with star point connection. Moreover, the dc-link voltage is also required for all three control strategies. Specifically, the dc-link voltage is necessary for generating pulse width modulated commands for the inverter switches in case the control of Fig. 2.10 and Fig. 2.17 is implemented. For the direct torque control of Fig. 2.15, the dc-link voltage is used to reconstruct the stator voltage vector for flux estimation and sextant identification as well as for torque estimation. Apart from these three variables, the rotor position is almost always measured for better control accuracy. Other quantities such the shaft torque and stator winding temperature are sometimes measured for better supervisory control and for safety reasons.

The measurement of current occurs either through current transformers or through high precision Hall Effect current sensors. The latter are usually preferred due to low cost and weight. The accuracy of commercially available Hall Effect current sensors ranges from 0.002% to 1%. Similarly, the accuracy of the voltage sensing devices used for dc-link voltage measurement goes from 0.2% to 1.2%.

Of the other measurement signals commonly used is the rotor position information. For closed loop speed control (of Fig. 2.10) and for position servo drives, the rotor position is so important that its direct measurement is preferred over its estimation (sensorless drives). The position sensing devices are usually of two types: (i) optical encoders, (ii) resolvers, and (iii) tachogenerators.

The optical encoders are either incremental type or absolute position indicators. They use a lined disc rotating between two light sources and optical detectors. The markings on the disc act as light barriers. Between two lines is a transparent gap that allows light to pass through the disc and strike the optical detectors which are usually photo-transistors. The optical detectors generate a voltage pulse every time they are illuminated. The two detectors are phase shifted so that their pulses are also phase shifted. The voltage pulses from these detectors are transmitted to the control system of Fig. 2.4. The train of pulses received is transformed to absolute or relative (to a reference point) rotor position. The position information obtained from the pulse train defines the type of the encoder: absolute or incremental.

A resolver is suited for position sensing in extreme environments and for drives needing high reliability. A resolver is a rotating transformer with two coils 90° apart on the stator and a single coil on the rotor. The rotor coil is supplied with a sinusoidal signal (through brushes or using brushless excitation) and with the rotor's mechanical rotation its coupling with the two stator coils changes continuously. The sinusoidal voltage induced in the two stator coils due to rotor excitation is modulated in terms of position due to rotor's rotation. Demodulating this stator voltage using the known excitation frequency of the rotor coil gives the rotor position.

A tachogenerator is a small generator mounted on the shaft whose speed is to be measured. At its stator terminals it produces a voltage (dc or ac) which is proportional to the speed of the shaft. They employ either coils or permanent magnets as their rotor excitation. The choice between coils and magnets is governed by the environment in which it is to be used. As they measure the speed and not the position, the position has to be obtained as an integral of the speed. Therefore they are preferred for mills and not for servomotors.

For the experimental work performed during the research and presented in this thesis, the incremental encoders are mostly used as position transducers. A resolver is only used for the closed-loop speed control of a synchronous machine used as prime mover for loading the test machines.

2.4.   Practical issues – inverter dead time effects

The definition of self-commissioning, which is the core theme of this thesis, imposes restrictions on the use of additional measuring and analysis equipment for the tests to be proposed here. These limitations force the use of only the available signals and measurements (as discussed in section 2.3 above). This gives rise to some practical issue that must be addressed. The consequence most relevant to the work presented here is the unavailability of the measure of machine terminal voltage. This signifies that the terminal voltage must be reconstructed from the switch commands (Fig. 2.3) and the measured dc-link voltage.

It can be observed in Fig. 2.2 that for obtaining the voltage at load terminals using the dc-link voltage and switch commands, the characteristics of the power semiconductor devices must be known. The phase voltage calculated upstream of the switches does not all appear at the load terminals due to the semiconductor switches in the middle. The effects of these switches are mainly four: (i) semiconductor switch threshold voltage necessary for driving them into conduction, (ii) a definite on-state resistance during conduction, (iii) the dead-time i.e. a finite time that must elapse between opening of upper switch of an inverter leg and closing of lower switch of the same leg (to avoid a shoot-through fault at the dc bus), and (iv) output voltage transition slope. The third and fourth are usually lumped together under the heading of dead time effects. The overall effect of inverter switches appears as voltage drop at the switches, which is a non-linear function of the current through the switches. This voltage drop acts as an error between the voltage reference command issued to PWM block (as per Fig. 2.3) and the actual voltage appearing across load terminals. These errors are commonly referred to as the inverter non-linearity effects.

The errors due to inverter non-linearity distort the machine currents when a sinusoidal voltage is applied. The distortion is the maximum around current zero-crossings as the switches alternate between inhibition and conduction modes. These errors affect low-speed performance of sensorless control schemes that rely on the voltage model flux estimation. In the scope of the work presented in this thesis, the inverter switches' non-linear behaviour affects the accuracy of machine parameters estimation. Therefore, these errors need to be taken care of while using the reference voltage to the PWM block as an alternative to the actual machine terminal voltage.

The inverter effects have been modelled in the past for their accurate compensation by [113]. The inverter non-linearity effects are identified through distortion in the current for a sinusoidal voltage application to a test induction machine. The distortions are removed using a compensation strategy which is carried out by modifying only one parameter called compensation time. A more recent work in this regard is that presented in [114] for sensorless induction motor drives and in [115] for generic ac drives. In these works, the inverter errors are quantified and stored in the form of look-up tables. These look-up tables are then accessed and interpolated during continuous operation and the voltage is corrected according to the current levels. In this thesis, the inverter non-linearity effects are compensated for through the look-up tables of these works.

This page was intentionally left blank

Chapter – 3

INDUCTION MOTOR DRIVE

3.1. <u>Motor equivalent circuits</u>

The induction motor is sometimes called a 'rotating transformer' because of the similarity of its working principle and equivalent circuit with those of a transformer. In fact, the most detailed single-phase equivalent circuit of the induction machine (Fig. 3.1) is termed the transformer equivalent circuit. Variants of this equivalent circuit exist and are discussed below along with the equations describing the operation mathematically in steady state and transient conditions.
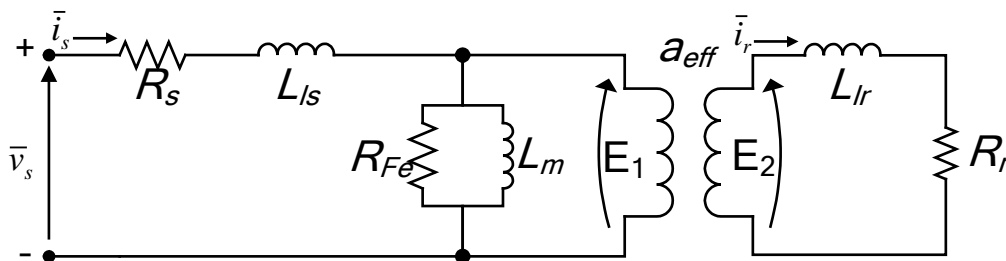
Fig. 3.1: Transformer equivalent circuit of induction machine

In the equivalent circuit of Fig. 3.1, R_s is the stator winding resistance and L_{ls} is the total stator leakage inductance that includes all the effects of slot leakage, tooth tip leakage, end-winding leakage, leakage due to harmonics, slot skewing leakage, and pole leakage. Similarly, R_r is the rotor resistance (winding resistance in case of wound rotor induction motor and rotor bars' resistance for squirrel cage rotor) and L_{lr} is the leakage inductance attributed to flux leakage due to rotor slots, slot skewing and harmonics [116, 117]. The magnetizing branch consists of magnetizing inductance L_m and the core loss equivalent resistance R_{Fe}. The stator and rotor sides are coupled through the airgap represented by an equivalent ideal transformer with effective turns ratio a_{eff}.

Since in a squirrel cage motor the rotor is not connected with any external voltage/current source, it is convenient to refer the rotor quantities to stator (using effective turns-ratio a_{eff} and the motor slip s). The new equivalent circuit is shown Fig. 3.2 retaining the notation for rotor quantities as in Fig. 3.1.
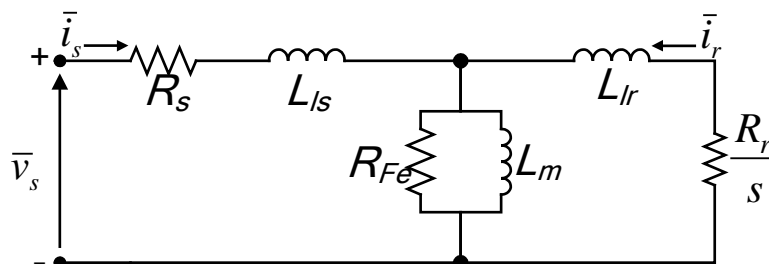
Fig. 3.2: Equivalent circuit with rotor quantities referred to stator side

The equivalent circuit of Fig. 3.2 is often called the 'T equivalent circuit' for its resemblance with the letter 'T' in shape. As an initial approximation, the core loss resistance R_{Fe} is neglected and the magnetizing branch consists solely of the magnetizing inductance.

Before writing the electromagnetic equations, following assumptions are made [118, 119]:

i)   Magnetic linearity i.e. machine inductances are independent of current levels

ii)   The stator winding, and hence mmf, distribution is perfectly sinusoidal

iii)   Slot openings are neglected, so the machine is perfectly isotropic

iv)   Rotor is perfectly cylindrical with no saliencies

v)   The laminations of stator and rotor are such that there are zero eddy currents

vi)   Hysteresis effects are neglected in both stator and rotor

vii)   The magnetic flux lines always cross the airgap radially

Although some of these assumptions will be relaxed later on to take into account the causes of parameter variation, they are necessary first up for developing equations. For instance the magnetic saturation is neglected as per assumption (i) but the same will be taken care of when its effects on magnetizing inductance variation will be analysed.

The stator and rotor voltage equations for the three phase machine are written in matrix form as:

$$
\begin{bmatrix} v_s^1 \\ v_s^2 \\ v_s^3 \end{bmatrix} = \begin{bmatrix} R_s & 0 & 0 \\ 0 & R_s & 0 \\ 0 & 0 & R_s \end{bmatrix} \cdot \begin{bmatrix} i_s^1 \\ i_s^2 \\ i_s^3 \end{bmatrix} + \frac{d}{dt} \begin{bmatrix} \lambda_s^1 \\ \lambda_s^2 \\ \lambda_s^3 \end{bmatrix}
\tag{3.1}
$$

$$
\begin{bmatrix} v_r^1 \\ v_r^2 \\ v_r^3 \end{bmatrix} = \begin{bmatrix} R_r & 0 & 0 \\ 0 & R_r & 0 \\ 0 & 0 & R_r \end{bmatrix} \cdot \begin{bmatrix} i_r^1 \\ i_r^2 \\ i_r^3 \end{bmatrix} + \frac{d}{dt} \begin{bmatrix} \lambda_r^1 \\ \lambda_r^2 \\ \lambda_r^3 \end{bmatrix}
\tag{3.2}
$$

The subscripts 's' and 'r' identify the stator and rotor quantities, respectively; phase numbers are given in the superscripts. Here λ^n is the flux linkage of phase 'n'.

A more compact and efficient way to write equations (3.1) and (3.2) is the 'vectorial notation' in which the voltages, currents and fluxes are represented by vectors (with an over-bar) as in (3.3) and (3.4).

$$
\bar{v}_s = R_s \bar{i}_s + \frac{d\bar{\lambda}_s}{dt}
\tag{3.3}
$$

$$
\bar{v}_r = R_r \bar{i}_r + \frac{d\bar{\lambda}_r}{dt}
\tag{3.4}
$$

The stator and rotor flux linkages, namely λ_s and λ_r, are defined as:

$$
\bar{\lambda}_s = L_s \bar{i}_s + L_m \bar{i}_r
\tag{3.5}
$$

$$\overline{\lambda}_r = L_m \overline{i}_s + L_r \overline{i}_r \tag{3.6}$$

here L_s is the total inductance seen from stator terminals with rotor side open-circuited and L_r is the inductance seen from rotor side with open stator terminals. The following relations hold.

$$L_s = L_{ls} + L_m \tag{3.7}$$

$$L_r = L_{lr} + L_m \tag{3.8}$$

Equations (3.5) and (3.6) are called the magnetic equations of the machine as they express the relationship between currents and magnetic flux.

Symmetrical three phase machines' equations are more conveniently analysed and solved by first converting them to their equivalent two phase machines. The two-phase equivalent is obtained by transforming the equations using Clarke's transform. The transformation matrices that convert three phase (*123* notation) magnitudes to equivalent two phases (αβ) and vice versa are as given by (3.9).

$$T = \underbrace{\begin{bmatrix} 1 & 0 & 0 \\ 0 & \dfrac{1}{\sqrt{3}} & \dfrac{-1}{\sqrt{3}} \end{bmatrix}}_{123 \rightarrow \alpha\beta} \qquad T^{-1} = \underbrace{\begin{bmatrix} 1 & 0 \\ \dfrac{-1}{2} & \dfrac{\sqrt{3}}{2} \\ \dfrac{-1}{2} & \dfrac{-\sqrt{3}}{2} \end{bmatrix}}_{\alpha\beta \rightarrow 123} \tag{3.9}$$

Expressing the three-phase quantities in equivalent two-phase (αβ) notation does not alter equations (3.3) and (3.4) or equations (3.5) and (3.6), they continue to hold good in their vectorial notation. However, since the scalars in the direction of unit vectors α and β are perpendicular to each other, they can also be written in complex numbers' notation.

$$\overline{v}_s^{\alpha\beta} = v_s^{\alpha} + j v_s^{\beta} = R_s \overline{i}_s^{\alpha\beta} + \frac{d\overline{\lambda}_s^{\alpha\beta}}{dt} \tag{3.10}$$

$$\overline{v}_r^{\alpha\beta} = v_r^{\alpha} + j v_r^{\beta} = R_r \overline{i}_r^{\alpha\beta} + \frac{d\overline{\lambda}_r^{\alpha\beta}}{dt} \tag{3.11}$$

Similarly, $\qquad \overline{i}_s^{\alpha\beta} = i_s^{\alpha} + j i_s^{\beta} \quad and \quad \overline{\lambda}_s^{\alpha\beta} = \lambda_s^{\alpha} + j\lambda_s^{\beta}$

A further transformation of these equations is the rotational transformation which carries these equations to an arbitrary rotating reference frame for convenience in dealing with them. Rotational transformation, also called dq transform, converts the equations of ac machines to an arbitrary rotating reference frame where sinusoidal quantities appear as vectors of constant magnitudes and angles fixed with respect to one another. Fig. 3.3 shows the geometrical relationship between vectors in different reference frames, ω is the speed (rad/s) of the dq rotating reference frame. All the vectors expressed in terms of this reference frame will have constant magnitudes.
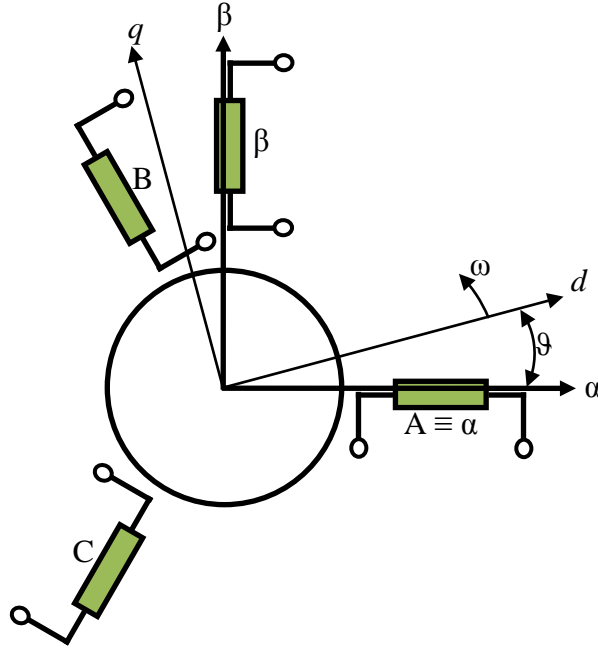
Fig. 3.3: Relationship between stator's three-phase and two-phase vectors

The rotational transformation occurs through transformation matrix R(ϑ) and the reverse, i.e. from constant dq quantities to αβ stationary reference frame, occurs through the $R^{-1}(\vartheta)$ matrix, the two matrices can also be defined in terms of complex rotational operator. The matrices along with complex operators are given in (3.12).

$$R(\vartheta) = \begin{bmatrix} \cos\vartheta & \sin\vartheta \\ -\sin\vartheta & \cos\vartheta \end{bmatrix} = e^{-j\vartheta} \qquad \underbrace{\qquad}_{\alpha\beta \to dq} \qquad R^{-1}(\vartheta) = \begin{bmatrix} \cos\vartheta & -\sin\vartheta \\ \sin\vartheta & \cos\vartheta \end{bmatrix} = [R(\vartheta)]^T = e^{j\vartheta} \quad (3.12)$$

We can now transform equations (3.10) and (3.11) to the reference frame rotating at a synchronous speed of ω radians per second as below.

$$e^{-j\vartheta} \left\{ \overline{v}_s^{\alpha\beta} = R_s \overline{i}_s^{\alpha\beta} + \frac{d\overline{\lambda}_s^{\alpha\beta}}{dt} \right\}$$

$$e^{-j\vartheta} \ \overline{v}_s^{\alpha\beta} = \overline{v}_s^{dq} \qquad and \qquad e^{-j\vartheta} \ \overline{i}_s^{\alpha\beta} = \overline{i}_s^{dq}$$

To transform $\dfrac{d\overline{\lambda}_s^{\alpha\beta}}{dt}$, care must be taken because it involves derivative with respect to time and the rotational transformation involves ϑ that is a function of time. The transformation is carried out as follows:

Since
$$\overline{\lambda}_s^{dq} = R(\vartheta)\overline{\lambda}_s^{\alpha\beta} = e^{-j\vartheta}\overline{\lambda}_s^{\alpha\beta}$$

so
$$\overline{\lambda}_s^{\alpha\beta} = R^{-1}(\vartheta)\overline{\lambda}_s^{dq} = e^{j\vartheta}\overline{\lambda}_s^{dq}$$

substituting this in the derivative term, we have

$$\frac{d}{dt}\left(e^{j\vartheta}\overline{\lambda}_s^{dq}\right) = \overline{\lambda}_s^{dq}\frac{de^{j\vartheta}}{dt} + e^{j\vartheta}\frac{d\overline{\lambda}_s^{dq}}{dt}$$

$$\frac{d}{dt}\left(e^{j\vartheta}\overline{\lambda}_s^{dq}\right)= j\overline{\lambda}_s^{dq}e^{j\vartheta}\frac{d\vartheta}{dt}+e^{j\vartheta}\frac{d\overline{\lambda}_s^{dq}}{dt}$$

$$= j\omega\overline{\lambda}_s^{dq}e^{j\vartheta}+e^{j\vartheta}\frac{d\overline{\lambda}_s^{dq}}{dt}$$

Now, multiplying the right-hand-side with the rotational operator, we get:

$$e^{-j\vartheta}\left\{ j\omega\overline{\lambda}_s^{dq}e^{j\vartheta}+e^{j\vartheta}\frac{d\overline{\lambda}_s^{dq}}{dt} \right\}= j\omega\overline{\lambda}_s^{dq}+\frac{d\overline{\lambda}_s^{dq}}{dt}$$

As said above, ω is the angular speed of the revolving reference frame dq with respect to the stationary stator windings. The voltage equations in dq reference frame can thus be written as below.

$$\overline{v}_s^{dq} = R_s\overline{i}_s^{dq} +\frac{d\overline{\lambda}_s^{dq}}{dt}+ j\omega\overline{\lambda}_s^{dq} \tag{3.13}$$

$$\overline{v}_r^{dq} = R_r\overline{i}_r^{dq} +\frac{d\overline{\lambda}_r^{dq}}{dt}+ j(\omega - p\omega_r)\overline{\lambda}_r^{dq} \tag{3.14}$$

In the rotor equation, Eq. (3.14), ω_r is the rotor mechanical speed (in rad/s) and p is the number of machine pole pairs. A special case of (3.13) and (3.14) is when the equations are referred to a common reference frame that is stationary with respect to both the stator and the rotor i.e. ω = 0. From Fig. 3.3, the stationary reference frame is αβ-frame so the equations (3.13) and (3.14) are written below with αβ superscripts.

$$\overline{v}_s^{\alpha\beta} = R_s\overline{i}_s^{\alpha\beta} +\frac{d\overline{\lambda}_s^{\alpha\beta}}{dt} \tag{3.15}$$

$$\overline{v}_r^{\alpha\beta} = R_r\overline{i}_r^{\alpha\beta} +\frac{d\overline{\lambda}_r^{\alpha\beta}}{dt}- jp\omega_r\overline{\lambda}_r^{\alpha\beta} \tag{3.16}$$

Equations (3.15) and (3.16) differ from (3.10) and (3.11) in that (3.10) and (3.11) were referred to the individual αβ-axes of the stator and rotor respectively. Now they are referred to a common reference frame which is stationary with respect to both (stator and rotor). It can be observed that (3.15) is the same as (3.10), however, (3.16) has an additional term with respect to (3.11) and it is the motional emf as a result of moving rotor with respect to stationary αβ-axes.

The vectors $\overline{v}_s^{dq}$, $\overline{i}_s^{dq}$, and $\overline{\lambda}_s^{dq}$ of equations (3.13) and (3.14) can all be represented on a complex plane as well, since the individual d and q components are perpendicular to each other, as per the definition (Fig. 3.3). Equations (3.13) and (3.14) in their individual d and q components are expanded below for clarity.

$$v_s^d = R_s i_s^d +\frac{d\lambda_s^d}{dt}- \omega\lambda_s^q \tag{3.17}$$

$$v_s^q = R_s i_s^q +\frac{d\lambda_s^q}{dt}+ \omega\lambda_s^d \tag{3.18}$$

$$v_r^d = R_r i_r^d + \frac{d\lambda_r^d}{dt} - (\omega - p\omega_r)\lambda_r^q \tag{3.19}$$

$$v_r^q = R_r i_r^q + \frac{d\lambda_r^q}{dt} + (\omega - p\omega_r)\lambda_r^d \tag{3.20}$$

The usefulness of transformations described above and the resulting equations will be evident when the control of the machine is discussed later in this chapter.

Coming back to equations (3.15) and (3.16) let $p = 1$ for simplicity. Omitting the superscripts 'αβ' for convenience and substituting (3.5) and (3.6) and, assuming that the rotor is squirrel-cage with no voltage source, we have the following voltage equations.

$$\bar{v}_s = R_s \bar{i}_s + \frac{d}{dt}\left(L_s \bar{i}_s + L_m \bar{i}_r\right) \tag{3.21}$$

$$\bar{v}_r = \bar{0} = R_r \bar{i}_r + \frac{d}{dt}\left(L_r \bar{i}_r + L_m \bar{i}_s\right) - j\omega_r \bar{\lambda}_r \tag{3.22}$$

The motional back-emf term ($j\omega_r\bar{\lambda}_r$) in the rotor equation is kept as it is for simplicity. Substituting further equations (3.7) and (3.8),

$$\bar{v}_s = R_s \bar{i}_s + \frac{d}{dt}\left(L_{ls} \bar{i}_s + L_m \bar{i}_s + L_m \bar{i}_r\right)$$

$$\bar{0} = R_r \bar{i}_r + \frac{d}{dt}\left(L_{lr} \bar{i}_r + L_m \bar{i}_r + L_m \bar{i}_s\right) - j\omega_r \bar{\lambda}_r$$

defining
$$\bar{i}_m = \bar{i}_s + \bar{i}_r$$

$$\bar{v}_s = R_s \bar{i}_s + \frac{d}{dt}\left(L_{ls} \bar{i}_s + L_m \bar{i}_m\right) \tag{3.23}$$

$$\bar{0} = R_r \bar{i}_r + \frac{d}{dt}\left(L_{lr} \bar{i}_r + L_m \bar{i}_m\right) - j\omega_r \bar{\lambda}_r \tag{3.24}$$

Equations (3.23) and (3.24) describe the induction machine in its T-equivalent circuit which is redrawn below, in Fig. 3.4, to signify the quantities appearing in the equations.
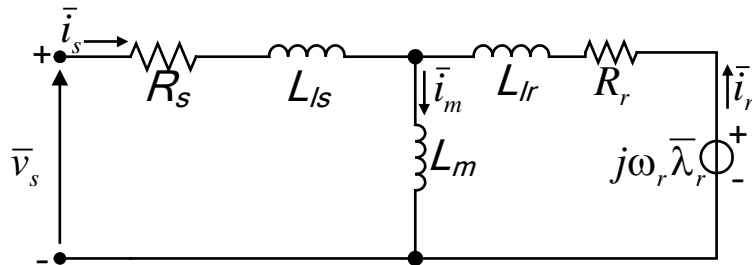
Fig. 3.4: T-equivalent circuit described by equations (3.23) and (3.24)

Other variants of induction motor equivalent circuit exist that reduce the number of unknown parameters in the circuit which help design controllers and simplify machine modelling (for simulation). One way to simplify the circuit is to lump the stator and rotor leakage inductances

(L_{ls} and L_{lr}) into one for two reasons: a) they are very small in value compared to the magnetizing (or main) inductance L_m; b) their values differ minutely from each other.

The alternative equivalent circuits are useful also for the parameter identification purposes which is the core objective of this thesis. The tests performed on the machines and observed signals are explained directly on the basis of these circuits. They are derived by manipulating the voltage equations (3.21) and (3.22) and are given appropriate names.

The equivalent circuit in which leakage inductances of the stator and the rotor both appear in stator branch is called the inverse–Γ equivalent circuit for it resembles the Greek capital letter Γ but mirrored. The circuit is obtained below.

By assuming that the entire leakage inductance is in the stator side, it is meant that the rotor side of the equivalent circuit contains only the rotor resistance and the motional back-emf. For this condition to hold, the equivalent circuit becomes as shown in Fig. 3.5 below. Except R_s, the components are not named in terms of machine parameters for their values are yet to be derived; also, the magnetizing current i_m is replaced by i_μ which is defined as:

$$\bar{i}_\mu = \frac{\bar{\lambda}_r}{L_m}$$ (3.25)
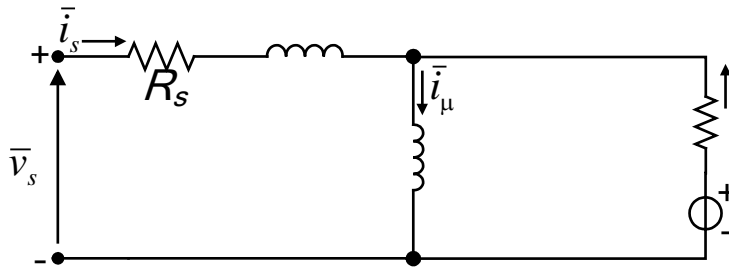
Fig. 3.5: Inverse-Γ equivalent circuit

Since there is no other inductance in the rotor branch, the rotor flux linkages are entirely caused by current through L_m (Fig. 3.4) and, from (3.6), we can write i_μ in terms of i_s and i_r wherefrom we can obtain (3.26).

$$\bar{i}_\mu = \frac{L_m \bar{i}_s + L_r \bar{i}_r}{L_m} = \bar{i}_s + \frac{L_r}{L_m}\bar{i}_r$$

$$\bar{i}_r = \frac{L_m}{L_r}\left(\bar{i}_\mu - \bar{i}_s\right)$$ (3.26)

Substituting (3.26) into (3.21)

$$\bar{v}_s = R_s\bar{i}_s + L_s\frac{d\bar{i}_s}{dt} + L_m\frac{d}{dt}\left(\frac{L_m}{L_r}\bar{i}_\mu - \frac{L_m}{L_r}\bar{i}_s\right)$$

Rearranging,
$$\bar{v}_s = R_s\bar{i}_s + \left(L_s - \frac{L_m^2}{L_r}\right)\frac{d\bar{i}_s}{dt} + \frac{L_m^2}{L_r}\frac{d\bar{i}_\mu}{dt}$$

Introducing total machine leakage factor (σ):

$$\sigma = 1 - \frac{L_m^2}{L_s L_r} \tag{3.27}$$

It can be easily deduced that: $\quad L_s - \dfrac{L_m^2}{L_r} = \sigma L_s \ $ and $\ \dfrac{L_m^2}{L_r} = (1 - \sigma) L_s$

Thus we have the stator voltage equations as:

$$\bar{v}_s = R_s \bar{i}_s + \sigma L_s \frac{d\bar{i}_s}{dt} + (1 - \sigma) L_s \frac{d\bar{i}_\mu}{dt} \tag{3.28}$$

For rotor equations, (3.26) is rearrange to get (3.29).

$$\bar{i}_s = \bar{i}_\mu - \frac{L_r}{L_m} \bar{i}_r \tag{3.29}$$

Substituting (3.29) along with (3.6) in (3.22):

$$\bar{0} = R_r \bar{i}_r + L_r \frac{d\bar{i}_r}{dt} + L_m \frac{d\bar{i}_\mu}{dt} - L_r \frac{d\bar{i}_r}{dt} - j\omega_r \left(L_r \bar{i}_r + L_m \bar{i}_\mu - L_m \frac{L_r}{L_m} \bar{i}_r \right)$$

$\rightarrow$
$$\bar{0} = R_r \bar{i}_r + L_m \frac{d\bar{i}_\mu}{dt} - j\omega_r L_m \bar{i}_\mu$$

Multiplying with $\dfrac{L_m}{L_r}$
$$\bar{0} = \frac{L_m}{L_r} R_r \bar{i}_r + \frac{L_m^2}{L_r} \frac{d\bar{i}_\mu}{dt} - j\omega_r \frac{L_m^2}{L_r} \bar{i}_\mu$$

or
$$\bar{0} = \frac{L_m^2}{L_r^2} R_r \left(\frac{L_r}{L_m} \bar{i}_r \right) + (1 - \sigma L_s) \frac{d\bar{i}_\mu}{dt} - j\omega_r (1 - \sigma L_s) \bar{i}_\mu \tag{3.30}$$

Equations (3.28) and (3.30) describe the inverse–Γ equivalent circuit shown in Fig. 3.6 below. From (3.30), it can be readily observed that the rotor resistance as seen from the stator terminals, called the referred rotor resistance, can be written as in (3.31).

$$R_{rref} = \frac{L_m^2}{L_r^2} R_r \tag{3.31}$$
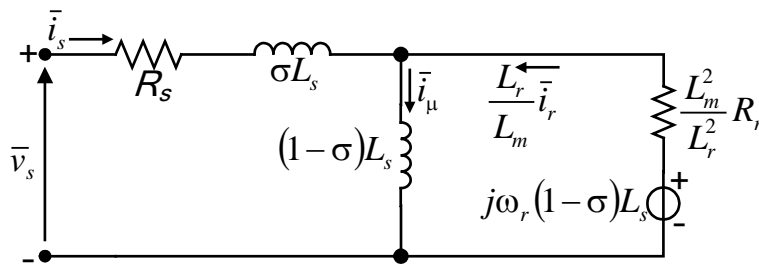
Fig. 3.6: Inverse–Γ equivalent circuit given by equations (3.28) and (3.30)

It follows naturally from inverse–Γ equivalent circuit above that the leakage inductances of stator and rotor can also be expressed in rotor side only. This gives rise to the Γ equivalent circuit for which the equations are derived analogously to inverse–Γ equivalent circuit below.

From the assumption that there is no leakage inductance in the stator branch, it immediately follows that entire stator flux is due to the current ($i_{\mu s}$) in the magnetizing branch. Recalling the definition of L_s, that it is the total inductance seen from stator terminals with rotor side open-circuited, it can be deduced that the magnetizing branch now consists of L_s and not L_m. So, the stator flux is given by:

$$\overline{\lambda}_s = L_s \overline{i}_{\mu s}$$

Using (3.5), we can derive (3.32) and (3.33).

$$\overline{i}_{\mu s} = \frac{L_s \overline{i}_s + L_m \overline{i}_r}{L_s} = \overline{i}_s + \frac{L_m}{L_s} \overline{i}_r$$

$$\overline{i}_s = \overline{i}_{\mu s} - \frac{L_m}{L_s} \overline{i}_r \tag{3.32}$$

$$\overline{i}_r = \frac{L_s}{L_m}\left(\overline{i}_{\mu s} - \overline{i}_s \right) \tag{3.33}$$

Substituting (3.33) in (3.21):

$$\overline{v}_s = R_s \overline{i}_s + L_s \frac{d\overline{i}_s}{dt} + L_m \frac{d}{dt}\left(\frac{L_s}{L_m} \overline{i}_{\mu s} - \frac{L_s}{L_m} \overline{i}_s \right)$$

$$\overline{v}_s = R_s \overline{i}_s + L_s \frac{d\overline{i}_{\mu s}}{dt} \tag{3.34}$$

For rotor equations, substituting (3.32) in (3.22):

$$\overline{0} = R_r \overline{i}_r + L_r \frac{d\overline{i}_r}{dt} + L_m \frac{d\overline{i}_{\mu s}}{dt} - \frac{L_m^2}{L_s} \frac{d\overline{i}_r}{dt} - j\omega_r \overline{\lambda}_r$$

Multiplying with $\frac{L_s}{L_m}$: $\overline{0} = R_r \frac{L_s}{L_m} \overline{i}_r + \frac{L_s}{L_m}\left(L_r - \frac{L_m^2}{L_s} \right)\frac{d\overline{i}_r}{dt} + L_s \frac{d\overline{i}_{\mu s}}{dt} - j\omega_r \frac{L_s}{L_m} \overline{\lambda}_r$

or $\overline{0} = \frac{L_s^2}{L_m^2} R_r \left(\frac{L_m}{L_s} \overline{i}_r \right) + \frac{L_s^2}{L_m^2}\left(L_r - \frac{L_m^2}{L_s} \right)\left(\frac{L_m}{L_s} \frac{d\overline{i}_r}{dt} \right) + L_s \frac{d\overline{i}_{\mu s}}{dt} - j\omega_r \frac{L_s}{L_m} \overline{\lambda}_r$

now $\frac{L_s^2}{L_m^2}\left(L_r - \frac{L_m^2}{L_s} \right) \Rightarrow \frac{L_s^2}{L_m^2} L_r \left(1 - \frac{L_m^2}{L_r L_s} \right) \Rightarrow \frac{L_s^2}{L_m^2} L_r \sigma \Rightarrow \frac{L_s \sigma L_s}{\dfrac{L_m^2}{L_r}} \Rightarrow \frac{L_s \sigma L_s}{(1-\sigma) L_s} \Rightarrow \frac{\sigma L_s}{(1-\sigma)}$

so, we have: $\overline{0} = \frac{L_s^2}{L_m^2} R_r \left(\frac{L_m}{L_s} \overline{i}_r \right) + \frac{\sigma L_s}{(1-\sigma)}\left(\frac{L_m}{L_s} \frac{d\overline{i}_r}{dt} \right) + L_s \frac{d\overline{i}_{\mu s}}{dt} - j\omega_r \frac{L_s}{L_m} \overline{\lambda}_r \tag{3.35}$

Equations (3.34) and (3.35) give the Γ equivalent circuit of the induction machine as shown in Fig. 3.7 below.
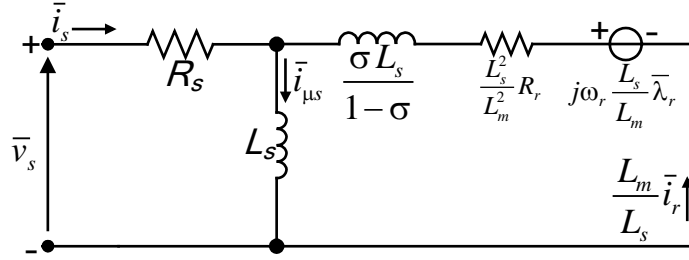
Fig. 3.7: Γ equivalent circuit given by equations (3.34) and (3.35)

3.2. <u>Control strategies</u>

Being an electromechanical power converter, any electric motor's output is mechanical power and that mechanical power needs to be controlled based on load requirements (Fig. 2.5). For a given rotational speed, it is the torque that decides the mechanical power produced/needed as in (3.36).

$$P_m = T_m \omega_r \tag{3.36}$$

So, the machine control essentially means controlling the mechanical torque for which torque expression is needed, the same is derived from machine's electrical equations. For induction machine, we use equations (3.13) and (3.14) here to express the power absorbed from the source (electrical) and imparted to the load.

Multiplying with $\bar{i}_s^{dq}$ $\qquad\qquad \bar{i}_s^{dq} \times \left\{ \bar{v}_s^{dq} = R_s \bar{i}_s^{dq} + \dfrac{d\bar{\lambda}_s^{dq}}{dt} + j\omega \bar{\lambda}_s^{dq} \right\}$

Multiplying with $\bar{i}_r^{dq}$ $\qquad\qquad \bar{i}_r^{dq} \times \left\{ \bar{0} = R_r \bar{i}_r^{dq} + \dfrac{d\bar{\lambda}_r^{dq}}{dt} + j(\omega - p\omega_r) \bar{\lambda}_r^{dq} \right\}$

The results of above operation can be separated in various components as below:

Input electrical power: $\qquad\qquad \bar{i}_s^{dq} \times \bar{v}_s^{dq} = i_s^d v_s^d + i_s^q v_s^q = |i_s|.|v_s| cos\,\varphi$

$cos(\varphi)$ is the input power factor whereas i_s and v_s are stator current and voltage, respectively.

Stator copper losses: $\qquad\qquad \bar{i}_s^{dq} \times R_s \bar{i}_s^{dq} = R_s \left(i_s^d i_s^d + i_s^q i_s^q \right) = R_s |i_s|^2$

Magnetic energy change in stator circuit: $\qquad \bar{i}_s^{dq} \times \dfrac{d\bar{\lambda}_s^{dq}}{dt}$

Rotor copper losses: $\qquad\qquad \bar{i}_r^{dq} \times R_r \bar{i}_r^{dq} = R_r \left(i_r^d i_r^d + i_r^q i_r^q \right) = R_r |i_r|^2$

Magnetic energy change in rotor circuit: $\qquad \bar{i}_r^{dq} \times \dfrac{d\bar{\lambda}_r^{dq}}{dt}$

The terms involving the speed (ω) of the revolving reference frame should not give any contribution in mechanical power for it would be against the physical sense. These terms have no physical significance and are a result of referring equations to an arbitrary reference frame.

so,
$$\bar{i}_s^{dq} \times j\omega\bar{\lambda}_s^{dq} = 0 \text{ and } \bar{i}_r^{dq} \times j\omega\bar{\lambda}_r^{dq} = 0$$

The only term that gives useful mechanical power is:

$$P_m = \bar{i}_r^{dq} \times \left(-jp\omega_r\bar{\lambda}_r^{dq}\right) \qquad \blacktriangleright \qquad P_m = p\omega_r\left(\bar{i}_r^{dq} \wedge \bar{\lambda}_r^{dq}\right)$$

Omitting superscripts '*dq*' and including the coefficients of two-phase to three-phase transformation, cf. (3.9), the expression for mechanical power is thus:

$$P_m = \frac{3}{2} p\omega_r\left(\bar{i}_r \wedge \bar{\lambda}_r\right) \qquad (3.37)$$

Substituting (3.37) in (3.36), we get an expression for torque generated by the machine as:

$$T_m = \frac{3}{2} p\left(\bar{i}_r \wedge \bar{\lambda}_r\right) \qquad (3.38)$$

Eq. (3.38) shows that the torque produced is the vector product of the rotor current vector $\bar{i}_r$ and the rotor flux-linkage vector $\bar{\lambda}_r$. Using basic relationships between various machine variables hitherto defined, the torque can also be expressed as a function of other vectors as given in (3.39), (3.40), (3.41), (3.42), and so forth.

Noting that the vector product of two identical vectors is zero i.e. $\bar{X} \wedge \bar{X} = 0$

Using (3.6):
$$T_m = \frac{3}{2} pL_m\left(\bar{i}_r \wedge \bar{i}_s\right) \qquad (3.39)$$

Using (3.6) to substitute for $\bar{i}_r$ in (3.39):
$$T_m = \frac{3}{2} p\left(\bar{\lambda}_s \wedge \bar{i}_s\right) \qquad (3.40)$$

From (3.6) substituting for $\bar{i}_r$ in (3.5), and then using (3.40):

$$T_m = \frac{3}{2} p\frac{L_m}{L_r}\left(\bar{\lambda}_r \wedge \bar{i}_s\right) \qquad (3.41)$$

Again, from (3.6) substituting for $\bar{i}_r$ in (3.5) and using the definition of leakage factor (σ) from (3.27), we have from (3.41):

$$T_m = \frac{3}{2} p\frac{1}{\sigma L_s}\left(\bar{\lambda}_r \wedge \bar{\lambda}_s\right) \qquad (3.42)$$

The most commonly used expression, however, is (3.41) in which the ratio of magnetizing inductance (L_m) to total rotor inductance (L_r) is defined as the '*stator-to-rotor coupling factor*' or simply '*rotor coupling factor*' k_r as:

$$k_r = \frac{L_m}{L_r} \qquad (3.43)$$

Having defined the induced torque in terms of machine variables, the techniques of controlling this torque are now presented. As discussed in the previous chapter, the vector control is the commonly used control strategy for almost all ac machines. In the following sections, the equations are derived for the rotor field oriented as well as unified direct flux vector control of induction machine. These two control strategies are used in this thesis for performance evaluation of motor control with and without self-commissioning.

3.2.1. Rotor Field Oriented Control

Referring to section 2.2.1 and Fig. 2.9, the rotor field oriented control of any ac machine dictates that the *d*-axis of the rotating reference frame must coincide with the rotor flux vector $\overline{\lambda}_r$. This allows the decoupled control of rotor flux (machine flux in general) and the electromagnetic torque. Fig. 2.9 also suggests that to vary flux in an induction machine, the component of the stator current along the *d*-axis of rotating reference frame be acted upon while there is no effect of *q*-axis component of current on $\overline{\lambda}_r$. The *q*-axis component of stator current can then independently be used for controlling the torque produced. While in the previous chapter, the rotor field oriented control is presented in its generic form, here the equations are derived particularly for the induction machine.

Revisiting equations (3.6) and (3.14), with rotor voltage zeroed, we can derive torque expression under the conditions just stated i.e. the *q*-axis component of rotor flux is always zero.

From (3.6), we have:
$$\overline{i}_r = \frac{\overline{\lambda}_r - L_m \overline{i}_s}{L_r} \tag{3.44}$$

Substituting (3.44) in (3.14):
$$\overline{0} = R_r \frac{\overline{\lambda}_r^{dq} - L_m \overline{i}_s^{dq}}{L_r} + \frac{d\overline{\lambda}_r^{dq}}{dt} + j(\omega - p\omega_r)\overline{\lambda}_r^{dq}$$

Defining the rotor time constant τ_r as:
$$\tau_r = \frac{L_r}{R_r} \tag{3.45}$$

$$\overline{0} = \tau_r^{-1}\left(\overline{\lambda}_r^{dq} - L_m \overline{i}_s^{dq}\right) + \frac{d\overline{\lambda}_r^{dq}}{dt} + j(\omega - p\omega_r)\overline{\lambda}_r^{dq}$$

Rearranging:
$$\tau_r \frac{d\overline{\lambda}_r^{dq}}{dt} + \left(1 + j(\omega - p\omega_r)\tau_r\right)\overline{\lambda}_r^{dq} = L_m \overline{i}_s^{dq}$$

Defining slip frequency ω_{sl} as:
$$\omega_{sl} = \omega - p\omega_r \tag{3.46}$$

Separating the *d*- and *q*-axis equations while noting that $\lambda_r^q = 0$:

$$\tau_r \frac{d\lambda_r^d}{dt} + \lambda_r^d = L_m i_s^d \tag{3.47}$$

$$\omega_{sl}\tau_r\lambda_r^d = L_m i_s^q \tag{3.48}$$

Expanding (3.41) with $\lambda_r^q = 0$:
$$T_m = \frac{3}{2} p k_r \left(\lambda_r^d i_s^q - \lambda_r^q i_s^d\right) = \frac{3}{2} p k_r \lambda_r^d i_s^q \tag{3.49}$$

The block diagram of Fig. 3.8 below gives the torque production in terms of the two orthogonal stator current components as expressed by (3.49). It can be observed that a faster torque

control can be obtained if the *q*-axis component of stator current is taken as a state variable for torque control. The *d*-axis component crosses a delay element equal to the rotor time constant to realize torque required, thus it is inherently slow.
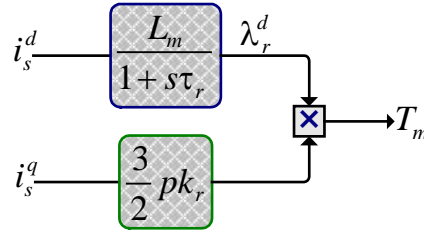
Fig. 3.8: Torque production of an induction motor

Having said that the torque induced is a function of *d*, *q* stator current components, it is useful to devise machine state-space model with the two current components as state variables. The state space model for rotor field oriented control of induction machine is derived below.

Substituting (3.44) in (3.5):
$$\overline{\lambda}_s = \sigma L_s \overline{i}_s + k_r \overline{\lambda}_r \tag{3.50}$$

Substituting it in *d*-axis equation of (3.13) and knowing that $\lambda_r^q = 0$:

$$v_s^d = R_s i_s^d + \sigma L_s \frac{di_s^d}{dt} + k_r \frac{d\lambda_r^d}{dt} - \omega \sigma L_s i_s^q$$

Assuming $\dfrac{d\lambda_r^d}{dt} = 0$:
$$v_s^d = R_s i_s^d + \sigma L_s \frac{di_s^d}{dt} - \omega \sigma L_s i_s^q$$

➔
$$\frac{di_s^d}{dt} = \frac{-R_s}{\sigma L_s} i_s^d + \omega i_s^q + \frac{1}{\sigma L_s} v_s^d \tag{3.51}$$

Similarly, the *q*-axis equation of (3.13) becomes:

$$v_s^q = R_s i_s^q + \sigma L_s \frac{di_s^q}{dt} + \omega \sigma L_s i_s^d + \omega k_r \lambda_r^d$$

➔
$$\frac{di_s^q}{dt} = \frac{-R_s}{\sigma L_s} i_s^q - \omega i_s^d + \frac{1}{\sigma L_s}\left(v_s^q - \omega k_r \lambda_r^d\right) \tag{3.52}$$

The state equations (3.51) and (3.52) are written in matrix form in (3.53).

➔
$$\frac{d}{dt}\begin{bmatrix} i_s^d \\ i_s^q \end{bmatrix} = \begin{bmatrix} \dfrac{-R_s}{\sigma L_s} & \omega \\ -\omega & \dfrac{-R_s}{\sigma L_s} \end{bmatrix}\begin{bmatrix} i_s^d \\ i_s^q \end{bmatrix} + \begin{bmatrix} \dfrac{1}{\sigma L_s} & 0 \\ 0 & \dfrac{1}{\sigma L_s} \end{bmatrix}\begin{bmatrix} v_s^d \\ v_s^q - \omega k_r \lambda_r^d \end{bmatrix} \tag{3.53}$$

The assumption $\dfrac{d\lambda_r^d}{dt} = 0$ is made on the basis that once established, the rotor flux is kept constant and variations are negligible. From (3.49), we have torque as a function of λ_r^d and i_s^q and, as seen in Fig. 3.8, λ_r^d is again a function of i_s^d. The two current components are to be controlled

according to their state equations (3.51) and (3.52). Now, it is the controller type used for this current control that is discussed.

Having current as a measured quantity in a standard drive the natural choice for current control is the feedback control. Proportional-Integral (PI) feedback controllers are well known for their fast response and disturbance rejection in steady state and are widely used in industry for over a century now. Fig. 3.9 shows a simple feedback proportional integral controller in which the error (*e*) is generated as a difference between reference and measured (or actual) value of the quantity to be controlled. The transfer function of this controller is given in (3.54), where k_p and k_i are the proportional and integral gains, respectively. The proportional gain decides the controller bandwidth and the integral part eliminates steady state error.
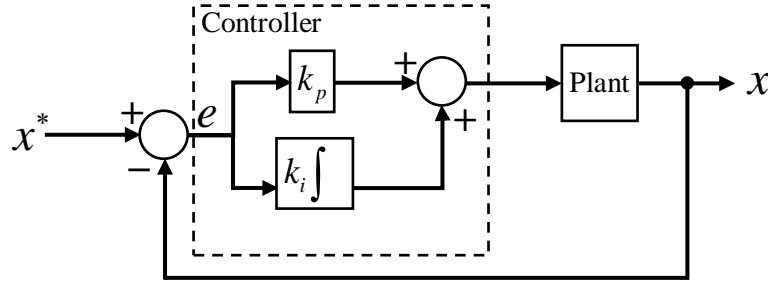
Fig. 3.9: Simple PI controlled system

$$G_{PI} = k_p + \frac{k_i}{s} \tag{3.54}$$

Having said that the field oriented control works with the *d*-axis fixed to the rotor flux, the rotor flux magnitude and angle are important to know accurately for acceptable control performance. Since the flux (whether it is stator flux, rotor flux or the airgap flux) is not among the directly measured quantities in a standard drive system, the only way out is to estimate it from the available electrical mechanical variables such as voltage, current and rotor speed or position. The flux estimate accuracy determines the degree of decoupling between flux and torque control.

For RFOC, the rotor flux magnitude and angle is required for correct alignment of *dq* axes of the rotating reference frame (Fig. 2.9). There are mainly two ways of estimating rotor flux $\overline{\lambda}_r$: from the stator voltage equations (3.15) and from the rotor equations (3.16).

Since (3.50) is valid either in rotating 'dq' reference frame or stationary 'αβ' frame we can use it invariably to substitute in (3.15) while omitting the superscripts 'αβ' to preserve generality:

$$\overline{v}_s = R_s \overline{i}_s + \frac{d}{dt}\left(\sigma L_s \overline{i}_s + k_r \overline{\lambda}_r\right) = R_s \overline{i}_s + \sigma L_s \frac{d\overline{i}_s}{dt} + k_r \frac{d\overline{\lambda}_r}{dt}$$

Rearranging:
$$k_r \frac{d\overline{\lambda}_r}{dt} = \overline{v}_s - R_s \overline{i}_s - \sigma L_s \frac{d\overline{i}_s}{dt}$$

Integrating we have:
$$\overline{\lambda}_r = \frac{1}{k_r} \int \left(\overline{v}_s - R_s \overline{i}\right) dt - \frac{\sigma L_s}{k_r} \overline{i}_s \tag{3.55}$$

The estimate of $\overline{\lambda}_r$ given in (3.55) is called the back-emf integration flux estimation, or more commonly, the voltage integral estimator. Equation (3.55) is shown graphically in Fig. 3.10. If the parameters appearing in (3.55) are all known accurately, the estimator gives accurate $\overline{\lambda}_r$, however, below a certain frequency (and therefore speed), the result is not as reliable due to

insufficient back-emf magnitude that causes integrator drift. The integrator drift is due to the open-loop integration that is integrator without negative feedback (Fig. 3.10).
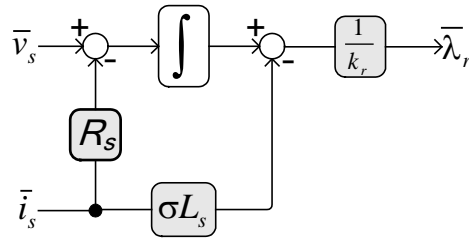
Fig. 3.10: Stator equation based flux estimation in stationary (αβ) frame

At lower speeds, the rotor equation based flux estimation works quite well. This flux estimator is derived from the rotor voltage equations (3.16), with $\overline{v}_r = \overline{0}$, in the stationary frame. The machine is assumed to be two-pole (i.e. $p = 1$) for simplicity. Superscripts 'αβ' are dropped here as well for consistency with (3.55) and Fig. 3.10.

Substituting (3.44) in (3.16): $\overline{0} = R_r\left(\dfrac{\overline{\lambda}_r - L_m\overline{i}_s}{L_r}\right) + \dfrac{d\overline{\lambda}_r}{dt} - j\omega_r\overline{\lambda}_r$

Using (3.45) and rearranging: $\tau_r\dfrac{d\overline{\lambda}_r}{dt} = \left(-1 + j\omega_r\tau_r\right)\overline{\lambda}_r + L_m\overline{i}_s$ (3.56)

The graphical representation of (3.56) given in Fig. 3.11 shows that this time the integrator does have a negative feedback that prevents accumulation in case it is fed with a constant. However, the rotor speed is required at all times that causes oscillations in flux estimate and may render it unstable at high speeds. This problem is countered by implementing the estimator in rotor mechanical coordinates (d^m, q^m) i.e. setting $\omega = p\omega_r$ in (3.14). Equation (3.56) in rotor mechanical coordinates is given below where 'm' stands for mechanical.

$$\tau_r\frac{d\overline{\lambda}_r^{dq^m}}{dt} = -\overline{\lambda}_r^{dq^m} + L_m\overline{i}_s^{dq^m}$$ (3.57)
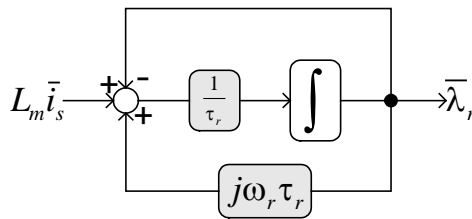
Fig. 3.11: Rotor equation based flux estimation in stationary (αβ) frame

Fig. 3.12 shows the flux estimation in rotor mechanical coordinates using (3.57).
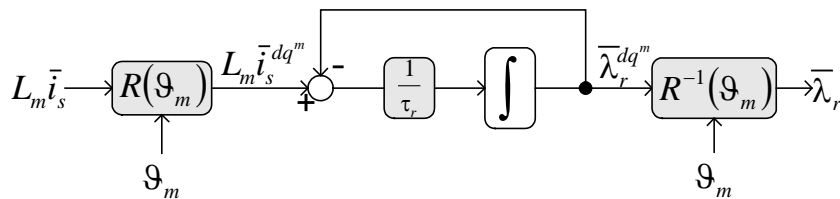
Fig. 3.12: Rotor flux estimation in rotor mechanical coordinates

The estimate heavily depends on machine parameters such as magnetizing inductance (L_m) and rotor time constant (τ_r). This rotor flux estimator is also called the I–ω estimator since the rotor speed (ω_r) is used either directly (Fig. 3.11) or for obtaining ϑ_m (Fig. 3.12).

The two flux estimators defined above are accurate at either low speed (Fig. 3.12) or high speed (Fig. 3.11) but not both at the same time. An intelligent control is that which gives high performance in all operating conditions, so a combination of the above two is required. The amalgamation of the stator and rotor equation models gives the full-range flux observer of Fig. 3.13.
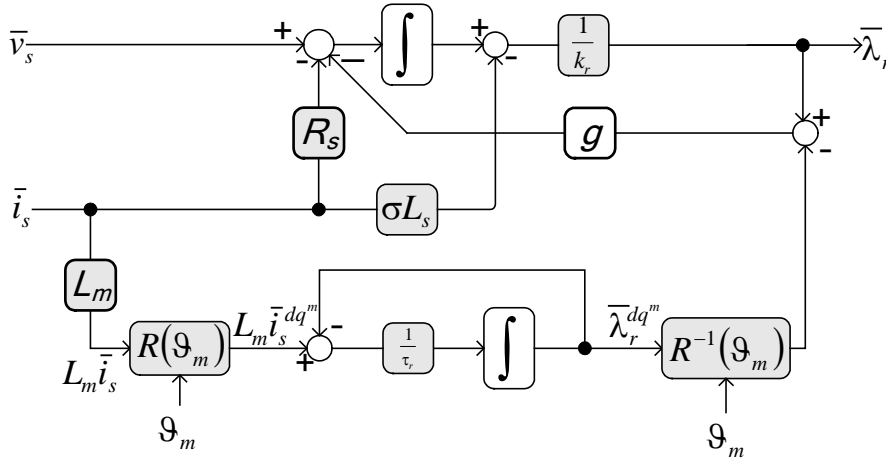
Fig. 3.13: Full speed range observer

The observer of Fig. 3.13 uses rotor model (3.57) at lower frequencies (speeds) and switches to stator model (3.55) as the (electrical) speed increases above **g** (rad/s), the cross-over frequency. The switching between the two models occurs smoothly with no oscillations. Even the full range observer is not immune to machine parameter errors; however, the impact of parameter mismatch reduces at higher speeds when the voltage integration (Fig. 3.10) model takes over the flux estimation task and the back-emf is sufficiently large compared to the stator resistance drop.

3.2.2. *Unified Direct Flux Vector Control*

Another control strategy [120] of induction machines is the technique of unifying the vector control presented above with the direct torque control (DTC) [112]. This Unified Direct Flux Vector Control (UDFVC), briefly described in the previous chapter, controls the machine flux the same way as it is done in DTC but preserves the current control method of RFOC for torque regulation. Unlike RFOC, the UDFVC works in stator flux coordinates and regulates stator flux with stator voltage instead of passing through the current control branch. This makes flux control faster. However, like RFOC, the torque regulation takes place through current controller. The equations for implementing this control in an induction motor drive are derived below.

The equations for this control are described based on the Stator Flux Oriented (SFO) reference frame defined in Fig. 3.14. The stator voltage equations (3.13) are referred to the stator flux oriented frame (d^s, q^s) whose angular speed with respect to stationary αβ-axes is defined in (3.58) by observing Fig. 3.14. The angle δ between stator flux vector $\overline{\lambda}_s$ and rotor flux vector $\overline{\lambda}_r$ is also called the 'load angle' of the induction machine.

$$\omega_s = \omega + \frac{d\delta}{dt} \qquad\qquad (3.58)$$

$$\overline{v}_s^{dq^s} = R_s \overline{i}_s^{dq^s} + \frac{d\overline{\lambda}_s^{dq^s}}{dt} + j\omega_s \overline{\lambda}_s^{dq^s}$$

The superscripts 'dq^s' signify that the equations are referred to the rotating reference frame 'dq^s' which is synchronous to stator flux vector $\overline{\lambda}_s$, omitting 's' from the superscripts for simplicity:

$$\overline{v}_s^{dq} = R_s \overline{i}_s^{dq} + \frac{d\overline{\lambda}_s^{dq}}{dt} + j\omega_s \overline{\lambda}_s^{dq} \tag{3.59}$$
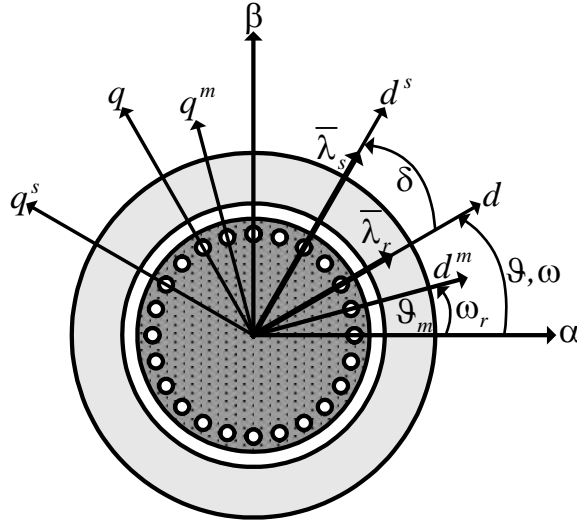
Fig. 3.14: Stator flux orientation reference frame definition

Substituting (3.58), we have:

$$\overline{v}_s^{dq} = R_s \overline{i}_s^{dq} + \frac{d\overline{\lambda}_s^{dq}}{dt} + j\overline{\lambda}_s^{dq}\left(\omega + \frac{d\delta}{dt}\right)$$

For stator field oriented control, we have $\lambda_s^q = 0$ such that:

$$\overline{\lambda}_s^{dq} = \lambda_s^d + j\lambda_s^q = \lambda_s^d + j0 = \lambda_s = \lambda$$

or
$$\overline{\lambda}_s^{dq} = \lambda \tag{3.60}$$

The *d*- and *q*-axis equations under stator field oriented condition become:

d-axis:
$$v_s^d = R_s i_s^d + \frac{d\lambda}{dt}$$

q-axis:
$$v_s^q = R_s i_s^q + \left(\omega + \frac{d\delta}{dt}\right)\lambda$$

The state-space model of the two axes is given in (3.61).

$$\frac{d}{dt}\begin{bmatrix} \lambda \\ \delta \end{bmatrix} = \begin{bmatrix} -R_s & 0 \\ 0 & \dfrac{-R_s}{\lambda} \end{bmatrix}\begin{bmatrix} i_s^d \\ i_s^q \end{bmatrix} + \begin{bmatrix} 1 \\ \dfrac{1}{\lambda} \end{bmatrix}\begin{bmatrix} v_s^d \\ v_s^q \end{bmatrix} + \begin{bmatrix} 0 \\ -\omega \end{bmatrix} \tag{3.61}$$

Eq. (3.61) shows that stator flux can be controlled directly through *d*-axis voltage and it does not suffer any cross-coupling effects from the *q*-axis control. This condition favours high bandwidth

control of stator flux which is a cornerstone of direct flux control strategy. However, the q-axis is not entirely independent of d-axis effects as is evident from (3.61).

For machine torque, among different expressions derived above, (3.40) gives torque in terms of stator quantities only. Expanding (3.40) while noting that $\lambda_s^q = 0$:

$$T_m = \frac{3}{2} p\left(\lambda_s^d i_s^q - \lambda_s^q i_s^d\right) = \frac{3}{2} p \lambda \ i_s^q \tag{3.62}$$

Comparing (3.61) and (3.62) reveals that the torque control requires controlling flux λ and q-axis current i_s^q, however the state equations contain λ and δ as state variables. To make control simple and less complicated, either torque be expressed in terms of λ and δ or the state equations be modified to contain i_s^q as state variable. We follow the latter since i_s^q is a measured quantity.

Inserting (3.46) in the rotor equations (3.14) while substituting for $\bar{i}_r$ from (3.5) and for $\bar{\lambda}_r$ from (3.50):

$$\bar{v}_r^{dq} = 0 = R_r\left(\frac{\bar{\lambda}_s^{dq} - L_s\bar{i}_s^{dq}}{L_m}\right) + \frac{d}{dt}\left(\frac{\bar{\lambda}_s^{dq} - \sigma L_s\bar{i}_s^{dq}}{k_r}\right) + j\omega_{sl}\left(\frac{\bar{\lambda}_s^{dq} - \sigma L_s\bar{i}_s^{dq}}{k_r}\right)$$

Rearranging to keep current ($\bar{i}_s^{dq}$) and flux ($\bar{\lambda}_s^{dq}$) terms together:

$$0 = -\left(\frac{R_r L_s}{L_m} + j\frac{\omega_{sl}\sigma L_s}{k_r}\right)\bar{i}_s^{dq} + \left(\frac{R_r}{L_m} + j\frac{\omega_{sl}}{k_r}\right)\bar{\lambda}_s^{dq} - \frac{\sigma L_s}{k_r}\frac{d\bar{i}_s^{dq}}{dt} + \frac{1}{k_r}\frac{d\bar{\lambda}_s^{dq}}{dt}$$

➔

$$\frac{d\bar{i}_s^{dq}}{dt} = \frac{k_r}{\sigma L_s}\left\{-\left(\frac{R_r L_s}{L_m} + j\frac{\omega_{sl}\sigma L_s}{k_r}\right)\bar{i}_s^{dq} + \left(\frac{R_r}{L_m} + j\frac{\omega_{sl}}{k_r}\right)\bar{\lambda}_s^{dq} + \frac{1}{k_r}\frac{d\bar{\lambda}_s^{dq}}{dt}\right\}$$

Using the definition of k_r from (3.43) and the rotor time constant (3.45)

$$\frac{d\bar{i}_s^{dq}}{dt} = -\left(\frac{1}{\sigma\tau_r} + j\omega_{sl}\right)\bar{i}_s^{dq} + \frac{1}{\sigma L_s}\left(\frac{1}{\tau_r} + j\omega_{sl}\right)\bar{\lambda}_s^{dq} + \frac{1}{\sigma L_s}\frac{d\bar{\lambda}_s^{dq}}{dt}$$

Substituting for $\frac{d\bar{\lambda}_s^{dq}}{dt}$ from (3.59)

$$\frac{d\bar{i}_s^{dq}}{dt} = -\left(\frac{1}{\sigma\tau_r} + j\omega_{sl}\right)\bar{i}_s^{dq} + \frac{1}{\sigma L_s}\left(\frac{1}{\tau_r} + j\omega_{sl}\right)\bar{\lambda}_s^{dq} + \frac{1}{\sigma L_s}\left(-R_s\bar{i}_s^{dq} - j\omega_s\bar{\lambda}_s^{dq} + \bar{v}_s^{dq}\right)$$

Defining stator time constant τ_s same as the rotor time constant of (3.45):

$$\tau_s = \frac{L_s}{R_s} \tag{3.63}$$

Substituting (3.63) and rearranging:

$$\frac{d\bar{i}_s^{dq}}{dt} = -\left(\frac{1}{\sigma\tau_s} + \frac{1}{\sigma\tau_r} + j\omega_{sl}\right)\bar{i}_s^{dq} + \frac{1}{\sigma L_s}\left(\frac{1}{\tau_r} + j(\omega_{sl} - \omega_s)\right)\bar{\lambda}_s^{dq} + \frac{1}{\sigma L_s}\bar{v}_s^{dq}$$

From (3.58), for $\dfrac{d\delta}{dt} = 0$, and from (3.46), for $p = 1$, we deduce that:

$$\omega_{sl} - \omega_s = -\omega_r$$

Substituting:

$$\frac{d\bar{i}_s^{dq}}{dt} = -\left(\frac{1}{\sigma\tau_s} + \frac{1}{\sigma\tau_r} + j\omega_{sl}\right)\bar{i}_s^{dq} + \frac{1}{\sigma L_s}\left(\frac{1}{\tau_r} - j\omega_r\right)\bar{\lambda}_s^{dq} + \frac{1}{\sigma L_s}\bar{v}_s^{dq} \tag{3.64}$$

Taking the q-axis part of equations (3.64) and using the condition for stator field orientation (3.60)

$$\frac{di_s^q}{dt} = -\left(\frac{1}{\sigma\tau_s} + \frac{1}{\sigma\tau_r}\right)i_s^q + \omega_{sl}i_s^d - \frac{\omega_r}{\sigma L_s}\lambda + \frac{1}{\sigma L_s}v_s^q$$

or

$$\sigma L_s \frac{di_s^q}{dt} = -\left(R_s + R_r\frac{L_s}{L_r}\right)i_s^q + \omega_{sl}\sigma L_s i_s^d + \left(v_s^q - \omega_r\lambda\right)$$

➔

$$\sigma L_s \frac{di_s^q}{dt} = -R'i_s^q + \omega_{sl}\sigma L_s i_s^d + \left(v_s^q - \omega_r\lambda\right) \tag{3.65}$$

Equation (3.65), in which $R' = R_s + R_r\dfrac{L_s}{L_r}$, is the second state equation for stator field oriented direct flux control. Eq. (3.65) shows that besides state variable transformation from δ to i_s^q, the q-axis control continues to see cross-coupling effects from the d-axis, however, the cross-coupling terms such as $\omega_{sl}\sigma L_s i_s^d$ and $\omega_r\lambda$ can be easily compensated through feed-forward since both i_s^d and ω_r are measured quantities. Combining (3.65) with d-axis part of (3.61), the final state equations for control can be written as in (3.66).

$$\begin{bmatrix} \dfrac{d\lambda}{dt} \\[3ex] \sigma L_s \dfrac{di_s^q}{dt} \end{bmatrix} = \begin{bmatrix} -R_s & 0 \\[1ex] \omega_{sl}\sigma L_s & -R' \end{bmatrix}\begin{bmatrix} i_s^d \\[1ex] i_s^q \end{bmatrix} + \begin{bmatrix} v_s^d \\[1ex] v_s^q - \omega_r\lambda \end{bmatrix} \tag{3.66}$$

Contrary to the uncontrolled induction motor drives, especially those which operate directly from the mains, the vector controlled drive can give controlled operation beyond rated speed of the machine. This feature, known as constant-power operation, is a unique property of adjustable speed drives that permits maximum machine utilization under all possible situations. The constant-power region of operation requires that with increasing rotor speed, the induced torque is reduced proportionately such that the product on the right-hand side of (3.36) is always constant.

With increasing speed and maximum torque demand, the machine load angle δ keeps on increasing till a point is reached where a further increase in δ causes torque reduction. To make the most of available inverter dc-link voltage, the angle δ must be limited to a value where the torque is at its peak. This condition is also called the maximum torque per volt (MTPV) state, that is, the peak torque that can be obtained per unit volt of dc-link. What value of δ gives maximum torque? This question is answered below by deriving torque in terms of load angle δ and finding the extrema of the torque as a function of δ.

Since δ is the angle between stator and rotor flux vectors (Fig. 3.14), taking rotor flux vector $\overline{\lambda}_r$ as reference and expressing stator flux $\overline{\lambda}_s$ in terms of angle δ simplifies the computation of load angle that gives maximum torque.

Based on Fig. 3.14 and equation (3.60), the rotor reference frame coordinates of stator flux $\overline{\lambda}_s$ are given in terms of δ as:

$$\lambda_s^d = \lambda \, cos \, \delta \tag{3.67}$$

$$\lambda_s^q = \lambda \, sin \, \delta \tag{3.68}$$

$$\lambda_s^d = \lambda \, cos \, \delta \ \text{ and } \ \lambda_s^q = \lambda \, sin \, \delta$$

In the rotor field oriented frame the assumption $\dfrac{d\lambda_r^d}{dt} = 0$ always holds good in steady state conditions and this turns (3.47) into (3.69).

$$\lambda_r^d = L_m i_s^d \tag{3.69}$$

Substituting (3.69) into the *d*-axis component of (3.50) and recalling the definition of leakage factor (3.27), we get:

$$\lambda_s^d = L_s i_s^d$$

or
$$i_s^d = \frac{\lambda_s^d}{L_s} \tag{3.70}$$

Similarly, after noting from the definition of RFO that $\lambda_r^q = 0$, the *q*-axis component of (3.50) becomes:

$$\lambda_s^q = \sigma L_s i_s^q$$

or
$$i_s^q = \frac{\lambda_s^q}{\sigma L_s} \tag{3.71}$$

Substituting (3.67), (3.68), (3.70) and (3.71) into (3.40), we have torque in terms of load angle δ as:

$$T_m = \frac{3}{2} p\left(\lambda_s^d i_s^q - \lambda_s^q i_s^d\right) = \frac{3}{2} p\left(\lambda \, cos \, \delta \frac{\lambda \, sin \, \delta}{\sigma L_s} - \lambda \, sin \, \delta \frac{\lambda \, cos \, \delta}{L_s}\right) = \frac{3}{2} p\left(\frac{1}{\sigma L_s} - \frac{1}{L_s}\right)\lambda^2 \, sin \, \delta \, cos \, \delta$$

or
$$T_m = \frac{3}{2} p\left(\frac{1-\sigma}{\sigma L_s}\right)\lambda^2 \frac{sin \, 2\delta}{2} \tag{3.72}$$

To compute δ for which the mechanical torque is maximum, we differentiate (3.72) with respect to δ and equate the result to zero.

$$\frac{\partial T_m}{\partial \delta} = \frac{\partial}{\partial \delta}\left\{\frac{3}{2} p\left(\frac{1-\sigma}{\sigma L_s}\right)\lambda^2 \frac{sin \, 2\delta}{2}\right\} \Rightarrow cos \, 2\delta = 0$$

That is:
$$\delta_{max} = 45°$$ (3.73)

Eq. (3.73) is the condition for maximum torque production, that is, the angle between stator and rotor flux vectors shall be limited to 45° when the voltage limited operation (in flux-weakening region) is in force.

The unified direct flux vector control scheme along with δ limitation for MTPV operation is shown in the block diagram of Fig. 3.15. Starting with a torque demand T^* the required q-axis current i_s^{q*} is computed based on the magnitude of stator flux. This i_s^{q*} command is passed to the PI-controller block that generates voltage commands $\bar{v}_s^{dq*}$ in the stator flux frame. There are two additional blocks shown in Fig. 3.15, which are the MTPA (Maximum Torque per Ampere) and the flux-weakening block. The MTPA block, that can be 'switched' on and off at the user's discretion, gives the optimal flux value for a given torque demand. The block used the machine's look-up tables that express torque as a function of flux obtained from no-load and short-circuit tests. The MTPA operation does improve machine efficiency, however, at the cost of slowing down of torque response.
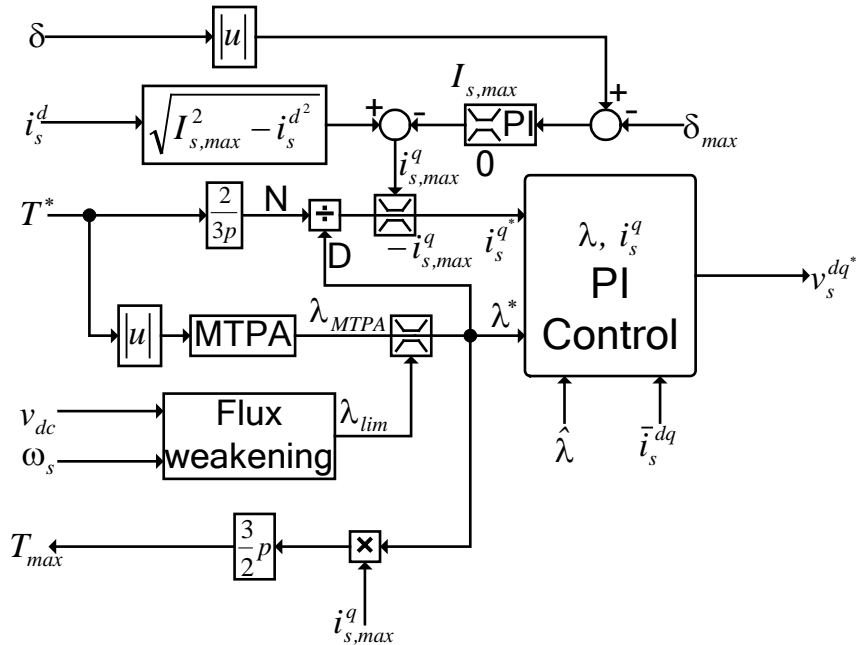
Fig. 3.15: UDFVC Scheme

The other block named 'flux-weakening', computes the maximum permitted flux based on the available dc-link voltage and machine's electrical speed. This block constantly monitors the rotor speed and available voltage to impose flux-limit to ensure smooth transition from constant flux to flux-weakening operation. The flux limit is computed from (3.59) based on the q-axis stator voltage equation as:

$$\lambda_{lim} = \frac{v_s^q - R_s i_s^q}{\omega_s}$$

Since
$$v_s^q = \sqrt{v_s^2 - v_s^{d^2}}$$

So
$$\lambda_{lim} = \frac{\sqrt{v_s^2 - v_s^{d^2}} - R_s i_s^q}{\omega_s}$$ (3.74)

Eq. (3.74) is the field-weakening law for setting the upper limit on flux demand and is valid in all operating conditions even with varying dc-link voltage since the maximum applicable phase voltage v_s is computed from the available dc-link voltage. This is particularly useful in electric traction applications when the voltage available to the inverter directly depends on the level of charge of the batteries. The drive does not run the risk of losing q-axis current control for the unavailability of sufficient q-axis voltage at higher speeds due to excessive flux; the flux is constantly limited through (3.74).

The load angle δ is limited with a PI-controller that keeps an eye on the actual load angle and continuously compares it with the maximum allowed value (3.73) and reduces the demanded q-axis current accordingly. This PI-controller based strategy ensures MTPV operation at all times regardless of whether the flux-weakening region is achieved.

Since the control works in stator coordinates and stator flux is controlled as a state variable through v_d^s (3.61) or (3.66), the flux observer of Fig. 3.13 is modified to give stator flux estimate. The modified flux observer is shown in Fig. 3.16. Since the rotor flux from the rotor equation is obtained in rotor field oriented coordinates same as in Fig. 3.13, the flux observer of Fig. 3.16 includes computation of load angle δ inside it for it is the angle of advance of stator flux vector. $\overline{\lambda}_s$ with respect to stationary rotor flux vector $\overline{\lambda}_r$. The angular speed ω_s of the rotating (d^s, q^s) reference frame for control orientation is also computed inside this block, as shown in Fig. 3.16.
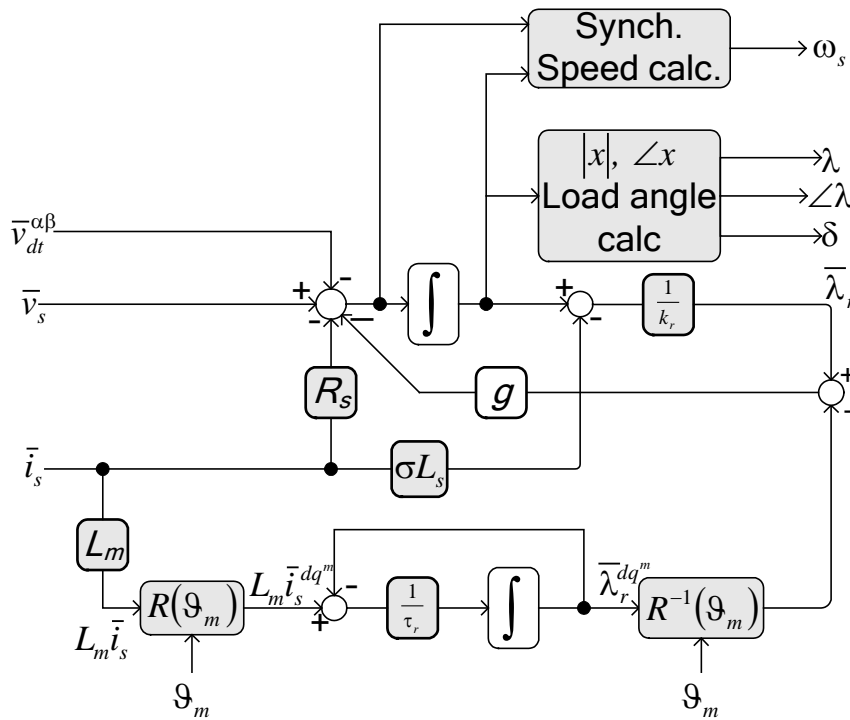
Fig. 3.16: Stator flux observer

With respect to Fig. 3.13, the flux observer of Fig. 3.16 contains an additional input named as the vector $\overline{v}_{dt}^{\alpha\beta}$. This is the inverter dead-time effects voltage vector in stationary αβ reference frame. This vector includes all the non-linearity effects of power switches as such as the semiconductor threshold voltage, on-state switch resistance drop and the safety time between opening of upper power semiconductor switch and closing of the lower switch of the same leg (Fig. 2.2). This dead-time is also called the blanking time and is necessary to prevent a short circuit across the dc-link (Fig. 2.2). The vector $\overline{v}_{dt}^{\alpha\beta}$ is particular of individual inverter and can be pre-

calculated as a function of current either through the components' datasheet or with dedicated tests performed on the inverter.

Based on the detailed description of the unified direct flux vector control and the conditions for maximum torque under flux-weakening region of operation, the overall control block diagram of Fig. 3.17 is now drawn. The drive is shown in closed-loop speed control mode; however, it is equally valid for torque control operation where the demand torque T^* is determined by the external control system, for instance, by the displacement of the accelerator in a traction application.
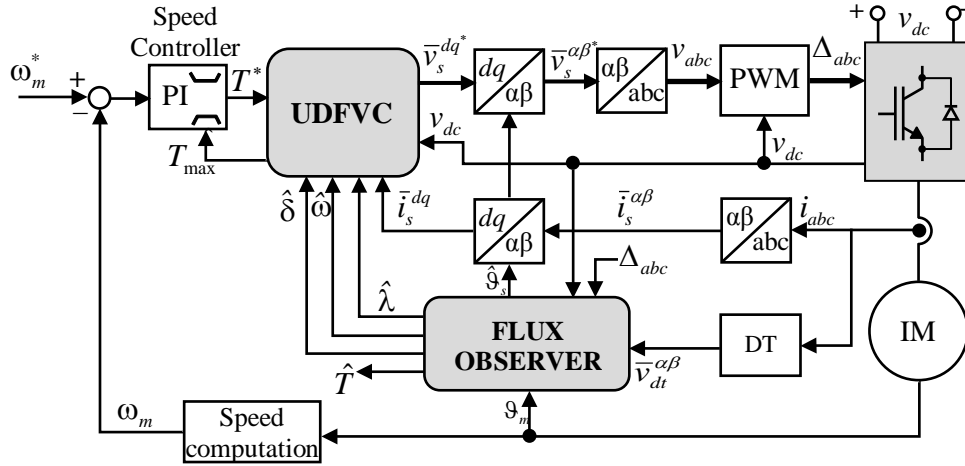
Fig. 3.17: Overall control block diagram

3.3.   Effects of parameter detuning on control performance

As seen above, whether it is a well-known rotor field oriented vector control with two current regulators or it is a unified direct flux vector control with a current and a flux regulator, the control performance heavily depends on machine's equivalent circuit parameters either directly or indirectly.

Direct dependence in terms of current controller's gain settings and indirect in the sense of flux control (in case of UDFVC) where, although the flux controller has a high bandwidth, the feedback it receives is not the measured flux but an estimate of it. Flux estimation accuracy is governed by the precision with which the machine's equivalent circuit parameters are known and, more importantly, how the parameter information adapts to actual load and ambient conditions. The effects of parameter errors are briefly discussed below.

3.3.1. Stator resistance error

The stator resistance R_s, as it appears in the flux observer of Fig. 3.16, affects stator flux magnitude estimation depending on both the speed and the cross-over frequency g (rad/s) between stator and rotor model. In case the gain g is set lower than the electrical speed at which the machine back-emf is less than or equal to the R_s drop, the flux estimate becomes sensitive to deviations in Rs from its actual value. Mathematically, the effects of R_s error can be understood from the d-axis equation of (3.59) in steady state after applying (3.75) while noting (3.60) as below.

In steady state conditions:
$$\frac{d}{dt} = j\omega_s \qquad (3.75)$$

$$V_s^d = R_s I_s^d + j\omega_s \lambda$$

or
$$|\lambda| = \frac{V_s^d - R_s I_s^d}{\omega_s} \qquad (3.76)$$

From (3.76), it is evident that if stator resistance is overestimated than its true value, the estimated flux magnitude will be lower than the actual machine flux, the underestimated Rs gives the opposite effect. Fig. 3.18 shows the two effects when unified direct flux vector control is simulated with the cross-over frequency g set as close to the value at which the back-emf and stator voltage drops are equal and the machine electrical speed is just above g. It can be seen that the observed flux magnitude is different from actual machine flux and the error depends on whether R_s is over- or underestimated. These results are consistent with [121] in which the stator resistance variation effects on DTC stability and performance are analysed.

(a)   (b)
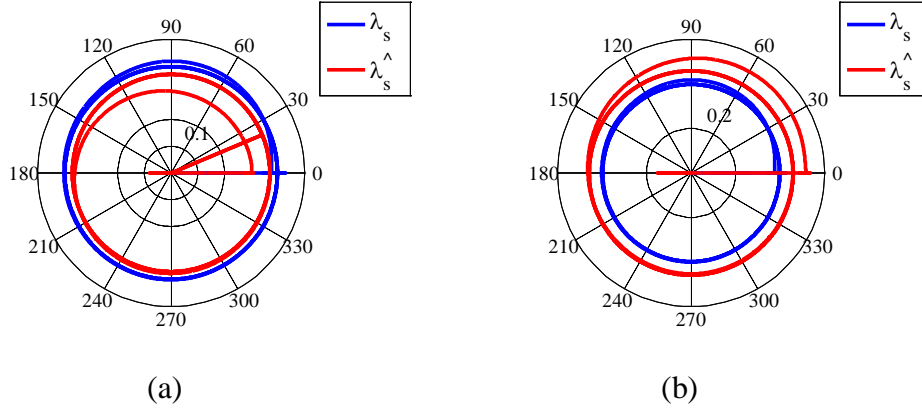
Fig. 3.18: Polar plots showing flux magnitude error due to R_s detuning (a) $\hat{R}_s = 1.2 R_s$ (b) $\hat{R}_s = 0.8 R_s$

The effects of stator resistance mismatch can be grave when the machine is in torque control mode and other machine parameters, especially the magnetizing inductance as a function of current, are not known and the control counts on back-emf integration estimate of stator flux. In this case the relationship between demanded torque and produced torque is not linear that degrades control.

3.3.2. Leakage inductances' effects

The stator and rotor leakage inductances, L_{ls} and L_{lr} respectively of Fig. 3.4, determine the bandwidth of the PI current controllers of Fig. 3.9, for the proportional gain k_p depends on total leakage inductance of the machine. The sum of the two leakage inductances referred to the stator side can be approximated to σL_s by using (3.7), (3.8), (3.27), and (3.43) as below.

Rotor leakage inductance L_{lr} can be referred to stator side by using rotor coupling factor (3.43) to give the sum L_{lt} as:

$$L_{lt} = L_{ls} + k_r L_{lr}$$

Substituting (3.7), (3.8) and (3.43): $L_{lt} = L_s - L_m + \dfrac{L_m}{L_r}\left(L_r - L_m\right)$

➜ $$L_{lt} = L_s - L_m + L_m - \frac{L_m^2}{L_r} = L_s\left(1 - \frac{L_m^2}{L_s L_r}\right)$$

Finally, substituting (3.27): $L_{lt} = \sigma L_s$ (3.77)

It is also evident from the inverse–Γ equivalent circuit (Fig. 3.6) that when both the stator and rotor leakage inductances are expressed in the stator branch only, the resultant total leakage inductance is numerically equal to σL_s.

The bandwidth of a feedback controller is the frequency at which the closed-loop gain is -3dB. It affects speed of controller response by altering rise time and settling time to a step input.

For the current feedback controller to give a certain bandwidth ω_{bw}, it is necessary that the proportional gain k_p is set equal to the reactance of the inductive branch at the bandwidth frequency as in (3.78). From Fig. 3.6 it can be seen that for a step current input, the only inductance that comes in the path of current is σL_s for the magnetizing branch inductance $(1-\sigma)L_s$ is too large to allow step change of current through it.

$$k_p = \omega_{bw}\,\sigma\,L_s \qquad\qquad (3.78)$$

For an optimal and stable control, the proportional gain k_p needs to be set precisely according to σL_s for which accurate knowledge of the machine leakage inductances is indispensable. The detuning effects of σL_s on control performance are realized through analysing the controller's step response.

In Fig. 3.19, the impact of underestimated total leakage inductance is seen as an overshoot of 21% instead of 15% that is achieved when exact values are used, similarly the settling time with detuned operation increases by 0.4ms compared to the situation when correct value of leakage inductance is incorporated to compute k_p. These effects weigh heavily when high dynamic performance is required.
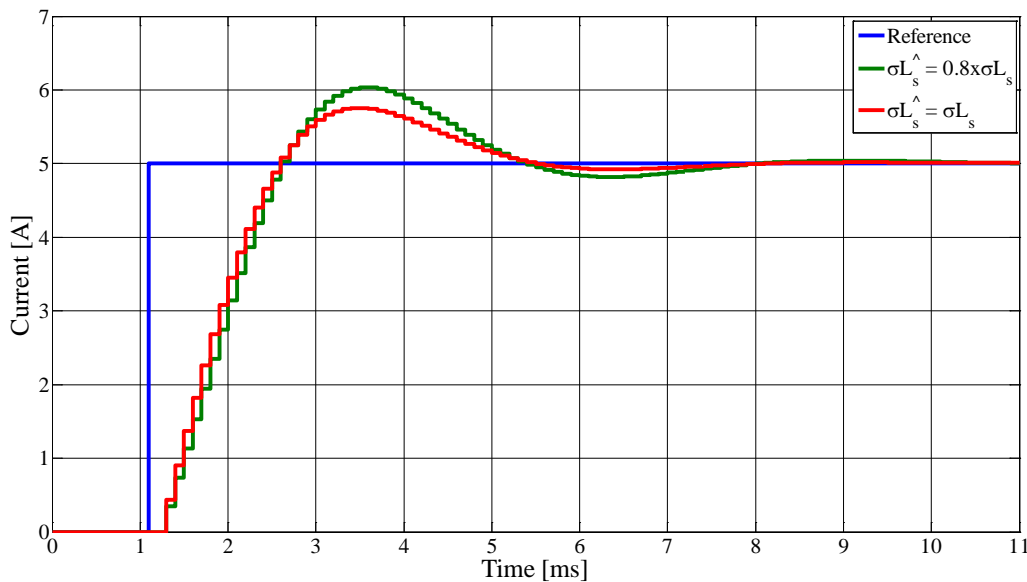
Fig. 3.19: σL_s error impact on overshoot and settling time

On the other hand, an overestimated σL_s would render the control unstable if the controller is designed close to the stability margin to achieve maximum possible dynamic performance. This situation is shown in Fig. 3.20 and Fig. 3.21. In Fig. 3.21 it is evident how only a 20% error in σL_s can provoke control instability.

In order to highlight the impact of detuned σL_s on control performance without any effect of other controller characteristics, the integral gain of the PI-controller is unvaried for the two cases shown above (Fig. 3.20, and Fig. 3.21). Also, in Fig. 3.19, the integral gain for both the step responses shown is the same and the difference in performance is only because of the variation in k_p due to σL_s variation.
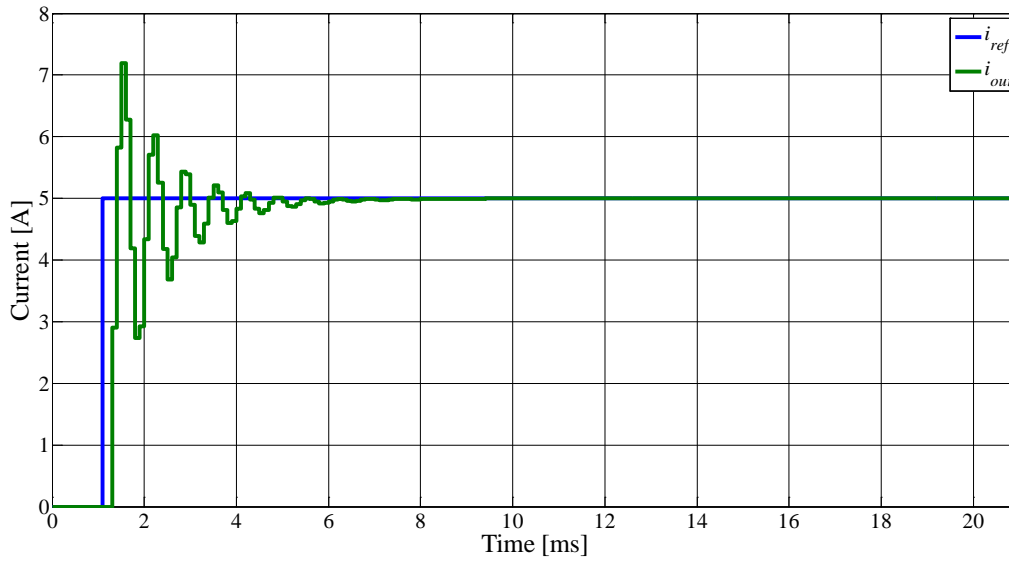
Fig. 3.20: Current control obtained for exact value of σL_s
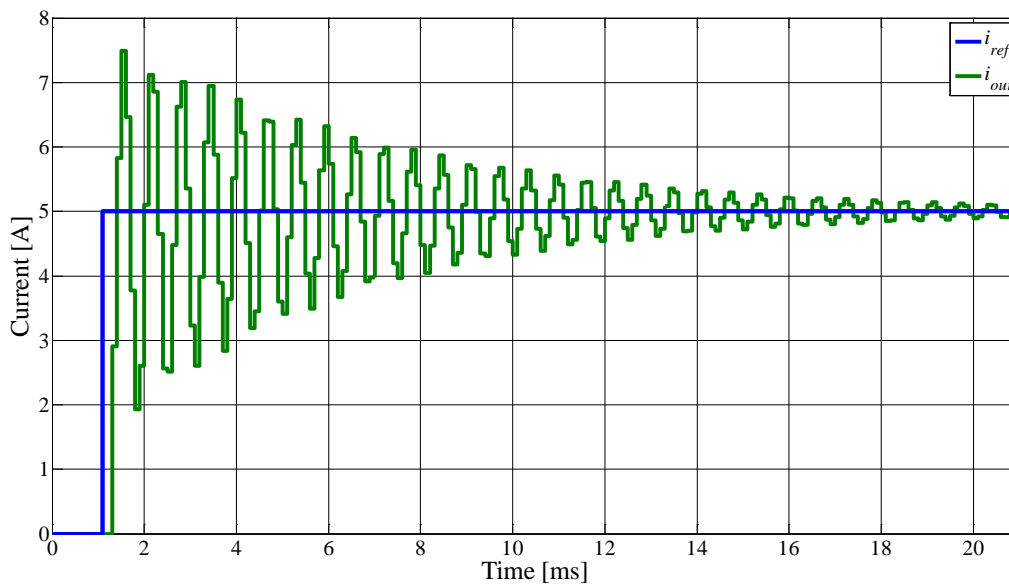
Fig. 3.21: Unstable control for overestimated σL_s i.e. $\sigma \hat{L}_s = 1.2 \times \sigma L_s$

3.3.3. *Magnetizing inductance error effects*

The machine's magnetizing inductance L_m appears in both stator and rotor branch equations for it determines the magnetic coupling between the two. For field oriented control discussed above, the accuracy with which L_m is known determines the correctness in the orientation of *dq* rotating reference frame which further decides the degree of decoupling between flux and torque control.

The rotor equation based flux observer (Fig. 3.11 or Fig. 3.12) that is useful at low speeds gives erroneous flux magnitude and phase for if the magnetizing inductance used does not correspond to the actual inductance. At higher speeds, though, the impact of L_m error diminishes for the back-emf integral flux estimation, which is immune to L_m errors, takes over.

Since the magnetizing inductance determines the magnitude of main flux inside the core, it is pivotal in torque estimation accuracy from machine's electrical variables as it appears in almost all the expressions for torque from (3.39) to (3.42) in one form or the other. The torque estimation

accuracy is sensitive to L_m variations especially when rotor equation model for flux estimation Fig. 3.12 is dominant in Fig. 3.13 (or in Fig. 3.16) at low speeds in which case the back-emf is not sufficient to give reliable flux estimate. Torque estimate, at low speeds, with and without L_m detuning is shown in Fig. 3.22 and Fig. 3.23, respectively. Fig. 3.22 shows that the estimation error is about 12.5% with detuned L_m that reduces to a mere 1% (Fig. 3.23) when magnetizing inductance is correctly estimated. It is to be noted that the detuning introduced in Fig. 3.22 is not through an external disturbance but it is achieved by ignoring saturation effects which are otherwise considered in Fig. 3.23.
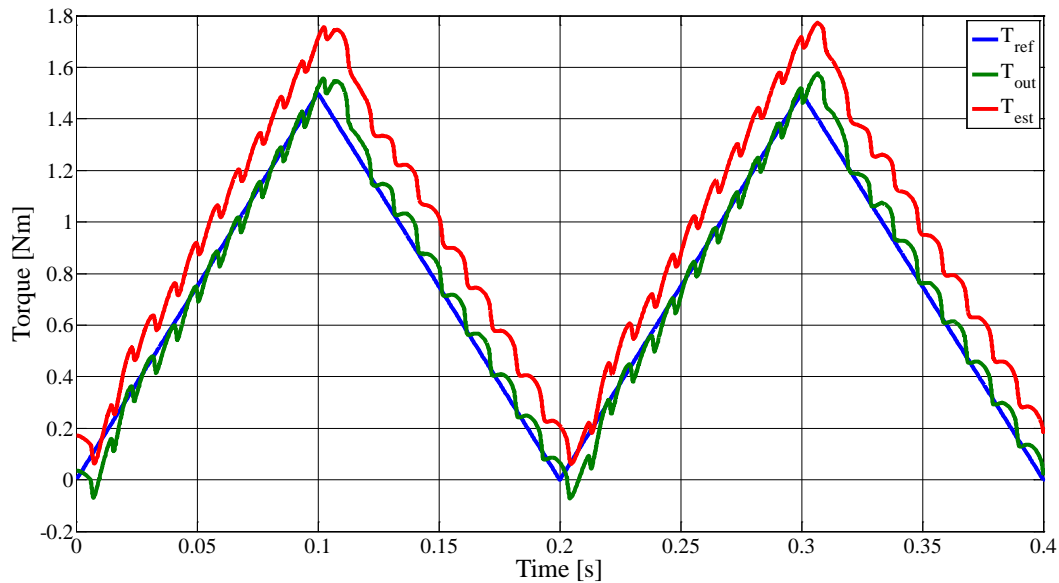
Fig. 3.22: Torque estimation error due to incorrect L_m
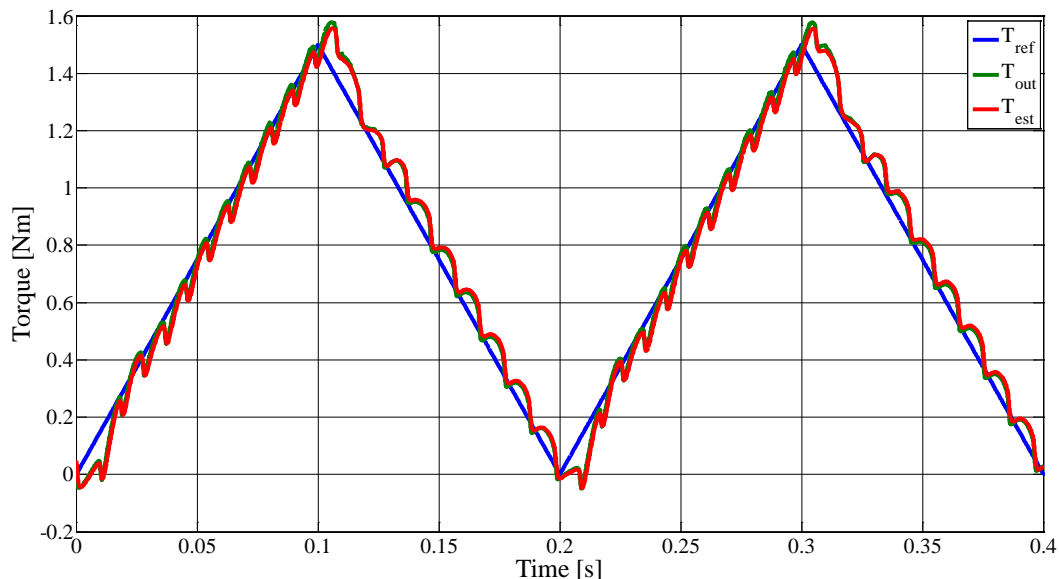
Fig. 3.23: Accurate torque estimation with exact value of L_m

Moreover, the magnetizing inductance also varies with magnetizing current since the ferromagnetic core behaves non-linearly due to magnetic saturation common in all electrical machines. Magnetic characterisation of the machine, done with traditional no-load test or with other methods proposed in literature, gives the relationship between no-load (or magnetizing) current and flux such as the one shown in Fig. 3.24 for one of the machines used in this thesis. Due to saturation

at higher magnetizing currents, the magnetizing inductance L_m decreases as can be seen in Fig. 3.25 whose effect on torque estimation is seen in Fig. 3.22 and Fig. 3.23.
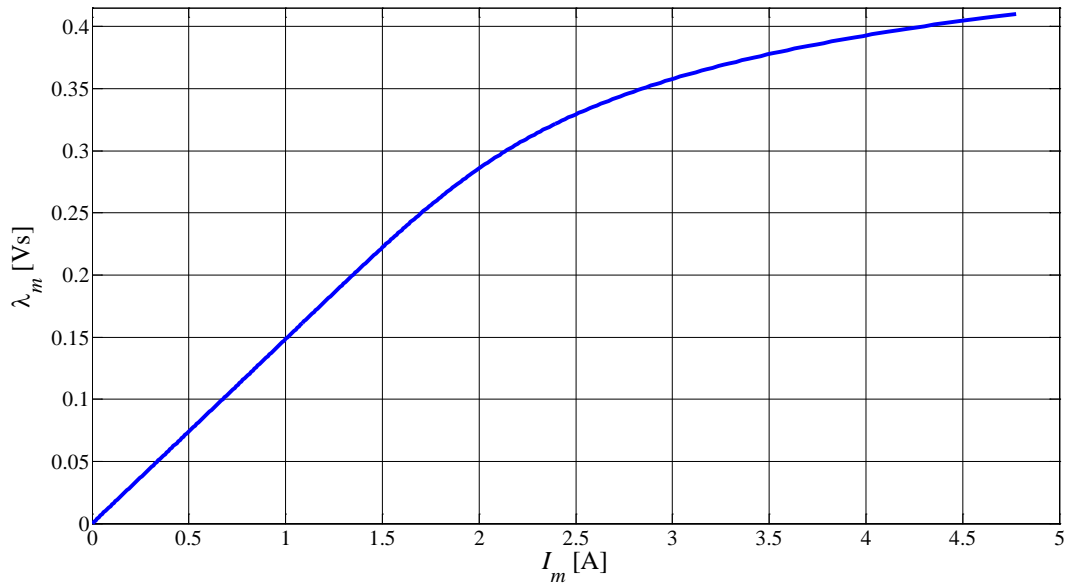
Fig. 3.24: Current-flux characteristic showing saturation for higher magnetizing currents
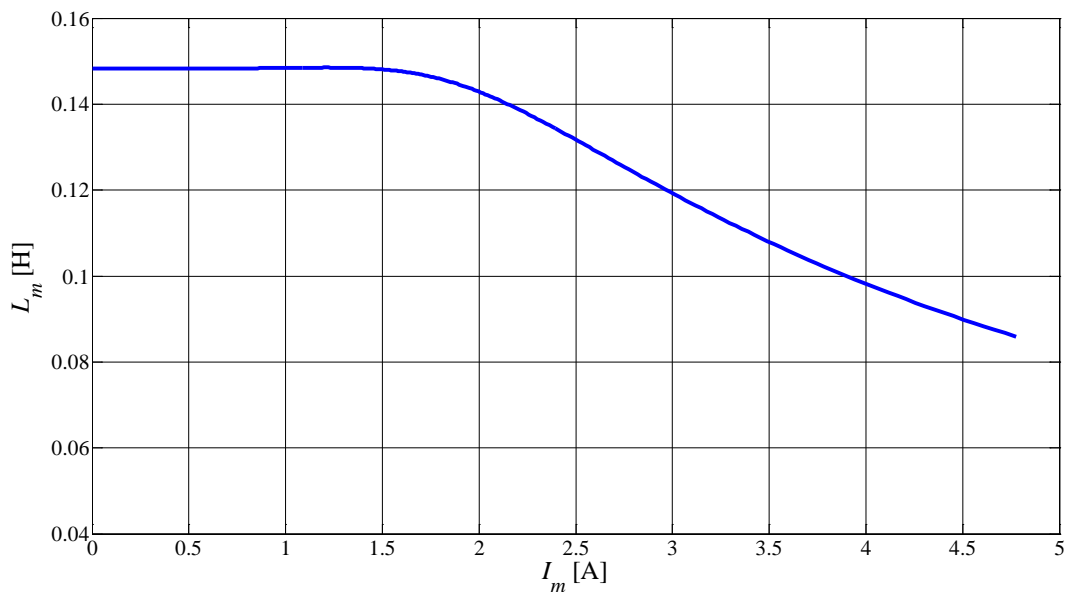
Fig. 3.25: Magnetizing inductance variation with magnetizing current

3.3.4. Rotor resistance variation effects

The rotor resistance R_r of a squirrel cage induction motor is the most sensitive and important parameter for three reasons: first, rotor currents in shorted rotor bars produce thermal drift in rotor resistance; secondly, R_r alters the rotor time constant τ_r (3.45) whose accurate information is important for rotor field oriented control's orientation (3.56), and third, its impact on τ_r affects flux estimation accuracy at low speeds (Fig. 3.12). The electrical inaccessibility of the rotor prevents direct measurement or estimation from its electrical circuit that further emphasises the importance of rotor resistance.

Since the errors in rotor resistance are seen directly in the rotor time constant and it is τ_r which is important from rotor field oriented control's point of view, therefore addressing τ_r

variations takes care of R_r changes automatically. Another reason for considering τ_r over R_r is that the rotor time constant is not only affected by rotor resistance but also by the total rotor inductance (3.8). The rotor inductance depends also on the magnetizing inductance L_m which makes analysis even more complicated especially under heavy saturation conditions Fig. 3.25.

The rotor time constant affects both magnitude and angle of rotor flux at speeds lower than g (rad/s) Fig. 3.16 which is shown below in Fig. 3.26. The error in rotor time constant along with degrading flux estimation degrades also the flux control as well as the dynamic response to step torque commands in case the machine is operated in torque control mode for the rotor flux build up occurs through the rotor time constant (3.47) and the induced torque follows rotor flux (3.49). The steady state torque estimation is also disturbed and has similar effects as in Fig. 3.22 for the situation of Fig. 3.26 i.e. with +50% error in R_r.

Magnitude error   = 0.053Vs
Angle error   = 4.2°
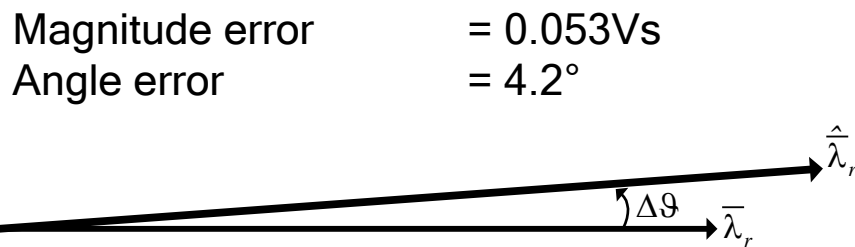
Fig. 3.26: Rotor flux estimate error for +50% error in rotor resistance

The other impact of rotor time constant error is in terms of non-linear relationship between demanded torque and produced torque for torque controlled drives. The correctness of rotor time constant is verified by various researchers by showing whether there is a linear relationship between commanded torque and measured torque. In case the rotor time constant incorporated in the controller is smaller than the actual value, there is a positive torque error (i.e. output torque is lower than the demanded value). On the contrary, if rotor time constant is greater than its true value, the error is negative. This fact can be readily verified by substituting (3.48) into (3.49).

The effects of rotor time constant errors are presented in detail in the literature, especially by [122, 123] which show the misalignment of RFO frames, torque estimation error as well as a sluggish torque response due to detuned rotor time constant value seen by the controllers and observers.

3.4.   Parameter Computation from Nameplate Data

The manufacturers provide machine's essential data on the nameplate attached to its frame. The photo of Fig. 3.27 shows an example of a typical induction motor nameplate, the motor shown is in fact one of the machines used for tests in this thesis.

Apart from showing the manufacturer's name, trademark symbol, address, product number, and the standards the machine conforms to, the nameplate also gives machine insulation class, duty type and the type of ingress protection it is designed for. However, the data of interest here is the machine's electrical and mechanical ratings information that is given in the form of a table. This data is reproduced in Table I below for reader's convenience.

Table I: Motor nameplate data

		Hz 50		
kW	Δ V Y	Δ A Y	cosφ	RPM
2.2	230 / 400	8.8 / 5.08	0.8	1400

From above discussion on control (section 3.2), it can be seen that the nameplate data is not sufficient for control purposes, hence we need to recover machine's electrical parameters needed for

control from this data and the basic knowledge of induction motor theory, making some rough assumptions.

Fig. 3.27: A 2.2 kW induction motor nameplate

Occasionally the stator resistance R_s is also given in the rating-plate data, however if it is not given, it has to be measured with a simple ohmmeter since it cannot be computed from the nameplate data. The stator resistance of the motor of Fig. 3.27 is measured as 3.37 Ω. The other parameters are computed below. Similarly, in the case of a wound rotor induction machine (WRIM), the resistance can either be read from the nameplate (if given) or measured with an ohmmeter. For a squirrel-cage rotor induction motor the rotor is not electrically accessible for resistance measurement, so the resistance must be estimated from given stator quantities, as will be seen below.

To begin with, a decision is made on the machine pole-pair number, if it is not directly given. From the given operating frequency we can have a table of various possible electrical speeds the machine can have depending upon the pole numbers. Table II gives these speeds of the motor at hand (50 Hz) for different pole-pair numbers. Next, the given mechanical speed is checked for closeness with any of the electrical speeds given in Table II. We find that 1400 rpm (given mechanical speed) is close to and less than 1500 rpm (electrical speed) so the machine has 2 pole-pairs. The rated slip can immediately be calculated as:

$$s = \frac{\omega_{elec} - \omega_{mech}}{\omega_{elec}} = 0.0667 = 6.67\%$$

It should be noted that for one pole-pair (3000 rpm electrical), the slip would be 53.3% which is too high a value. According to NEMA (National Electrical Manufacturers Association) standards, the highest slip occurs for design class D motors but that too is only 17%. So, for the given mechanical speed and operating frequency the only logical pole-pair number is 2 (cf. Table II).

Table II: Possible electrical speeds

Hz	50	
Pole-pairs	Electrical speed [rad/s]	Electrical speed [rpm]
1	314.16	3000
2	157.08	1500
3	104.72	1000
4	78.54	750
5	62.83	600

Now, referring to the T-equivalent circuit of Fig. 3.2 (iron losses neglected) and considering that at rated load conditions, the voltage drop in stator resistance and in machine's leakage inductances (L_{ls} and L_{lr}) is too small compared to the drop in magnetizing inductance L_m and the rotor branch resistance at steady state conditions is R_r/s (with s being the slip) and it is augmented by low value of slip. The equivalent circuit of Fig. 3.2 in steady state then simplifies to that of Fig. 3.28.
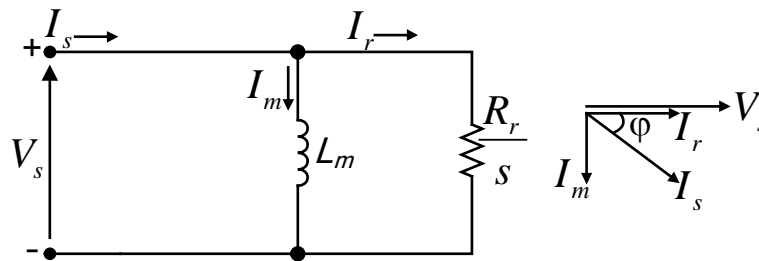
Fig. 3.28: Steady state simplified equivalent circuit and phasor diagram

Knowing the rated machine current and the power factor from nameplate data (Table I), the current components in phase and at quadrature with voltage vector can be determined as:

$$I_r = I_s \cos \varphi = 5.08 \times 0.8 = 4.064 A$$

and

$$I_m = I_s \sin \varphi = 5.08 \times 0.6 = 3.048 A$$

At this point we can compute L_m and R_r for we know the rated machine terminal voltage V_s., the machine slip at rated conditions and the operating frequency (from Fig. 3.27).

$$V_s = j2\pi f L_m I_m \Rightarrow L_m = \frac{400}{\sqrt{3} \times 2\pi \times 50 \times 3.048} = 0.24 H$$

similarly

$$V_s = I_r \frac{R_r}{s} \Rightarrow R_r = \frac{400 \times 0.0667}{\sqrt{3} \times 4.064} = 3.79 \Omega$$

For leakage inductances, let us assume that the starting current of the machine is 5 times the rated current and at start the slip is unity. Further, assuming that the voltage drop in stator and rotor resistances is negligible at start up, besides the magnetizing inductance L_m is too large to permit rapid current rise through it (this is true for starting). The equivalent circuit of Fig. 3.2 then changes to the one shown in Fig. 3.29.
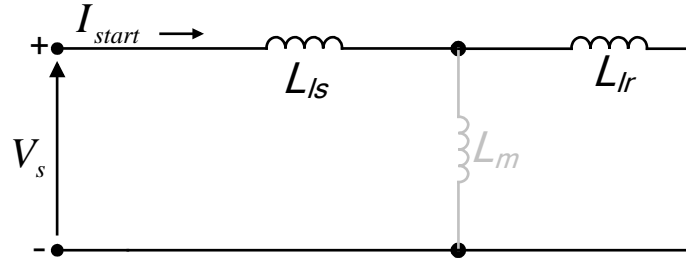
Fig. 3.29: Equivalent circuit for starting conditions

The sum of stator and rotor leakage inductances can be computed as:

$$V_s = j2\pi f\left(L_{ls} + L_{lr}\right)I_{start} \Rightarrow L_{ls} + L_{lr} = \frac{400}{\sqrt{3}\times 2\pi \times 50 \times 5 \times 5.08} = 0.029H$$

Separating the stator leakage inductance from rotor leakage inductance can be a difficult task, therefore they are usually assumed to be equal. However, one way to give each of them its precise value could be dividing them in the ratio of square of resistances since the resistance of a coil is proportional to the number of turns (given the conductor area and the length of a turn remains constant) and its inductance is proportional to its square. The stator and rotor leakage inductances can thus be given as:

$$\frac{L_{ls}}{L_{lr}} = \frac{R_s^2}{R_r^2} = \frac{3.37^2}{3.79^2} = 0.79 \Rightarrow L_{ls} = 0.013H \ \ and \ \ L_{lr} = 0.016H$$

The equivalent circuit parameters of the given induction motor are thus determined from its nameplate data. The accuracy of these parameters can be verified by comparing them with the parameters estimated through standard no-load and short-circuit tests performed following the procedure of [6]. The comparison is given in Table III along with the error in each parameter value.

Table III: Comparison of parameters estimated from nameplate data with those obtained through standard test

2.2kW induction motor equivalent circuit parameters				
Parameter	Unit	Value (nameplate estimate)	Value (tests [6])	Error $\left(\left(\dfrac{estimated}{known}-1\right)\times 100\%\right)$
R_s	Ω	--	3.37	--
L_{ls}	mH	13	16	−18.75%
L_m	mH	240	283	−15.20%
L_{lr}	mH	16	16	0.00%
R_r	Ω	3.79	2.2	+72.27%
τ_r	s	0.068	0.129	−47.55%

As can be seen in Table III, the parameters estimated from the nameplate data contain gross errors and they may render control performance inadequate (cf. section 3.3 above). These inaccuracies drive the motivation behind the work undertaken in this thesis.

3.5.   Parameter identification

As said in chapter 1, the available scientific literature is replete with various approaches adopted in estimating/predicting the induction motor parameters both when the machine is idle and when it is operating while delivering mechanical power to the connected load. Some of the most

promising techniques of identifying parameters essential for control performance are studied here in a greater detail and are tuned to give more accurate results. These techniques are combined in an optimal combination and are implemented both in simulation as well as on experimental rig for verification. Only offline estimation strategies are considered for they fit the scope of this thesis.

Offline parameter identification methods determine motor parameters while the machine is idle. Only those methods are considered here that conform to the definition of self-commissioning i.e. parameter identification without machine rotation, rotor mechanical blocking, isolation of load, and any additional/special supply or measuring equipment. The estimation of parameters from nameplate data (cf. 3.4) does respect the definition of self-commissioning (except stator resistance measurement); however, the estimation errors are too large (Table III) for the control to work with.

3.5.1. Stator resistance

The stator resistance at rotor standstill through power converter can be estimated in two ways: i) by applying a constant dc current through PI current regulators; and ii) with single phase voltage application at two different frequencies. For the first method to work properly, the current regulators must be tuned a priori. In the absence of other parameter values, the current regulators are hard to set, however, thanks to the well known gain-scheduling of PI controllers, they can be set to give desirable performance. Additionally, both the methods require that the inverter non-linearity effects be considered and removed from measurements. These effects can either be pre-determined (through inverter commissioning and look-up tables) or by eliminating them from the measurement by taking more than one readings.

For the dc injection tests, an appropriate constant current is controlled inside any of the machine phases and the voltage at the terminals is measured (or reconstructed). Since the rotor is stationary, hence $\omega_r = 0$, and a direct current is used, thus $\omega = 0$, the stator voltage equation (3.13) in steady state dc will simplify to simple Ohm's law relation of (3.79). Fig. 3.30, single-phase equivalent circuit of Fig. 3.2 without core loss resistance, shows the current path inside the machine for a constant dc injection. The resistance can be recovered from (3.79). For the sake of accuracy, the resistance is estimated in all three phases individually and their average is taken to ensure that correct value has been estimated.
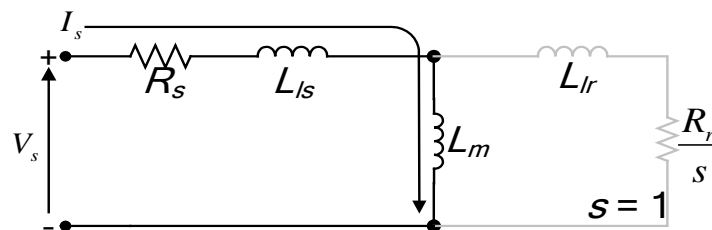
Fig. 3.30: Current path for dc injection

$$V_s = R_s I_s \tag{3.79}$$

This method is the most widely used [8-11, 30, 43, 46, 47] for stator resistance estimation not just for induction machine but also for any other kind of ac machine with concentrated or distributed windings; however, care must be taken in case of permanent magnet or reluctance machines for rotor movement due to alignment and reluctance torque respectively. This will be discussed in the subsequent chapters on other ac machines.

High precision current sensors are used in standard drive hardware for measuring machine phase currents as the current measurement is not only indispensable for control but is required for protection and, sometimes, for estimating the electrical power supplied to the machine. However, the machine terminal voltage, which is needed for applying (3.79), is not usually a measured

quantity. The terminal voltage can be reconstructed from the inverter duty cycle and known dc link voltage if the inverter voltage drop is known. Reconstruction of terminal voltage is also necessary for flux observer of Fig. 3.13 to give accurate flux magnitude information. For this reason, it is desirable to have the inverter non-linearity effects known beforehand.

The inverter's power switches have a typical behaviour of semiconductor devices in that they require a certain threshold voltage for turning on and have a non-zero on-state resistance that gives their current voltage curve as shown in Fig. 3.31. In this figure, R_{on} (a) is the on-state resistance of the switch and R_{eq} (b) is the total resistance of the switch and connected load, it can be seen that at higher currents the switch resistance is constant and small and thus the switch behaves linearly. It is imperative for resistance estimation accuracy that this characteristic is taken care of by appropriate measures.
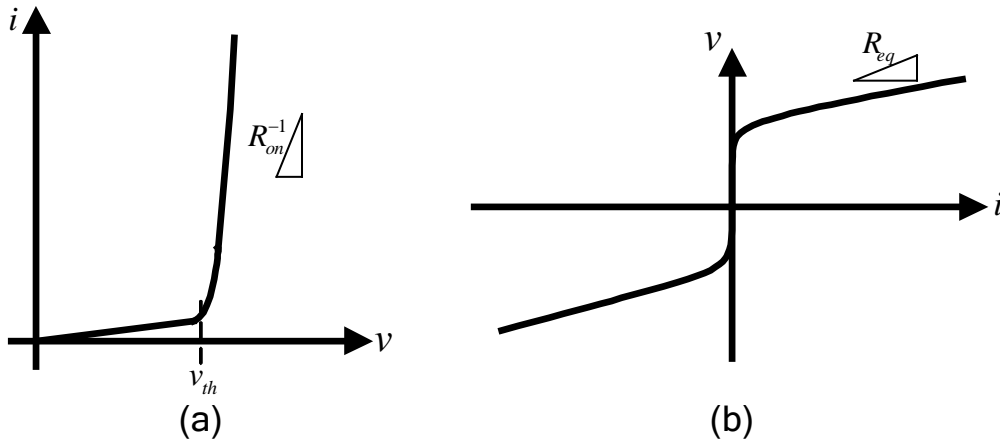
Fig. 3.31: Typical power semiconductor switch characteristic: (a) *vi* curve for switch alone, (b) *iv* curve with load

One way to exclude the inverter non-linearity effect from affecting stator resistance estimation is to use two levels of direct current and compute the resistance from the difference as in (3.80). However, care must be taken that the two current levels I_1 and I_2 are close enough such that the voltage drop in the on-state resistance of the switches (Fig. 3.31) is minimal for the current difference ΔI. Fig. 3.32 shows the results of a resistance detection test performed on one of the test machines. It can be observed that the controller response is rather sluggish; this is because the PI controller (Fig. 3.9) gains k_p (3.78) and k_i are not set according to actual machine parameters – a typical situation encountered in practice. However, as the current and controller output voltage settle in steady state, the resistance estimation through (3.80) returns accurate value.

$$R_s = \frac{V_2 - V_1}{I_2 - I_1} = \frac{\Delta V}{\Delta I} \tag{3.80}$$

Although the method of using two-level dc injection is of the most accurate and simple to implement, it does have its shortcomings when the stator resistance is extremely small as is the case for large power machines. For instance, a 30 kW machine used in tests has a stator phase resistance of 9 mΩ. If the measurement errors are significant, this method loses its robustness. Additionally, such a small stator resistance is comparable with the power switches' on-state resistance (Fig. 3.31), thus it becomes hard to separate the two. Nevertheless, as the machine and semiconductor switch resistances are seen by the controller in series, so separating them does not serve any significant purpose. However, if the same machine is to be used with a different converter, it is necessary to perform stator resistance verification test in the new system. Therefore, the stator resistance (and

power switch series resistance) estimation is included in almost all the control strategies as one of the drive start-up sequences executed before actual operation begins.
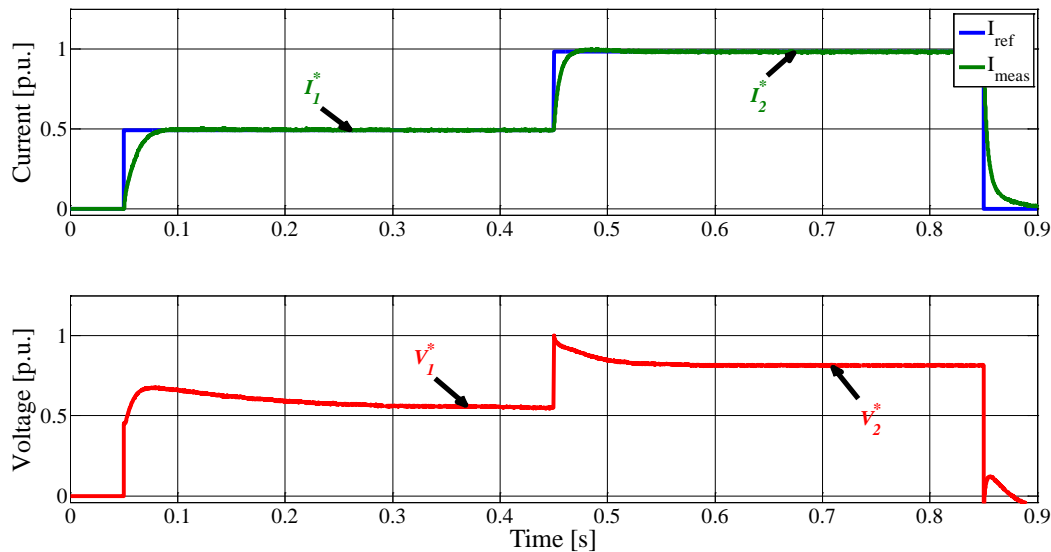
Fig. 3.32: Stator resistance estimation: reference and measured current (top), controller output voltage (bottom)

Furthermore, the magnitude of the injected current as well as the time for which it persists is to be carefully chosen. The magnitude should not exceed the machine's nameplate rated value. This necessitates that the available nameplate data is read into the control algorithm before performing self-commissioning tests. The time, for which this constant test current is maintained inside each of the machine phases, has to be minimum possible so as not to cause excessive heating that would increase the resistance, this causes erroneous results especially in the case when the duration of injection in the three phases is different. This is again a consideration to be made for large power machines as the injected test current could be high to detect a sufficient voltage difference ΔV to apply (3.80) fairly accurately.

3.5.2. Rotor resistance

Induction machine rotors are of two types: wound rotor and squirrel-cage rotor. Whereas the wound rotor induction motors are relatively rare the squirrel-cage induction machines are most commonly used in industry for power ranges up to 400 kW [124]. For wound rotor machines, the rotor resistance can be measured with an ohmmeter (as said in section 3.4 above) or by using the same strategy adopted for stator resistance estimation i.e. using the rotor supply circuit, if possible, to inject a constant current and observing the terminal voltage. However, if the wound rotor is short-circuited as occurs in cases when the rotor winding is included only to increase rotor mechanical inertia, this case becomes analogous to squirrel-cage rotor induction motors. For squirrel-cage rotor machines, the rotor is not electrically accessible, thus the resistance must be estimated from the measured stator quantities.

The rotor resistance of a squirrel-cage induction motor is the most important and critical parameter. Important because it appears in the rotor time constant (3.45) which determines the dynamic response to flux changes; and it is critical due to the fact that it varies over time as a result of temperature rise (or fall) due to increase (or decrease) in load. Rotor resistance variations due to temperature change can go up to 50% or even 100%. For field-oriented control, the rotor resistance error affects the control orientation Fig. 3.26 that degrades dynamic torque response.

The rotor resistance has been in the focus for the past many years, but more attention has been directed towards its online estimation [60-62, 64, 66, 68, 75, 77, 78, 125-128] rather than offline prediction discussed here. Offline estimation does serve for starting and low speed flux

estimation purposes, however, as soon as the machine is loaded, the heat generated by circulating rotor currents in shorted rotor bars renders the initial value erroneous. This does not rule out the importance of estimating it in rest conditions, since from the initial value the changed value can be calculated if the machine contains temperature sensors. Alternatively, if the online resistance estimation methods are implemented, the rotor temperature can be estimated from the change in resistance from its initial/offline value.

Estimating rotor resistance at standstill without mechanically blocking the rotor does respect the definition of self-commissioning established in this thesis, but the value obtained may differ from the actual operating point resistance a great deal depending on the way the test is conducted. This makes the standstill rotor resistance estimation a less reliable source of parameter information. Nevertheless, the standstill estimation is preferred over computation from nameplate data (Table III) or the traditional tests [6] for accuracy and convenience, respectively.

Estimation methods used to obtain rotor resistance at rotor standstill without rotor mechanical locking and without shaft rotation fall in two categories: first, employing impressed direct current as that for stator resistance, and second, applying low-frequency ac injection. Both these methods use current regulators for maintaining desired current and frequency and use the controller output voltage for resistance estimation. Each of these methods uses different equivalent circuit and, therefore, the parameter meaning for rotor resistance.

The estimation using direct current as proposed in [10] requires a constant steady state current inside the machine regulated through current controller in any phase. The path followed by this current is that shown in Fig. 3.30 since the magnetizing inductance acts as a short circuit for dc. This current is subsequently reversed in a step. As the magnetizing inductance is too large to allow step current reversal through it, the current follows the path through the rotor branch (Fig. 3.33), at least during the first few instants of reversal until the magnetizing inductance allows change in current direction through it.
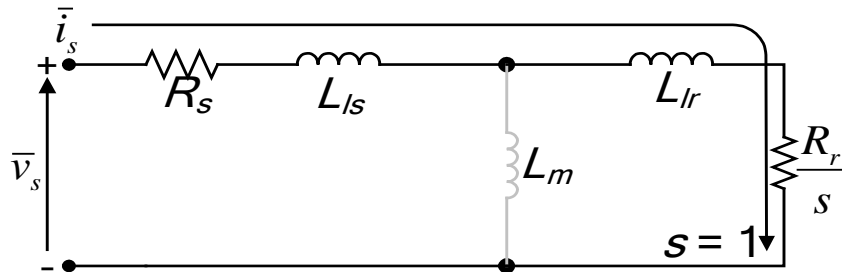
Fig. 3.33: Current path for rapid current reversal through stator terminals

After the transient in the controller output voltage due to the stator and rotor leakage inductances has passed, the controller output voltage can be used for computing the rotor resistance given that the stator resistance is already estimated [10]. The power switch voltage drop Δv_{err} must be known beforehand to calculate rotor resistance referred to stator side $\hat{R}_{rref}$ from (3.81).

$$\hat{R}_{rref} = \frac{v_s^* - R_s I_s^* - \Delta v_{err}}{I_s^*} \tag{3.81}$$

In (3.81), v_s^* is the controller output voltage at the instant when the phase current reaches the reference value I_s^*. From this equation it can be seen that the rotor resistance estimation heavily depends on the accuracy of stator resistance already estimated and the inverter error voltage must be known to have a reliable estimate of this important parameter.

A modified expression is proposed here to do away with this dependence. The controller output voltage in steady state contains both stator resistance effect and the switch drop as said above in section 3.5.1, without separating these two the rotor resistance can be calculated from (3.82), where v_s^* has the same meaning as in (3.81), but V_s is the steady state controller voltage required for maintaining positive I_s^*.

$$\hat{R}_{rref} = \frac{v_{ds}^* - V_s}{I_s^*} \tag{3.82}$$

The advantage of preferring (3.82) over (3.81) is that even if the stator resistance is not estimated correctly or has changed from its value estimated from (3.80) due to temperature variation, the rotor resistance does not see this effect. The switch voltage drop, that is a function of current, also has no effect on rotor resistance estimation since the closed loop proportional-integral current control outputs exactly the voltage V_s to drive the required current I_s^* inside the machine in steady state.

Fig. 3.34 shows the result of this test being conducted on the test machine of Table III. Initially, a negative steady state current is maintained in one phase which is then reversed to a positive current value. The controller output voltage is observed. At the point where the measured current reaches the reference value, the voltage of the controller is read which is used in (3.81) or in (3.82) as v_s^*. It can be seen that this voltage is higher than the steady state value V_s reached later on. This is due to the fact that the current flows in the higher resistance path of the rotor branch instead of the magnetizing inductance during this instant. The difference between the voltage at this point and the steady state voltage is the rotor resistance drop. Knowing the current, the rotor resistance referred to the stator side is computed from (3.82).
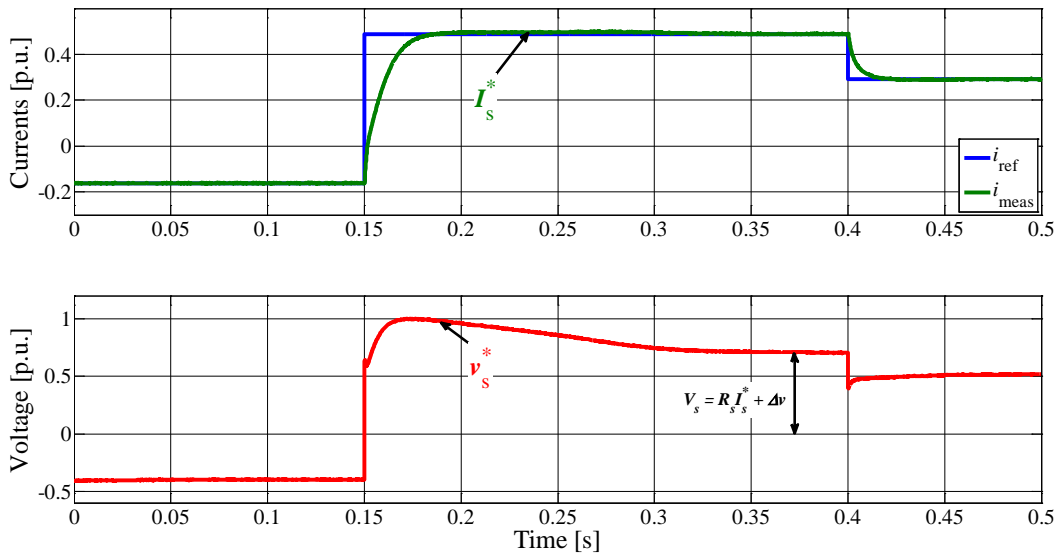
Fig. 3.34: Rotor resistance estimation test: reference and measured current (top), controller output voltage (bottom)

The ac injection method of rotor resistance estimation [11, 129] proposes a low frequency single phase supply to the inverse–Γ equivalent circuit of Fig. 3.6. This supply should be generated through the inverter to respect the definition of self-commissioning. A single phase supply to a three-phase or multiphase induction machine does not produce any rotating magnetic field and hence no torque is induced, so rotor mechanical blocking is ruled out.

In the equivalent circuit of Fig. 3.6, the reactive part of the rotor branch, i.e. the rotor leakage inductance, has been shifted to the left of the magnetizing branch, thus only the active/resistive part remains on the right of magnetizing branch. When a single phase ac supply is used, only the component of current that is in phase with the input voltage flows in the rotor branch. From Fig. 3.6, it can be observed that the voltage across the central branch, i.e. the magnetizing branch, is the same as the voltage across the rotor branch. This voltage can be derived by combining equations (3.28) and (3.30) into (3.83) while noting that $\omega_r = 0$ for a stationary rotor and taking care of the convention for the direction of rotor current $\bar{i}_r$ (3.90).

$$\bar{v}_s = R_s \bar{i}_s + \sigma L_s \frac{d\bar{i}_s}{dt} + \frac{L_m^2}{L_r^2} R_r \left(-\frac{L_r}{L_m} \bar{i}_r \right)$$

or
$$\bar{v}_s = R_s \bar{i}_s + \sigma L_s \frac{d\bar{i}_s}{dt} + R_{rref} \bar{i}_s \tag{3.83}$$

Here R_{rref} is substituted from (3.31).

With a sinusoidal ac source in steady state, equation (3.83) can be rewritten as (3.84) by substituting the derivative term with the frequency of the injected signal as in (3.75).

$$\overline{V}_s = R_s \overline{I}_s + j\omega_l \sigma L_s \overline{I}_s + R_{rref} \overline{I}_s \tag{3.84}$$

ω_l is the frequency of the injected signal. If a sinusoidally varying voltage is generated through the inverter and applied along the α-axis of Fig. 3.3, the current vector given by (3.84) will have two orthogonal components: the first, in phase with the voltage called the resistive component I_R and the second the reactive component I_X caused by the leakage inductance σL_s and the magnetizing branch $(1-\sigma)L_s$ and in quadrature with the applied voltage vector. The phasor diagram of Fig. 3.35 shows these two components of current with respect to the applied voltage vector.
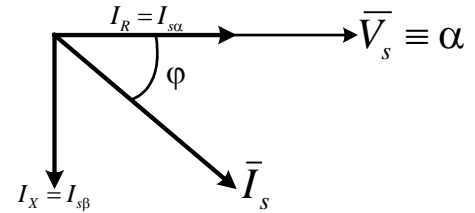
Fig. 3.35: Phasor diagram for sinusoidal voltage applied at stator terminals

The voltage across the rotor branch of Fig. 3.6 can be obtained from (3.84) in its αβ components as in (3.85).

$$\overline{V}_{rs} = V_{rs\alpha} + jV_{rs\beta} = \overline{V}_s - (R_s + j\omega_l \sigma L_s)\overline{I}_s \tag{3.85}$$

The subscript 'rs' signifies that the rotor voltage is due to the voltage applied at the stator terminals.

Since there is only the rotor resistance in the rotor branch, the current component that is in phase with stator voltage only flows in the rotor branch. This current component can be obtained from the phase angle between voltage and current shown as φ in Fig. 3.35 using (3.86).

$$I_R = I_{s\alpha} = \left| \overline{I}_s \right| cos\, \varphi \tag{3.86}$$

The rotor resistance referred to stator can be computed from the ratio of the voltage magnitude across rotor branch and the current component in phase with the voltage vector (3.86) as:

$$R_{rref} = \frac{\left|\overline{V}_{rs}\right|}{\left|\overline{I}_s\right| cos\,\varphi}$$

The definition of scalar product (3.87) can be exploited to simplify the above expression for R_{rref} computation to (3.88).

$$\overline{V}_{rs} \times \overline{I}_s = \left|\overline{V}_{rs}\right|\left|\overline{I}_s\right| cos\,\varphi = V_{rs\alpha} I_{s\alpha} + V_{rs\beta} I_{s\beta} \tag{3.87}$$

$$R_{rref} = \frac{\left|\overline{V}_{rs}\right|^2}{V_{rs\alpha} I_{s\alpha} + V_{rs\beta} I_{s\beta}} \tag{3.88}$$

Using (3.88) to obtain rotor resistance referred to stator poses a particular challenge of extracting α- and β-axis components of the stator current. And, in the presence of inverter non-linearity effects near current zero crossings, this becomes a difficult task if the inverter characterization data is not available. The inverter non-linearity problem can be solved by applying a dc-bias voltage on which the injected ac is superimposed, this avoids current zero crossings and at the same time gives sinusoidal current and voltage for correctly applying (3.88).

The frequency of the applied ac signal is of paramount importance and must be chosen to be below rated machine slip frequency so that the skin effect of rotor bars does not cause the estimate to differ much from rotor resistance under normal operating slip values.

While [129] proposes the open-loop application of sinusoidal voltage to estimate rotor resistance referred to stator, in this thesis a closed-loop current regulated strategy is adopted. The magnitude of the voltage used for test depends purely on the experience of the commissioning engineer which makes the method riskier for the machine and the converter. However, if closed-loop current control is used, the applied voltage to the machine is automatically limited to safe value such that the risk of excessive current is minimized.

Fig. 3.36 shows the simulation results for using the proposed technique of rotor resistance estimation from the inverse–Γ equivalent circuit of induction machine. A dc-bias is used to avoid current zero crossings that distort controller output voltage due to inverter non-linearities. Fig. 3.37 highlights these distortions due to current zero crossings when the dc-bias is excluded.

It must be noted that the results presented here are obtained for ac injection tests using the current regulated injection strategy. As can be observed from Fig. 3.36 and Fig. 3.37, the current inside the machine is feedback-controlled at all times throughout the test which renders this method safer than the open-loop voltage application alternative. The peak current reached with ac component superimposed on dc value must remain within the machine and converter limits and it can be ensured by reading the nameplate data into the test algorithm. Although the machine can withstand a current higher than its ratings during the tests, it should be avoided for the following reason. Since the injection frequency is low, sufficient number of cycles is required for establishing voltage and current phase relationship; this may overheat the machine and change the stator and rotor resistances due to thermal drift.
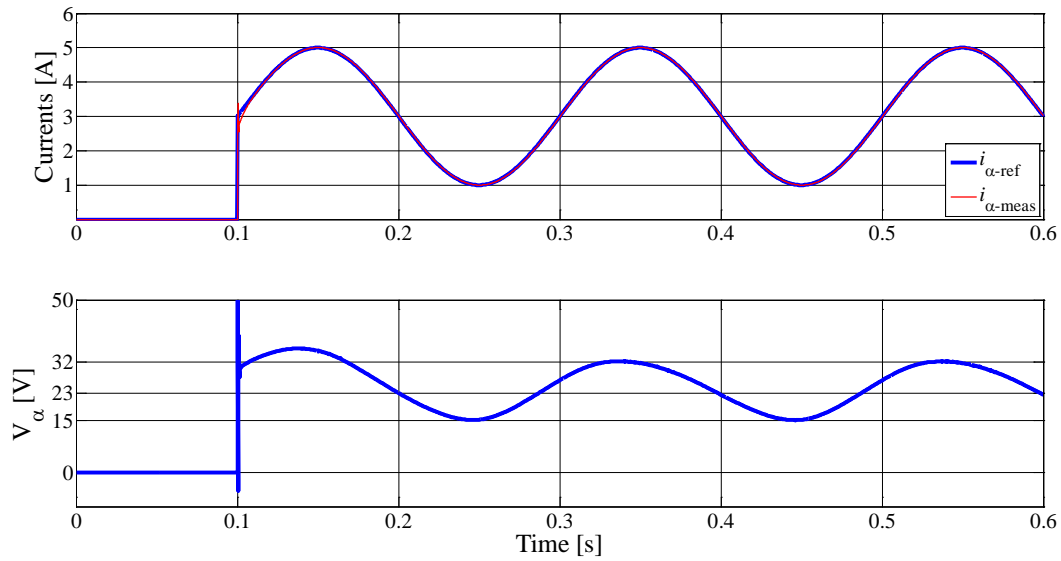
Fig. 3.36: Rotor resistance estimation test through dc-biased ac injection: reference and measured current (top axis), controller output voltage (bottom axis)
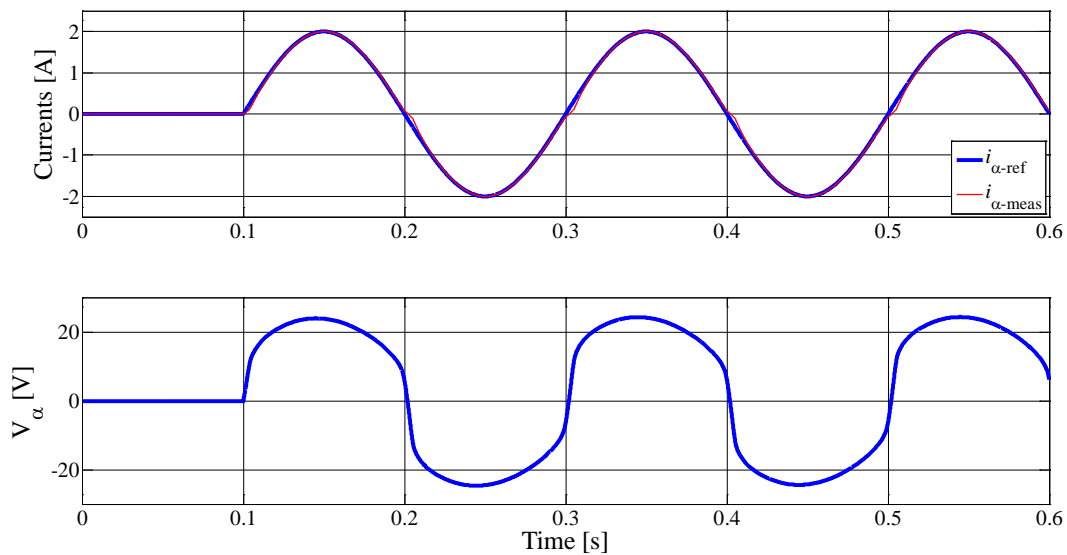
Fig. 3.37: Ac injection for rotor resistance estimation without dc-bias – distorted controller output voltage (bottom axis)

The procedure outlined here can equally be used for computing the magnetizing inductance of the machine. The magnetizing inductance in case of inverse–Γ equivalent circuit of Fig. 3.6 is $(1-\sigma)L_s$ which can be obtained from the reactive current component of (3.85) through the same procedure as followed for rotor resistance estimation. However, the dc-bias introduced to do away with inverter non-linearities changes the magnetization state of the machine which gives magnetizing inductance value at that particular current. Furthermore, since the applied ac signal is a sinusoid, the magnetizing inductance changes at each point of the current wave of Fig. 3.36 that makes the inductance estimation through phasor treatment of (3.85) unreliable.

3.5.3. Leakage inductances

The leakage inductance is an equivalent inductance attributed to all the flux leakages occurring in the induction machine's stator and rotor slots, stator tooth tip, end-winding, pole shoe, and flux leakages caused by harmonics, slot skewing (see section 3.1 on page 25). This leakage

inductance determines the bandwidth and stability of current control (cf. section 3.3.2 and Fig. 3.21); therefore it is of critical importance with regards to control even if it is sometimes dubbed insignificant for its small magnitude compared to main (magnetizing) inductance of the machine.

It should be noted here that the leakage inductance is not always harmful and does not always contribute in increasing the power losses of the entire drive system. Occasionally, the leakage inductance is deliberately increased to reduce the locked-rotor current for containing supply voltage dips. For PWM inverter-fed induction motors, for instance, the leakage inductance works as a filter for high frequency switching pulses inherent in PWM based motor supply. From the data of the 2.2 kW machine used in tests given in Table III, it can be seen that the magnetizing inductance L_m (283 mH) is too large to allow high frequency current components through it, so the only path left for these current components is through stator and rotor resistances and leakage inductances (Fig. 3.4). The time constant of this current path can be calculated from data in Table III as 5.75 ms, which is a perfect low-pass filter for switching impulses of 0.1 ms period (10 kHz switching frequency). This inherent filtering renders motor phase currents smooth and free of any switching spikes that would otherwise make the induced torque nervous and harmonically polluted which may in turn be harmful to motor bearings and the load alike while causing additional noise.

The leakage inductances as calculated from nameplate data (section 3.4) are fairly close to values obtained by standard tests; however, the assumption made about the starting/locked-rotor current to be 5 times the rated current may not be true across a vast range of machine power ratings. This leaves the assumption at the discretion and experience of control/commissioning engineer that makes the parameter prone to human error. Furthermore, the locked-rotor current for machines rated at same power but different voltage ratings or design classes may differ by as much as 50% [124], section 12.35. This renders the assumption on starting current increasingly erroneous if applied across the entire range of machine designs that further emphasizes the importance of on-site measurement/estimation of leakage inductances.

The standard practice of estimating machine leakage inductances requires blocking the rotor by mechanical means and applying a reduced voltage, rated frequency, ac supply that maintains rated current in the stator [6]. For this test, high precision voltage, current and power measurement equipments are needed along with safe means of locking the rotor, additionally motor isolation from load may also be necessary. Overheating of the machine during the tests may render it unusable immediately after the tests. This necessitates that, for a quick start-up, minimum off-time and least operational difficulties, an alternative for estimating leakage inductances is investigated.

To comply with the definition of self-commissioning and to keep within the constraints imposed by it (cf. section 1.1 on pp. 1), the leakage inductances are required to be estimated using the standard power converter supplying the machine and with the sensors already available onboard. Of the methods already proposed in the literature, the technique employing voltage pulse [8, 10, 43] gives reliable results and is simple to implement. However, it does come with some shortcomings which are discussed and are done away with by a new strategy proposed in this thesis. Although the total machine leakage inductance varies with the flux level inside the machine [130], it is computed from the tests conducted at the rated machine flux level in this thesis.

A voltage pulse can be produced by binary control of inverter switches (without PWM) that will connect machine phases to the dc-link as shown in Fig. 3.38. The figure shows phase–A being connected to the positive terminal of the dc-link and phases B and C to the negative, the phases can be interchanged without any effect on the test result, in fact it is advisable that the test is performed with all three phases for validity. The inverter of Fig. 2.2 is represented by simple make-and-break switches for simplicity.
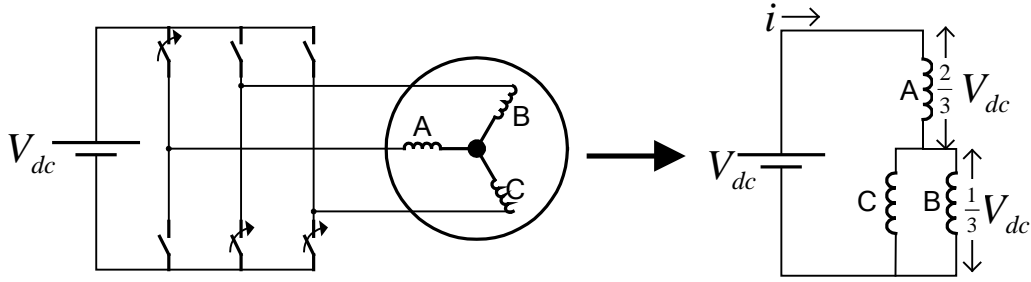
Fig. 3.38: Connections with binary control of inverter switches

Of course, a positive voltage pulse would drive a positive current in the machine whose maximum value is determined by the dc-link voltage and the total resistance in the current path i.e. the sum of stator and rotor resistances (Fig. 3.39); however, the leakage inductances would retard the rise in current and it is this delay that helps calculate the leakage inductances. It is seen that the magnetizing inductance is excluded from the current path. The reason for this exclusion is its large value, compared to the leakage inductances (cf. Table III), that does not permit a rapid current rise through it for a short voltage pulse applied. Fig. 3.39 shows the current path for voltage pulse application.
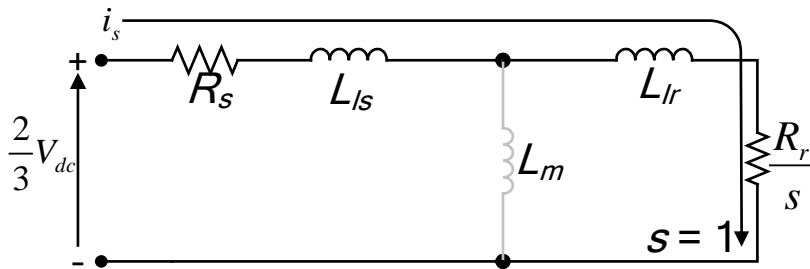
Fig. 3.39: Current path for voltage pulse application

The expression for determining leakage inductances can be obtained by applying Kirchoff's voltage law for the current loop shown in Fig. 3.39 as:

$$v_s = R_s i_s + L_{ls}\frac{di_s}{dt} + L_{lr}\frac{di_s}{dt} + R_r i_s$$

$$v_s = (R_s + R_r)i_s + (L_{ls} + L_{lr})\frac{di_s}{dt} \qquad (3.89)$$

It must be reiterated here that in equation (3.89) the rotor resistance R_r and rotor leakage inductance L_{lr} are rotor quantities referred to the stator side as in Fig. 3.2. Before commenting on (3.89) and deriving expression for leakage inductances' estimation, equations (3.3) and (3.4) are revisited for an important equivalence that would simplify computations as well as validate the assumptions made later in this chapter.

Equations (3.3) and (3.4) are written for current directions shown in Fig. 3.2. The voltage, current and flux vectors are referred to individual reference frame of stator and rotor. The rotor side parameters, namely rotor resistance (R_r) and leakage inductance (L_{lr}), can be considered either referred to stator side or considered to be on the rotor side of the transformer equivalent circuit of Fig. 3.1. Let us assume that R_r and L_{lr} are on the rotor side and the transformer equivalent turns ratio a_{eff} is the rotor coupling factor k_r of (3.43). Now, for the direction of i_r reversed in Fig. 3.39 with respect to Fig. 3.2 and from the basic transformer theory, we can write i_r in terms of i_s as in (3.90).

$$\bar{i}_r = \frac{-1}{k_r}\bar{i}_s \tag{3.90}$$

The magnetic equations of the machine (3.5) and (3.6) are valid irrespective of whether the quantities are referred to stator or rotor side of the transformer and are not affected by the reference frame considered. Using (3.43) in (3.90) and substituting the result in (3.5) we have:

$$\bar{\lambda}_s = L_s\bar{i}_s + L_m\left(-\frac{L_r}{L_m}\bar{i}_s\right) = L_s\bar{i}_s - L_r\bar{i}_s$$

Using (3.7) and (3.8), we get: $$\bar{\lambda}_s = (L_{ls} - L_{lr})\bar{i}_s$$

Using it in (3.3), we have: $$\bar{v}_s = R_s\bar{i}_s + L_{ls}\frac{d\bar{i}_s}{dt} - L_{lr}\frac{d\bar{i}_s}{dt} \tag{3.91}$$

Repeating the above operations on (3.6) and (3.4) for rotor equations

Putting (3.43) in (3.90) and the result in (3.6): $\bar{\lambda}_r = L_m\bar{i}_s - \frac{L_r^2}{L_m}\bar{i}_s$

Using it along with (3.90) in (3.4) while noting that $\bar{v}_r = 0$

$$0 = R_r\left(-\frac{L_r}{L_m}\bar{i}_s\right) + L_m\frac{d\bar{i}_s}{dt} - \frac{L_r^2}{L_m}\frac{d\bar{i}_s}{dt}$$

Using (3.8) and rearranging: $$-L_{lr}\frac{d\bar{i}_s}{dt} = R_r\bar{i}_s + L_m\frac{d\bar{i}_s}{dt} - \frac{L_m^2}{L_r}\frac{d\bar{i}_s}{dt} \tag{3.92}$$

Substituting (3.92) in (3.91):

$$\bar{v}_s = R_s\bar{i}_s + L_{ls}\frac{d\bar{i}_s}{dt} + R_r\bar{i}_s + L_m\frac{d\bar{i}_s}{dt} - \frac{L_m^2}{L_r}\frac{d\bar{i}_s}{dt}$$

➔ $$\bar{v}_s = (R_s + R_r)\bar{i}_s + \left(L_{ls} + L_m - \frac{L_m^2}{L_r}\right)\frac{d\bar{i}_s}{dt}$$

Substituting (3.7): $$\bar{v}_s = (R_s + R_r)\bar{i}_s + \left(L_s - \frac{L_m^2}{L_r}\right)\frac{d\bar{i}_s}{dt}$$

Using (3.27): $$\bar{v}_s = (R_s + R_r)\bar{i}_s + \sigma L_s\frac{d\bar{i}_s}{dt} \tag{3.93}$$

A quick comparison of (3.93) with (3.89) suggests that the sum of stator leakage inductance L_{ls} and the rotor leakage inductance referred to stator L_{lr} is equal to the total machine leakage factor σ, defined by (3.27), multiplied with total stator inductance L_s i.e. inductance seen from the stator terminals with rotor side open-circuited (see page 27 in section 3.1). This result also confirms (3.77) and permits us to write (3.94). This result for the total leakage inductance is also consistent with the inverse–Γ equivalent circuit of Fig. 3.6 in which the leakage inductances of stator and rotor are combined and are included on the stator side of the equivalent circuit. σL_s is also called the stator

transient inductance since it determines the response to a transient at the machine terminals, as it was seen while computing stator and rotor leakage inductances from starting/inrush current in section 3.4.

$$\sigma L_s = L_{ls} + L_{lr} \tag{3.94}$$

Having defined the equation for machine response to a voltage pulse, (3.89) or (3.93), and the equivalence between total leakage inductance and the stator transient inductance (3.94), the details of estimating this parameter are now discussed. A positive voltage pulse is applied by commanding the inverter switches as in Fig. 3.38, and the resultant current is observed till it reaches a set maximum as shown in Fig. 3.40. Although the machine can sustain a current higher than about 5 to 7 times its rated value for a short time for which the pulse is applied, the power semiconductor switches cannot. Therefore the maximum current point (in Fig. 3.40) should be preset according to the power switches' ratings in order to avoid inverter failure.

Using (3.89) or (3.93) and neglecting the voltage drop in stator and rotor resistances which is usually small compared to the dc-link voltage, the expression for stator transient inductance can be obtained in terms of applied voltage and current derivative as in (3.95). The derivative/slope of current can be computed by counting the number of samples, which give the time, it takes for the current to rise to I_{max} (Fig. 3.40).
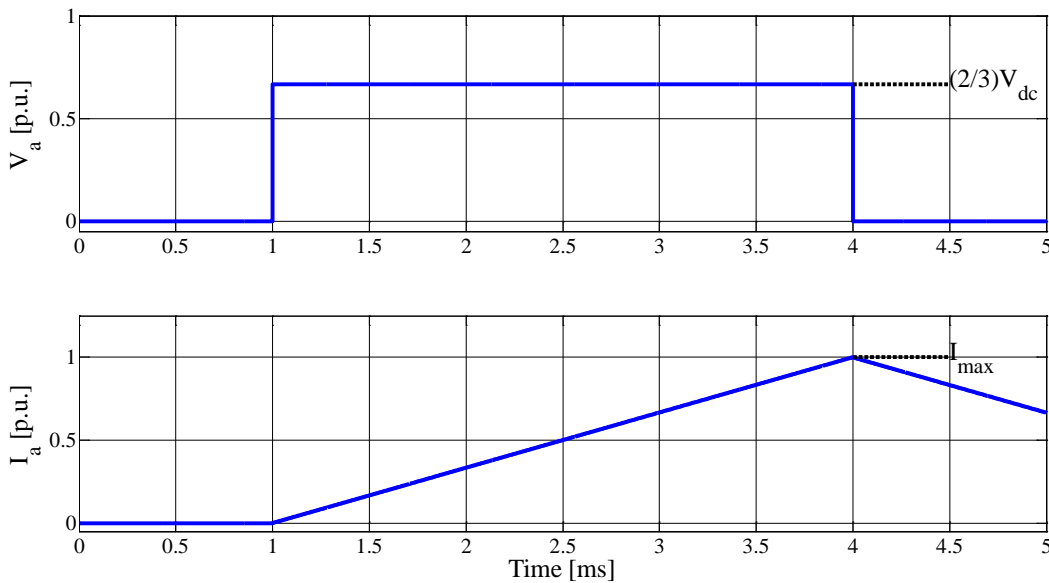
Fig. 3.40: Positive voltage pulse applied to phase-A and resultant current (data used is purely indicative)

$$\sigma L_s = L_{ls} + L_{lr} = \frac{2}{3} V_{dc} \left(\frac{\Delta I}{\Delta t} \right)^{-1} \tag{3.95}$$

Although the inductance can be computed only with positive pulse, the application of a subsequent negative pulse would give more current difference and more current samples being collected that makes the result more reliable. Fig. 3.41 shows the application of a positive pulse followed by a negative voltage pulse for σL_s estimation for the test machine whose data is given in Table III. After the current reaches a set maximum, the command is removed till the instant at which the current reduces to a value approximately equal to the rated magnetizing current. The magnetizing current can be computed from the rated current and rated power factor both included in the nameplate data (Fig. 3.27 and Table I). At this point a negative pulse is applied as depicted in

Fig. 3.41. The sequence of positive and negative pulses as shown in Fig. 3.41 is not a strict requirement; it can be reversed without affecting the results.
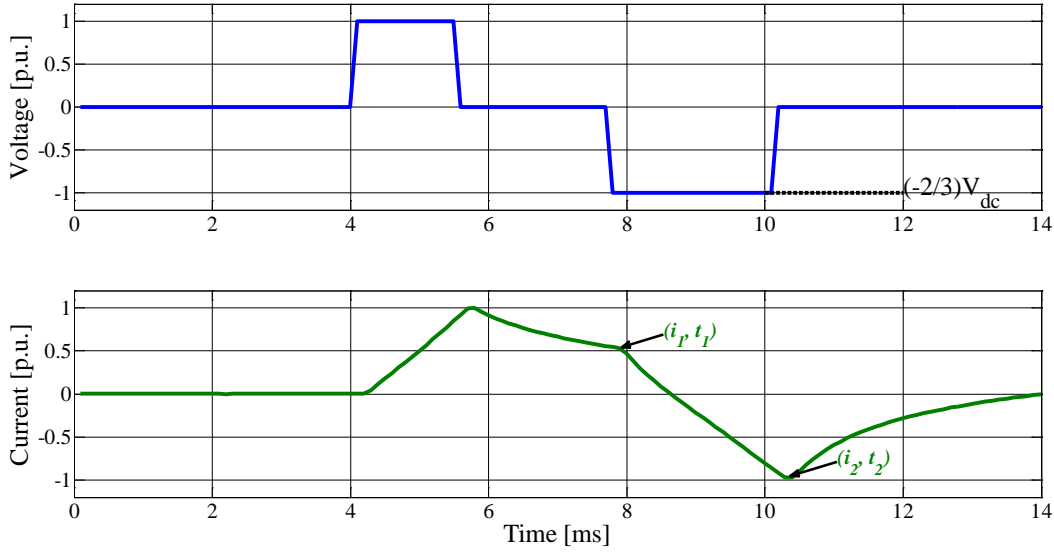
Fig. 3.41: Positive voltage pulse followed by a negative pulse: points for computing $\dfrac{\Delta I}{\Delta t}$ are marked

Observing Fig. 3.41 (and Fig. 3.42 below), it can be seen that during the interval between removal of positive pulse and application of negative pulse, the phase current follows a quasi exponential decay. The time constant (τ_σ) of this decay can be recovered by considering any two points along the curve. If the current path assumption of Fig. 3.39 during the decay also holds good, which it does given the decay is faster than what the magnetizing inductance can permit (i.e. $\tau_\sigma \ll \tau_r$), the time constant of the current decay gives the total resistance in the current path of Fig. 3.39. Knowing the stator resistance (3.80) from section 3.5.1 and σL_s estimated here, the rotor resistance referred to stator can be recovered from (3.96). This acts as a cross-check for the value established in (3.81), (3.82) or (3.88). However, the result for R_{r_ref} in (3.96) may be altered by the power semiconductor switches' equivalent resistance that must be appropriately compensated for.

$$R_{r\_ref} = \frac{\sigma L_s}{\tau_\sigma} - R_s \qquad (3.96)$$

Unlike stator resistance estimation (3.5.1), this method is relatively immune to inverter non-linearity effects because the voltage applied to the machine terminals is 66.7% of the dc-link voltage that is much higher than the threshold voltage and resistive drops in inverter switches combined. Additionally, the assumption made for neglecting the stator and rotor resistance drops in deriving (3.95) does not weigh heavily on estimation as these drops are also negligible compared to dc-link voltage normally used in drives applications. However, care must be taken in case of traction applications when the dc-link voltage derived from accumulators is very low in which case the inverter non-linearity effects and stator and rotor resistance drops must be taken into account. For low dc-link voltages, when the stator and rotor resistance drops as well as semiconductor switch effects make up a considerable proportion of available dc bus voltage, the current rise will not be as linear as seen in Fig. 3.40. In such situations, the magnetizing inductance L_m also plays its part and the problem becomes complicated. Therefore, this method is useful for applications with high dc-link voltages.

Further, although the method gives correct results for stator transient inductance estimation for low-power machines that usually have high reactance, it poses serious risks for high-power,

low-reactance machines for which a new method is proposed in this thesis. It is discussed in the next section.

3.5.4. *Transient inductance estimation – low reactance machines*

The stator transient inductance detection method described in the previous section requires direct connection of machine phases to the dc-link voltage; this exposes the stator phase windings to an unusually high voltage. For instance, in case of phase-A, the voltage appearing across it is two-third of the total dc-link voltage (Fig. 3.38). For large machines that have low total leakage inductance, this voltage would cause a significant current in the windings. High-power drives are also designed with high dc-link voltage and low switching and sampling frequencies. Since the power semiconductor devices must commutate high dc-link voltage, the frequency of commutation is kept low to give more time for reverse recovery of diodes (of Fig. 2.2). The sampling frequency is also low because the current magnitudes are so high, and slow varying, that acquiring too many samples in a small current variation range becomes impractical and demanding on the data acquisition system.

The impracticability of the above method was observed for one of the machines used in tests. The situation is explained presenting actual system data along with numeric calculations for a 32 kW induction motor used for compressor application. The machine has a stator and rotor leakage inductance of 0.165 mH and 0.226 mH, respectively. The dc-link voltage is 550 V and the switching frequency is 8 kHz. Sampling is synchronized with switching so the sampling frequency is also 8 kHz that gives a sampling period of 0.125 ms. Neglecting the stator and rotor resistance voltage drops, the total leakage inductance of 0.391 mH is exposed to a voltage of 367 V. The resulting current between two sampling instants can be computed either from (3.89) or (3.93) in their discrete form (3.97). Assuming that the current is zero before applying voltage pulse and Δt is one sampling period (i.e. 0.125 ms). The current at the next sampling instant is computed as 117.3 A.

$$\frac{\Delta i_s}{\Delta t} = \frac{1}{L_{ls} + L_{lr}} v_s = \frac{1}{\sigma L_s} v_s \tag{3.97}$$

$$I_1 - I_o = \frac{1}{\sigma L_s}\left(\frac{2}{3} V_{dc}\right)\Delta t \quad \Rightarrow \quad I_1 = 117.3 A$$

The rated current of this machine is 120 A and the switches are rated at 160 A, therefore the overcurrent protection is set at 150 A (allowing a safety margin for switches). After the first sampling instant the current is sampled as 117.3 A, as it is below the protection threshold, the software protection does not trip. However, at the next sampling instant if the voltage persists the current is double the earlier value i.e. 234.6 A. Although, the software protection would operate and shut the system down, the damage is already done to the power semiconductor devices by this current. In case there is a hardware overcurrent protection, which is usually present in the form of fuses, it will operate to protect the power switches, however the number of samples collected for estimating transient inductance is extremely small (only one) which precludes correct use of (3.95).

Due to the inappropriateness of, and practical limitations in the use of, above method for estimating transient inductance of high power machines, a new method is investigated here. The foremost objective is to exclude the need for direct connection of machine terminals with dc-link. Instead a controlled voltage is applied such that the current remains under protection threshold at all times. The pulse width modulation based strategy comes in handy in such situations.

There are two ways of applying a controlled voltage across machine terminals: (i) imposing a sufficient constant voltage through PWM that would cause a ramp-like stator current as shown in

Fig. 3.40 (bottom curve), (ii) using current regulators to control the current inside the machine having the shape of a ramp.

In the absence of parameter information, it is hard to decide on the voltage to be applied that ensures that the inverter ratings are not exceeded, however, from the already estimated stator and rotor resistances (see sections 3.5.1 and 3.5.2) and the known machine rated current (I_n), a voltage that can produce 5 times the nominal current can be computed from (3.98). This voltage can be applied by appropriately commanding the inverter switches till the current reaches the point I_{max} of Fig. 3.40 (that can either be the machine rated current I_n or the software protection threshold). At this point the voltage command is reversed (with same magnitude) as shown in Fig. 3.42.

$$V_s = (R_s + R_r) \times I_n \times 5 \tag{3.98}$$

The relation of (3.95) can now be used for computing σL_s, however the voltage used is not $\frac{2}{3}V_{dc}$ anymore but that given by (3.98).

This technique does estimate stator transient inductance, however, obtaining correct voltage magnitude to be applied (3.98) depends on the estimation accuracy of the other parameters, namely, stator and rotor resistances. Choosing correct inrush current factor is also important. This makes the method dependent on external factors that affect accuracy.
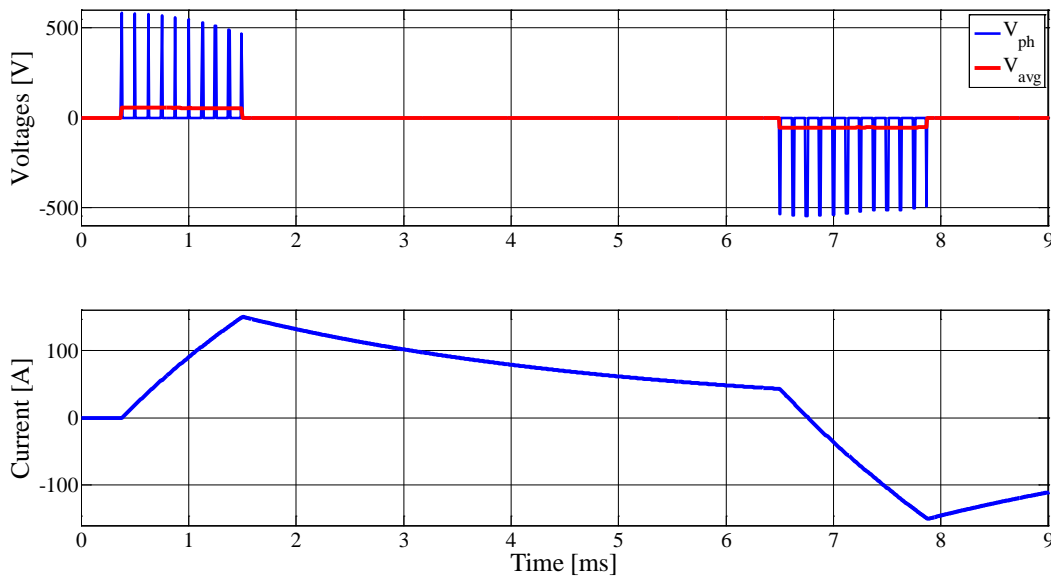
Fig. 3.42: Positive and negative voltage applied through PWM and resultant phase current

The second way is to apply a fast current ramp which makes the procedure the exact opposite of the voltage pulse application method described in section 3.5.3. In this case as well the machine is not directly connected across the dc-link but is supplied with a voltage determined by the current controller output and applied to the machine through PWM control of inverter switches.

A fast but controlled current ramp is injected through current controllers. The controller output voltage for the entire duration of current ramp reaching its maximum value is averaged over time to get its mean value. The mean value of controller output voltage is then used in (3.95) along with known current derivative from the applied ramp. The feedback controlled nature of this new technique would prevent any risk of excessive current flowing through the power semiconductor switches.

The nature of the ramp injected needs some detailed analysis. In order ensure that the applied current follows the path through rotor branch without passing through the magnetizing inductance (Fig. 3.39), the ramp should be fast enough for the validity of the assumption that the magnetizing inductance acts as an open circuit. For this condition to be true, (3.99) must be respected. With the switching frequencies commonly used in drives, this condition can easily be satisfied.

$$L_m \frac{di}{dt} > v_s \qquad (3.99)$$

For realizing a fast current ramp that ensures that (3.99) holds good, a high bandwidth current regulator is required. However, as seen in Fig. 3.21, current controller designed near the maximum possible bandwidth runs the risk of going unstable. Here, the techniques of gain scheduling prove extremely useful in selecting proper controller gains. Gain scheduling is used for results shown in the later sections of this chapter.

Fig. 3.43 shows a 10 kA/s current ramp applied for estimating the transient inductance of the 32 kW machine used in simulation. The controller output voltage is also shown in this figure. The transient inductance estimated through this method for this particular machine gave an error of 0.03 mH (8%), however, the power switches are not stressed beyond their capacity and at the same time the direct connection of the low-reactance machine across high dc bus voltage is avoided.
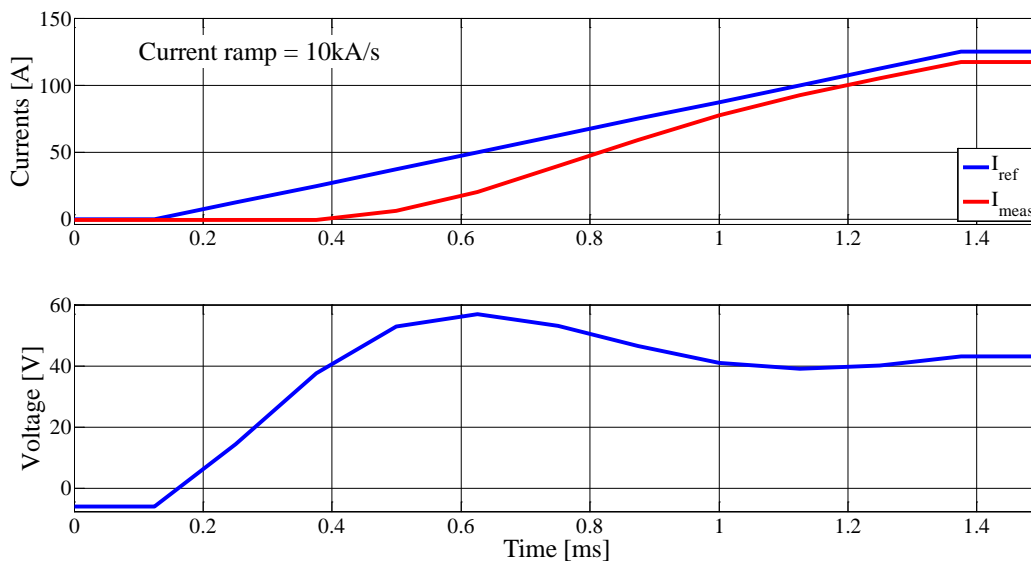
Fig. 3.43: Stator transient inductance estimation with new method: current ramp (top), controller output voltage (bottom)

3.5.5. Rotor time constant

Field oriented control, whether direct or indirect, is extremely sensitive to the rotor time constant since an error in this parameter causes the orientation to be lost (Fig. 3.26). Its direct dependence on other machine parameters, such as rotor resistance (3.45) and magnetizing and leakage inductances (3.8), makes its estimation at standstill complicated. Moreover, it changes with machine temperature and magnetization state during operation; for this reason much effort is directed towards its online tracking (as for rotor resistance, cf. 3.5.2). As observed for rotor resistance, the rotor time constant estimated at standstill loses meaning once the machine takes on the load and rotor temperature rise alters rotor resistance and consequently the time constant. Nevertheless, it is important to have its initial value. This serves not only for starting sensorless drives, but also used by online updating algorithms for cross-verification purposes.

Many efforts in the past have been directed towards determining the rotor time constant using various techniques, those fitting the definition of self-commissioning (cf. section 1.1 on page 1) are relatively fewer. Some of them are discussed with improvements proposed here for rendering the identification procedures automatic, fast, safe, and more accurate.

The first method discussed here is the single-phase current injection strategy [10] in which low-frequency ac is applied to the inverse–Γ equivalent circuit of Fig. 3.6, which is then switched to a constant current, equal to the rated magnetizing current of the machine, at a precise instant of time as shown in Fig. 3.44. The magnetizing current can be estimated from the nameplate data (Fig. 3.27).
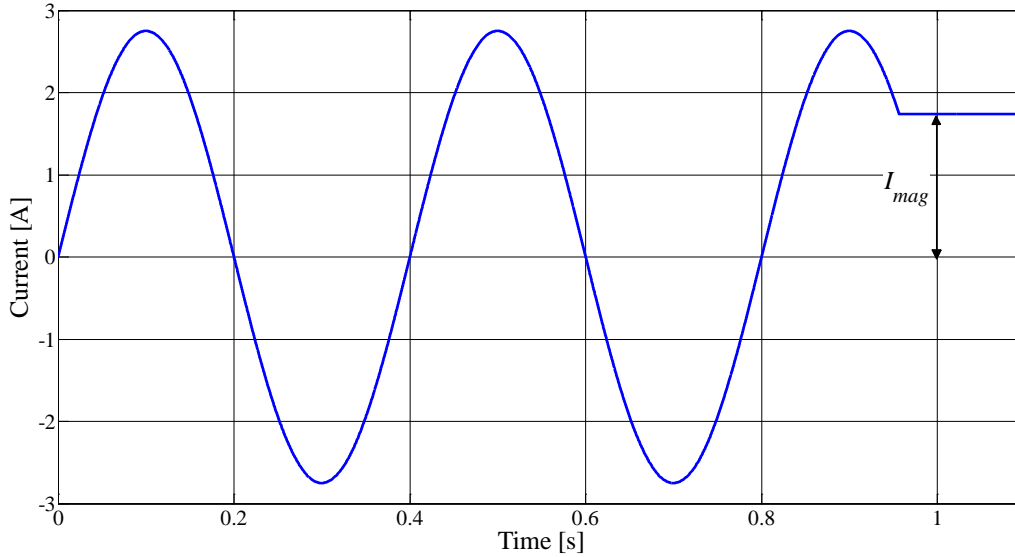
Fig. 3.44: Single-phase sinusoidal ac switched to constant dc for rotor time constant estimation

Referring to Fig. 3.6 again, the equivalent circuit is valid both in steady state and transient conditions. Both these conditions are exploited here to devise the procedure for rotor time constant calculation proposed in [10]. When the applied sinusoidal current reaches steady state, the current divides into flux component (through magnetizing branch) and torque component (in the rotor branch). The proportion of division depends on injection frequency as the impedance of magnetizing branch changes with frequency. If the rotor field oriented control equations (of section 3.2.1) are considered, the magnetizing component of current gives rise to rotor flux and thus becomes i_s^d (3.69) and the torque component becomes i_s^q (3.49).

At the instant the current is abruptly switched to constant dc, the stator terminal voltage is observed. After an initial transient, it either increases or decreases exponentially over time depending on the frequency of the injected signal. This behaviour can be explained based on the equations developed earlier.

Since the rotor remains stationary with single-phase supply, the speed voltage term containing ω_r is zero in Fig. 3.6 and the slip frequency is equal to the frequency of the injected signal. The actual rotor flux in terms of injection frequency can be obtained from (3.48) after replacing ω_{sl} by ω_{inj} and L_m by the magnetizing branch inductance of Fig. 3.6 to give (3.100). The flux is in inverse proportionality to the injection frequency.

$$\lambda_r^d = \frac{(1-\sigma)L_s i_s^q}{\omega_{inj}\tau_r} \tag{3.100}$$

73

In the first case, with $\omega_{inj} < \omega_{sl}$, at the time when the current is switched to a constant value equal to the rated magnetizing current (Fig. 3.44), the rotor flux as given by (3.100) is higher than the rated flux caused by rated magnetizing current. Since, the rotor flux must return to the rated value after switching, the excess current of the magnetizing branch follows the rotor-side loop till the excess energy stored in magnetizing inductance vanishes by dissipation in rotor resistance. As the current in the magnetizing branch changes (reduces), the induced voltage will act in such a way that it prevents the current change, thus the induced voltage has a negative sign compared to that of stator resistance drop. At the stator terminals, the effect of this energy transfer, from magnetizing inductance to rotor resistance, is an initial dip in voltage that exponentially increases to the steady state value as shown in Fig. 3.45.

The second case of $\omega_{inj} > \omega_{sl}$ shall produce an effect exactly opposite to the previous one. That is, the magnetizing current and the rotor flux, at the time of switching to dc, are both below their nominal values. Switching to dc would mean that the rotor flux must rise to the nominal value. For this to happen the current through magnetizing branch must increase and the direction of induced voltage (to oppose this change) is the same as the stator resistive drop. The net effect at the stator terminals is an initial high voltage that exponentially decays down to the steady state value. It is also shown in Fig. 3.45. It is opportune to mention here that in steady state, the magnetizing inductance acts as a short to dc and the steady state voltage in the two cases must be equal (stator resistance and semiconductor switch voltage drop), this is verified in Fig. 3.45.
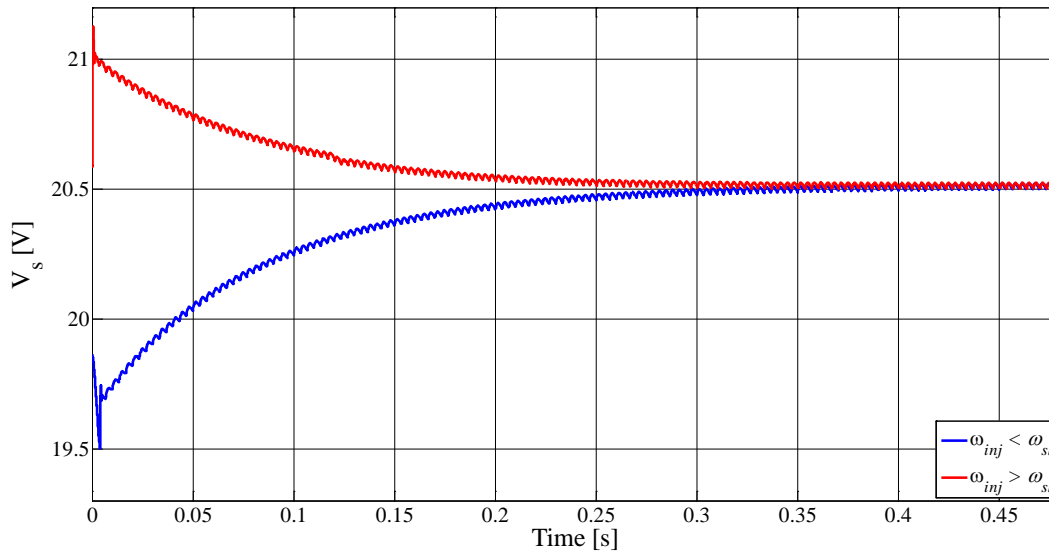
Fig. 3.45: Voltage at stator terminals for two different injection frequencies

The rotor time constant is obtained through an iterative process. The idea is to adjust the injection frequency at subsequent iterations until the voltage deviation from steady state value at the instant of switching (as seen in Fig. 3.45) reduces below a set tolerance. In that situation, the injection frequency would closely match the rated slip frequency of the machine and at the time the current is switched to constant dc in Fig. 3.44, the magnetizing current and rotor flux would be close to their nominal values and the transient at stator terminals would be the minimum. Under this condition the rotor time constant can be computed from (3.101) which is obtained by dividing (3.48) by (3.47) and rearranging.

$$\tau_r = \frac{1}{\omega_{inj}} \frac{i_s^q}{i_s^d} \qquad (3.101)$$

The method in its original version [10] requires that the stator terminal voltage must be measured and filtered in order to observe the effects of Fig. 3.45. This additional measurement may not always be available. Installing voltage sensor at the machine terminals for this test increases cost and renders the estimation procedure inconsistent with the definition of self-commissioning. Furthermore, the injection frequency is used as a parameter for next iterations and when it is sufficiently close to the slip frequency, the voltage transient of Fig. 3.45 is the smallest. However, from the machine nameplate data (Fig. 3.27), the rated slip (and hence slip frequency) can be easily calculated (cf. section 3.4) that makes the iterative procedure meaningless.

In this thesis, this method is modified so as to do away with both the inconsistencies mentioned in the previous paragraph. Since a current regulated PWM inverter is used to generate both the sinusoidal current as well as constant dc of Fig. 3.44, any transients in terminal voltage are also seen in the controller output voltage as the high-fidelity current controller matches the reference current at each sampling instant. Instead of measuring the stator terminal voltage, the controller output voltage is used here as the correction criterion in the iterative process.

Having known the rated slip frequency, the use of (3.101) becomes straightforward but the ratio $\dfrac{i_s^q}{i_s^d}$ for which the voltage transient is a minimum is not known, and it is this ratio which is used as the criterion for the iterative process here. From (3.100) it can be observed that varying i_s^q has the same effect on rotor flux as that of ω_{inj} but in reverse proportionality. Keeping i_s^d constant, and equal to magnetizing current of the machine, and changing i_s^q means modulating the amplitude of the injected signal Fig. 3.44 based on whether the transient in controller output voltage is exponentially increasing or decreasing. Furthermore, it is easy to decide on the amplitude of the reference current to start with as it can be kept equal to the machine's rated current, subsequent corrections in the amplitude are done using (3.102).

$$i_{ref}(n) = i_{ref}(n-1) + C\,\Delta v \qquad\qquad (3.102)$$

Here, i_{ref} is the amplitude of the injected current, n is the number of iteration, C is the correction factor and Δv is the peak voltage deviation from steady state value (see Fig. 3.45). $\Delta v > 0$ when the ratio $\dfrac{i_s^q}{i_s^d}$ is too small, the reverse ($\Delta v < 0$) is true when the ratio is too large.

C has the units of conductance (Ω^{-1}) and can either be constant or adapted from the magnitude of voltage difference, Δv, after each iteration, it decides the convergence speed and accuracy. The iterative process is terminated when the modulus of voltage deviation Δv is below a set tolerance ε (i.e. $|\Delta v| < \varepsilon$). At this point, the rotor time constant is computed from (3.101), which in terms of i_{ref} and known slip/injection frequency is written as (3.103).

$$\tau_r = \frac{1}{\omega_{sl}} \frac{\sqrt{i_{ref}^2 - i_s^{d\,2}}}{i_s^d} \qquad\qquad (3.103)$$

Fig. 3.46 shows the method proposed here used for estimating rotor time constant, the frequency of injection is kept fixed and is chosen as the slip frequency of the machine obtained from rating plate (Fig. 3.27). Fig. 3.47 illustrates how the voltage transient diminishes gradually due to current amplitude change through (3.102) till the transient becomes negligibly small. The initial current amplitude is chosen as the rated machine current. It is subsequently changed according to (3.102) at each iteration till the voltage error vanishes. It can be observed in Fig. 3.46 that the estimation process converges to a rotor time constant error of less than 2.5% in about four seconds.

It must be mentioned here that the process of estimating rotor time constant shown in Fig. 3.46 is fully automatic and does not require any visual observation of the terminal voltage nor operator intervention for adjusting the injection amplitude. The machine's rating plate data is the only input required as is the case with all other parameter identification methods discussed so far.
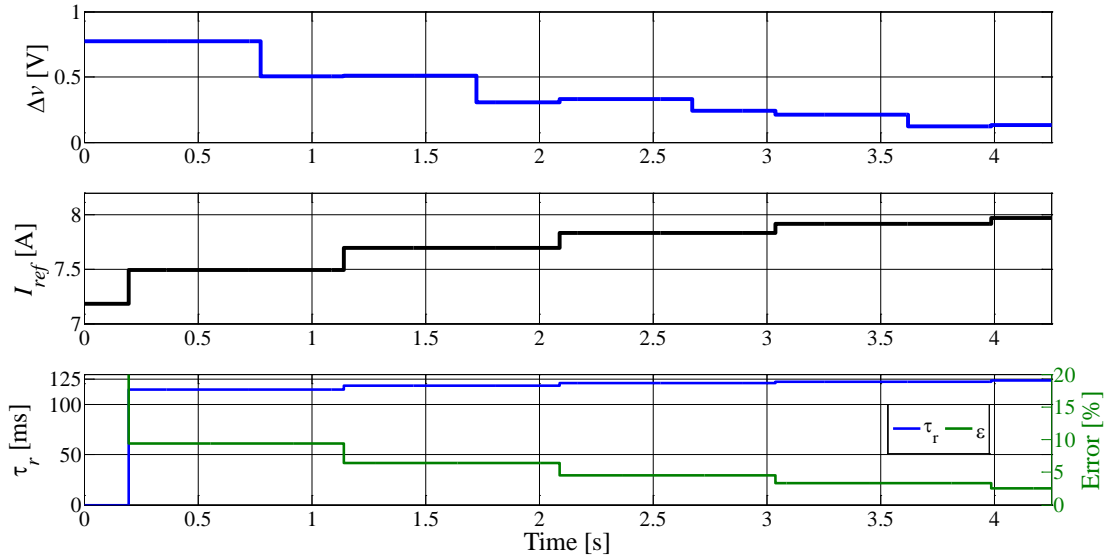
Fig. 3.46: τ_r estimation with iterative method using (3.102) for $C = 0.5$ (constant): voltage error (top axis), reference current correction (middle axis), rotor time constant and error in it (bottom axis)
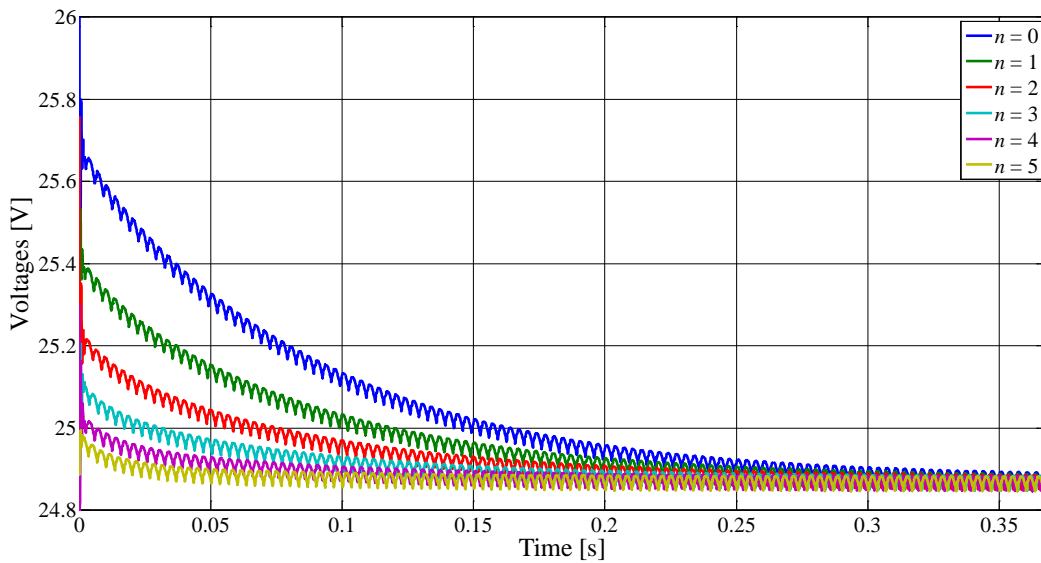
Fig. 3.47: Controller voltage transient from current switching instant (Fig. 3.44) to steady state at various iterations (n is the iteration number and at $n = 0$ $i_{ref} = I_{rated}$)

The second method for the estimation of rotor time constant at standstill is again an iterative approach but does not involve any ac injection. The method is proposed in detail in [27]. As with the ac injection technique discussed earlier this approach also uses the inverse-Γ equivalent circuit of Fig. 3.6 with the rotor field orientation convention (presented in section 3.2.1) to derive the theoretical basis for the procedure. It makes use of the rotor equation model of the flux observer (Fig. 3.11) assuming, however, the standstill rotor conditions i.e. $\omega_r = 0$ such that the flux observer transforms into a simpler version shown in Fig. 3.48 (a). In Fig. 3.48 (b), the d-axis equation is shown that is effectively the graphical representation of (3.47) with integrator replaced by

appropriate transfer function containing the rotor time constant. Additionally, in Fig. 3.48 (c), the condition under which the inverse–Γ equivalent circuit is derived (3.25) is used at the output such that the transfer function between input d-axis current and the magnetizing current i_μ is (3.104).

$$\frac{i_\mu}{i_s^d} = \frac{1}{1 + s\tau_r}$$ (3.104)

The transfer function (3.104) is effectively a low-pass filter with time constant equal to the rotor time constant. The rotor time constant is assumed incorrect and an iterative process similar to the one of the previous method is used to obtain its correct value. Current controller is used to impose the test current through the machine terminals like the previous method. Unlike the previous estimation process that started with only the nameplate data of the machine as input, this method does require an initial estimate of the rotor time constant, along with other nameplate data, to begin with. Starting with the user-defined initial value, the method makes subsequent corrections to converge to actual value of τ_r by minimizing the difference between observed magnetizing current i_μ through (3.104) and actual magnetizing current that would be caused by actual rotor time constant. The difference between the two is observed in the form of a voltage transient at stator terminals similar to the one shown in Fig. 3.45. The explanation of this voltage transient is similar to the one given in the previous paragraphs. The method is discussed below.
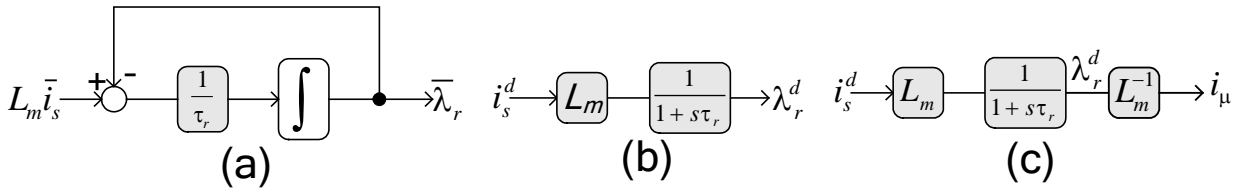
Fig. 3.48: Rotor equation based flux observer with stationary rotor: (a) vector block diagram, (b) d-axis only, (c) d-axis after applying (3.25) at the output

Through the current regulator, that may be a simple PI controller of Fig. 3.9, a constant current equal to rated machine current is injected in the d-axis, which can be the same as A-phase of the machine stator (cf. Fig. 3.3) since $\omega = 0$ for dc. The magnetizing current i_μ is allowed to build up since it occurs through a delay element τ_r of (3.104). In steady state dc conditions, the leakage inductance and magnetizing branch of Fig. 3.6 are both short-circuited so that the entire stator current flows in the magnetizing branch (see also section 3.5.1 above). Moreover, when steady state is reached, the rotor flux also builds up to a constant value given by (3.69). At this point, the current through the stator terminals is reversed in a step change and the estimated magnetizing current $\hat{i}_\mu$ is observed using (3.105) which is the same as (3.104) but with estimated quantities instead of actual ones of (3.104).

$$\hat{i}_\mu = \frac{1}{1 + s\hat{\tau}_r} i_s^d$$ (3.105)

Based on whether the rotor time constant incorporated in (3.105) is greater than or less than the one used in (3.104), the observed magnetizing current $\hat{i}_\mu$ would be different from the actual magnetizing current. The two situations are illustrated in Fig. 3.49 below. The figure also shows a further change in the reference d-axis current at a precise instant of time. This instant is chosen as the point when the estimated magnetizing current reaches the rated magnetizing current (but in negative direction). The reference current is step changed again to the negative magnetizing current value. At this instant the rotor flux must also be equal to the rated flux if the estimated magnetizing current is the same as the actual magnetizing current. However, if the rotor time constant used in

(3.105) is different from the correct value, the rotor flux at the instant of switching is different from the rated flux. Thus at the time the input d-axis current is switched, a voltage transient appears at the stator terminals.
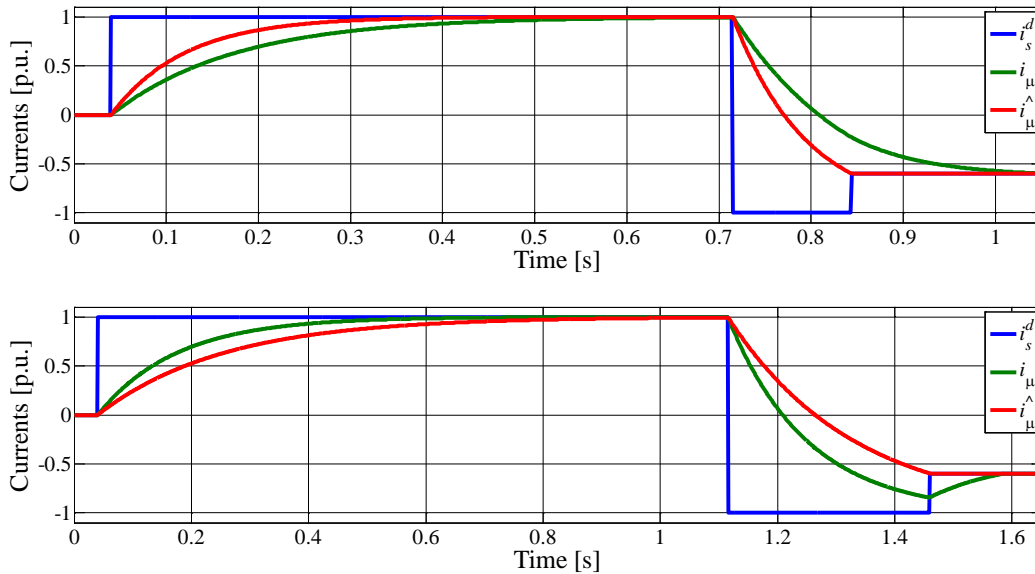
Fig. 3.49: Estimated and actual magnetizing current obtained using (3.104) and (3.105), respectively, following a step change in d-axis current: $\hat{\tau}_r < \tau_r$ (top axis), $\hat{\tau}_r > \tau_r$ (bottom axis)

The theoretical explanation of this transient is similar to the one given for the switching to dc from injected ac of Fig. 3.44. In the first case when $\hat{\tau}_r < \tau_r$, at the time when i_s^d is changed to (negative) magnetizing current, the actual rotor flux is greater than the value it should have with the rated magnetizing current flowing in the stator terminals. In order for flux to return to rated value, the excess magnetizing current must be discharged through rotor branch containing rotor resistance. As the current through magnetizing branch cannot change abruptly, the discharging of this excess current takes place with a delay. The voltage induced in the magnetizing inductance is such that it opposes the current decrease through it, thus it has the direction opposite to the stator resistance drop. The effect of this induced voltage on the stator terminal voltage is an initial dip that exponentially increases to a steady state value equal to the stator resistance drop.

Analogously, when $\hat{\tau}_r > \tau_r$, the rotor flux at the time of switching is under the rated value since the actual magnetizing current has receded below the rated magnetizing current (Fig. 3.49, lower axis). The flux therefore tends to rise with an increase in magnetizing branch current. However, the induced voltage in the magnetizing inductance prevents this current rise and thus has the same direction as the stator resistance drop. The net effect at the terminals is an initial high voltage that exponentially decays down to the steady state value exactly equal to the stator resistance drop. Expected voltage at the stator terminals for the two cases is shown in Fig. 3.50.

As seen in Fig. 3.50, the error in rotor time constant is seen as a voltage transient at the stator terminals. The magnitude and subsequent rise or decay of this transient depends on whether the rotor time constant incorporated in (3.105) is under- or overestimated, respectively. Similar to the ac injection method, this technique of rotor time constant is based on iterative process that reduces the voltage transient by subsequently correcting the estimated value of rotor time constant. Of course, when the rotor time constant estimate is close to the actual value, the transient disappears because the estimated (3.105) and actual (3.104) magnetizing currents would be approximately equal. Therefore, this transient is used as criterion for the iterative process and when it is below a

set tolerance, the iterative process terminates and the closest estimate of rotor time constant is obtained.
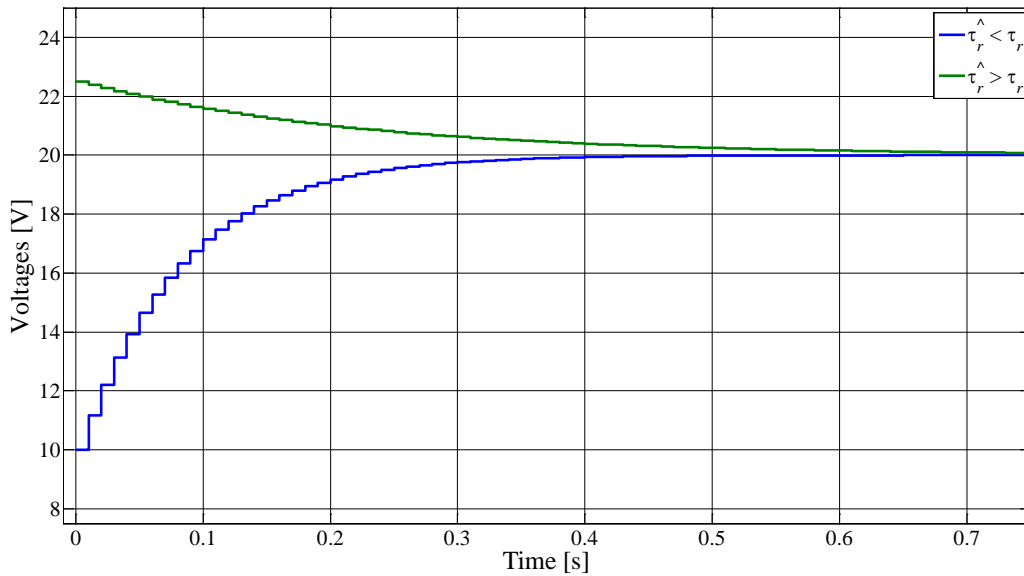
Fig. 3.50: Expected voltage at stator terminals after switching of *d*-axis current to rated magnetizing current (Fig. 3.49)

To see the effects of Fig. 3.50 for different time constant values adopted, the terminal voltage needs to be measured. However, in order not to add additional voltage measuring and filtering equipment, the current controller output, which is a voltage command for the inverter, is used as the correction criterion for the iterative process. Fig. 3.51 shows the controller output voltage from one of the tests conducted here for the two cases depicted in Fig. 3.49. Comparing the curves of Fig. 3.50 and Fig. 3.51 reveals that whether stator terminal voltage is used or the controller output voltage, the effect of detuned rotor time constant can be equally seen. The correction strategy adopted here is slightly different from (3.102) (or Fig. 3.47) in that here the area under the voltage curves of Fig. 3.50 or Fig. 3.51 is used as correction criterion.
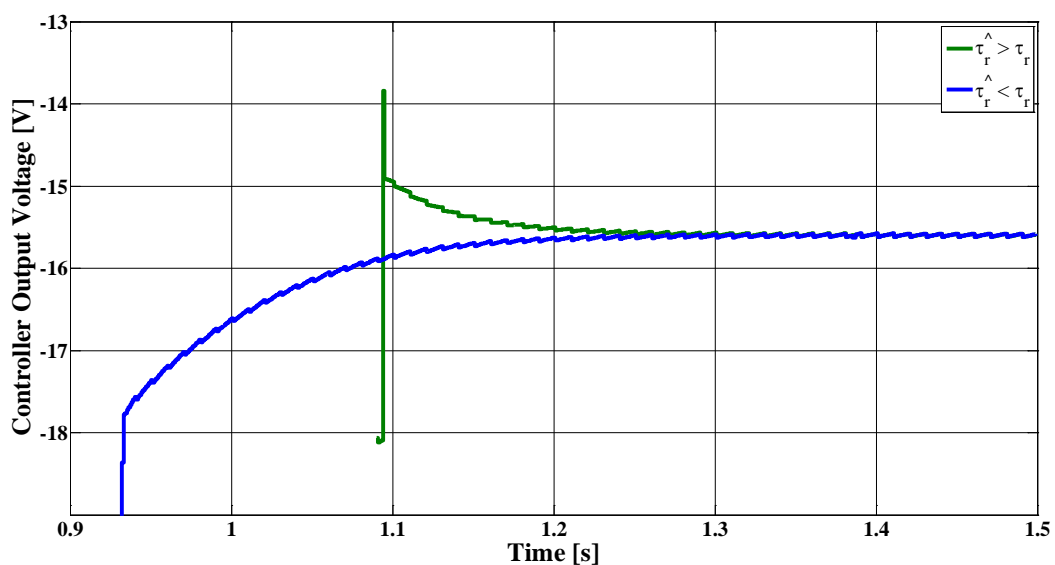
Fig. 3.51: Controller output voltage observed on the test bench after switching of *d*-axis current to rated magnetizing current (Fig. 3.49)

The area under the stator terminal voltage curve is divided in two parts as shown in Fig. 3.52 for the two cases of Fig. 3.50. The difference between these two sections (ΔA) is used with a constant to correct the next value of the rotor time constant using (3.106).

$$\hat{\tau}_r(n) = \hat{\tau}_r(n-1) + k\,\Delta A \qquad\qquad (3.106)$$

The constant k is similar to the constant C of (3.102) but has the units of volt-inverse (V^{-1}). As said for C, k can either be fixed or can be adapted based on the area difference (ΔA) magnitude after each iteration. The value of k determines convergence speed and accuracy of the result.

As can be observed from Fig. 3.52, the area difference for underestimated initial value of rotor time constant (left curve) is greater than that obtained with the overestimated one (right curve), this fact is also supported by the experimental results of Fig. 3.51. Thus, it is convenient to initialize the iterative process with $\hat{\tau}_r < \tau_r$. This is the first improvement proposed and implemented in this thesis. This not only gives faster conversion, but also resolves the problem of choosing a suitable initial value. Since the rating-plate data is the first available information about the machine, the rotor time constant estimated from the nameplate data (cf. section 3.4) is in fact an underestimate (Table III) and the same is used in this work to start the iterative estimation algorithm.
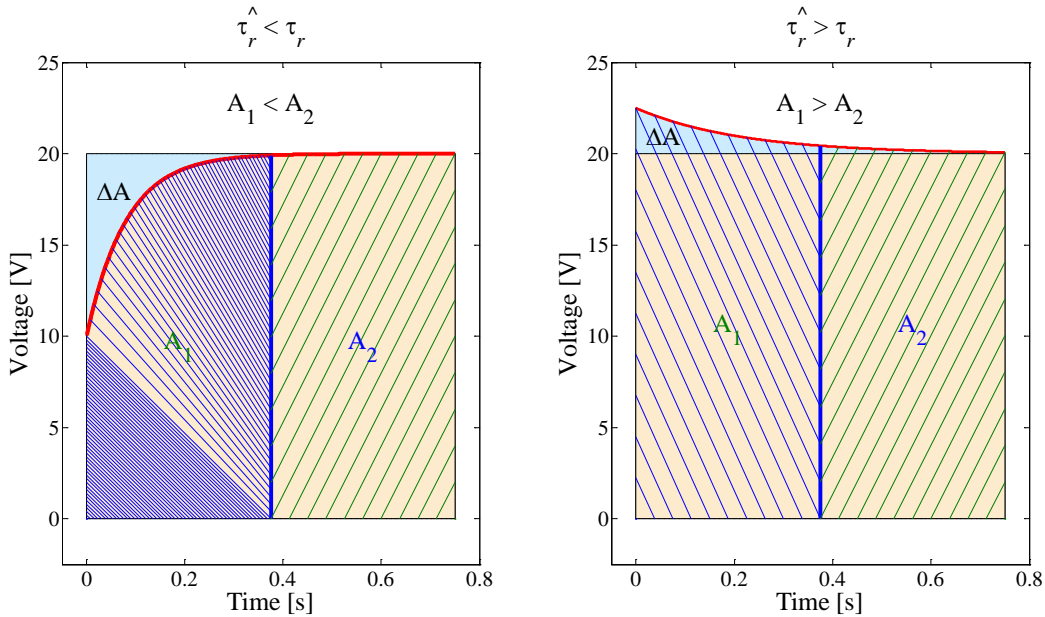
Fig. 3.52: Area under the controller output voltage and the area difference: $\hat{\tau}_r < \tau_r$ (left), $\hat{\tau}_r > \tau_r$ (right)

The method is applied to two different power-rating machines used in this thesis with the estimation algorithm being initialized with underestimated rotor time constant. Fig. 3.53 and Fig. 3.54 show the results of one iteration cycle for one of the test machines.
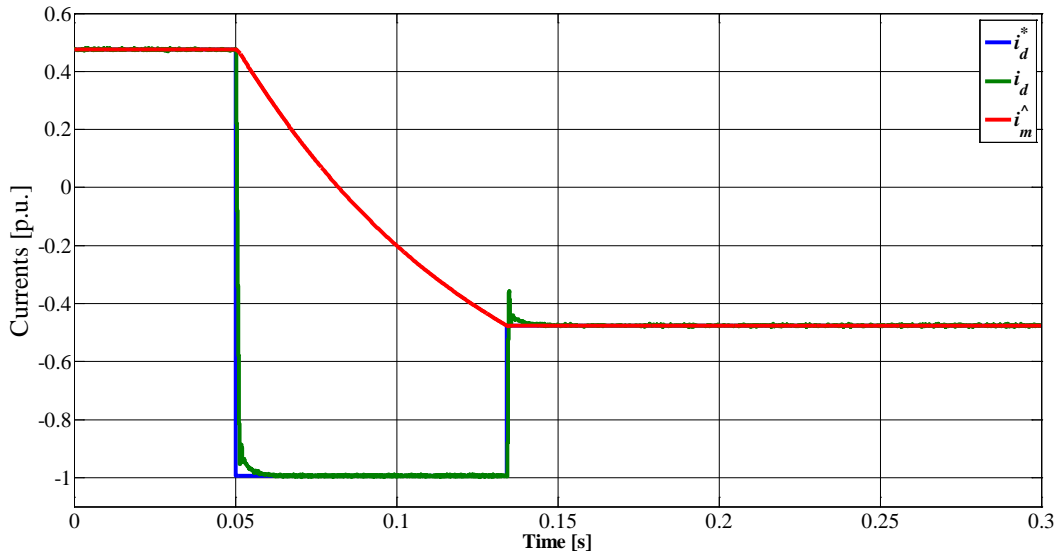
Fig. 3.53: Currents, starting from steady state dc value, during one iteration cycle of the tests performed on test rig
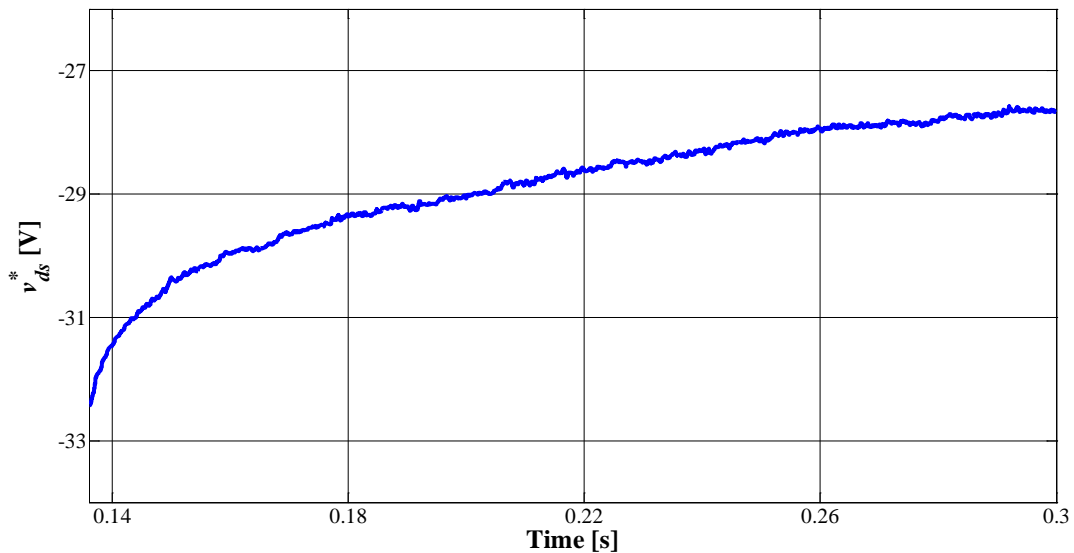
Fig. 3.54: Controller output voltage (magnified immediately after the second switching instant of Fig. 3.53): $\hat{\tau}_r < \tau_r$

Another important observation, which applies to both the methods of rotor time constant estimation discussed thus far, made here is about the value of the magnetizing current considered in the tests. From (3.45) and (3.8), it is easy to infer that the rotor time constant depends on the magnetizing inductance which in turn is a function of the magnetizing current (Fig. 3.25). Since [10] and [27] propose the no-load test to obtain the rated magnetizing current to be used for tests, this violates the definition of self-commissioning strictly followed here. In the absence of no-load tests' data, the only source of rated magnetizing current information remains is the machine nameplate (Fig. 3.27) and the magnetizing current obtained from the rated current and rated power factor is used here to conduct the tests. The impact of using nameplate estimate on test results is found to be minimal. However, it must be noted that as the value of the magnetizing current considered here is unique, the rotor time constant estimated is valid only at that particular current. It is therefore advisable to operate the machine at constant rated flux which means a constant magnetizing current and a unique rotor time constant.

In fact, most of the induction motor control schemes, at low speeds, work at constant rotor flux conditions for reasons of faster dynamic response. Since variation of rotor flux by *d*-axis current control occurs through a first order delay due to rotor time constant (3.47), the rotor flux is seldom used as torque control variable, rather the *q*-axis current is chosen as torque control variable (3.49). Hence, the constant rotor flux operation is assumed here for which the parameters obtained thus far are valid. An exception to constant flux operation is, however, the flux-weakening regime. The flux-weakening mode of operation begins when the machine speed goes higher, above the nameplate rated speed, at which point the available dc-link voltage may not be sufficient to sustain operation at rated flux due to high back-emf. The flux is thus reduced in proportion to speed according to (3.74). Although the parameters, such as the magnetizing inductance and the rotor time constant vary from the values estimated during above tests, this variation does not pose significant problems for field orientation since at higher speeds the back-emf integral part of flux observer is dominant in Fig. 3.13 or Fig. 3.16.

For applications where efficiency improvement has priority over fast dynamic response, the rotor flux is varied as function of demanded torque such that the torque produced per ampere of stator current is always at the peak – this operating condition in the technical jargon is called the Maximum Torque Per Ampere (MTPA) condition. For knowing the optimum value of rotor flux that gives maximum efficiency performance in all operating conditions, the no-load test is inevitable in order to determine the MTPA characteristic of the machine. Fig. 3.55 gives the MTPA characteristic of the 2.2 kW induction machine determined from its no-load test data. Fig. 3.56 shows the experimental validation of the MTPA characteristic of Fig. 3.55, the figure suggests a close matching between expected and experimentally observed stator phase current. Fig. 3.57 highlights the benefits of working with variable flux over constant flux in terms of operating efficiency comparison, it can be seen that at lower load torque values the efficiency is high with variable flux than the one obtained by working at constant flux.
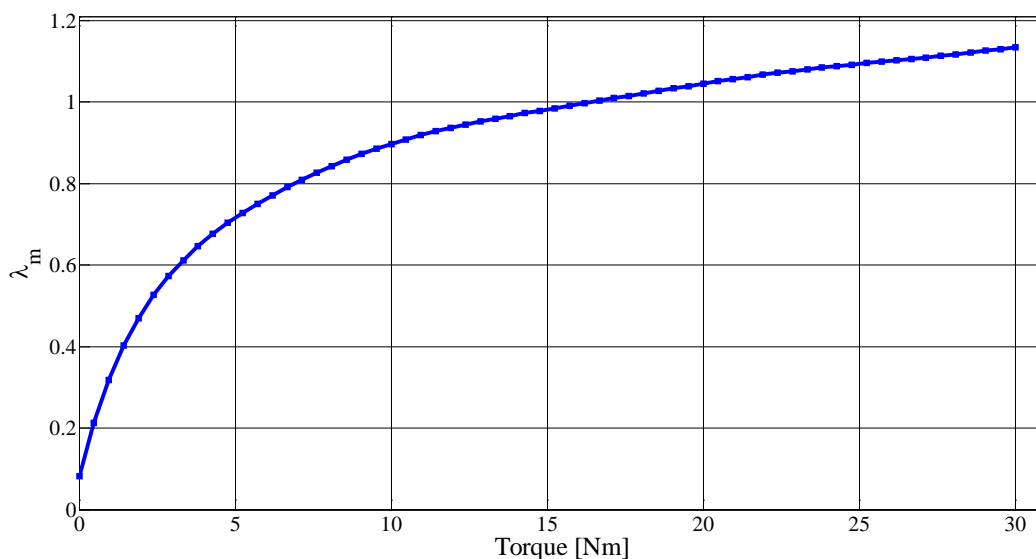
Fig. 3.55: Machine flux as a function of torque that gives maximum torque per ampere
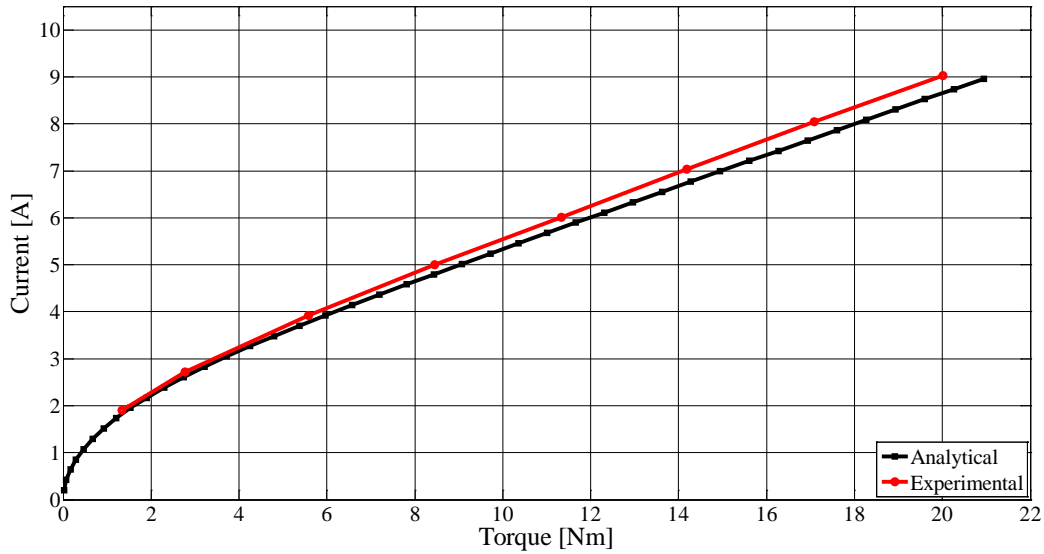
Fig. 3.56: Stator current absorbed at various load torque magnitudes with machine flux obtained from Fig. 3.55

Some magnetic characterization methods are proposed in literature that identify the machine magnetization characteristics such as [14, 17, 20, 25, 30, 35, 36, 51, 131] from which the characteristic of Fig. 3.55 can be obtained.
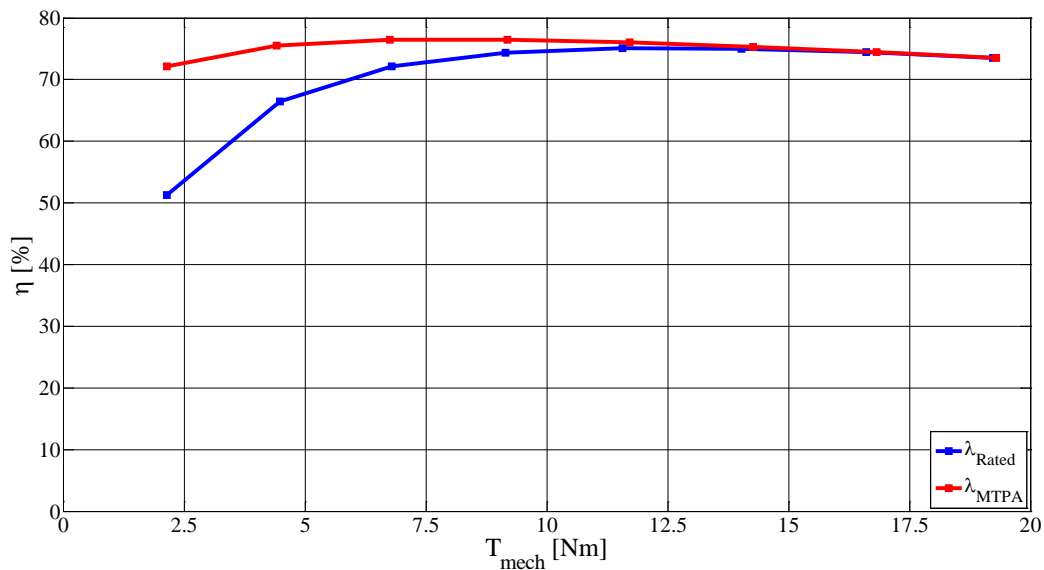
Fig. 3.57: Efficiency improvement over constant flux operation by using MTPA characteristic of Fig. 3.55

3.5.6. Single-phase tests with Sinusoidal Signal Integrators

Parameter identification tests discussed above identify individual parameters by performing dedicated test for each. In this section the single-phase tests that give the equivalent circuit parameters except stator resistance are dealt with. The stator resistance is obtained by the dc injection method of section 3.5.1. The IEEE standard [6] outlines test procedure for computing machine parameters from the total impedance seen from the stator terminals when the machine is supplied with sinusoidal three-phase supply conforming to its ratings. The three-phase supply generates rotating magnetic field around rotor periphery that gives rise to torque. However, if the machine is supplied with a single-phase supply the absence of rotating magnetic field keeps the rotor stationary while giving the same effect at stator terminals for the applied sinusoidal supply.

Conducting single-phase tests with sinusoidal supply would require a dedicated supply and a wattmeter to separate active and reactive components of current for impedance vector computation. This makes the tests unsuitable for self-commissioning. Therefore, the single-phase supply is generated through the inverter to do away with the need for additional power supply as proposed by [41] for standard three-phase tests. The voltage at the stator terminals is reconstructed from the inverter switches' duty cycles and the measured dc-link voltage. The problem of accurately identifying the phase angle between reconstructed stator terminal voltage and stator current for impedance vector computation is solved by implementing sinusoidal signal integrators.

To formulate the equations for parameter identification through single-phase tests, the inverse-Γ equivalent circuit of Fig. 3.6 is considered. The inverse-Γ equivalent circuit is selected for its simplicity and because (3.77) or (3.94) permit its easy conversion to its T-equivalent circuit (Fig. 3.4). A sinusoidal supply generated through the PWM control of inverter switches is applied along one of the phases of the machine at a certain frequency (ω_1) and the impedance vector is computed from the applied voltage and resultant current vectors using (3.107), where R_{Tot1} and X_{Tot1} are the real and imaginary parts, respectively, of the impedance vector at frequency ω_1.

$$Z(\omega_1) = R_{Tot1} + jX_{Tot1} = \frac{\overline{V}_s}{\overline{I}_s} = \frac{|\overline{V}_s|\angle 0}{|\overline{I}_s|\angle\varphi_1} \tag{3.107}$$

At any frequency (ω), the total impedance seen at the terminals of Fig. 3.6 can be computed from the basic circuit theory. For simplifying the derivation of formulae, a few new symbols are defined as:

$$L_l = \sigma L_s, \qquad M = (1-\sigma)L_s \qquad R = \frac{L_m^2}{L_r^2}R_r$$

Using the above symbols in Fig. 3.6, the total input impedance at ω rad/s is:

$$Z = R_s + j\omega L_l + \frac{R(j\omega M)}{R + j\omega M} = R_s + j\omega L_l + \frac{R(\omega M)^2 + jR^2\omega M}{R^2 + (\omega M)^2}$$

Separating the real and imaginary parts and calling them R_Γ and X_Γ, respectively:

$$R_\Gamma = R_s + \frac{R(\omega M)^2}{R^2 + (\omega M)^2} \quad and \quad X_\Gamma = \omega L_l + \frac{R^2\omega M}{R^2 + (\omega M)^2}$$

Since the stator resistance is to be estimated separately, the resistive part of the above expression can be modified, for convenience, as:

$$R'_\Gamma = R_\Gamma - R_s = \frac{R(\omega M)^2}{R^2 + (\omega M)^2}$$

By comparison with (3.107), the total resistance and reactance at frequency ω_1 are:

$$R_{Tot1} = \frac{R(\omega_1 M)^2}{R^2 + (\omega_1 M)^2} \tag{3.108}$$

$$X_{Tot1} = \omega_1 L_l + \frac{R^2\omega_1 M}{R^2 + (\omega_1 M)^2} \tag{3.109}$$

From (3.108) and (3.109), it can be observed that the number of unknowns, namely R, L_l and M, is three whereas there are only two equations available to solve for these unknowns. For this reason, an impedance vector at a different frequency ω_2 is required to solve for the unknowns, the new impedance vector can be computed same as that of (3.107). Assuming that the rotor resistance rise due to skin effect is negligible between ω_1 and ω_2 and the machine inductances do not differ much, equations (3.110) and (3.111) are the equivalent of (3.108) and (3.109) at ω_2. Now, with four equations at hand, the three unknowns can be derived easily as below.

$$R_{Tot2} = \frac{R(\omega_2 M)^2}{R^2 + (\omega_2 M)^2} \tag{3.110}$$

$$X_{Tot2} = \omega_2 L_l + \frac{R^2 \omega_2 M}{R^2 + (\omega_2 M)^2} \tag{3.111}$$

Solving (3.108) for M^2:

$$R_{Tot1} R^2 + \omega_1^2 M^2 R_{Tot1} = R \omega_1^2 M^2 \quad \Rightarrow \quad M^2 = \frac{R_{Tot1} R^2}{R \omega_1^2 - \omega_1^2 R_{Tot1}}$$

Substituting in (3.110) for M^2:

$$R_{Tot2} = \frac{R \omega_2^2 \left(\dfrac{R_{Tot1} R^2}{R \omega_1^2 - \omega_1^2 R_{Tot1}} \right)}{R^2 + \omega_2^2 \left(\dfrac{R_{Tot1} R^2}{R \omega_1^2 - \omega_1^2 R_{Tot1}} \right)} \quad \Rightarrow \quad R_{Tot2} = \frac{\omega_2^2 R^3 R_{Tot1}}{R^2 \left(R \omega_1^2 - \omega_1^2 R_{Tot1} + \omega_2^2 R_{Tot1} \right)}$$

Rearranging:
$$R = \frac{R_{Tot1} R_{Tot2} \left(\omega_2^2 - \omega_1^2 \right)}{R_{Tot1} \omega_2^2 - R_{Tot2} \omega_1^2} \tag{3.112}$$

Substituting in (3.112)(3.110) in expression for M^2:

$$M = \frac{R_{Tot1} R_{Tot2} \left(\omega_2^2 - \omega_1^2 \right)}{\omega_1 \omega_2 \left(R_{Tot1} \omega_2^2 - R_{Tot2} \omega_1^2 \right)} \sqrt{\frac{R_{Tot1} \omega_2^2 - R_{Tot2} \omega_1^2}{R_{Tot2} - R_{Tot1}}} \tag{3.113}$$

From (3.111), the expression for L_l can be written in terms of R and M as:

$$L_l = \frac{X_{Tot2}}{\omega_2} - \frac{R^2 M}{R^2 + (\omega_2 M)^2} \tag{3.114}$$

Having expressed the machine parameters in terms of real and imaginary parts of the impedance vectors at the two test frequencies through (3.112), (3.113) and (3.114), the individuation of the resistive and reactive components of the impedance vectors is the next task. In the midst of inverter non-idealities, the stator current resulting from commanded sinusoidal voltage is not sinusoidal, that makes the phasor treatment of stator current incorrect. To filter out inverter non-linearity effects, various alternatives have been proposed in literature [28, 32, 132, 133]. While [28] and [32] require additional computational power to carry out Fourier series expansion, the offset introduced in [132] changes the machine magnetization state for which the magnetizing inductance is different from the unsaturated value. Sinusoidal signal integrators [134-136], also known as resonant filters, come in handy in such situations as they neither require extra memory

onboard nor burden the processor with additional computations. These are employed here to extract the phase-angle between voltage and current vectors to compute machine parameters.

As with the ac injection method of rotor resistance estimation (cf. 3.5.2), an open-loop test is avoided and closed-loop current regulation is used to inject the test current. This keeps the current inside the machine within its ratings and reduces the risk of damage due to testing. For a sinusoidal current to be maintained in the machine, the commanded voltage must include the power semiconductor switch effects which distort the commanded voltage. These distortions can be filtered through the resonant filter tuned exactly at the injection frequency (ω_1 or ω_2). The filter transfer function is given by (3.115) whereas the bode plot is shown in Fig. 3.58. It can be seen that signals having frequencies different from the tuning frequency are effectively attenuated. The filter gain k_f decides the sharpness with which the desired frequency is picked and others rejected.

$$G_{cl} = \frac{k_f s}{s^2 + k_f s + \omega^2} \tag{3.115}$$
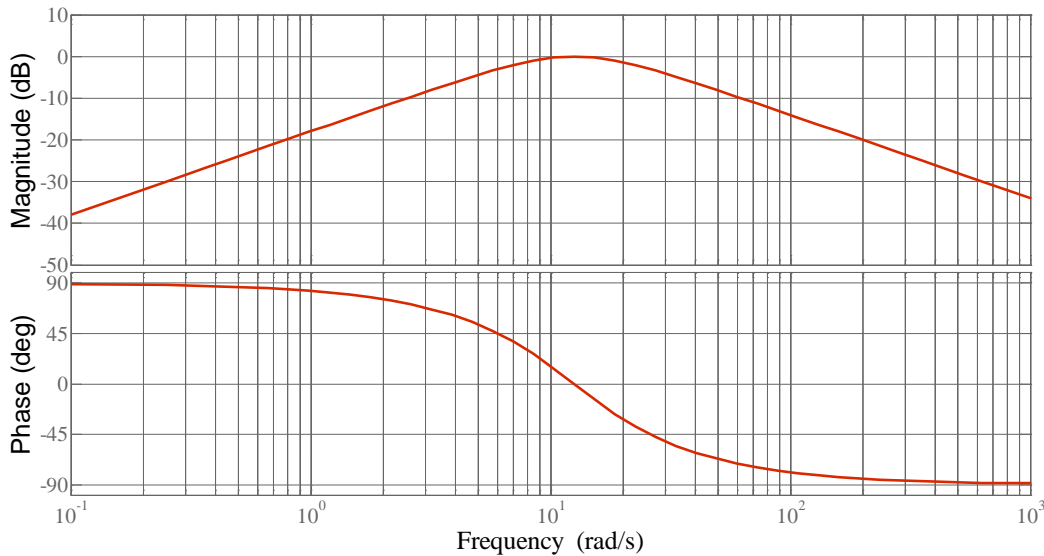
Fig. 3.58: Bode plot of the sinusoidal signal integrator (3.115): pick-up frequency = 25 Hz

In order to inject controlled current inside the machine such that the machine and inverter ratings are not exceeded, current controller of Fig. 3.9 is used. A sinusoidal current reference is employed and the controller output voltage is filtered by (3.115) that gives a sinusoidal voltage vector. The angle between reference current and filtered voltage vector can be determined if one of them is treated as the reference vector. The vector diagram of Fig. 3.59 shows the relative position of injected current and filtered voltage vectors. Since the rotor is stationary and the current is injected along one of the phases, the stationary α-axis of Fig. 3.3 is congruent to the *d*-axis as shown.
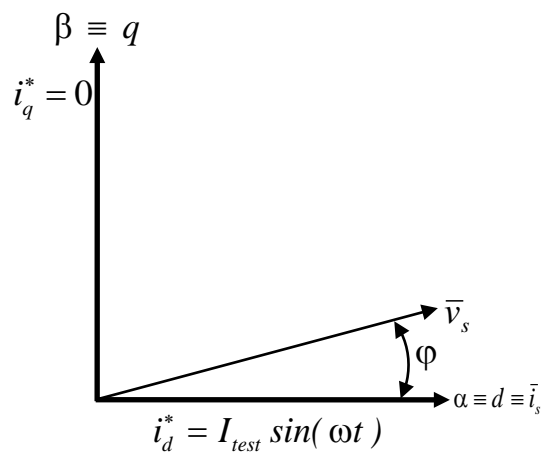
Fig. 3.59: Relative position of reference current and filtered voltage vectors

The block diagram of Fig. 3.60 explains how the phase angle between voltage and reference current vectors is obtained. The inputs are the voltage vector given by the filter and the known injection frequency of the reference current vector. The rotational transformation resolves the voltage vector

into its *d*- and *q*-axis components. These components express the voltage vector in the *dq*-plane of Fig. 3.59, the phase angle can be easily recovered through arc-tangent operation as shown.
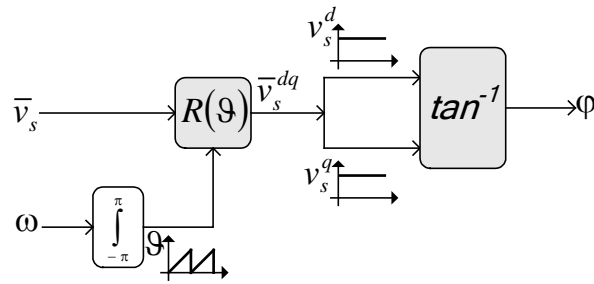
Fig. 3.60: Block diagram for obtaining phase angle between reference current and filtered voltage vectors

The method is applied on a 3 kW induction machine for verification. Fig. 3.61 shows the injected reference and measured current. Controller output voltage and filtered voltage waveforms, after steady state is reached, are also shown. Fig. 3.62 illustrates the phase angle variation throughout the test duration. It can be observed that in steady state the phase angle contains ripples which are done away with by implementing a moving average filter. Table IV gives a comparison between the known and estimated values of the machine parameters.
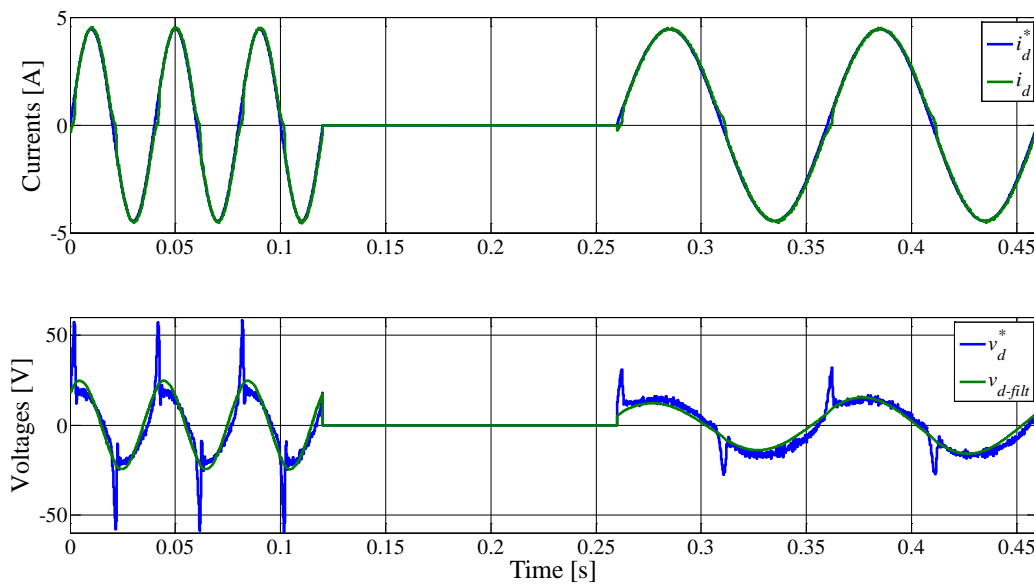
Fig. 3.61: Reference and measured *d*-axis current (top axis), controller output and filtered voltage (bottom axis)

Table IV: Two-frequency test results compared with known machine parameters

3.0kW induction motor equivalent circuit parameters			
Parameter	Unit	Value (known)	Value (estimated)	Error $\left(\dfrac{estimated}{known}-1\right)\times100\%$
R_s	Ω	1.50	1.54	+2.67%
L_{ls}	mH	8	9	+12.5%
L_m	mH	194	189	−2.58%
L_{lr}	mH	8	9	+12.5%
R_r	Ω	1.57	1.71	+8.92%
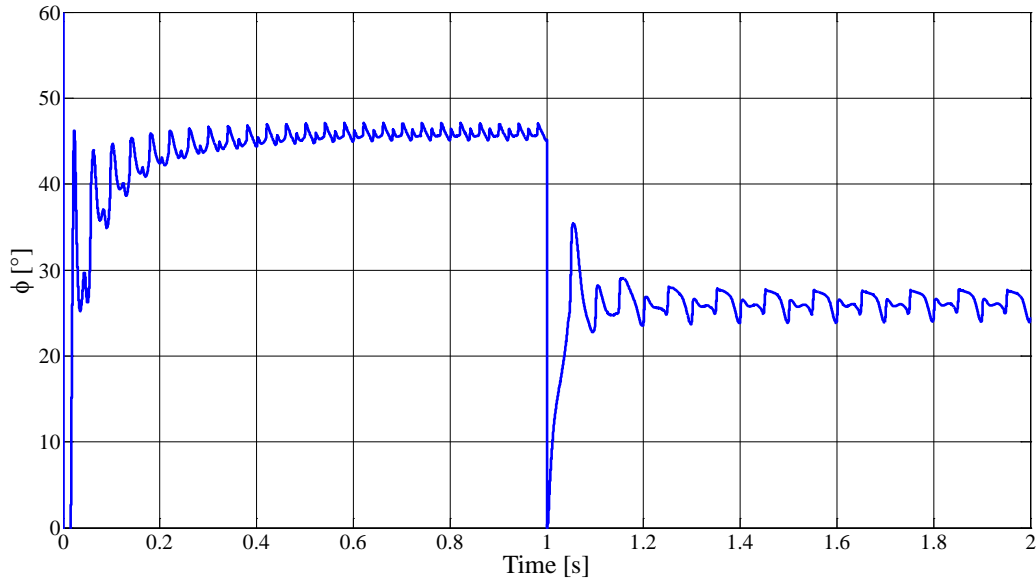
Fig. 3.62: Phase angle during the tests at two different frequencies

3.6.   Fully automated induction motor drive operation routine – simulation results

Having outlined the procedures for estimating machine parameters through various tests discussed at length in section 3.5, the machine control schemes incorporating self-commissioning algorithms are developed and tested. In this section simulation results are presented when the algorithms are applied to Matlab Simulink model of a 32 kW compressor induction motor.

In the identification process given in the previous sections, it is seen that current regulators are used for almost all the tests to be performed. However, optimum gains for the PI current controller (Fig. 3.9) cannot be known unless the total machine leakage inductance and resistance are not known. The technical optimum approach [43] of setting controller gains requires that the proportional gain k_p be selected according to (3.116) and the integral gain k_i as (3.117). Where L is the total inductance seen in series to a step input and R is the resistance to steady state dc. Regardless of which equivalent circuit of the machine is used, the inductance is invariably the total leakage inductance σL_s and the resistance is R_s.

$$k_p = \omega_{bw} L = \omega_{bw}\, \sigma L_s \qquad\qquad (3.116)$$

$$k_i = \omega_{bw} R = \omega_{bw} R_s \qquad\qquad (3.117)$$

However, having a motor as good as a black box as far as the knowledge of its parameters is concerned; it is not possible to assign values to k_p and k_i using (3.116) and (3.117). A simple and easy trick to find the correct gains *a priori* is to attempt setting them while observing the machine response. This approach has also been used by [54] implementing Fuzzy logic that is avoided here to keep it simple. The method proceeds as follows: the integral gain is kept to zero and a step reference current input is applied with an initial arbitrarily chosen, non-zero, positive value of k_p and the machine current is observed. If it is set very low initially, the machine current will not reach the desired level; k_p is subsequently increased unless an overshoot in the current is observed. If, however, a large overshoot is observed at the beginning, this signifies that k_p is set excessively high and needs decrement unless a modest overshoot remains. This k_p is correct at least as a first approximation and can be updated once the parameters are fully identified. Afterwards, k_i is calibrated to wipe out steady state error and to obtain a suitable settling time. All this can be done automatically by a start-up routine that sets the PI gains. The only external input required is an

approximation of the rated machine current or exact value from the nameplate data. Fig. 3.63 and Fig. 3.64 below show two different situations of automatic commissioning of k_p.

In Fig. 3.63, the proportional gain is initially set low which gives current undershoot as seen, thus the gain is increased at each subsequent iteration till a slight overshoot is observed. On the other hand, in Fig. 3.64, the arbitrarily chosen initial value of the k_p is too high that gives current overshoot and therefore needs to be reduced, the bottom axis of the figure in fact shows a gradual decrement after every test iteration. After the proportional gain is set, the integral gain can be approximated. A good approximation is to set the controller time constant equal to 3 ms that gives a bandwidth of 300 rad/s. Fig. 3.65 illustrates the step response of the current regulator with the proportional and integral constants are commissioned.
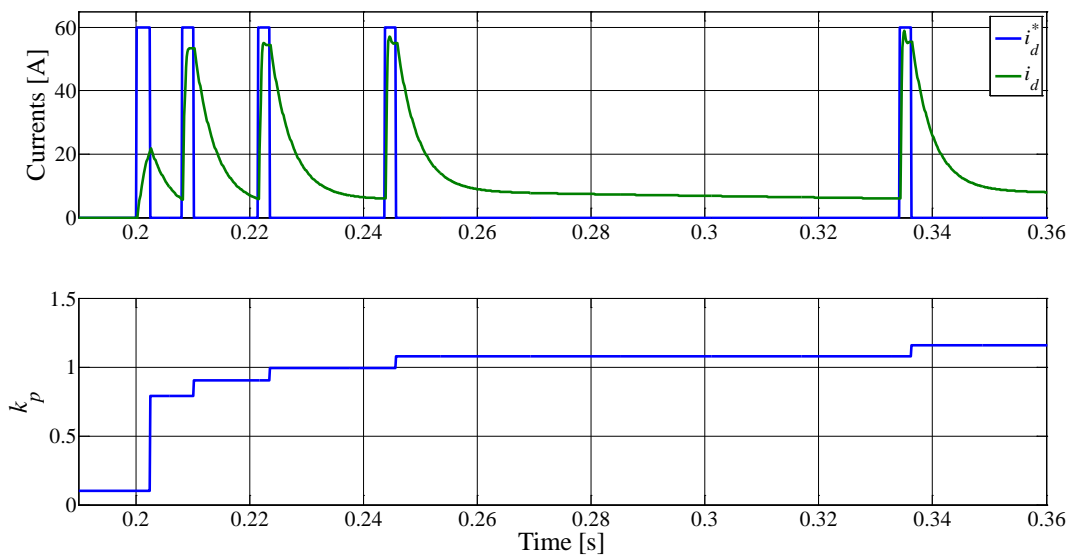
Fig. 3.63: Current response (top axis) and k_p adjustment (bottom axis) from an initial low value
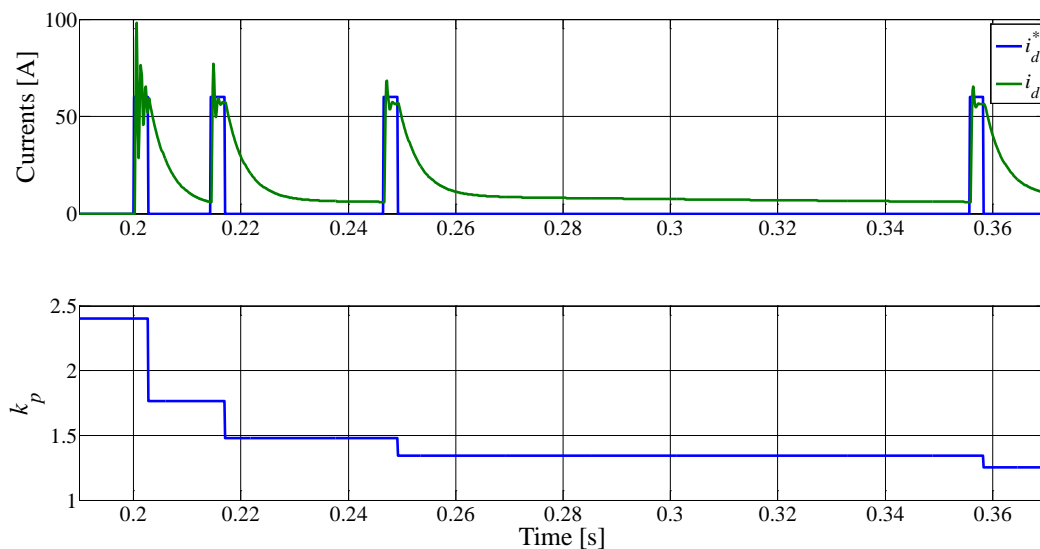
Fig. 3.64: Current response (top axis) and k_p adjustment (bottom axis); k_p is initially set high
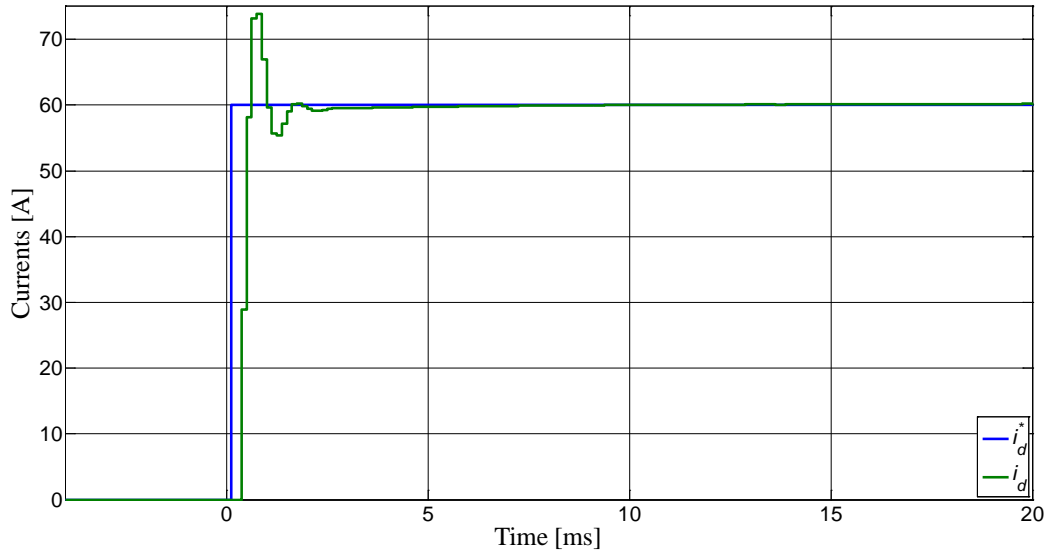
Fig. 3.65: Current controller response with optimum gains

The stator and rotor resistances are identified in a single test as shown in Fig. 3.66. The stator resistance is obtained from the steady state values of voltage and current using (3.80) while the rotor resistance is computed through (3.82) before the controller output voltage follows an exponential decay as seen in the lower curve of Fig. 3.66.
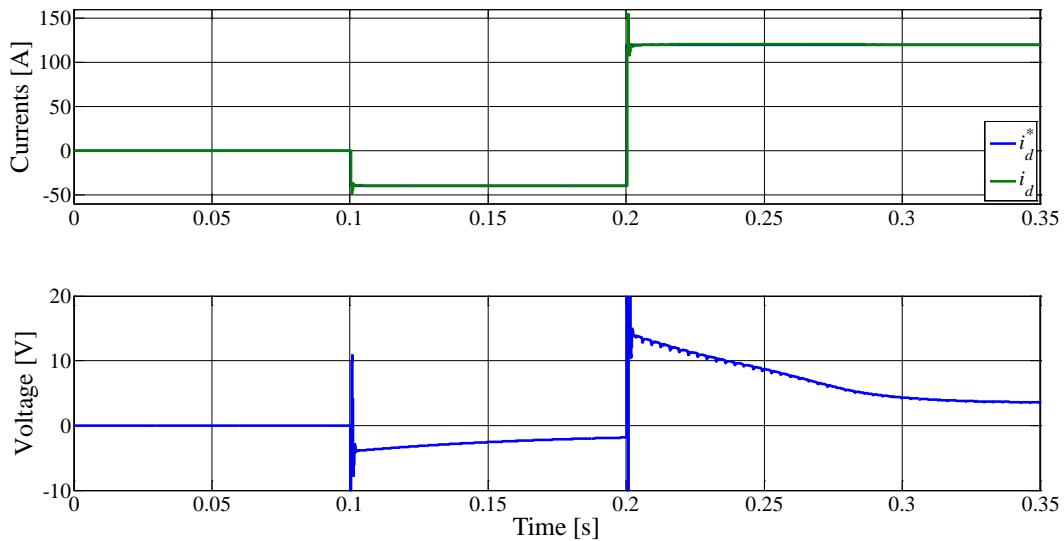
Fig. 3.66: Stator and rotor resistance estimation: test current (top axis), controller output voltage (bottom axis)

The total transient inductance is computed from the results of fast current ramp method of section 3.5.4 (Fig. 3.43) since the machine has a very low short circuit reactance. The rotor time constant is estimated using mutual current observer error (3.105) with dc injection. Fig. 3.67 shows the results for one estimation iteration. Fig. 3.68 gives the time required for estimating each of the parameters above along with total duration of the entire self-commissioning process.
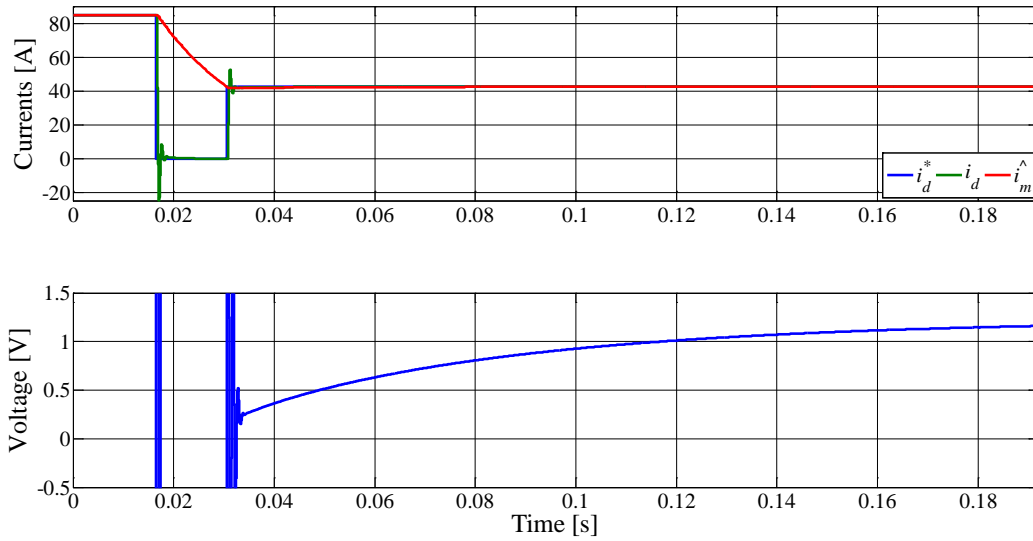
Fig. 3.67: Rotor time constant estimation: mutual current observer result (top axis), controller voltage zoomed for showing the exponential curve area under which is used as in Fig. 3.52
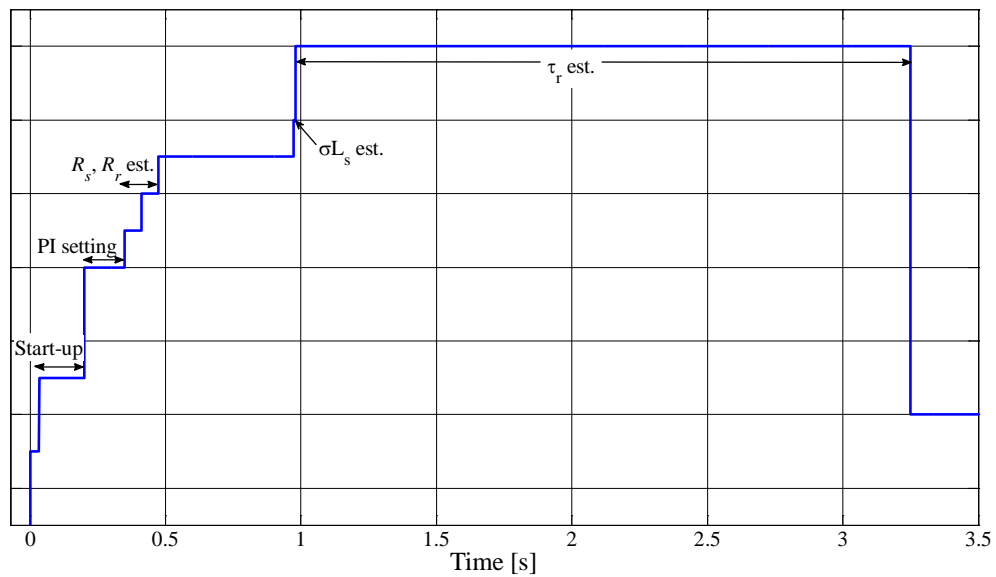
Fig. 3.68: Timing diagram of commissioning process

To verify control performance with the parameters obtained through automatic identification process, a sensorless indirect rotor field oriented control is implemented. The machine is speed controlled and is started from zero speed without any position information from shaft sensors; the vector control relies purely on the parameters estimated as above. Once the machine reaches a set speed, the speed command to the speed controller is reversed in a step as shown in Fig. 3.70. The q-axis current, which is the torque component, increases to supply the necessary torque for reversing the speed. As can be seen in Fig. 3.69, the d-axis current remains quasi constant for there is no flux change required during speed reversal whereas the q-axis current is positive to give positive torque of Fig. 3.70.
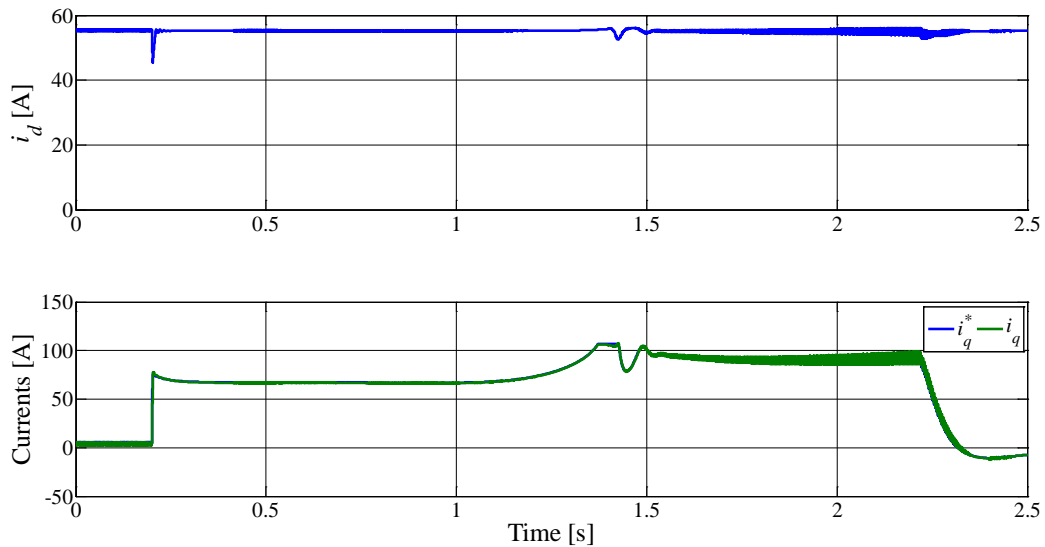
Fig. 3.69: Current control for speed reversal: machine parameters estimated through self-commissioning
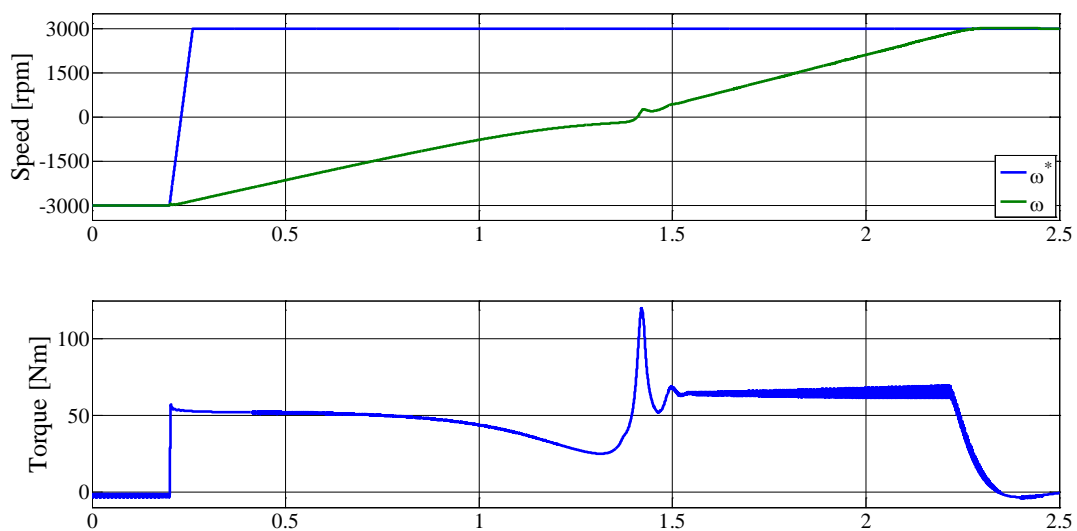
Fig. 3.70: Step speed reversal with sensorless control: machine parameters estimated through self-commissioning

3.7.   Unified Direct Flux Vector Control with self-commissioning – experimental results

The self-commissioning algorithms are verified on experimental rig by implementing unified direct flux vector control of Fig. 3.15 (section 3.2.2). The results of parameter identification tests are shown in previous sections from the experimental rig in Fig. 3.32, Fig. 3.34, Fig. 3.41, Fig. 3.51, Fig. 3.53, and Fig. 3.54, therefore they are not repeated here. However, performance comparison with and without self-commissioning is given to highlight the benefits of using exact machine parameters over their detuned values. The performance metrics for a drive system can be the dynamic response, controlled variable (position, speed or both) accuracy and, in some applications, the torque estimation accuracy.

To verify the effects of parameter detuning, a closed-loop speed control is implemented. The speed controller is a PI regulator of Fig. 3.9 whose feedback is the machine shaft speed computed from the signal received from optical encoder mounted on the shaft. Unified direct flux vector control is implemented with constant flux such that the inherent delay in rotor flux build-up of

(3.47) does not affect performance. Although (3.47) is applicable in rotor field oriented control scheme, it does hold good even in direct flux control. In UDFVC, only stator flux control has high bandwidth, the rotor flux rise is slowed down by the rotor time constant. The results showing this effect are shown in latter part of this section.

The dynamic response to a step speed reference shown in Fig. 3.71 is obtained when the magnetizing inductance value used in control is the one computed from the nameplate data (as given in Table I), while the speed response of Fig. 3.72 is achieved with parameters identification through self-commissioning procedure. By comparing Fig. 3.71 and Fig. 3.72, it can be observed that the drive acceleration obtained with exact machine parameters is better than in the case of detuned parameters. The overshoot in the measured speed of Fig. 3.71 is also higher than that of Fig. 3.72, with same speed regulator gains.
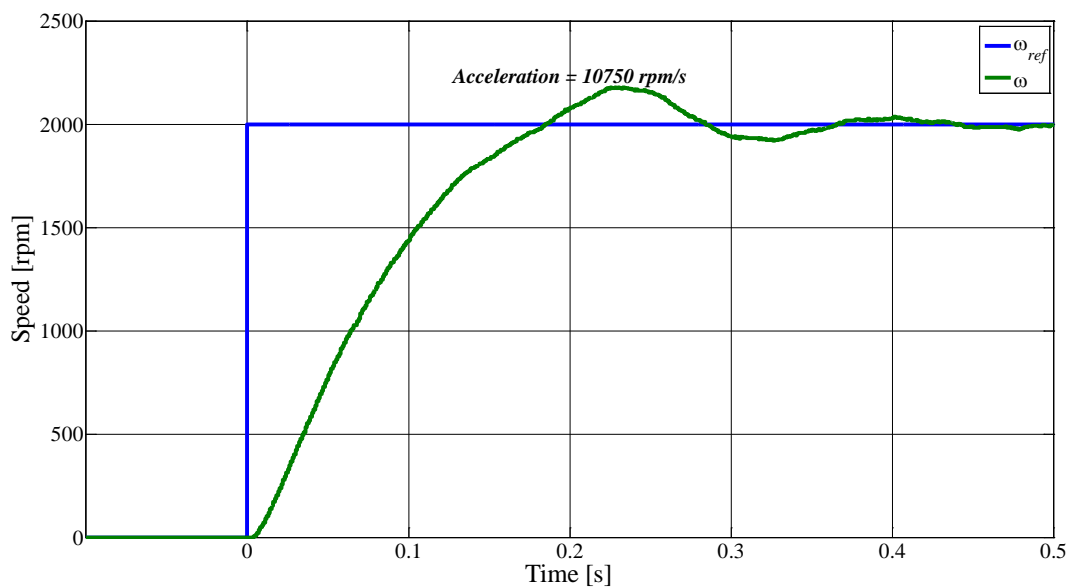
Fig. 3.71: Speed step response without self-commissioning due to –20% error in magnetizing inductance value used in control
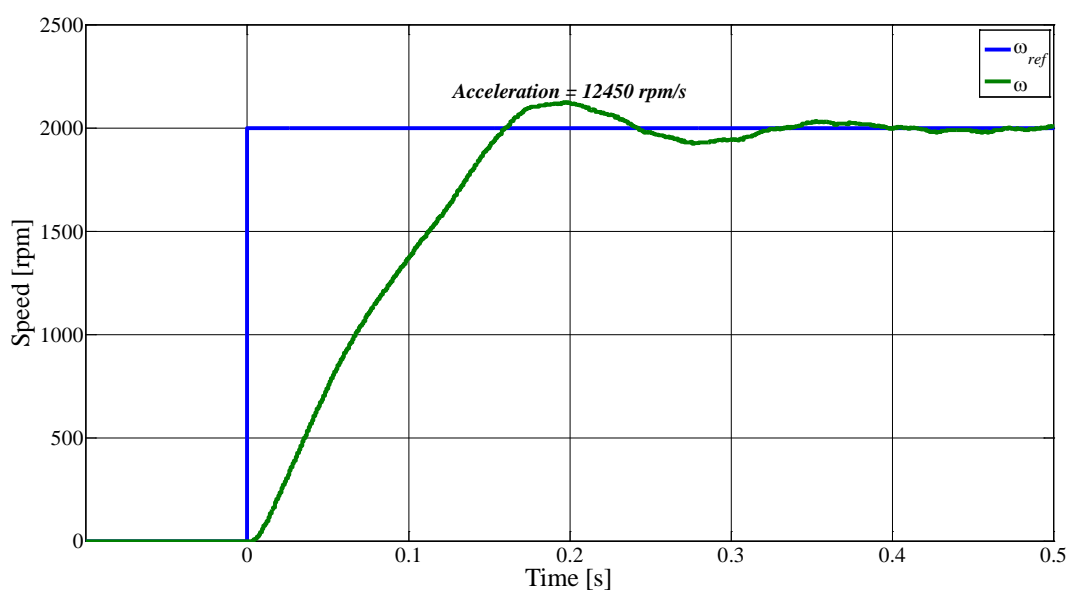
Fig. 3.72: Speed step response with self-commissioning all the parameters used in control are estimated through identification tests

The estimation accuracy of induced torque is another metric for stating the usefulness of self-commissioning. The torque produced by the machine can be estimated from the electrical variables used inside the control from any of the torque expressions given in section 3.2 such as (3.41). When the machine parameters fed to the control do not correspond to actual parameters, the effect is seen as error in the estimated torque. This effect is verified by comparing the estimated torque with the measured torque. The torque at the shaft is measured with a high precision torque-sensor.

The induction machine under test is mechanically coupled with a synchronous motor that acts as a prime mover. The synchronous machine is separately controlled through its dedicated drive. The speed of rotation of the shaft is set by the synchronous that works in speed control mode. The induction machine works in torque control mode. It must be noted, however, that the torque is not feedback controlled and the output of torque sensor is used just to verify the developed torque at the shaft and compare it with the estimate obtained from equation (3.41). Fig. 3.73 shows the experimental setup built for conducting this test.
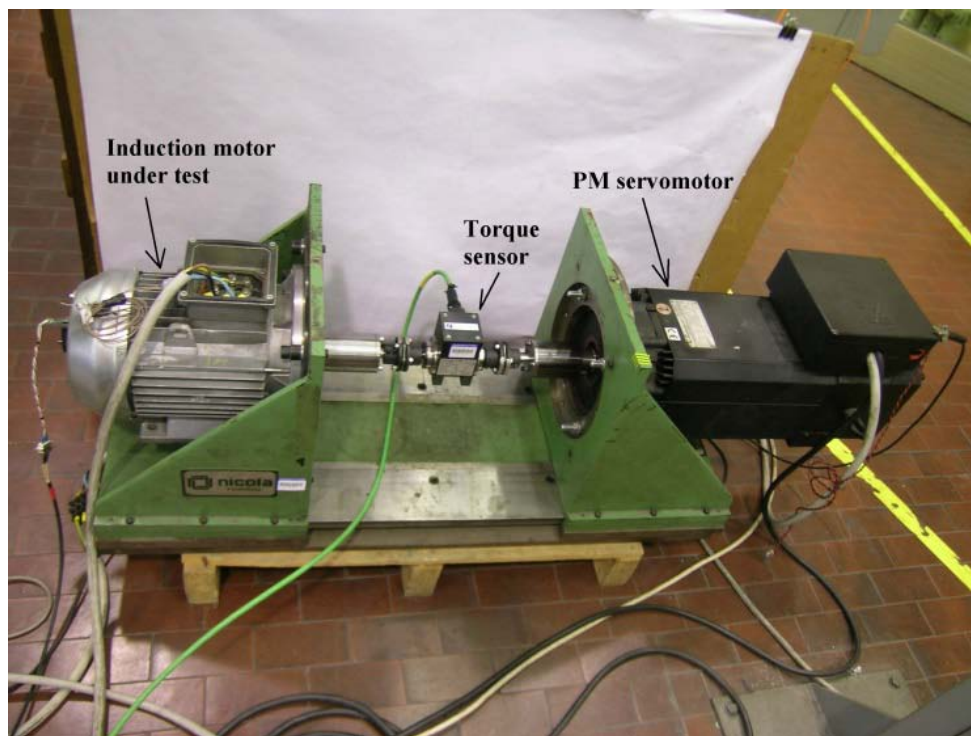
Fig. 3.73: Experimental rig showing induction machine under test, torque sensor and the prime mover

Fig. 3.74 shows the torque step response of the machine when the self-commissioning at start-up is disabled and the parameters incorporated in the control are inexact. A large steady state error between the estimated torque and actual (measured) torque persists. Besides, the torque response is sluggish for the applied step. This is not the case when machine parameters identification routine is executed before allowing the machine take on the load as in Fig. 3.75. In Fig. 3.75, it can be seen that the measured and estimated torques reach their peak values three times faster than that in Fig. 3.74. The steady state error also reduces by as much as 11%. This result is important from the traction applications' point of view where exact torque estimate is required especially on curves when each wheel is fitted with an individual motor.
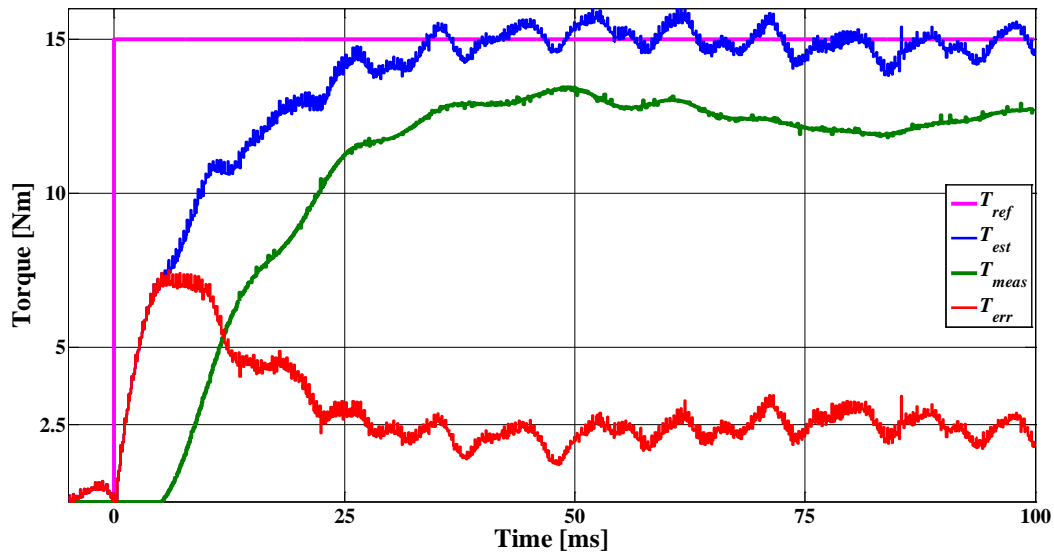
Fig. 3.74: Torque step response without self-commissioning: steady state error = 17%
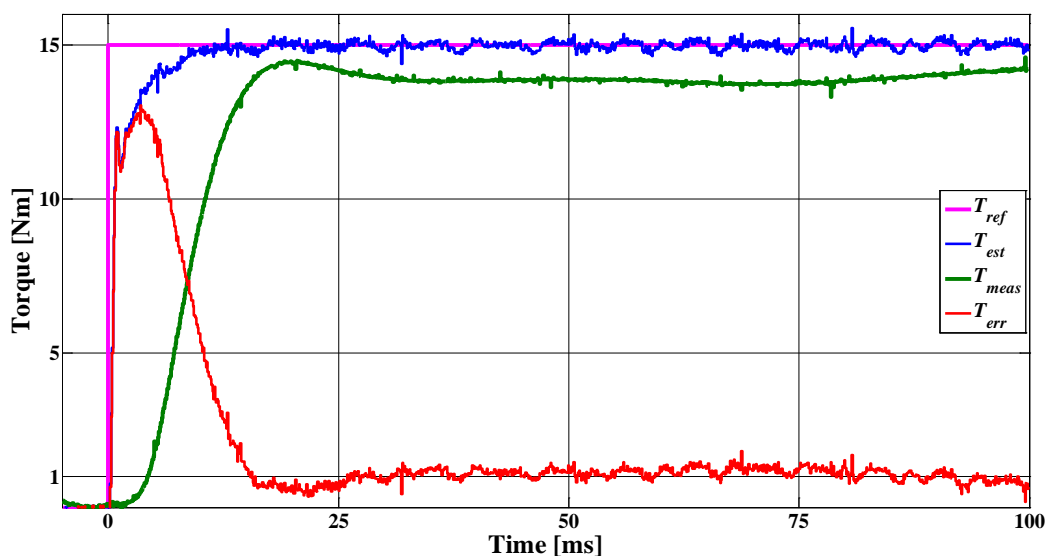
Fig. 3.75: Torque step response with self-commissioning enabled: steady state error = 6%

As said earlier, the constant flux operation is preferred over variable flux for reasons of dynamic performance. Nevertheless, the variable flux operation gives better efficiency at all load conditions (Fig. 3.57), however, it deteriorates the dynamic performance. This is highlighted by comparing machine response to a rapid torque transient with constant flux (Fig. 3.76) and with variable flux (Fig. 3.77). It can be observed that with constant flux operation the demanded torque is realized in just over one millisecond, whereas the same is not the case in variable flux operation where the response time increases to about 75 ms. The middle axis of Fig. 3.77 explains the reason for this sluggish torque response. At no-load, i.e. at zero torque demand, the flux is kept minimum for keeping the stator copper losses low, when an instantaneous torque is demanded the flux must increase and this increase is governed by the d-axis current (bottom axis of Fig. 3.77). Although the flux controller has high bandwidth as it is directly controlled by d-axis voltage (3.61), this voltage is limited to a value such that the total phase current is within inverter limits during all operating conditions including load transients. The limit imposed on available d-axis voltage causes voltage

command saturation and therefore the *d*-axis current remains constant, thus the flux rise is slow as seen in Fig. 3.77.
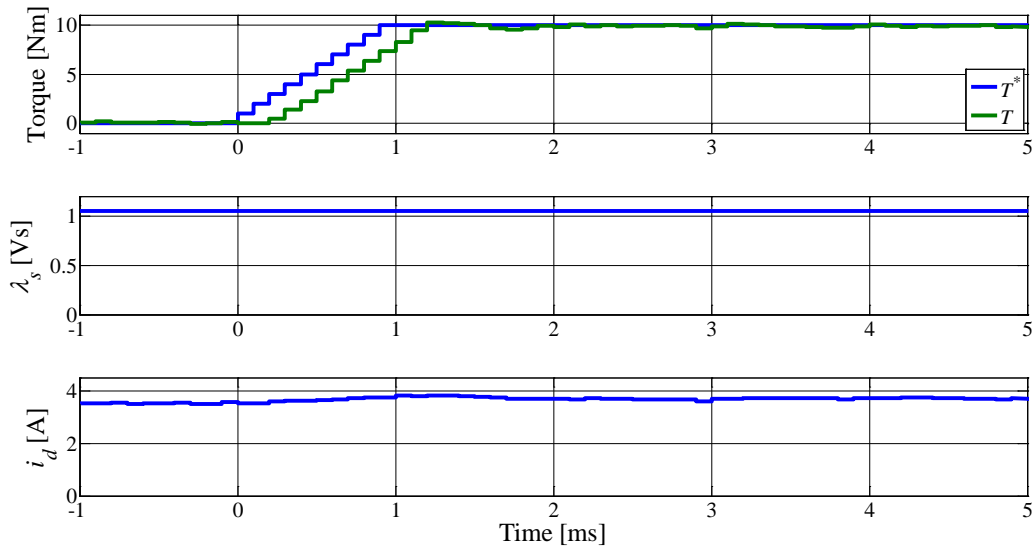
Fig. 3.76: Torque response (top axis), stator flux (middle axis), *d*-axis current (bottom axis) at constant flux
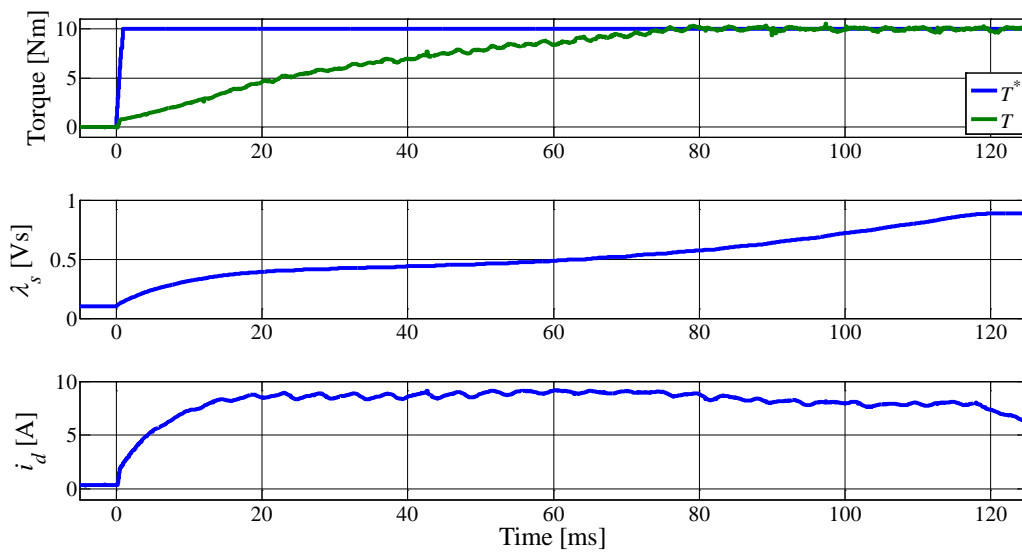
Fig. 3.77: Torque response (top axis), stator flux (middle axis), *d*-axis current (bottom axis) with variable flux

Fig. 3.78 gives a comparison of the total phase current during the torque transient for the situations of Fig. 3.76 (constant flux) and Fig. 3.77 (variable flux). It can be seen that in constant flux case, the total phase current (Fig. 3.78, top axis) remains well within the machine's rated peak current (see Fig. 3.27), whereas in variable flux case (bottom axis of Fig. 3.78) the total phase current remains above machine ratings for entire duration of the load transient (cf. Fig. 3.77). Although the machine can withstand this excessive current that lasts for over 100 milliseconds, the inverter switches must be capable of withstanding this excessive current, this adds to the cost of the drive system.
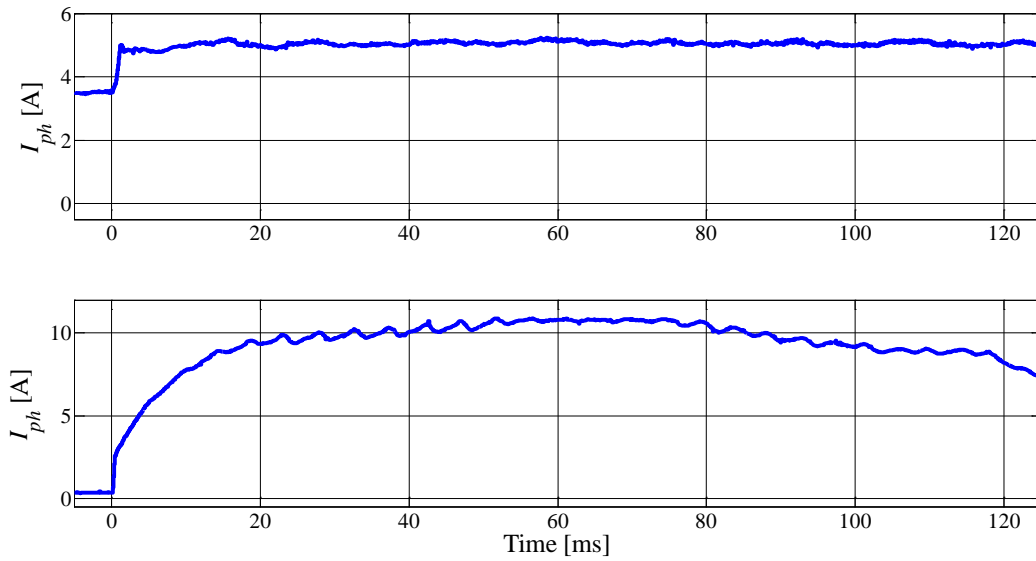
Fig. 3.78: Phase current due to torque transient: constant flux (top), variable flux (bottom)

In order to improve the dynamic response, the limit on *d*-axis voltage is relaxed and the result is a better transient torque response of Fig. 3.79 over that of Fig. 3.77. However, this improved response comes at the cost of even higher *d*-axis and, therefore phase, current. Fig. 3.80 gives a comparison of total phase current drawn by the machine during the three cases of Fig. 3.76, Fig. 3.77 and Fig. 3.79.
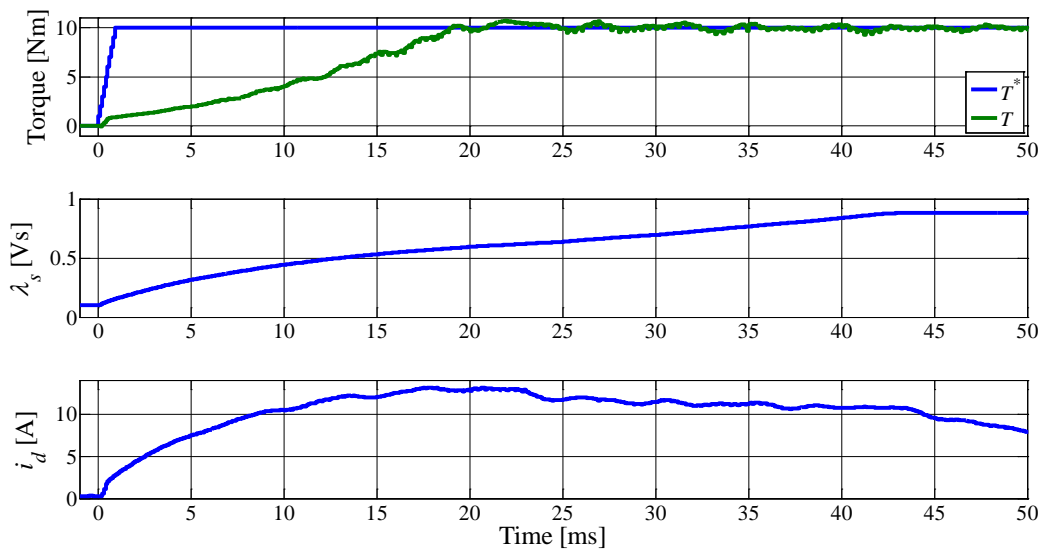
Fig. 3.79: Torque response (top axis), stator flux (middle axis), *d*-axis current (bottom axis) with variable flux
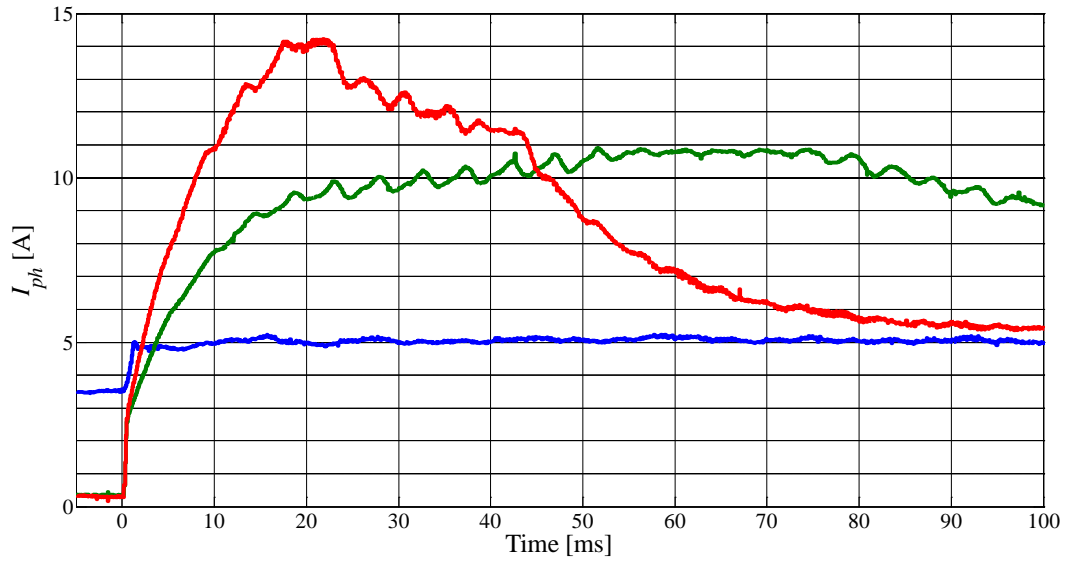
Fig. 3.80: Total phase current: blue curve (constant flux Fig. 3.76), green curve (variable flux Fig. 3.77), red curve (variable flux and increased *d*-axis voltage Fig. 3.79)

To conclude, the choice between constant and variable flux operation depends on the specific application at hand. Both of them have advantages and disadvantages. The constant flux mode of operation gives better dynamic performance Fig. 3.76 but has poor efficiency profile at partial loads (Fig. 3.57). On the other hand, the variable flux strategy has superior efficiency at all loads, it comes up with a rather poorer transient performance that leads to sluggish torque response (Fig. 3.77 and Fig. 3.79).

Appendix

This section gives the nameplate and equivalent circuit parameters' data of the induction machines used in tests.

Machine – 1: CESET 700W Prototype – CIM2/55-132/ZN

Nameplate Data*			
Nominal power	0.7 [kW]	Pole pairs	1
Rated voltage	195 [V]	Rated current	3 [A]
Rated speed	-- [rpm]	Max. frequency	300 [Hz]
Power factor	--		

* The machine nameplate is not mounted as it is a prototype

Equivalent circuit parameters		
Parameter	Value	Unit
R_s	3.25	Ω
L_{ls}	3.90	mH
L_m	148.30	mH
L_{lr}	6.60	mH
R_r	1.64	Ω

Machine – 2: Electro Adda – MOT. 3~FCP100L – 4

Nameplate Data			
Nominal power	2.2 [kW]	Pole pairs	2
Rated voltage	230Δ/400Y [V]	Rated current	8.8Δ/5.08Y [A]
Rated speed	1400 [rpm]	Rated frequency	50 [Hz]
Power factor	0.8		

Equivalent circuit parameters		
Parameter	Value	Unit
R_s	3.37	Ω
L_{ls}	16.00	mH
L_m	283.30	mH
L_{lr}	16.00	mH
R_r	2.20	Ω

Machine – 3: Electro Adda – MOT. 3~ FCP-112MT-4

Nameplate Data			
Nominal power	4.0 [kW]	Pole pairs	2
Rated voltage	230Δ/400Y [V]	Rated current	15.2Δ/8.8Y [A]
Rated speed	1410 [rpm]	Rated frequency	50 [Hz]
Power factor	0.8		

Equivalent circuit parameters		
Parameter	Value	Unit
R_s	1.42	Ω
L_{ls}	8.20	mH
L_m	157.50	mH
L_{lr}	8.20	mH
R_r	1.70	Ω

Machine – 4: Siemens D-91066 Erlangen Compressor

Nameplate Data			
Nominal power	32.0 [kW]	Pole pairs	2
Rated voltage	230Δ/400Y [V]	Rated current	123Δ/71Y [A]
Rated speed	-- [rpm]	Rated frequency	170 [Hz]
Power factor	--		

Equivalent circuit parameters		
Parameter	Value	Unit
R_s	0.029	Ω
L_{ls}	0.165	mH
L_m	5.00	mH
L_{lr}	0.226	mH
R_r	0.078	Ω

Machine – 5: Inversys, Brook Crompton Motor

Nameplate Data			
Nominal power	3.0 [kW]	Pole pairs	2
Rated voltage	220Δ/380Y [V]	Rated current	15.4Δ/8.9Y [A]
Rated speed	1450 [rpm]	Rated frequency	50 [Hz]
Power factor	0.7		

Equivalent circuit parameters[†]		
Parameter	Value	Unit
R_s	1.50	Ω
L_{ls}	8.00	mH
L_m	194.00	mH
L_{lr}	8.00	mH
R_r	1.57	Ω

† No-load and short circuit data not available, nameplate estimate

Chapter – 4

INTERIOR PERMANENT MAGNET SYNCHRONOUS MOTOR DRIVE

4.1.   Introduction

Permanent Magnet (PM) machines are the rapidly growing motive elements used widely across all industrial applications and have an ever increasing market share over the last decade or so. This growth is mainly due to their efficient, and hence economic, operation. The exclusion of rotor currents to generate magnetic field for electromechanical energy conversion makes the PM machines have lesser losses and keeps them from attaining higher temperatures. As the magnetic field is produced by the magnets, there are no magnetising currents required, that translates into more torque/power per ampere of input current, which is the reason why they can operate at higher power factors making the power electronic converters supplying them operate at higher efficiencies. The relatively lighter permanent magnets constituting most of the rotor mass render the rotor inertia lower compared to all-metal rotors (squirrel cage rotor of induction machine) and hence have a better dynamic performance and allow construction of rotors with larger radii. The manufacturing process is relatively simple (if compared with wound-field induction or dc machines) because of the elimination of brushes. The absence of brushes and commutator reduces maintenance cost as well as outage times. These machines allow construction with high pole number that makes them particularly suitable for direct-drive applications.

The higher power factor operation makes the PM machines a preferred choice over their magnet-less counterparts such as induction machine. The excitation through permanent magnets allows drawing only active power from the source i.e. no or less reactive power required of source. This permits only active component of current being drawn from the supply which saves on inverter sizing and hence the cost. However, unlike induction machines, they can not be operated directly from the mains that imposes a restriction on their use in simple applications such as fans and compressors. The high cost of permanent magnet materials pushes the total machine cost up and thus makes the choice of PM machines less favourable. However, the cost is reduced by design optimization techniques that minimize magnet volume for a given application. Since the permanent magnets lose their magnetization at higher temperatures, the PM machines are not suitable for extremely hot environments. Nevertheless, these machines are finding increasing use in special applications, such as vehicles, thanks to their high efficiency and high power-to-weight and/or torque-to-volume ratio. The ever decreasing cost of semiconductor devices allows realizing drives employing PM machines at affordable price.

The IPM is among the widely used PM machines and is the second machine type studied for parameter identification in this thesis. Their robust high-power operating capability at higher inverter and motor efficiencies for a wide constant-power speed range makes them bid well for different industrial and domestic applications [3].

An interior permanent magnet synchronous motor (IPMSM) drive has essentially the same structure as described in chapter 2 (section 2.1). The electric machine here is an IPMSM instead. Hence the same power converter and control system used for induction machine can be employed

for controlling the IPMSM. This highlights one of the advantages of variable frequency drives: the universality.

As described in chapter 1, an IPMSM can be built of the same stator as that of an induction machine, containing sinusoidally distributed windings, by replacing the rotor. However, fractional-slot concentrated winding IPMs are also in vogue these days because of the ease with which they can operate in flux-weakening regime compared to their distributed winding counterparts. Low cogging torque and higher efficiency at full or partial loads are among other advantages they have over distributed winding machines [137, 138].

The rotor of an IPM is anisotropic in shape and hosts permanent magnets 'interior' to the ferromagnetic core, hence the name 'interior permanent magnet'. Fig. 4.1 shows some of IPM configurations with various rotor geometries that can be used. The stator winding type is chosen according to the specific application at hand for which the rotor design is then optimized.

<center>(a)   (b)   (c)   (d)</center>
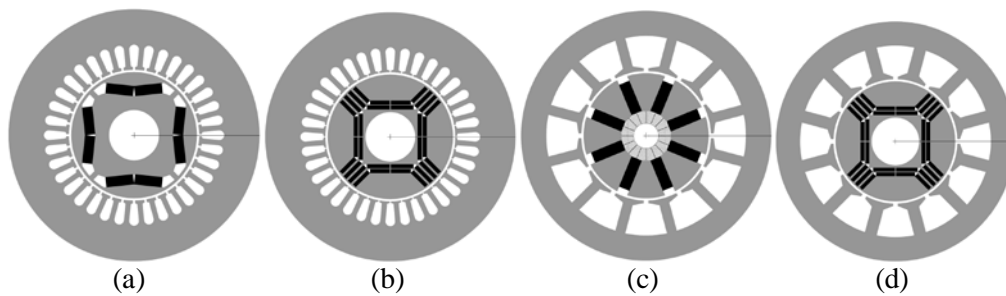
Fig. 4.1: Various IPM configurations: distributed windings (a and b), concentrated windings (c and d)

In this chapter, machine model is devised from its equivalent circuit in section 4.2 and machine control is described in section 4.3. The torque characteristics are studied at length in section 4.4 while rotor construction variants are discussed in section 4.5. Section 4.6 gives an insight into flux-weakening capability and its dependence on saliency. Machine parameter identification techniques are studied in 4.7 and a new method of parameter identification is presented in section 4.8. An estimation method for permanent magnet flux linkage is described in section 4.9. Finally, section 4.10 outlines how the Maximum Torque Per Ampere (MTPA) characteristic of the machine is obtained from tests proposed here.

4.2.   Machine model

The model of any physical system describes the system behaviour in terms of mathematical equations. The model of an electrical system is further described by putting these equations in the form of an equivalent circuit consisting of basic electrical components. The equivalent circuit of any synchronous machine is given in Fig. 4.2. The same is valid for the IPMSM under study here. This equivalent circuit is simpler than that of induction machine in that there are no rotor currents to be included in the equivalent circuit. Unlike induction machine, the rotor of a synchronous machine rotates at the same angular speed as the rotating magnetic field produced by the stator, in other words, there is no slip and no relative motion between stator and rotor magnetic fields. The rotor 'locks' in synchronism with the stator magnetic field thus the name 'synchronous' machine. Like any externally excited synchronous machine, the back-emf (E) induced in the stator windings by the rotor magnetic field appears in the equivalent circuit.

In the equivalent circuit of Fig. 4.2, R_s is the stator per-phase resistance, L is the phase inductance and λ_m is the permanent magnet flux linkage. The stator phase inductance is a function of the rotor position which is true for all salient pole synchronous machines. As the rotor has anisotropic shape (Fig. 4.1), the inductance of each stator phase varies with twice the rotor mechanical angle. Fig. 4.3 shows a rather simpler two-pole metal structure and shows how the inductance of phase A behaves over 180° mechanical rotation of the metal piece. This variation in

inductance can be expressed in terms of rotation angle as in (4.1). The same is valid for the rest of the phases of the machine. The inductance variation as a function of angle is exploited in anisotropic permanent magnet machines as well to obtain an additional torque component which will be discussed in the subsequent paragraphs.

$$L_a = L_\circ + L_1 \, cos(2\vartheta) \tag{4.1}$$
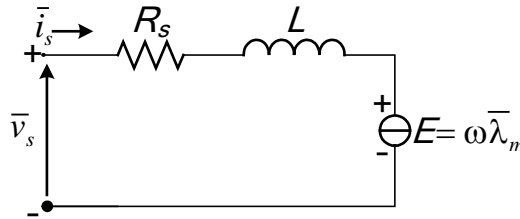
Fig. 4.2: Synchronous machine equivalent circuit
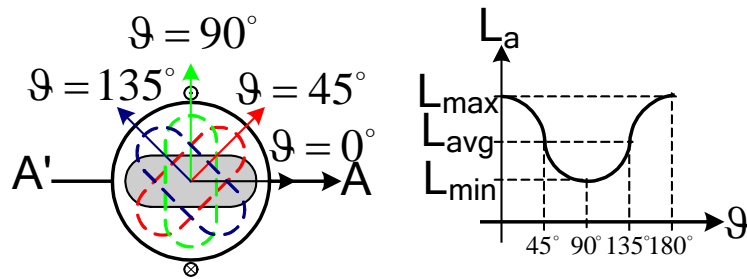
Fig. 4.3: Phase inductance as a function of rotor position

The electrical behaviour of the machine can be described by its voltage equations. In the absence of rotor currents, the electrical equations of the machine are essentially the stator voltage equations (4.2) written in vectorial notation in the stator's stationary reference frame, these equations are equally valid in the (αβ) reference frame.

$$\bar{v}_s = R_s \bar{i}_s + \frac{d\bar{\lambda}_s}{dt} \tag{4.2}$$

As with any three-phase machine, converting the equations to two-phase equivalent and then transforming to an arbitrarily chosen reference frame makes the analysis easier, same goes for the IPMSM here. Before transforming its equations (4.2), a reference frame is defined. Unlike induction machine that has a cylindrical rotor which permits purely arbitrary fixing of *d*-axis of the synchronously rotating reference frame, the case of a PM machine requires particular attention in this regard. Although the reference frame can be fixed at any position, provided it is maintained throughout the process, for practical reasons, either the axis along the magnets or perpendicular to them is chosen for convenience. In general, the *d*-axis is assumed along the north pole of the magnet as shown in Fig. 4.4. Here, ω is the angular speed of the *dq* rotating reference frame which is the same as *p* times the rotor speed ω_r; *p* is the number of machine pole-pairs.

Having defined the reference frame, the machine equations (4.2) can now be transformed to the *dq* reference frame using the same transformation operator developed in chapter 3.

$$\bar{v}_{sdq} = R_s \bar{i}_{sdq} + \frac{d\bar{\lambda}_{sdq}}{dt} + jp\omega_r \bar{\lambda}_{sdq} \tag{4.3}$$
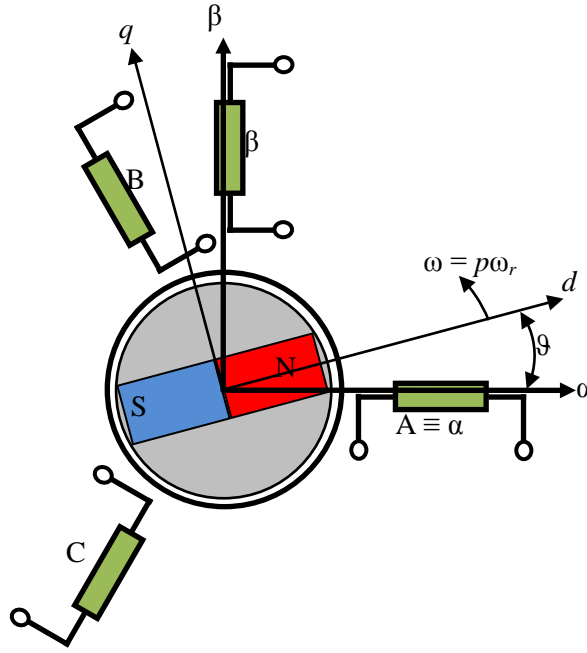
Fig. 4.4: Reference frame definition for IPM

In (4.3), the prefix 's' in the subscripts can be omitted since only stator quantities will be dealt with. $\overline{\lambda}_{sdq}$ is the flux vector in the *dq* reference frame which is defined by (4.4), with modified subscript. The magnetic equations include the flux component contributed by the permanent magnets. L_d and L_q are inductances seen through the *d*- and *q*-axis of Fig. 4.4, respectively.

$$\overline{\lambda}_{dq} = \begin{bmatrix} \lambda_d \\ \lambda_q \end{bmatrix} = \begin{bmatrix} L_d & 0 \\ 0 & L_q \end{bmatrix} \begin{bmatrix} i_d \\ i_q \end{bmatrix} + \begin{bmatrix} \lambda_m \\ 0 \end{bmatrix} \tag{4.4}$$

From Fig. 4.4 it is evident that the *d*-axis of the reference frame sees permanent magnet in its flux path whereas the *q*-axis flux path consists mostly of the iron core (grey area) with a small permanent magnet cross-section. From the basics characteristics of permanent magnet materials, it is known that they have low permeance compared to the ferromagnetic core used in electrical machines. Thus the inductance seen along the *d*-axis is lower compared to that seen from the *q*-axis. This difference in the *d*- and *q*-axis inductances gives this type of PM machine a peculiar characteristic called saliency. Machine saliency is defined as the ratio between *q*- and *d*-axis inductances. For an IPM with *dq*-reference frame chosen as in Fig. 4.4, the inequality (4.5) always holds.

$$L_d < L_q \tag{4.5}$$

Substituting (4.4) in (4.3) and writing the *d*- and *q*-axis equations separately:

$$v_d = R_s i_d + L_d \frac{di_d}{dt} - p\omega_r L_q i_q \tag{4.6}$$

$$v_q = R_s i_q + L_q \frac{di_q}{dt} + p\omega_r L_d i_d + p\omega_r \lambda_m \tag{4.7}$$

Fig. 4.5 and Fig. 4.6 show the *d*- and *q*-axis equivalent circuits, respectively.
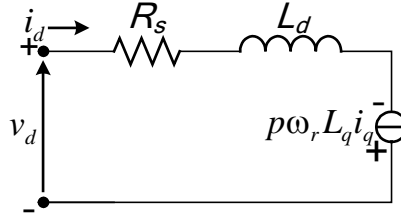
Fig. 4.5: *d*-axis equivalent circuit: eq. (4.6)
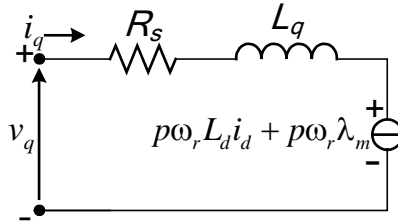
Fig. 4.6: *q*-axis equivalent circuit eq. (4.7)

As for induction machine, the mechanical torque produced by this machine is also given by the vector product of flux and current vectors (4.8).

$$T = \frac{3}{2} p\left(\bar{\lambda}_{dq} \wedge \bar{i}_{dq}\right) = \frac{3}{2} p\left(\lambda_d i_q - \lambda_q i_d\right) \tag{4.8}$$

Substituting for λ_d and λ_q from (4.4):

$$T = \frac{3}{2} p \left[\left(L_d i_d + \lambda_m\right)i_q - L_q i_q i_d\right]$$

Rearranging:
$$T = \frac{3}{2} p\lambda_m i_q + \frac{3}{2} p\left(L_d - L_q\right) i_d i_q \tag{4.9}$$

Equations (4.3) through (4.9) describe the electromechanical energy conversion process taking place in an IPMSM. It is important to note that the rotor position is always required to maintain the *d*- and *q*-axis aligned with respect to the magnets as in Fig. 4.4.

4.3.   Machine Control

As for other ac machines, vector control is the most common control strategy for IPM as well. For having continuous and ripple-free torque, the current vector has to have a fixed direction with respect to the magnets. From the machine torque equation (4.9), it can be intuited that once the *d*- and *q*-axis are defined (Fig. 4.4) and identified, the machine control is essentially the control of i_d and i_q. For a rotating reference frame synchronous to the PM flux, constant *d*- and *q*-axis currents give constant torque. For controlling the currents, a PI current control similar to that discussed for induction machine can be implemented. The control strategies used for this machine are briefly discussed below.

4.3.1. Rotor Field Oriented Control

The rotor field oriented control (RFOC) discussed for induction machine is equally applicable to synchronous machines including the IPM. Due to the absence of slip and rotor currents, the RFOC of synchronous machines is rather simpler. Fig. 4.7 illustrates (4.9) in graphical representation and describes how torque can be controlled by varying both *d*- and *q*-axis currents

without any delay (unlike induction machine where the *d*-axis current was less suited for torque control).
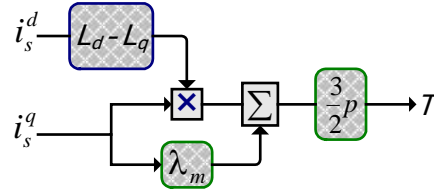
Fig. 4.7: Graphical representation of eq. (4.9)

The linear dependence of torque on the current makes the permanent magnet machines torque response faster and gives them edge over induction machine. The bandwidth of the torque control is governed by the current-loop bandwidth that can be maximized by adjusting gains.

The rotor field oriented control requires the information about the rotor flux vector. For the IPM with the *dq*-axes defined in Fig. 4.4, the rotor flux direction is simply the direction of magnets' north pole, which can be obtained through a shaft encoder usually included for high-performance vector control drives. In the absence of position sensors, sensorless control is the only choice in which the rotor flux vector is estimated through stator quantities.

For realizing the torque through i_d and i_q, the state equations of the machine are required with state variables as i_d and i_q. These equations are derived from equations (4.6) and (4.7) as given below.

$$\frac{d}{dt}\begin{bmatrix} i_d \\ i_q \end{bmatrix} = \begin{bmatrix} -\dfrac{R_s}{L_d} & p\omega_r\dfrac{L_q}{L_d} \\ -p\omega_r\dfrac{L_d}{L_q} & -\dfrac{R_s}{L_q} \end{bmatrix}\begin{bmatrix} i_d \\ i_q \end{bmatrix} + \begin{bmatrix} \dfrac{1}{L_d} \\ \dfrac{1}{L_q} \end{bmatrix}\begin{bmatrix} v_d \\ v_q - p\omega_r\lambda_m \end{bmatrix} \tag{4.10}$$

Observing the state equations (4.10) and noting inequality (4.5) it is evident that the current control loops for *d*- and *q*-axis must have different gains to give the same bandwidth. The cross-coupling between the two axes is also significant. The well known feed-forward compensation techniques can be used to mitigate the cross-coupling effects as well as to compensate, in the *q*-axis, for the back-emf induced by PM flux (λ_m).

The proportion in which the *d*- and *q*-axis currents are injected decides the contribution of reluctance and magnet alignment torque, respectively, in the total torque. These currents are optimized for maximum torque and minimum losses and depend on the magnitude of permanent magnet flux and saliency. Section 4.4 discusses at length the optimum current vector selection.

4.3.2. *Unified Direct Flux Vector Control*

As discussed in previous chapters, the unified direct flux vector control is a control strategy midway between rotor field oriented control (of section 4.3.1) and direct torque control. Unlike rotor field oriented control where two current control loops are required (4.10), this control has just one current control loop. The other control loop involved is a high bandwidth flux control loop. Machine flux is controlled through *d*-axis voltage only and torque demand is met by controlling *q*-axis current.

Since this works in stator field oriented frame, therefore a new reference frame must be defined for this control. Fig. 4.8 shows the definition of the *dq* rotating reference frame. Here the rotor's mechanical position coincides with the rotor flux vector signifying the rotor rotates at synchronous speed and there is no slip. The angle δ between stator and rotor flux vectors is the load

angle, sometimes called as the torque angle. Depending on the load torque, this angle varies from zero (at no load) to a maximum value (at full load) determined by the machine's parameters.

The equations (4.3) in the new stator flux oriented reference frame can be written as below.

From Fig. 4.8, $\omega = p\omega_r$ $$\overline{v}_{sdq^s} = R_s \overline{i}_{sdq^s} + \frac{d\overline{\lambda}_{sdq^s}}{dt} + j\overline{\lambda}_{sdq^s}\left(\omega + \frac{d\delta}{dt}\right)$$ (4.11)

The subscript dq^s signifies quantities in stator flux oriented frame of Fig. 4.8, the subscript 's' denotes 'stator' quantities and it can be dropped since only the stator quantities are treated here.
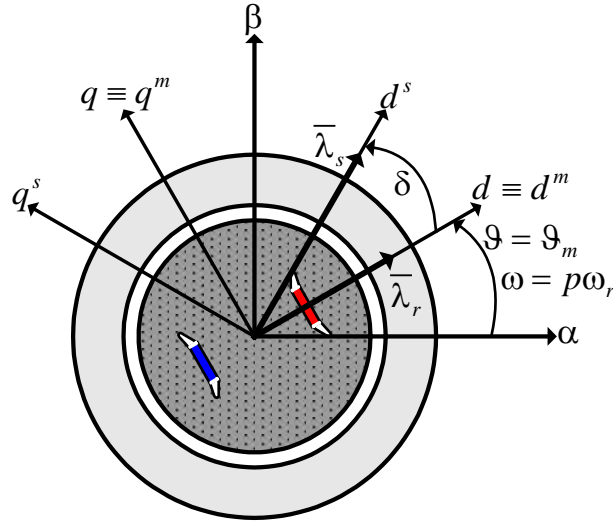
Fig. 4.8: Stator flux oriented reference frame definition

With the stator flux definition as in Fig. 4.8, written as (4.12), the voltage equations for the d- and q-axis can be derived from (4.11).

$$\overline{\lambda}_{dq^s} = \lambda_{d^s} + j\lambda_{q^s} = \lambda_{d^s} + j0 = \lambda$$

or $$\overline{\lambda}_{dq^s} = \lambda$$ (4.12)

d-axis: $$v_{d^s} = R_s i_{d^s} + \frac{d\lambda}{dt}$$ (4.13)

q-axis: $$v_{q^s} = R_s i_{q^s} + \left(\omega + \frac{d\delta}{dt}\right)\lambda$$ (4.14)

The developed torque in terms of quantities of stator flux oriented frame can be obtained by substituting (4.12) into (4.8) to get (4.15).

$$T = \frac{3}{2} p \lambda i_{q^s}$$ (4.15)

The state-space model of the two axes is given in (4.16).

$$\frac{d}{dt}\begin{bmatrix}\lambda\\\delta\end{bmatrix}=\begin{bmatrix}-R_s & 0\\0 & \dfrac{-R_s}{\lambda}\end{bmatrix}\begin{bmatrix}i_{d^s}\\i_{q^s}\end{bmatrix}+\begin{bmatrix}1\\\dfrac{1}{\lambda}\end{bmatrix}\begin{bmatrix}v_{d^s}\\v_{q^s}\end{bmatrix}+\begin{bmatrix}0\\-\omega\end{bmatrix}\tag{4.16}$$

A quick comparison of (4.15) and (4.16) reveals that the torque control variables are λ and i_{q^s} whereas the state variables are λ and δ. For speed and simplicity of control, the torque control variable i_{q^s} must also be the state variable for which the q-axis equation (4.14) must be manipulated. The q-axis equation with q-axis current as state variable is derived below.

Referring to Fig. 4.8, let i_d and i_q be the d- and q-axis currents, respectively, in the rotor field oriented frame dq, as in (4.6) and (4.7). The q-axis current i_{q^s} in the stator field oriented frame can also be written in terms of i_d and i_q and the load angle δ as (4.17).

$$i_{q^s}=i_q\cos\delta-i_d\sin\delta\tag{4.17}$$

Similarly, the flux in rotor field oriented dq-frame can be obtained from Fig. 4.8 as:

$$\lambda_d=\lambda\cos\delta\quad\text{and}\quad\lambda_q=\lambda\sin\delta$$

In the rotor field oriented frame where the d-axis is aligned with the north pole of the magnets (cf. Fig. 4.4), the equation (4.4) can be applied to express i_d and i_q in terms of λ of (4.12).

$$i_d=\frac{\lambda_d-\lambda_m}{L_d}=\frac{\lambda\cos\delta-\lambda_m}{L_d}$$

$$i_q=\frac{\lambda_q}{L_q}=\frac{\lambda\sin\delta}{L_q}$$

Substituting for i_d and i_q in (4.17):

$$i_{q^s}=\frac{\lambda}{L_q}\sin\delta\cos\delta-\frac{\lambda}{L_d}\sin\delta\cos\delta+\frac{\lambda_m}{L_d}\sin\delta$$

➡ $$i_{q^s}=\frac{1}{L_d}\left\{\left(\frac{L_d}{L_q}-1\right)\lambda\frac{\sin2\delta}{2}+\lambda_m\sin\delta\right\}\tag{4.18}$$

Differentiating (4.18) with respect to time:

$$\frac{di_{q^s}}{dt}=\frac{1}{L_d}\left\{\left(\frac{L_d}{L_q}-1\right)\frac{\sin2\delta}{2}\frac{d\lambda}{dt}+\left(\frac{L_d}{L_q}-1\right)\lambda\cos2\delta\frac{d\delta}{dt}+\lambda_m\cos\delta\frac{d\delta}{dt}\right\}\tag{4.19}$$

From state equation (4.16), we have:

$$\frac{d\lambda}{dt}=v_{d^s}-R_si_{d^s}\quad\text{and}\quad\lambda\frac{d\delta}{dt}=v_{q^s}-R_si_{q^s}-\omega\lambda$$

Substituting for these two elements in (4.19), we have:

$$\frac{di_{q^s}}{dt} = \frac{1}{L_d}\left[\left(\frac{L_d}{L_q}-1\right)\frac{sin\,2\delta}{2}\left(v_{d^s}-R_s i_{d^s}\right)+\left\{\left(\frac{L_d}{L_q}-1\right)cos\,2\delta+\frac{\lambda_m\,cos\,\delta}{\lambda}\right\}\left(v_{q^s}-R_s i_{q^s}-\omega\lambda\right)\right]$$

Rearranging:

$$L_d\frac{di_{q^s}}{dt} = -\left(1-\frac{L_d}{L_q}\right)\frac{sin\,2\delta}{2}\left(v_{d^s}-R_s i_{d^s}\right)+\left\{-\left(1-\frac{L_d}{L_q}\right)cos\,2\delta+\frac{\lambda_m}{\lambda}cos\,\delta\right\}\left(v_{q^s}-R_s i_{q^s}-\omega\lambda\right)$$

Defining the two factors k and b as in (4.20) and (4.21), respectively, for simplicity:

$$k = \frac{1}{2}\left(1-\frac{L_d}{L_q}\right)sin\,2\delta \tag{4.20}$$

$$b = -\left(1-\frac{L_d}{L_q}\right)cos\,2\delta+\frac{\lambda_m}{\lambda}cos\,\delta \tag{4.21}$$

Thus the q-axis state equation becomes:

$$\frac{di_{q^s}}{dt} = -\frac{k}{L_d}\left(v_{d^s}-R_s i_{d^s}\right)+\frac{b}{L_d}\left(v_{q^s}-R_s i_{q^s}-\omega\lambda\right) \tag{4.22}$$

Having defined (4.22), the state equations of the machine for direct flux vector control in stator flux oriented frame of Fig. 4.8 can be written as in (4.23) with λ and i_{q^s} as state variables:

$$\frac{d}{dt}\begin{bmatrix}\lambda\\i_{q^s}\end{bmatrix}=\begin{bmatrix}-R_s & 0\\ \dfrac{kR_s}{L_d} & -\dfrac{bR_s}{L_d}\end{bmatrix}\begin{bmatrix}i_{d^s}\\i_{q^s}\end{bmatrix}+\begin{bmatrix}1 & 0\\ -\dfrac{k}{L_d} & \dfrac{b}{L_d}\end{bmatrix}\begin{bmatrix}v_{d^s}\\v_{q^s}\end{bmatrix}+\begin{bmatrix}0\\ -\dfrac{b}{L_d}\omega\lambda\end{bmatrix} \tag{4.23}$$

It is evident from (4.23) that whereas the flux control (d-axis equation) is free from any disturbance in the q-axis, the control of i_{q^s} in the q-axis is not completely independent of the d-axis. For this reason, the current control in q-axis must be enhanced with feed-forward to mitigate the effects of cross-coupling caused by variations in d-axis quantities.

The set of equations (4.15) and (4.23) can be called the control equations of the machine in that the torque (4.15) is given by the state variables of (4.23). However, the dual of this set of equations can also be derived by using (4.16) as the state equation and replacing i_{q^s} in the torque expression by δ, the second state variable in (4.16).

Substituting (4.18) into (4.15):

$$T = \frac{3}{2}p\lambda\left[\frac{1}{L_d}\left\{\left(\frac{L_d}{L_q}-1\right)\lambda\frac{sin\,2\delta}{2}+\lambda_m\,sin\,\delta\right\}\right]$$

Rearranging:
$$T = \frac{3}{2}p\frac{1}{L_d}\left\{\left(\frac{L_d-L_q}{L_q}\right)\lambda^2\frac{sin\,2\delta}{2}+\lambda\lambda_m\,sin\,\delta\right\} \tag{4.24}$$

The second set of equations is therefore (4.16) and (4.24) since the state variables λ and δ of (4.16) appear in the torque expression of (4.24). It must be noted, however, that the first set with λ and i_q^s is preferable over the second because, unlike δ, the q^s-axis current i_q^s is a directly measured quantity in standard drive hardware. On the contrary, δ must be estimated from the feedback quantities and its estimate is also machine parameters and speed dependent. Thus, using i_q^s brings the advantage of simplicity of control.

Nevertheless, expression (4.24) is important for determining the load angle that gives maximum torque. Beyond a certain load angle δ_{max} the torque diminishes. The angle δ_{max} can be derived by differentiating (4.24) with respect to δ and equating the result to zero, as below.

$$\frac{\partial T}{\partial \delta} = \frac{\partial}{\partial \delta}\left[\frac{3}{2}\,p\,\frac{1}{L_d}\left\{\left(\frac{L_d - L_q}{L_q}\right)\lambda^2\,\frac{sin\,2\delta}{2} + \lambda\lambda_m\,sin\,\delta\right\}\right] = 0$$

$$\left(\frac{L_d - L_q}{L_q}\right)\lambda^2\,cos\,2\delta + \lambda\lambda_m\,cos\,\delta = 0 \tag{4.25}$$

Replacing δ with δ_{max} and rearranging:

$$\left(\frac{L_q - L_d}{L_q}\right)\lambda\left(2\,cos^2\,\delta_{max} - 1\right) - \lambda_m\,cos\,\delta_{max} = 0$$

Further
$$2\lambda\left(\frac{L_q - L_d}{L_q}\right)cos^2\,\delta_{max} - \lambda_m\,cos\,\delta_{max} - \lambda\left(\frac{L_q - L_d}{L_q}\right) = 0$$

This is a quadratic equation in $cos\delta_{max}$, using quadratic formula to solve for $cos\delta_{max}$, then δ_{max} is given by (4.26):

$$\delta_{max} = cos^{-1}\left\{\frac{L_q}{4\lambda\left(L_q - L_d\right)}\left(\lambda_m \pm \sqrt{\lambda_m^2 + 8\lambda^2\left(\frac{L_q - L_d}{L_q}\right)^2}\right)\right\} \tag{4.26}$$

A comment is needed here for the choice of correct δ_{max} value of the two solutions given by (4.26). Noting (4.5), it can be intuited from (4.24) that δ values between 90° and 180° give positive maximum torque. However, exactly where δ_{max} lies depends on the permanent magnet flux λ_m and the machine saliency. Nevertheless, the two boundary values can be defined as follows.

For $\lambda_m \rightarrow 0$: $\delta_{max} \rightarrow 135°$ \hfill (4.27)

For $L_d \rightarrow L_q$: $\delta_{max} \rightarrow 90°$ \hfill (4.28)

Eq. (4.27) is a typical condition for maximum torque of synchronous reluctance machines where permanent magnets are not used and (4.28) is the optimum load angle for isotropic rotor synchronous machines such as a surface mounted permanent magnet synchronous machine (SPMSM). The optimum load angle for an IPM is governed by machine design and the volume of permanent magnet material used. Besides, the load angle is heavily dependent on the operating conditions of the machine as well. For instance, the permanent magnet flux λ_m is temperature dependent as seen in Fig. 4.9 that shows BH curves at different temperatures of one of the many permanent magnet materials used in PM machines [139]; the temperature coefficient of magnetic

flux density is -0.12%/°C for this particular material. Additionally, the machine inductances (L_d and L_q) vary with current in the respective axes and also with the current in the cross-axis. The variation of L_d and L_q with i_d and i_q, respectively, can be observed in Fig. 4.19. Despite all these dependencies on operating conditions the interval between which δ_{max} of an IPM lies can be defined by combining (4.27) and (4.28) into (4.29).

$$90° < \delta_{max} < 135° \tag{4.29}$$
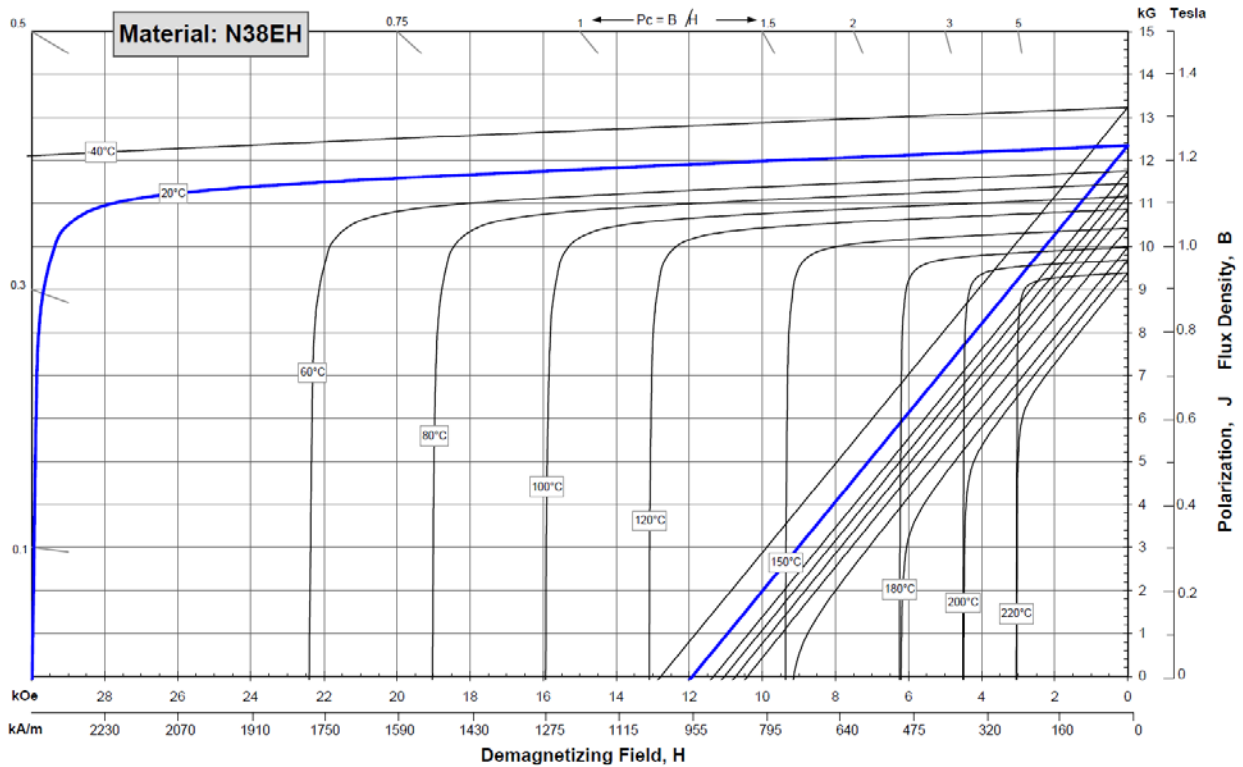
Fig. 4.9: BH-characteristics of Neodymium-Iron-Boron (NdFeB) material [139] – an example

Coming back to the state equations (4.16) or (4.23), both have stator flux λ as the state variable, however, it is not usually measured with flux sensors as that would increase the cost of the drive system. It must therefore be estimated from the available electrical quantities (e.g. phase currents and dc-link voltage). The stator flux can be estimated either by using (4.2) and integrating the voltage (back-emf integration) or using the magnetic equations (4.4). Since equations (4.4) are valid in rotor field oriented frame of Fig. 4.4, the flux must be transformed to stator field oriented reference frame of Fig. 4.8 for which angle δ must always be known (4.11).

As with induction machine, the voltage integration for flux estimation fails at low speeds due to insufficient back-emf, however, the magnetic model of the machine gives accurate results at low speeds. Therefore a complete flux observer valid also at low speeds is needed. The flux observer of Fig. 4.10 is similar to the one devised for induction machine with minute differences.

In Fig. 4.10, $\bar{v}_{dt}^{\alpha\beta}$ is the voltage vector for inverter non-linearity compensation and g is the observer gain that decides the speed (in electrical rad/s) at which the transition for flux estimation from magnetic model to voltage integration takes place.

The block 'Mag. Mod.' (short for Magnetic Model) contains the machine magnetic model in terms of flux-current look-up tables in the rotor field oriented frame where (4.4) can be applied. These look-up tables are obtained during machine commissioning on the test bench for different *d*- and *q*-axis current vectors and observing the flux. Due to saturation and cross-saturation effects

common in ac machines, the flux in the *d*- and *q*-axis is a function of current in the two axes for which (4.30) can be written.

$$\overline{\lambda}_{dq} = f\left(i_d, i_q\right) \tag{4.30}$$
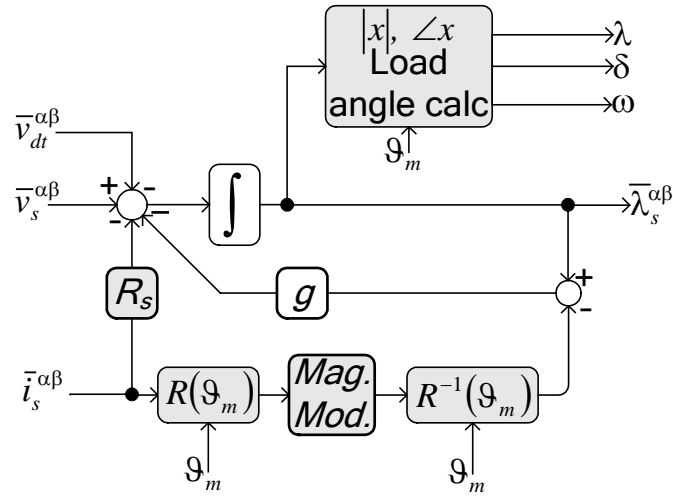
Fig. 4.10: Stator flux observer

Fig. 4.11 illustrates the *d*-axis flux as a function of i_d and i_q, while in Fig. 4.12 the graph of *q*-axis part of (4.30) is drawn for different i_d values. The results shown are obtained through experimental characterization of one of the test machines under study. The machine's look-up tables constructed from Fig. 4.11 and Fig. 4.12 are stored for each value of cross-axis current. For every pair of *dq*-axis current values (i_d, i_q), the flux observer of Fig. 4.10 reads the look-up tables stored in on-board memory and returns the pair (λ_d, λ_q).
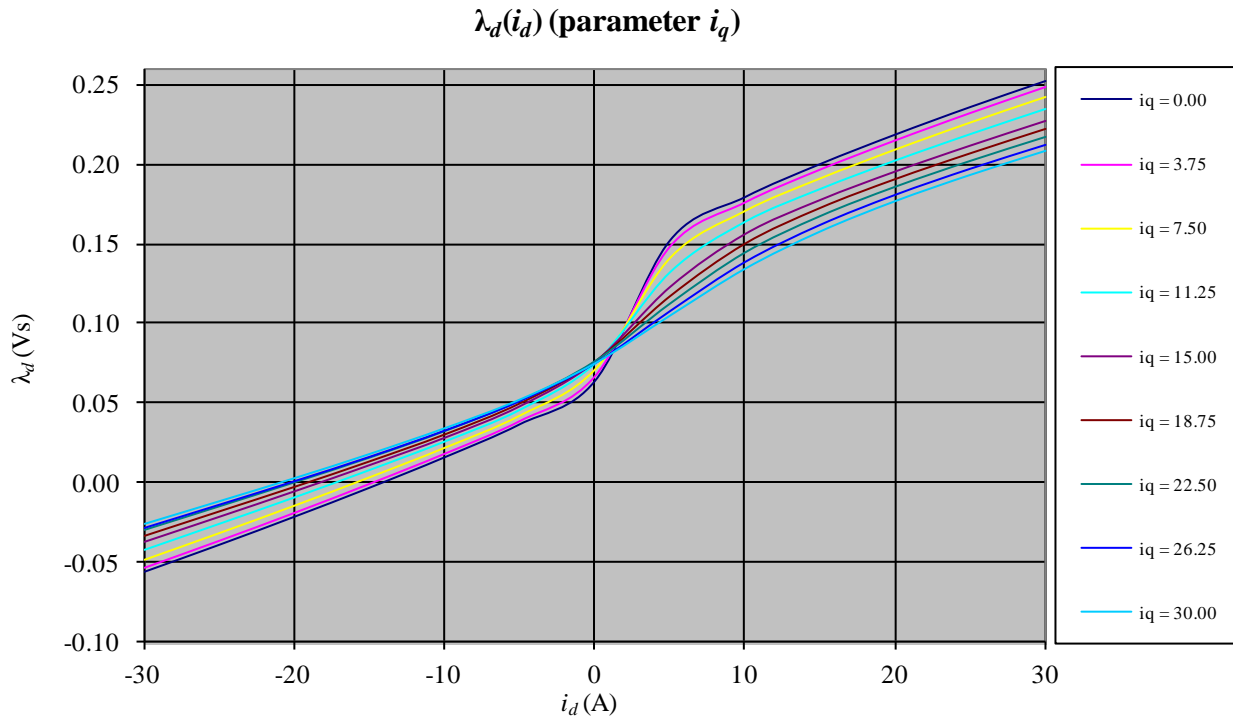
Fig. 4.11: *d*-axis flux as a function of i_d and i_q (4.30)
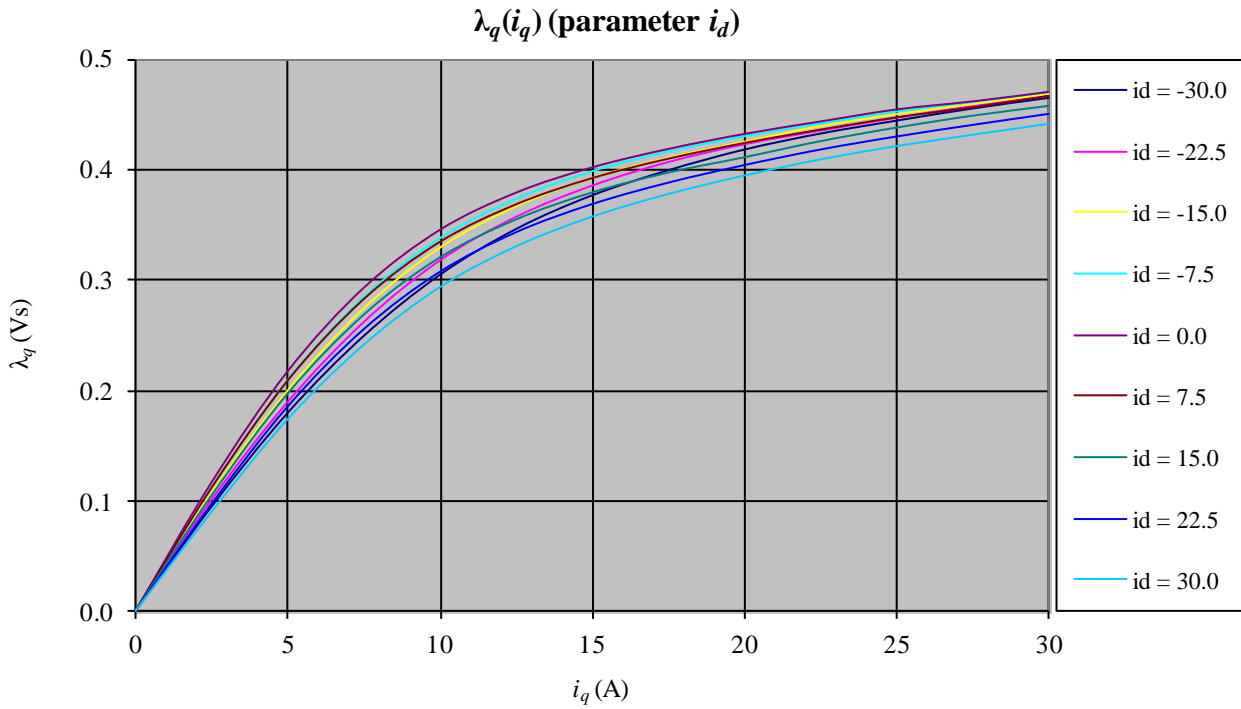
Fig. 4.12: q-axis flux as a function of i_q and i_d (4.30)

In Fig. 4.11, the effect of q-axis current is all too evident on the d-axis flux. The d-axis flux for maximum d-axis current varies by as much as 38% when there is maximum current in the q-axis compared to when i_q is zero. On the other hand, the q-axis magnetic characteristic tells a different story in Fig. 4.12. Here the effects of core saturation are far more significant than the cross-saturation. The curve shows typical ferromagnetic core behaviour in that the q-axis current saturates the core independent of whether there is a d-axis current or not. Nevertheless, the cross-saturation effect does exist and it is more evident in the linear region (i.e. when $i_q < 15$A) than in saturation ($i_q > 20$A).

The highly non-linear behaviour of the machine's magnetic model as highlighted by Fig. 4.11 and Fig. 4.12 not only affects flux estimation accuracy at low speeds (Fig. 4.10), it also has impact on the efficiency of control when the MTPA operation is required. This is discussed in the next section.

4.4.   Motor Characteristics – torque components and MTPA

From the torque equation (4.9), it can be noted that the torque produced by the machine is composed of two components that add up to give total torque. These torque components are called the magnet alignment (4.31) and reluctance (4.32) torque components, respectively.

$$T_{mag} = \frac{3}{2} p \lambda_m i_q \qquad (4.31)$$

$$T_{rel} = \frac{3}{2} p \left(L_d - L_q \right) i_q i_d = \frac{3}{2} p \Delta L i_q i_d \qquad (4.32)$$

Here ΔL is the inductance difference between the two axes. Whereas the magnet alignment torque is a function of q-axis current and the permanent magnet flux, which in turn also depends on temperature (Fig. 4.9), the reluctance torque, however, depends on both the d- and q-axis currents as well as on the inductance difference. The inductance of each axis is again a function of the current

in that axis (due to saturation) and in the orthogonal axis (due to cross-saturation). Comparing (4.5) and (4.32), it is evident that the reluctance torque is positive only for negative i_d values.

For maximizing the total torque for a given current magnitude i.e. the operation under MTPA condition, a current vector with suitable i_d and i_q values is required. The torque expression of (4.9) can be used for finding optimum current vector. However, since torque in (4.9) is expressed both in terms of d- and q-axis currents, the function can not be optimized for both at the same time, therefore a current vector with angle γ is defined as in Fig. 4.13. At a given current magnitude I, the value of angle γ is used as the optimization parameter, for which (4.9) must be derived in terms of γ.
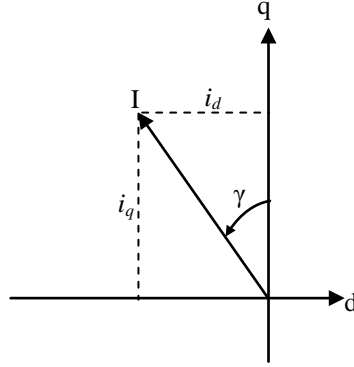
Fig. 4.13: Defining the current angle γ

From Fig. 4.13: $\qquad\qquad\qquad\qquad i_d = -I\,sin\,\gamma \quad \text{and} \quad i_q = I\,cos\,\gamma$

Substituting for i_d and i_q in (4.9):

$$T = \frac{3}{2}\,p\lambda_m I\,cos\,\gamma - \frac{3}{2}\,p\left(L_d - L_q\right)I^2\,sin\,\gamma\,cos\,\gamma$$

Rearranging:

$$T = \frac{3}{2}\,p\left[\lambda_m I\,cos\,\gamma - \left(L_d - L_q\right)I^2\,\frac{sin\,2\gamma}{2}\right]$$

Differentiating with respect to γ and equating the result to zero:

$$\frac{\partial T}{\partial \gamma} = \frac{\partial}{\partial \gamma}\left\{\frac{3}{2}\,p\left[\lambda_m I\,cos\,\gamma - \left(L_d - L_q\right)I^2\,\frac{sin\,2\gamma}{2}\right]\right\} = 0$$

$$\frac{3}{2}\,p\left[-\lambda_m I\,sin\,\gamma - \left(L_d - L_q\right)I^2\,cos\,2\gamma\right] = 0$$

➔ $\qquad\qquad\qquad\quad \lambda_m\,sin\,\gamma + \left(L_d - L_q\right)I\left(1 - 2\,sin^2\,\gamma\right) = 0$

$\Delta L = L_d - L_q$ from (4.32): $\qquad -2\Delta LI\,sin^2\,\gamma + \lambda_m\,sin\,\gamma + \Delta LI = 0$

Solving for $sin\gamma$: $\qquad\qquad sin\,\gamma = \dfrac{-\lambda_m \pm \sqrt{\lambda_m^2 + 8\Delta L^2 I^2}}{-4\Delta LI}$

➔ $\qquad\qquad\qquad\quad \gamma = sin^{-1}\left(\dfrac{-\lambda_m \pm \sqrt{\lambda_m^2 + 8\Delta L^2 I^2}}{-4\Delta LI}\right)$ $\qquad\qquad$ (4.33)

Fig. 4.14 shows two torque components for one of the test machines as a function of angle γ at a certain phase current magnitude and the total torque as well. For $\gamma < 0°$, the current i_d is positive (cf. Fig. 4.13) and the reluctance torque is opposite to the magnet alignment torque. The total torque with $i_d > 0$ is below the magnet alignment torque, thus it is not favourable to operate in $\gamma < 0°$ regime. On the other hand, with $\gamma > 0°$, the reluctance torque acts additively to the alignment torque giving more torque than that caused by magnets alone. Simultaneously, $i_d < 0$ is helpful in flux-weakening as the flux produced by the negative d-axis current is in direct opposition to the magnet flux (4.4) (see also Fig. 4.11).
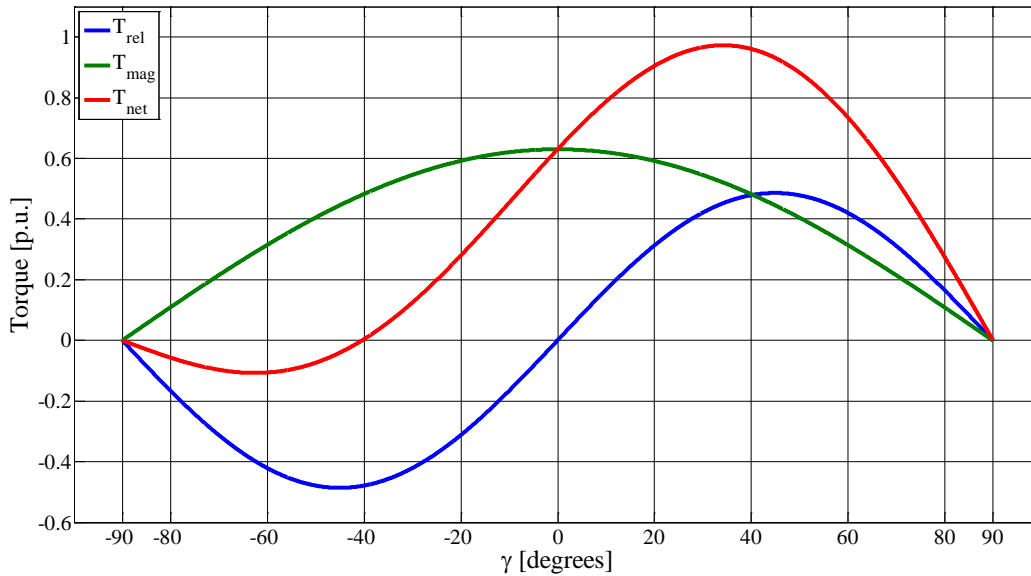
Fig. 4.14: Torque components as a function of γ at a constant current magnitude

Comparing Fig. 4.13 and Fig. 4.8, the relationship between γ and δ can be written as (4.34). The torque versus current angle plot of Fig. 4.14 can therefore be interpreted in terms of load angle δ and the condition for positive maximum torque as described by (4.29) can be readily verified in the graph of Fig. 4.14.

$$\gamma = \delta - 90° \tag{4.34}$$

The value of γ computed from (4.33) is valid for a given current magnitude I and it changes for other current values as shown in Fig. 4.15. So, it is imperative to calculate optimum current angle at the applied current vector. Apart from assuming constant permanent magnet flux, the expression (4.33) for γ assumes that the machine inductances do not vary with current, which is not true for most of the anisotropic-rotor machines including those employing permanent magnets. The machine's magnetization map changes with current because of non-idealities in the iron core used (cf. Fig. 4.11 and Fig. 4.12). In case of PM machines, the magnetic non-linearities are even more significant since the core is permanently magnetized by the magnets, sometimes to the extent of saturating it along the magnets' flux path. In the presence of PM flux, any current in the d-axis would either reinforce or nullify the flux along the d-axis (Fig. 4.11) that changes the d-axis inductance and hence ΔL. Therefore, the simplistic approach of (4.33) loses effectiveness. A more practical machine magnetic model is required that takes into account inductance variations with current to obtain true MTPA trajectory under varying machine magnetization state.

Fig. 4.16 shows machine torque as a function of d- and q-axis currents. These curves are obtained through the load tests of the machine. The motor is mechanically coupled to a prime mover that sets the shaft speed. A torque sensor is installed on the shaft connecting the two

machines. A current magnitude is selected for which the angle γ is varied to obtain i_d and i_q (Fig. 4.13). The angle at which the produced torque is maximum for that particular current magnitude is the MTPA angle (see Fig. 4.18 blue curve) and the pair of values (i_d, i_q) define the optimum current vector in the dq-plane. Fig. 4.16 shows the torque as a function of individual dq currents. It should be noted that the d-axis current is negative and its absolute value is shown in Fig. 4.16. For i_d and i_q values intermediate to the data points shown in Fig. 4.16, quadratic interpolation can be used to get maximum torque with minimum phase current. The three-dimensional area plot of Fig. 4.17 shows torque as a function of both i_d and i_q and it illustrates the intermediate points as well. Fig. 4.18 gives a comparison of γ values for MTPA obtained experimentally with the ones calculated analytically using (4.33) that assumes constant ΔL.
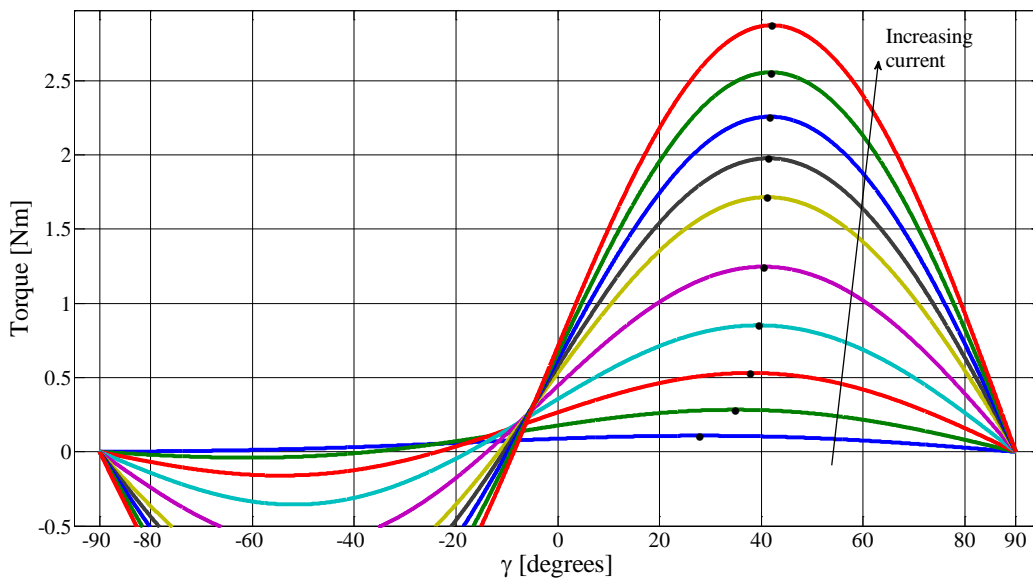
Fig. 4.15: Total torque as a function of γ at various current magnitudes for a machine used in tests: MTPA points are marked
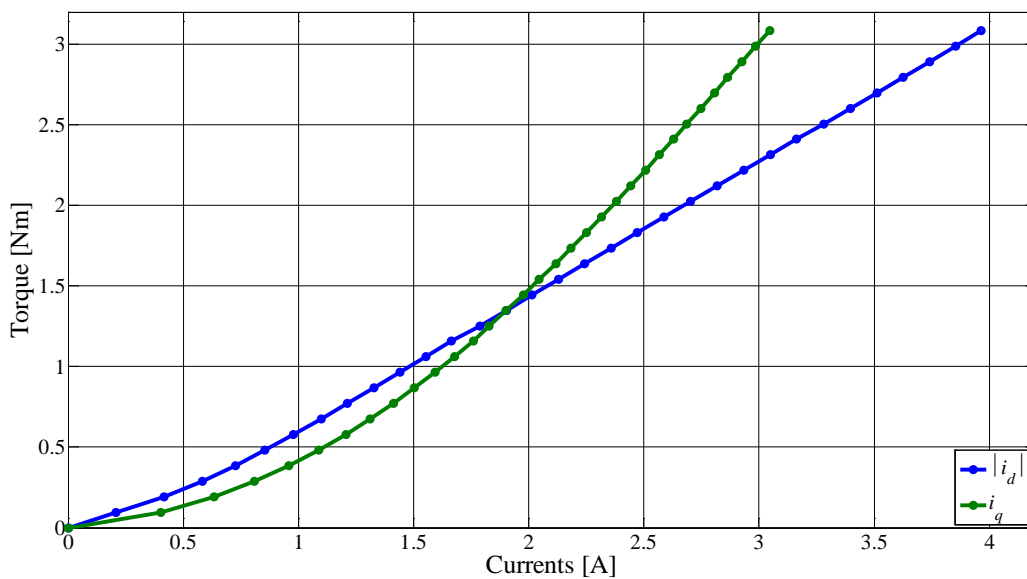
Fig. 4.16: Optimum d- and q-axis currents for maximum torque per ampere obtained experimentally through load tests of the machine conducted on the test bench (note: the d-axis current is negative and its modulus is plotted here)

116
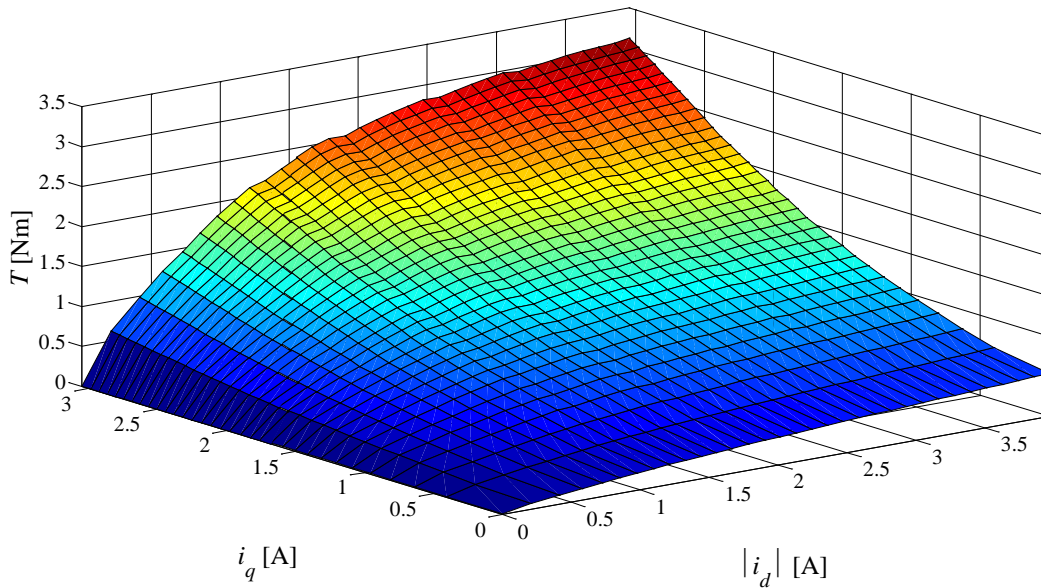
Fig. 4.17: Maximum torque as a simultaneous function of *d*- and *q*-axis currents
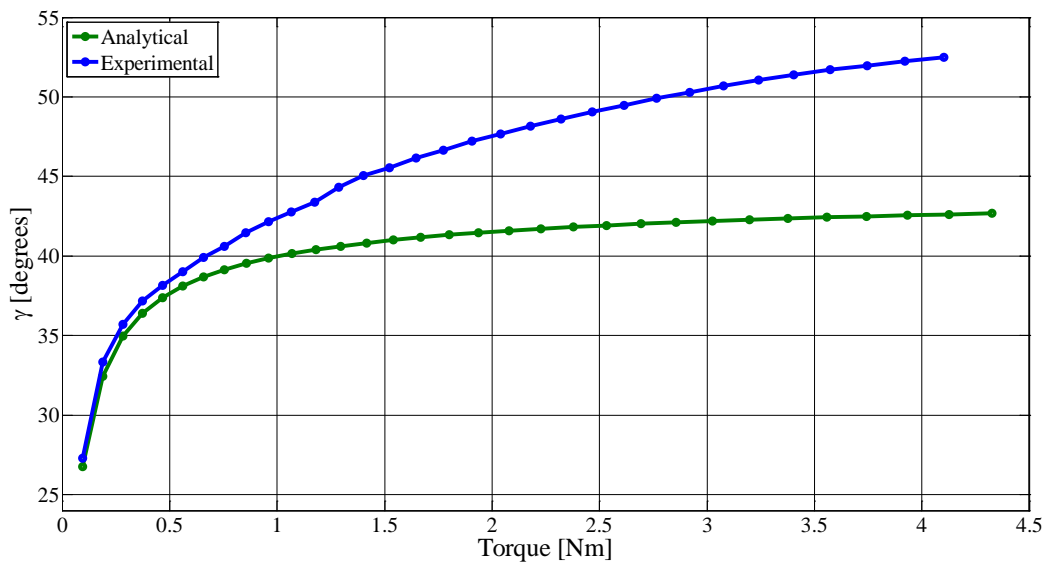
Fig. 4.18: Angle γ as a function of produced torque for maximum torque per ampere – analytical: computed with (4.33) assuming constant Δ*L*, experimental: obtained through load tests of the machine similar to Fig. 4.16

The inductance variation due to current is shown in Fig. 4.19 for both *d*- and *q*-axis. The *d*- and *q*-axis currents at which these inductances are calculated are the MTPA current values for the respective axes as shown in Fig. 4.16. It should be noted that the inductances are affected both by self-axis as well as cross-axis current, this phenomenon is known as the cross-saturation effects in magnetically anisotropic machines [140, 141]. The cross-saturation effects render the expression (4.33) useless in practical situations when machine saliency is a function of current in the two orthogonal axes. Fig. 4.20 shows how Δ*L* behaves with respect to the total phase current when the current angle γ is the MTPA value (Fig. 4.18 blue curve). A Δ*L* variation of as much as 40% can be seen in the curve of Fig. 4.20. This variation directly affects the optimum current angle for maximum torque and explains the deviation between analytical and experimental values of Fig. 4.18.
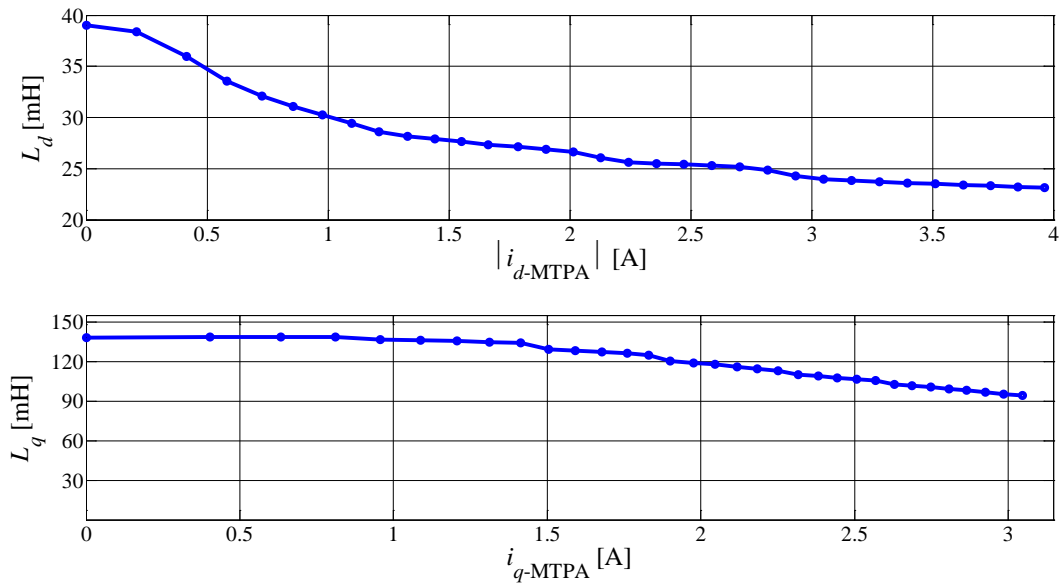
Fig. 4.19: Inductance variation with current magnitude (observed experimentally): *d*-axis (top), *q*-axis (bottom)
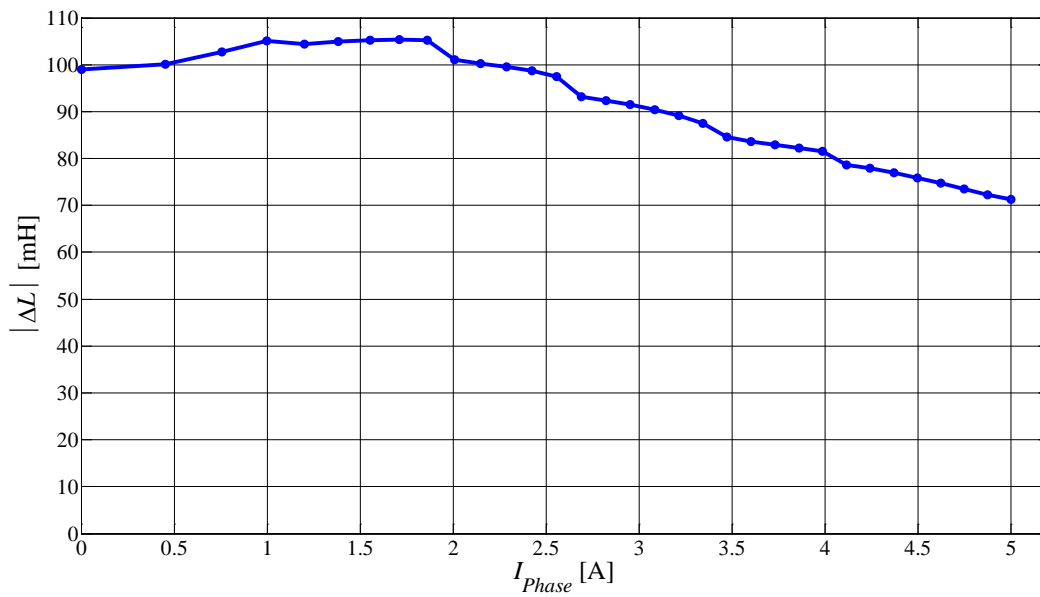
Fig. 4.20: ΔL as a function of phase current from experimentally observed data

Having noted the shortcomings of treating inductances constant over current in Fig. 4.18, it is imperative that the effects shown in Fig. 4.19 and Fig. 4.20 be appropriately taken care of while optimizing machine control. It is worth mentioning here that the experimentally computed values of γ for maximum torque inherently take care of the inductance variations with current since the torque produced by the machine and measured at the shaft is in that particular magnetization state of the machine.

4.5.   Rotor construction – variants

An IPM differs from other permanent magnet ac motors in the construction of its rotor. The electrical and magnetic characteristics of the machine depend largely on rotor geometry. The most important parameters that the rotor geometry affects are saliency and flux-weakening capability of the machine. Apart from designs for general purpose applications like the ones presented in

Fig. 4.1, other rotor geometries can be employed to serve the purpose of particular application at hand. The literature reports various application-specific rotor designs (e.g. the Integrated Starter Alternator (ISA) motor [142]). Fig. 4.21 reports another set of rotor structures proposed for reducing the cogging torque of the machine [143].

Fig. 4.21: Various rotor designs [143]

The rotor saliency as defined above as the ratio of q-axis to d-axis inductance is a measure of how closely the permanent magnet machine resembles a synchronous reluctance machine that is magnet-less. It also decides the contribution of the reluctance torque in the total torque produced by the machine (4.32). Apart from rotor design, the saliency also depends on the type of stator winding employed (namely distributed or concentrated, cf. Fig. 4.1). For a given winding type, the rotor saliency plays an important role in the machine's torque production and, with concentrated winding, on field-weakening operation. The saliency is controlled by changing the magnet area and disposition inside the rotor. In Fig. 4.22, in which two rotors with different number of flux barriers interposed between magnets are shown, the saliency ratio for the four-barrier rotor is greater than that of the three-barrier one [144].
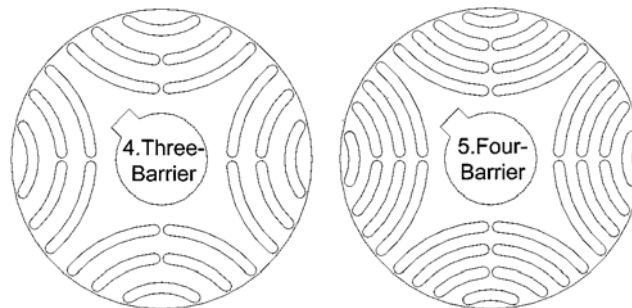
Fig. 4.22: Rotor design with flux barriers [144]

Fig. 4.23 and Fig. 4.24 show stator assembly and rotor structure of two of the machines used for tests in this thesis, the rotor of a third machine is not shown for reasons of confidentiality.
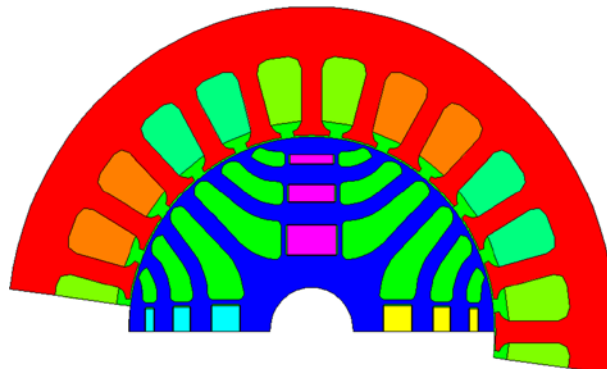
Fig. 4.23: A four-pole machine with three-barrier rotor and permanent magnets [90]
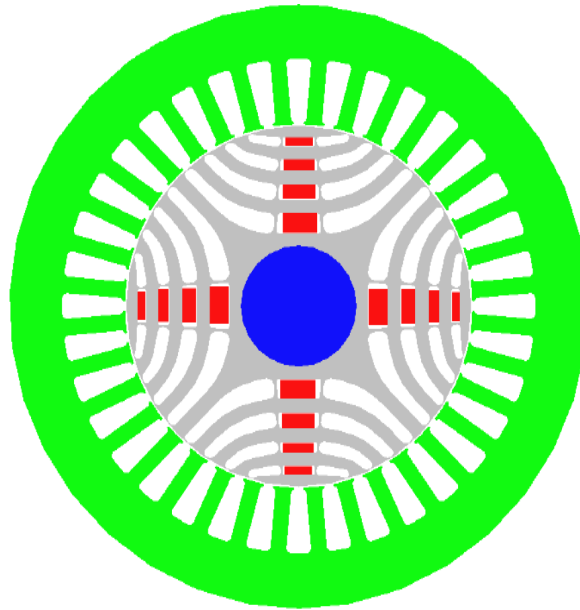
Fig. 4.24: A four-pole machine with four-barrier rotor and permanent magnets [145]

4.6.   **A word on saliency and flux–weakening**

Compared to isotropic rotor permanent magnet synchronous machines such an SPMSM discussed in the next chapter that have no or negligible saliency, the machines such as an IPM under discussion here have an additional torque component due to anisotropic structure of the rotor (4.9). This surplus torque makes the IPM resemble, and acquire characteristics of, a synchronous reluctance (SynchRel) machine. An IPM is thus a hybrid of SPMSM and SynchRel in that it has both magnet alignment and reluctance torque components. This fact is also stated by (4.29) by showing that the load angle for maximum torque of an IPM lies between that of an SPMSM (4.28) and a SynchRel (4.27).

In the machine design phase, the size (and hence volume) of permanent magnets is reduced due to high cost and the total machine torque is optimized between magnets and reluctance torque as a function of cost. This renders reluctance torque component more important than just a surplus. However, for maximizing the reluctance torque it is not enough to just have a high L_q-over- L_d ratio, which, nevertheless, is important for improving power factor. The difference between the two axes' inductances should be high to give maximum reluctance torque as it is the difference ΔL that appears in the reluctance torque expression (4.32).

To obtain high ΔL, either L_q be increased or L_d be decreased. L_q can be increased by increasing the ferromagnetic material along the q-axis (Fig. 4.4); however, this would reduce the area left in the rotor for the magnets. The other way is to lower L_d by either saturating the core through higher PM flux linkage (cost rises) or by introducing more flux barriers (Fig. 4.22). More flux barriers means less volume of permanent magnets and hence reduced magnet alignment torque.

Lowering L_d comes with another operational inconvenience in that the flux-weakening capability of the machine is drastically affected if L_d is reduced too much. The flux-weakening capability of the machine allows constant power operation (Fig. 4.26) which is essential in most applications. At high operating speeds when the machine back-emf increases to the extent that it approaches the maximum phase voltage that can be applied through the inverter with the available dc-link voltage, the machine flux needs to be reduced to allow controlled operation at those speeds. For the permanent magnet machines, the permanent magnet flux needs to be countered by injecting appropriate d-axis current. The flux due to this current is dependent on inductance L_d.

In the context of flux-weakening, the machine characteristic current is defined as the d-axis current at which the total d-axis flux reduces to zero. This condition can be written mathematically from (4.4) as in (4.35). The machine is said to be capable of constant power operation at infinite speed if this characteristic current is less than or equal to the rated phase current of the machine. From Fig. 4.25 that shows the d-axis magnetic characteristics of one of the tests machines, it can be noted that the current at which the total d-axis flux (λ_d) approaches zero is about half the rated machine current of 5A, thus this machine is capable of operating at literally infinite speed at constant power. The maximum speed in this case is limited by mechanical constraints.

$$\lambda_d = L_d i_d + \lambda_m = 0$$

$$i_d = i_{char} = -\frac{\lambda_m}{L_d} \tag{4.35}$$

$\lambda_d(i_d)$ (parameter i_q)
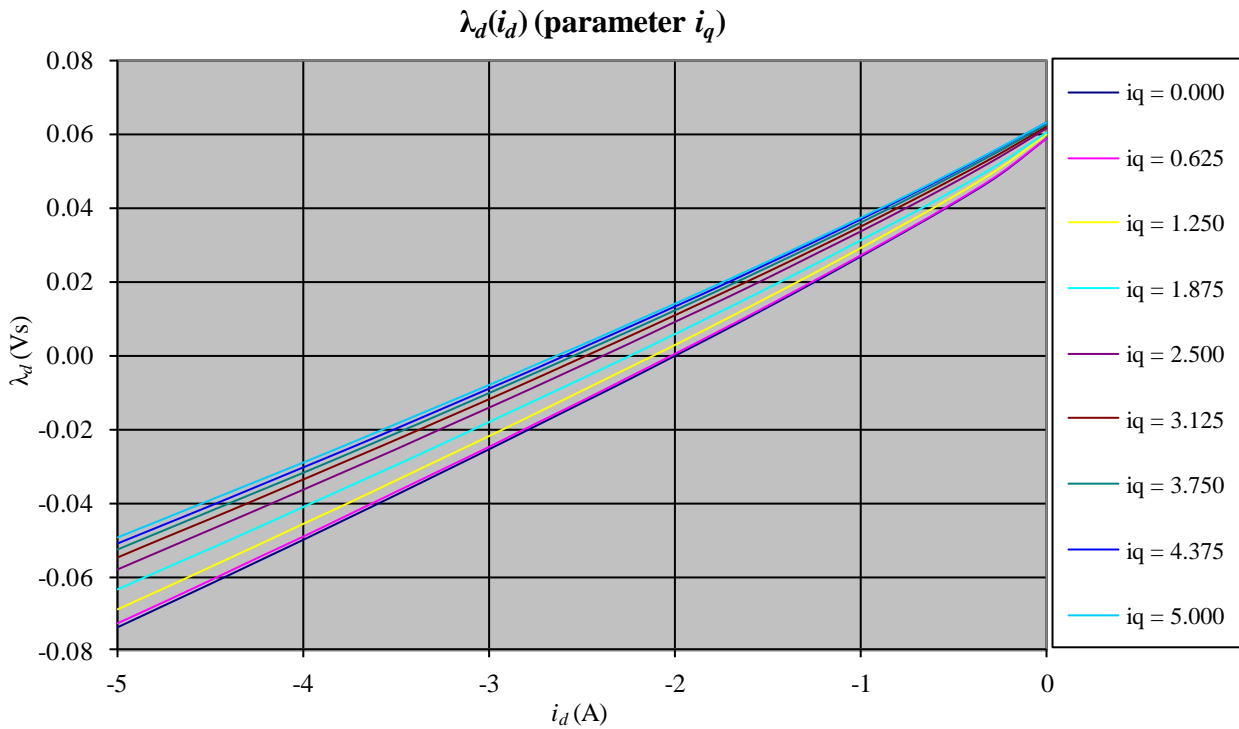
Fig. 4.25: d-axis flux as a function of i_d at various i_q values

It is again evident from Fig. 4.25 that the cross-axis current (i_q here) plays an important role in deciding the magnitude of i_d that is required to bring the d-axis flux down to zero for ideal flux-weakening. As the current i_q rises, more i_d is needed to reduce d-axis flux to zero, i.e. the effect of cross-axis current adversely affects flux-weakening capability. Additionally, more i_d entails more copper losses in the stator that would deteriorate efficiency. The same is true for the second machine whose d-axis characteristics are shown in Fig. 4.11.

Since the characteristic current as given by (4.35) is inversely proportional to L_d, reducing L_d beyond L_d' (4.36) would penalize the flux-weakening performance and limit the maximum achievable speed at constant power.

$$i_{char} = I_{rated} = \left| \frac{\lambda_m}{L_d'} \right| \tag{4.36}$$

Besides affecting the flux-weakening performance through modifying the characteristic current, the d-axis inductance also influences machine behaviour following a fault. Under three-phase short-circuit fault conditions, the short-circuit current is limited in part by the inductance L_d. For this reason a high L_d is desirable; in fact machine design with the permanent magnet flux to L_d ratio under 1.0 is often desired for reducing stresses on the power semiconductor switches should a fault occur [146]. Additionally, the ratio λ_m-to-L_d has a vital impact during the so-called 'uncontrolled generator operation' which is an anomalous condition following a fault when the inverter switches lock open and the machine keeps rotating due to inertia [147]. Having permanent magnets producing the necessary rotating magnetic field, the machine acts as a generator. In this condition, the freewheeling diodes of the inverter work as uncontrolled rectifiers and the voltage at the machine terminals may charge the dc-link capacitors to dangerously high voltages. [147] has shown that the machines with λ_m-to-L_d ratio lower than unity are less perilous for the inverter switches as well as the dc-link capacitors.

Thus, it is important to take into account all the aspects of application at hand, including maximum speed requirement and available dc-link voltage while designing the machine. This makes the machine design process dependent on the parameters external to the motor and the load.

In the constant power regime (Fig. 4.26) when the shaft torque decreases linearly with the rotor speed, because the total flux is reduced to contain the back-emf within the inverter limits, the induction machine bids well compared to the machines employing permanent magnets. Since in the induction machine the flux reduction comes with lower phase current and hence copper losses, in the permanent magnet machines, however, the flux-weakening involves injecting additional current to counter the PM flux, this increases the copper losses in the stator. Therefore, in the field-weakening regime the induction machine gives superior efficiency compared to PM machines, but at the cost of over-sizing of the inverter (low power factor).

The speed at which flux-weakening begins is marked ω_{base} in Fig. 4.26 which is roughly the rated machine speed at which the back-emf is slightly below the available dc-link voltage (translated into phase value). The flux-weakening capability of the motor-drive system is often described as the ratio between maximum achievable speed to base speed (e.g. 3:1 as in Fig. 4.26).
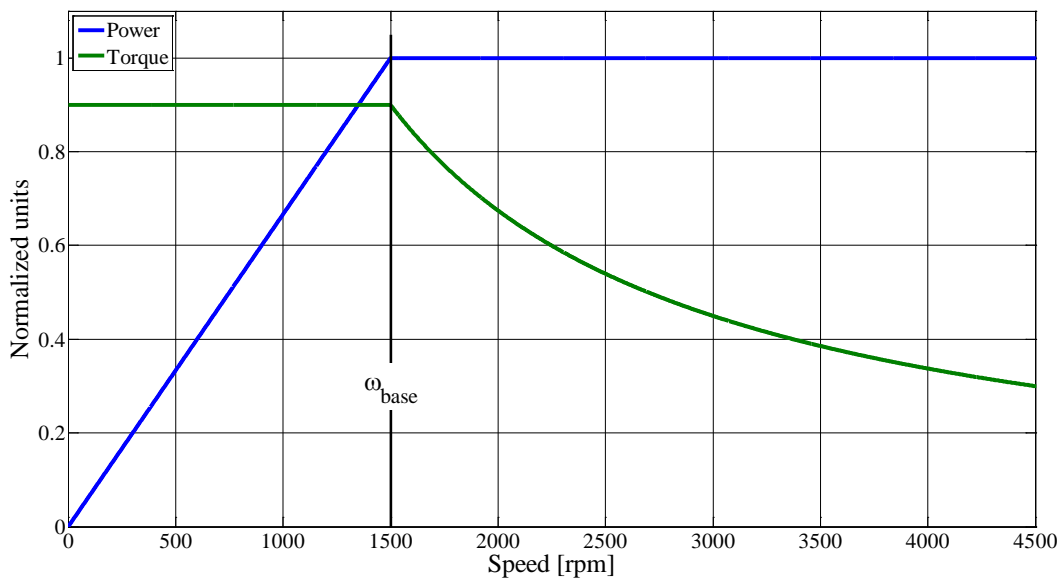
Fig. 4.26: Power and torque profile up to and beyond base speed (ω_{base})

In the flux-weakening region, it is no longer possible to maintain optimum current angle γ (of Fig. 4.18) for MTPA operation since the d-axis current must be controlled so as to reduce the

total d-axis flux. Here the maximum realizable torque depends on the available dc-link voltage thus the maximum torque per volt (MTPV) operation is needed. The machine load angle as defined in Fig. 4.8 can be kept to an optimum value so as to give maximum torque per volt of available dc-link voltage in the flux-weakening region of operation.

For the unified direct flux vector control of section 4.3.2, the factor b defined by (4.21) decides the stability of the q-axis control as seen in the state equations (4.23). The control for i_q^s is stable only if $b > 0$. At the same time, by comparing (4.25) with (4.21) it can be deduced that $b = 0$ is a condition for maximum torque. Thus $b = 0$ is the boundary for control stability and maximum torque under any operating conditions including, of course, the flux-weakening regime [148].

In the flux-weakening region, therefore, the MTPV condition overrides the MTPA condition and the current angle γ is not as given by (4.33) or Fig. 4.18 but it is determined by using (4.34) from the maximum load angle. The load angle and hence the current angle that give maximum torque in the flux-weakening region, i.e. above base speed, again depends on the machine saliency [120].

4.7.   Identification techniques

Having emphasised, as above, the dependence of control stability, efficiency, performance and safety (under faults) on the machine parameters and operating conditions (load, speed, and temperature), the machine parameter identification techniques are now explored. An IPM motor drive is no different from other drives when it comes to the need of the knowledge of machine parameters under actual machine operating and ambient conditions. As with other drives, the parameter identification of IPM motor drives had been the focus of numerous researchers and a number of algorithms and techniques have been developed and put forward. The available identification techniques can be categorized in the two main categories as standstill identification techniques and identification methods for a running machine. These are briefly investigated below.

4.7.1. Standstill identification

The methods that fall in this category observe and analyse the response of the machine to various injected signals called *stimuli*. Being able to be described through basic elements such as resistance and inductance (Fig. 4.2), the machine's response to the injected signals gives numerical values for the parameters shown in Fig. 4.5 and Fig. 4.6.

The stimulus (injected signal) can be generated either through a dedicated signal generator or through the inverter used for supplying the machine during normal operation. [87] has proposed machine testing through signals of various frequencies generated through a power amplifier, the authors call the method as broadband excitation. Starting from frequencies as low as 10 Hz, the machine is injected with frequencies up to 1200 Hz with a 10 Hz step. The measured voltage and current values are used to calculate impedance at all frequencies. The impedance is then used to estimate resistance and inductance of the axis (d or q) in which the signal is applied. Three different signal types have been analysed, vis-à-vis, multisine with flat amplitude, multisine with increasing harmonic amplitude, and swept multisine signal. The saturation and cross-saturation effects have been studied with the same method. However, with the necessity of additional (and special) power amplifier, the method fares less to be considered for self-commissioning of the drive system which is the raison d'être of the work undertaken in this thesis.

The test signals generated using the power converter respect the constraints imposed by the definition of self-commissioning. [84, 93] use the inverter to excite the machine for parameter estimation. While [84] considers a detailed machine model by including the d- and q-axis damper windings to create a state-space model, [93] uses the simple dq-axes models of Fig. 4.5 and Fig. 4.6. In [84], a step input is applied to the machine at standstill and the output is measured. At the same time, an estimate of the output is also generated from the state-space model initialized with an

initial 'guess' of parameters. The measured and estimated outputs are used in output-error (OE) estimation strategy of system identification theory to estimate parameters. Though the method does give parameters values satisfactorily, it needs to be initialized with an estimate of parameters and the authors propose that the initial parameters can be obtained from the motor design data, this may be a limitation on the use of this method as the design data is hard to obtain more often than not.

The method described in [93] adopts the strategy of applying a square-wave voltage pulse in self-axis and constant current in the orthogonal axis to traverse the entire range of machine operating region for analysing the effects of cross saturation. From the measured machine current and estimated flux, the flux-current curves are constructed, thus giving estimates of machine parameters with and without cross-saturation. However, it has not been described how the voltage is recorded (whether at machine terminals or at controller output), it is not clear whether inverter non-linearity effects are taken into account or not. If not considered, these may adversely affect the results at low test current (e.g. 2.5 A) and voltage (e.g. 25 V) levels. If the voltage is measured at machine terminals using additional voltage measurement system, then the method does not fit well in the definition of self-commissioning. Furthermore, the intermediate results for d-axis tests are not given which are more important since the permanent magnets are aligned to the d-axis (Fig. 4.4). Besides, the rotor blocking cannot be ruled out if the voltage pulses are applied in the q-axis as it would cause severe vibrations given the shape of the pulse proposed.

The d-axis inductance of the machine is identified at standstill through a multi-sinusoidal signal in [149]. DC-bias is first used to bring the machine magnetizing state to a level where the inductance is required and the multiple-frequency signal is superimposed onto this constant current. The self-axis saturation effects are verified by varying the dc-bias. The method however does not take into account the cross-magnetizing saturation effects arriving from the q-axis.

4.7.2. Identification for a 'running' machine

The subject of parameter estimation with machine rotating at a certain speed is studied at length by various authors. The flux estimate from voltage equations is used by [89] to give an estimate of motor inductances. It is noted that the knowledge of flux is sufficient to control the machine without going further into identification of L_d and L_q. It is claimed that the estimation is not influenced by the machine space harmonics as it takes into account the voltage at stator terminals that, for a sinusoidal current, contains all the harmonic distortions within itself. The stator voltage is first filtered then transformed using Fast Fourier Transform (FFT) to obtain fundamental voltage, the current is obtained in a similar fashion and flux is estimated. The method requires that the rotor position be known at all times. The method would not work, however, below a certain speed due to insufficient back-emf to estimate flux. Also, in simulation it is observed that if the machine is operated at no-load, the voltage and current magnitudes are too small to give a better signal-to-noise ratio for reliable flux estimates. This technique requires stator terminal voltage measurement facility and post-processing of measured data.

Motor parameters' identification for high speed flux-weakening has been taken up by [99]. Torque angle perturbation techniques have been used to identify L_d, L_q, R_c, and E_o (where R_c and E_o are, respectively, core-loss resistance and back-emf). The voltage and current values obtained at two different operating points (with a small perturbation of 0.1° in torque angle) are used to calculate parameters.

It can be noted, again, that the method works for a certain speed below which it is not possible to estimate parameters. Besides, the machine needs to be appropriately loaded so that the torque angle perturbation gives reliable results. It is not clear, however, why there is a need of inductances at high speed when flux can be accurately estimated at those speeds (from voltage integration, Fig. 4.10) and can directly be incorporated in torque equation for optimum control.

Machine state-space model is used by [94] for correct parameter identification in a given operating condition. A number of input-output pairs of values are taken which are then subjected to a quadratic error minimization criterion. The method is shown to have converged to correct parameter values within first 10 to 20 iterations. However, it is necessary to initialize the algorithm with a rough estimate of parameter values. Furthermore, it has not been commented if the algorithm works even with machine heavily saturated, in which case the model becomes non-linear and this non-linearity needs to be taken into account.

Sensorless control based on EEMF (Extended Electromotive Force) model of the machine is discussed and parameters are identified in [104]. The method is again based on system identification theory using least squares optimization algorithm. The interesting aspect to note is that it is shown that the parameters' estimation does not depend on rotor position and speed. It is done by manipulation of matrices. The results for an IPM show that the resistance is not identified properly for changing load conditions and this drawback has been attributed to various factors, such as: motor non-linearity which is disregarded in model, *dq*-axes' mutual inductances, saturation, and core losses. Under changing load conditions, it is observed that the parameters change. The changing parameters include the stator resistance as well that heavily affects the position estimation (given that the control is sensorless).

Online parameter identification with multi-model approach is proposed dealt with in [105]. Separate machine models are used for motor control and parameters identification, thus the name multi-model. A machine with non-sinusoidal back-emf waveform is considered and therefore extended Park's transformation is used in the model to take into account all the space harmonics that, if neglected, render the identified parameters inaccurate. The model used for control is based on de-normalized extended Park's transformation. Recursive Least Squares (RLS) algorithm is used to identify parameters. For this RLS based method to converge satisfactorily, however, the value of *forgetting factor* should be carefully chosen. This method fails below a certain speed which is a concern if the drive is for position control in actuators where rated speed is hardly ever reached due to intermittent operation.

An improvement over the load test method of parameter estimation is discussed in [95] using regression and neural networks. Current and voltage samples are recorded which are then processed to give the best linear regression on all the inputs. Parameters are determined from the steady state motor equations. The parameter results are then compared with Finite Elements Method (FEM) simulations and it is shown that the results concord. However, a large number of samples are required to give accurate results (on the order of 2000 samples), this may be a limitation on drives having no or scarce on-board memory available.

Of all the methods investigated above for parameter identification of IPM machines, none fits the definition of self-commissioning as followed in this thesis. The methods discussed in section 4.7.1 either require additional test equipment or need rotor mechanical blocking for identifying machine parameters. On the other hand, the identifications techniques discussed under the heading of "Identification for a 'running' machine" clearly stretch out of the bounds imposed by the definition of self-commissioning in that the machine must always be free to rotate. Therefore, a new method of machine parameter identification is proposed here that neither requires additional test equipment nor imposes any mechanical precondition on the machine operation.

4.8.   <u>Self-commissioning with high frequency injection</u>

The method of high frequency injection for parameter identification is proposed in this thesis. The closed-loop current controllers are used to inject currents of pre-determined magnitudes and frequencies to determine machine electrical parameters. The test signals are generated through the inverter supplying the machine and the measurements available in the standard drive hardware are used without necessity of special sensors. The closed-loop current control ensures safe testing

and avoids exposing the machine to damagingly high voltages and currents. The theoretical basis and practical implementation issues are discussed in the following sections.

The d- and q-axis equivalent circuits of the machine shown in Fig. 4.5 and Fig. 4.6 respectively, in the dq rotating reference frame fixed with the rotor north pole, transform to simple series RL circuits if the rotor is at standstill (i.e. $\omega_r = 0$). Fig. 4.27 shows the resultant circuit which is valid for d-axis as well as for the q-axis. The number of parameters to be determined to describe the machine at standstill reduces to three: the stator resistance R_s, the d-axis inductance L_d and the q-axis inductance L_q. The fourth unknown parameter i.e. the permanent magnet flux λ_m disappears (at least for now).
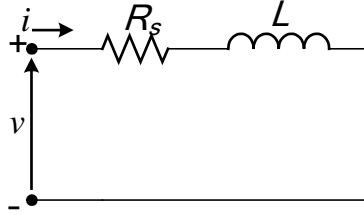
Fig. 4.27: Equivalent circuit at rotor standstill (valid for both d and q axes)

If a sinusoidal current of known magnitude and frequency is injected along the d-axis, while keeping current in the q-axis to zero, the machine terminal voltage can be written in phasor notation as in (4.37) where Z_d is the impedance of the d-axis. At the same time the rotor continues to be stationary for the absence of q-axis current means no torque is generated (4.9). However, the machine terminal voltage is not always the measured quantity in a standard drive setting. In this case, the controller output voltage can be used in equation (4.37) by appropriately taking care of the inverter non-linearity effects, if the inverter identification look--up tables are available.

$$\overline{V}_d = \overline{Z}_d \overline{I}_d \tag{4.37}$$

Similar equation results in the q-axis (4.38) when the injection is in the q-axis. However, the current must be zero-centred with sufficiently high frequency such that the net torque on the rotor is zero and the stationary conditions preserve.

$$\overline{V}_q = \overline{Z}_q \overline{I}_q \tag{4.38}$$

High frequency signal injection in permanent magnet machines is common in practice as it is used for rotor position estimation for sensorless control or for initial rotor position estimation [106, 150-153]. Here it is used for estimating the machine parameters given that the rotor position is known.

The impedance as expressed in (4.37) and (4.38) and obtained through (4.39) consists of real and imaginary terms with real being the resistive term and imaginary, the inductive reactance. The two terms can only be separated if the phase angle φ between voltage and current vectors is known; the angle is defined in Fig. 4.28.

$$\overline{Z} = \frac{\overline{V}}{\overline{I}} = \frac{|\overline{V}|}{|\overline{I}|} \angle \varphi \tag{4.39}$$

Referring to Fig. 4.28, the resistance and inductive reactance in terms of impedance and phase angle can be written as in (4.40) and (4.41), respectively. Then, using the definition of

inductive reactance, the inductance in the *d*- or *q*-axis can be recovered from the known injection frequency *f* and (4.42).
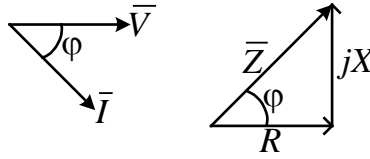
Fig. 4.28: Phase angle between current and voltage vector is the same as impedance angle

$$R_s = |\overline{Z}|\cos\varphi \tag{4.40}$$

$$X = |\overline{Z}|\sin\varphi \tag{4.41}$$

$$L = \frac{X}{2\pi f} \tag{4.42}$$

As said above, the injection frequency must be high enough so as not to cause any rotor movement when the current injection is in the *q*-axis. Although the absence of *d*-axis current will ensure that there is no reluctance torque (4.32), the magnet alignment torque (4.31) due to *q*-axis injection may cause rotor rotation or vibration in case the injection frequency is low. However, as the test signals are generated through the inverter, the upper limit on the injection frequency is imposed by the inverter switching frequency. A good rule of thumb to determine the highest injection frequency is to make sure that one cycle of the injected wave contains at least 12 switching periods. For instance, if the inverter switching frequency is 20 kHz the injection frequency should not exceed 1.67 kHz.

The choice of injection frequency is very important in that if the injection frequency is too low, the frequency dependent imaginary component of the voltage in (4.37) and (4.38) may not be sufficient enough to give reliable results. However, if the injection frequency is too high, skin effect of the conductors weighs in to alter resistance and hence displace the test results from normal operating conditions of the machine. For this reason, the injected frequency is kept around nominal operating frequency of the machine. Tests at machine operating frequency resemble single-phase testing, however, in single-phase tests a nominal frequency voltage is applied in one of the phases regardless of rotor position; with high-frequency current injection in *d*-axis as proposed here, the rotor position is taken into account so that the impedance seen by the injected current is precisely the *d*-axis impedance; the same is true for the *q*-axis.

In the absence of actual machine terminal voltage, the controller output voltage is used in equations (4.37) and (4.38) to compute the impedance of respective axis. This controller output voltage, along with machine impedance drops, also contains the inverter switches' resistive drops and inverter blanking time effects that must be compensated for before using the voltage for impedance computation. The inverter non-linearity effects are removed here from the inverter identification tables generated through the inverter self-commissioning procedure outlined in [115].

For high frequency injection, simple PI controllers as discussed in chapter 3 do not give optimum performance as they require very high bandwidth for high frequency injection. A resonant term added to the standard PI controller enhances the control and fits well the requirements of high frequency injection. The resonant frequency of the controller is set as the injection frequency. The ideal controller transfer function in the frequency domain is given by (4.43), where k_{res} is the controller gain and ω_o is the resonant frequency. However, for practical considerations, a damping factor of ζ is usually added as in (4.44) to shave the peak of the controller response. Fig. 4.29 shows Bode plot of controller response with and without damping.

$$H_{Res} = 2k_{res} \frac{s}{s^2 + \omega_\circ^2} \tag{4.43}$$

$$H_{Res} = 2k_{res} \frac{s}{s^2 + 2\zeta\omega + \omega_\circ^2} \tag{4.44}$$
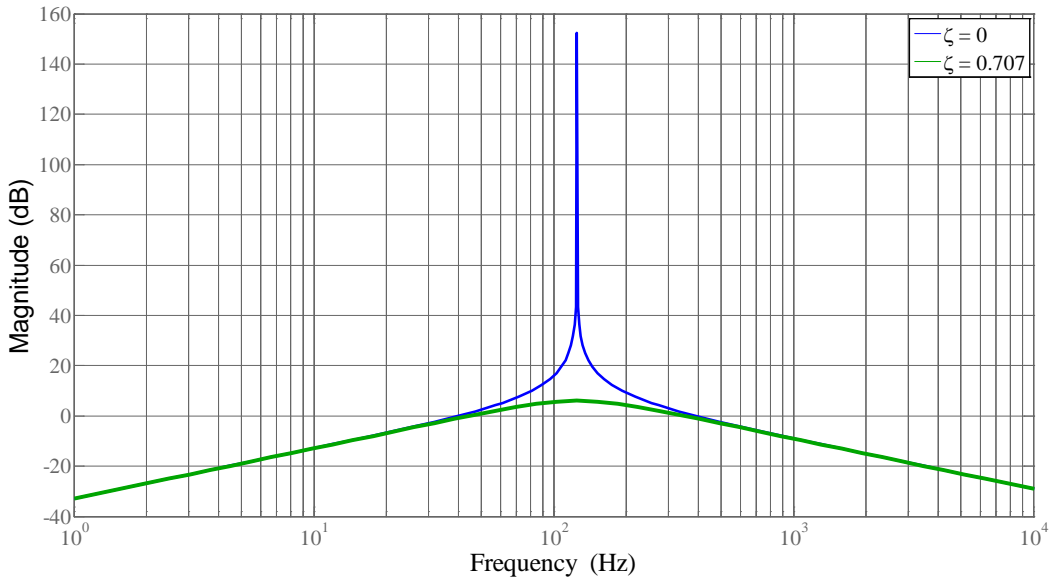
Fig. 4.29: Resonant controller response with and without damping

Fig. 4.30 shows system block diagram for high-frequency injection. Accurate rotor position information is important for injection correct *d-* and *q*-axis. In case the rotor position sensor is not mounted, the initial rotor position estimation algorithms must be implemented to establish the *dq*-axes as per Fig. 4.4 before conducting the tests. Incorrectly aligned *dq*-axes give results that cannot be used for correct identification. Fig. 4.31 shows the experimental test rig for one of the test machines.
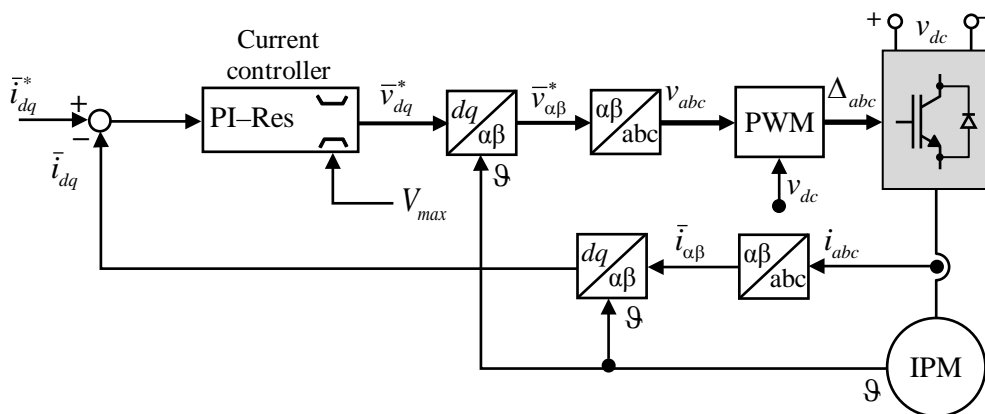
Fig. 4.30: System block diagram for tests with high frequency injection through PI resonant controllers
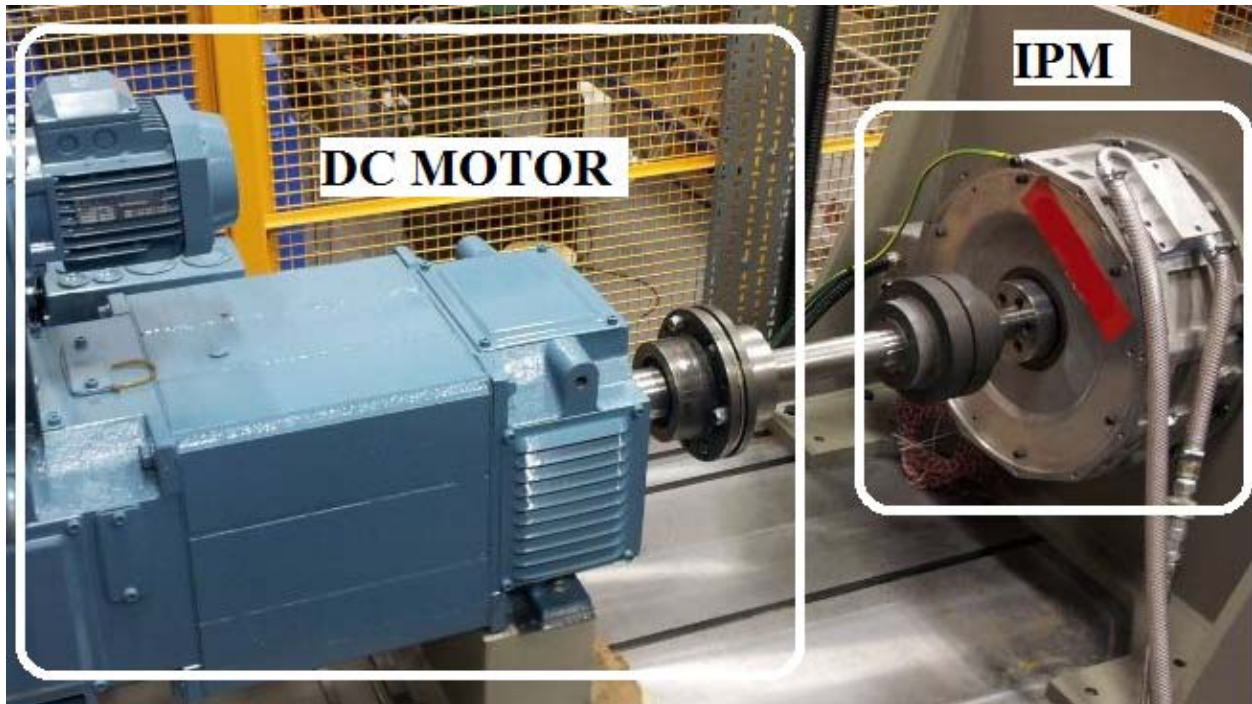
Fig. 4.31: Test bench for one of the test machines: a 30kW traction motor prototype

Fig. 4.32 shows high frequency current injection in *d*-axis of one of the test machines. The current controller used is the PI controller enhanced with resonant term (cf. Fig. 4.30). It can be seen that the controller output voltage is not perfectly sinusoidal for sinusoidal current. Here, the inverter error compensation is disabled at first to show the voltage distortions due to inverter non-linearities. The disturbances in the controller output voltage are more significant especially during current zero crossings as the inverter effects are maximum at these points. Fig. 4.33 illustrates various harmonics present in the controller output voltage. Discrete Fourier Transform (DFT) is used to extract these harmonics. The odd harmonics seen in Fig. 4.33 (also in Fig. 4.35) are caused by inverter non-linearity effects. Injection results along the *q*-axis are shown in Fig. 4.34 and Fig. 4.35.
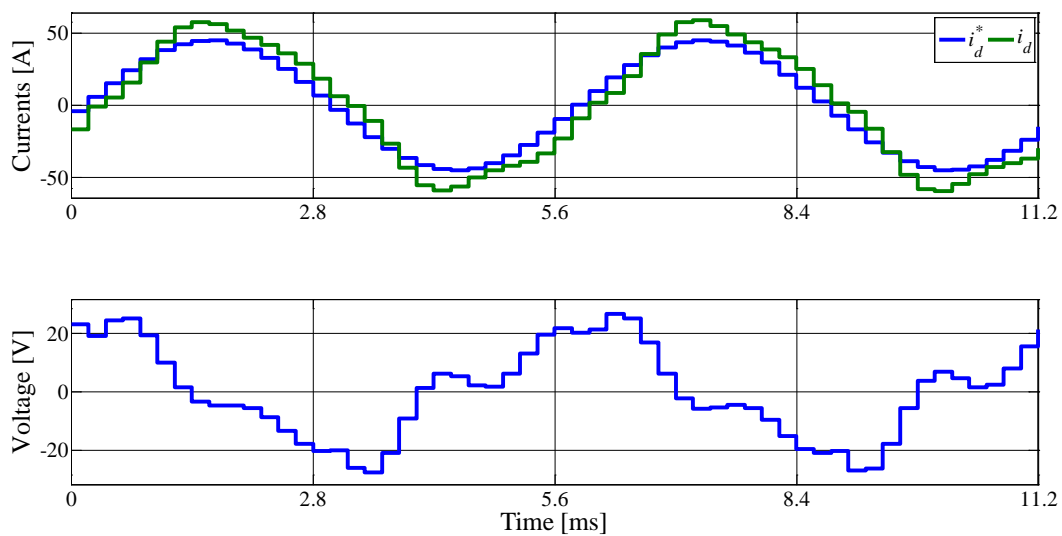
Fig. 4.32: *d*-axis injection at 175Hz with $i_q = 0$: currents (top), controller output voltage (bottom)
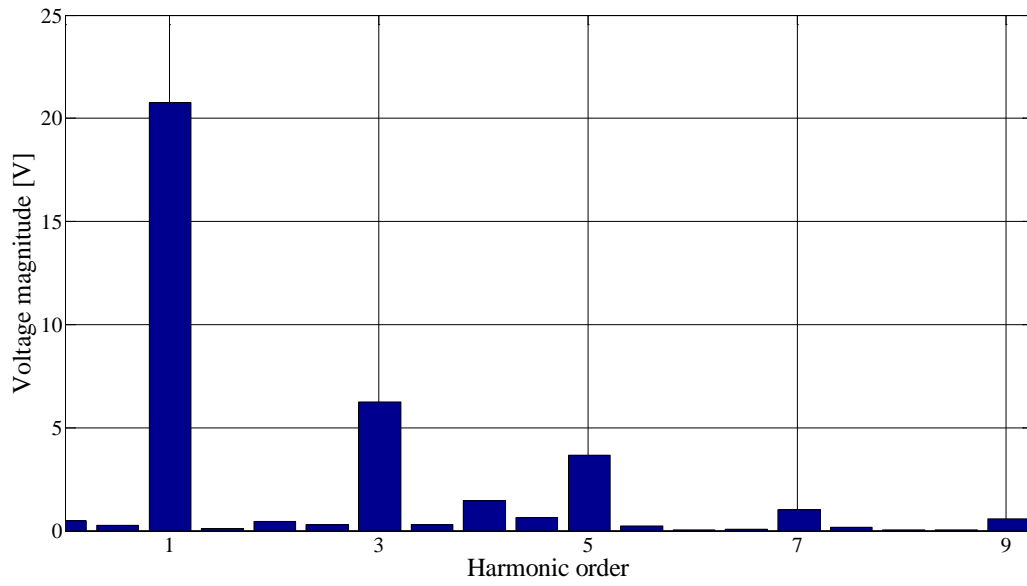
Fig. 4.33: *d*-axis injection with $i_q = 0$: controller output voltage harmonics extracted with DFT
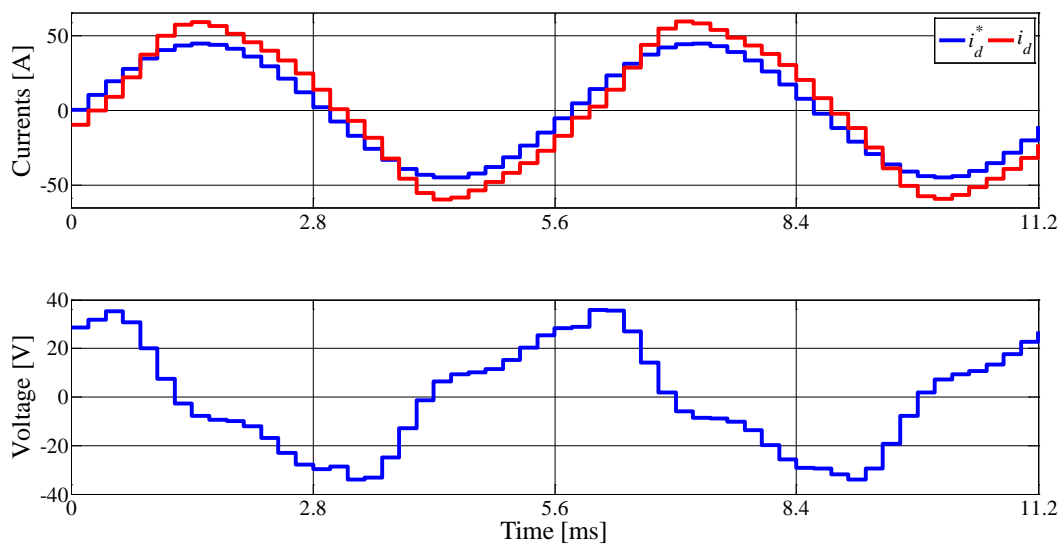
Fig. 4.34: *q*-axis injection at 175Hz with $i_d = 0$: currents (top), controller output voltage (bottom)
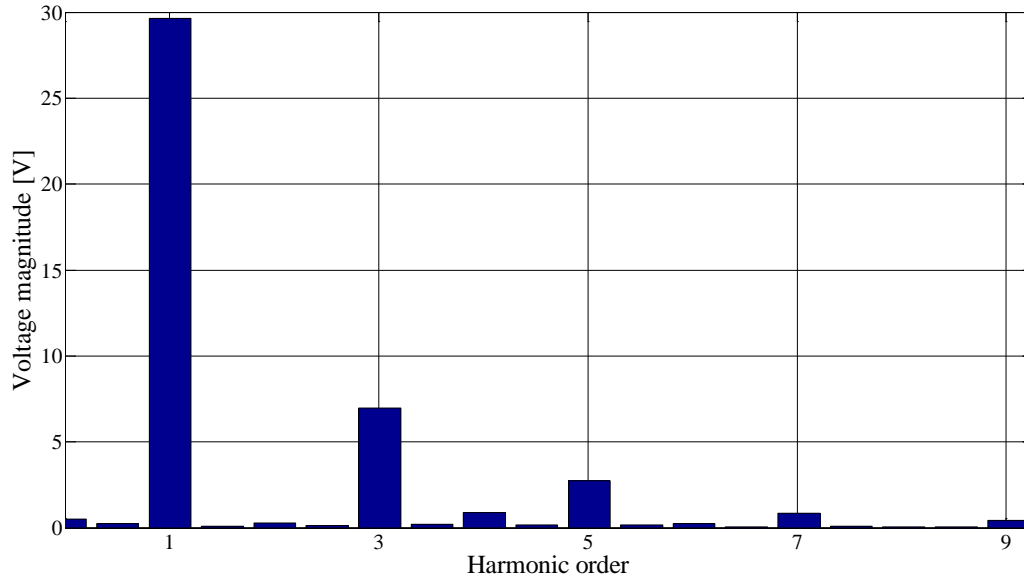
Fig. 4.35: *q*-axis injection with $i_d = 0$: controller output voltage harmonics extracted with DFT

Fig. 4.36 shows *d*- and *q*-axis inductances obtained at fixed current injection amplitude but different frequencies. It is observed that the estimates are substantially independent of injection frequency and at higher frequencies the estimates degrade due to measurement noise and scarcity of the sufficient number of samples available for DFT analysis and hence for accurate impedance estimation. For this reason the injection frequency is set close to the machine's rated operating frequency (173.33Hz for the machine in question, cf. Fig. 4.32 and Fig. 4.34) to emulate actual operating conditions.
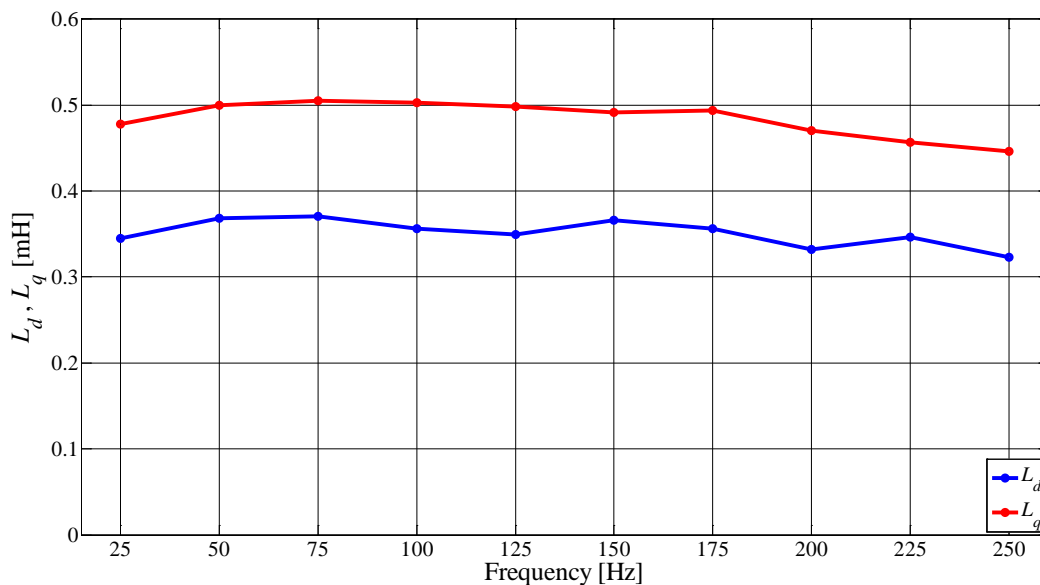
Fig. 4.36: *d*- and *q*-axis estimated inductances as a function of injection frequency

Another source of voltage waveform distortion is the machine itself but only in the *d*-axis. As seen in the current-flux graph of Fig. 4.11, the machine inductance changes highly non-linearly especially when the *d*-axis current switches direction. The machine presents different reactance to positive and negative half-cycle of the injected wave and therefore the effects are seen again in the controller output voltage. The *d*-axis magnetic behaviour of Fig. 4.11 is typical of IPM machines.

Since flux is integral of voltage and a constant permanent magnet flux means a non-zero average value (Fig. 4.37) for the voltage which transforms to even harmonics in the controller output voltage as seen in Fig. 4.38. The fact that even harmonics are caused primarily by the permanent magnet flux is reiterated by their absence in the q-axis waveforms. The q-axis controller output voltage is quite smooth sinusoid (Fig. 4.39) and the harmonic content of Fig. 4.40 shows only odd harmonics due to inverter non-linearity effects.
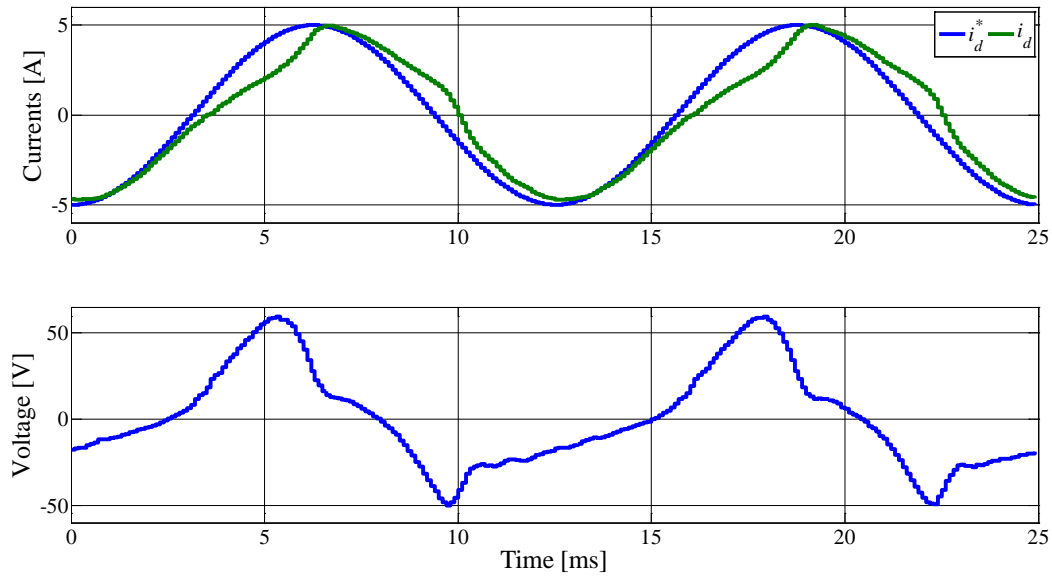
Fig. 4.37: d-axis injection with $i_q = 0$: currents (top), controller output voltage (bottom) – current is not perfectly sinusoidal due to PM flux and voltage wave is not exactly zero centred
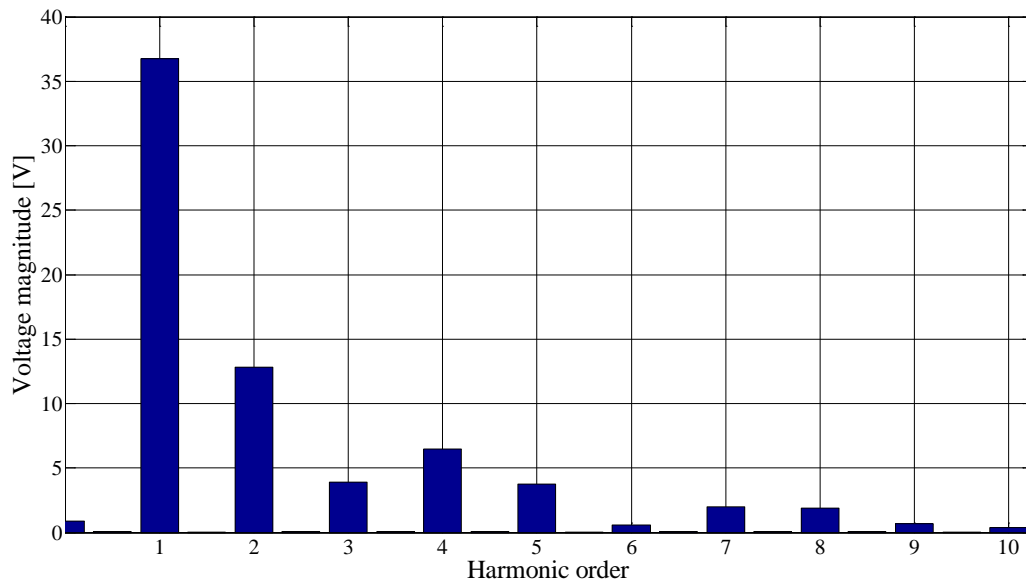
Fig. 4.38: d-axis injection with $i_q = 0$: controller output voltage harmonics extracted with DFT – both even and odd harmonics are present
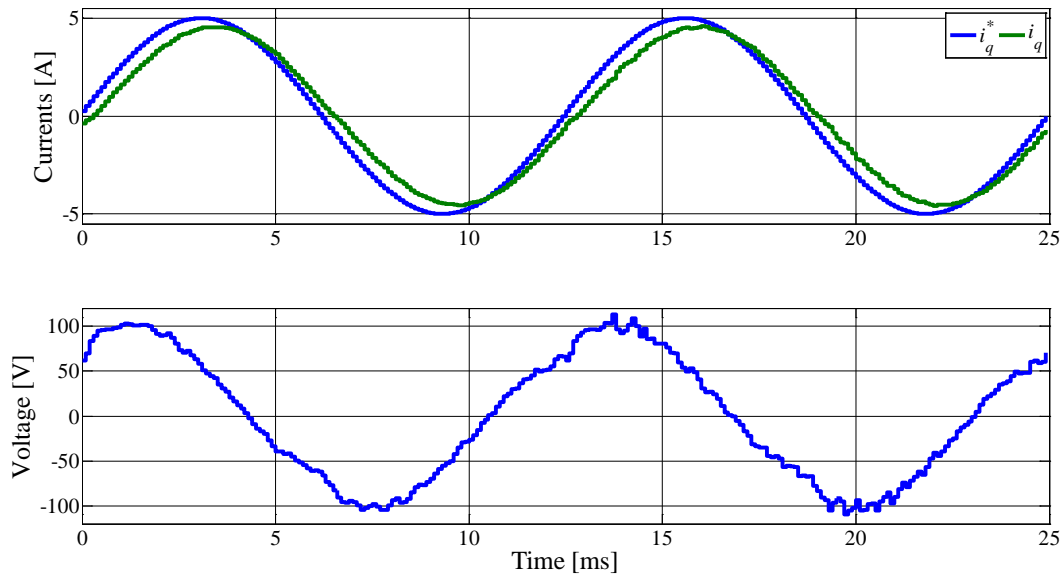
Fig. 4.39: q-axis injection with $i_d = 0$: currents (top), controller output voltage (bottom) – the controller output voltage is nearly sinusoidal for the disturbances caused by PM flux are not seen in the q-axis
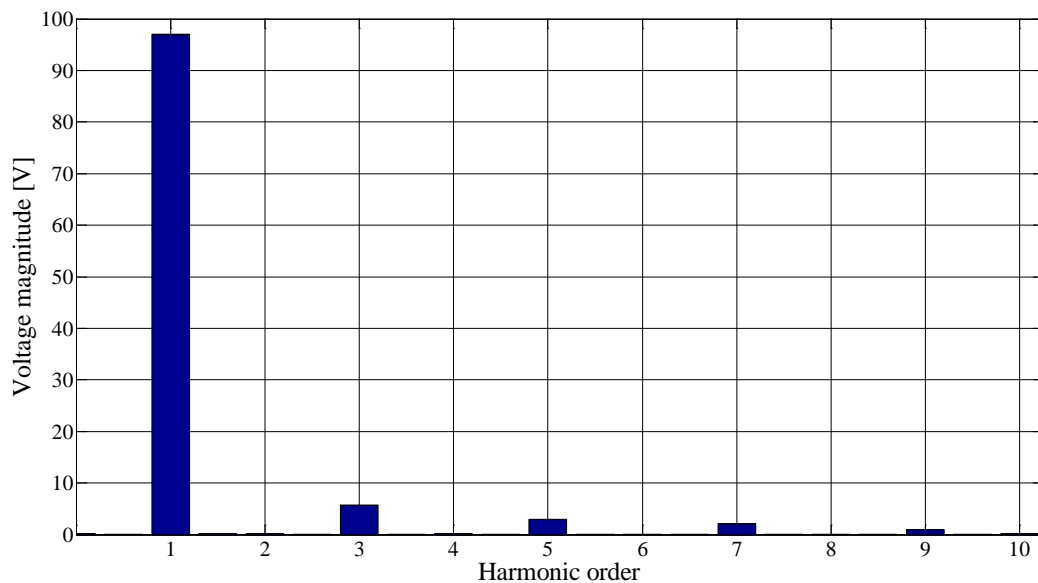
Fig. 4.40: q-axis injection with $i_d = 0$: controller output voltage frequency spectrum showing only odd harmonics due to inverter non-linearity effects

Comparing Fig. 4.33 with Fig. 4.38, an inconsistency in the results is observed in that the even harmonics caused by permanent magnet flux in Fig. 4.33 have too small a magnitude than they have in Fig. 4.38. This is because of the different machine reactances and inverters used for the two machines. The machine of Fig. 4.33 has low reactance and the controller output voltage is low for driving a current as high as 50 A (Fig. 4.32) and, at these low voltages, the inverter switch drops are so significant that the odd harmonics dominate making even harmonics look quite low (nevertheless they do exist). This explanation is true also for the differences seen between Fig. 4.34 and Fig. 4.39 in that the inverter non-linearities in Fig. 4.34 are almost 41% (3rd harmonic) of the fundamental voltage (cf. Fig. 4.35) whereas in the latter case, the greatest odd harmonic magnitude amounts to merely 6% of the fundamental component (Fig. 4.40).

Due to the disturbances discussed above in the controller output voltage, equations (4.37) and (4.38) cannot be applied for they are for phasor quantities which are perfectly sinusoidal, by definition. Further, the phase angle φ between voltage and current vectors, which is necessary to apply (4.40) and (4.41), cannot be established in the midst of these distortions. In order to do away with these disturbances and to obtain a definite value of machine inductance at the applied current magnitude, the fundamental components extracted through DFT from the machine current and controller output voltage can be used. Fig. 4.41 shows extracted fundamental current and voltage plotted along with the measured values for the highly distorted waves of Fig. 4.37. The DFT tool of Matlab also gives the phase of fundamental frequency component and of each harmonic. Phase angle φ between voltage and current needed for applying (4.40) and (4.41) is obtained from the DFT tool.
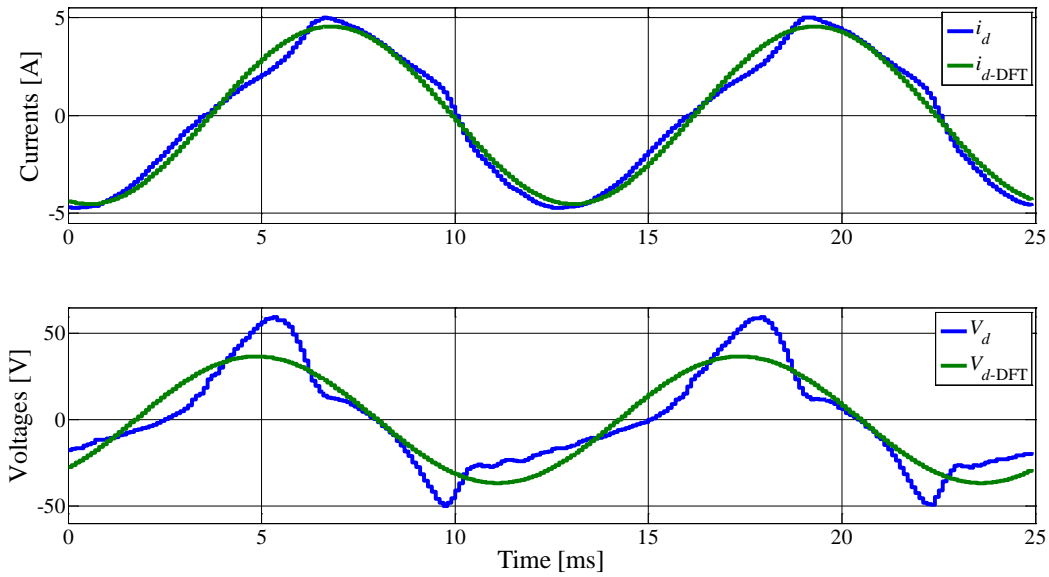
Fig. 4.41: Extracted fundamentals for *d*-axis injection with $i_q = 0$: currents (top), controller output voltage (bottom)

To simplify the self-commissioning procedure and reduce the computational load on the processor, the necessity of phase angle φ between the fundamental current and voltage vectors can be excluded by first estimating the stator resistance R_s (appearing in Fig. 4.27) through the dc injection test (as discussed in detail for induction machine in the previous chapter). In that case, the phase angle is not necessary to compute inductive reactance through (4.41); instead, (4.45) can be used for the magnitude of impedance is already computed from the magnitudes of fundamental voltage and current vectors through (4.39). The reactance computed from (4.45) can then be used in (4.42) to obtain inductance in *d*- or *q*-axis.

$$X = \sqrt{\left|\overline{Z}\right|^2 - R_s^2} \tag{4.45}$$

For most ac machines, the stator resistance R_s is negligible compared to the inductive reactance; especially at higher frequencies, the negligibility of R_s is more evident for the inductive reactance increases proportionately with frequency while R_s is unchanged. Although skin effect at high frequencies increases R_s from its dc value, this increment is not as significant as to violate (4.46). If (4.46) holds, the reactance can be approximated as equal to the impedance (4.47). However, in order to render the results as accurate as possible, (4.45) is used here.

$$R_s \ll X \tag{4.46}$$

➔ $$X \cong \left| \overline{Z} \right| \tag{4.47}$$

4.8.1. Magnetic saturation effects

Magnetic saturation is a commonly occurring phenomenon in electrical machines where the ferromagnetic core through which magnetic flux lines pass is not ideal. The IPM under discussion here is no different and the magnetic characteristics of one of the test machines shown in Fig. 4.11 and Fig. 4.12 show magnetic saturation at higher current levels. The magnetic saturation alters machine inductance depending on the current and needs to be taken care of while identifying machine inductances.

The magnetic equations of the machine (4.4) can be rewritten to give inductances in *d*- and *q*-axis as in (4.48) and (4.49), respectively. Observing Fig. 4.11 and Fig. 4.12 reveals that as the magnetic flux in each orthogonal axis is a non-linear function of current, the same is true for L_d and L_q through (4.48) and (4.49), respectively.

$$L_d = \frac{\lambda_d - \lambda_m}{i_d} \tag{4.48}$$

$$L_q = \frac{\lambda_q}{i_q} \tag{4.49}$$

In order to quantify the magnetic saturation effects and obtain machine inductances at various current levels, the high frequency injection method under study here can be used with amplitude modulation of the injected current to compute inductances at various current levels in both *d*- and *q*-axis.

It is worth mentioning here that as the impedance is computed from the magnitude (peak value) of the current and fundamental component of voltage wave obtained through DFT using (4.39), the impedance is true at that particular point of machine magnetization state. Thus by varying the amplitude, the point at which machine is excited corresponds to the peak of the applied current amplitude. Machine inductances are then plotted against current magnitude in the two axes as shown in Fig. 4.42 and Fig. 4.43.
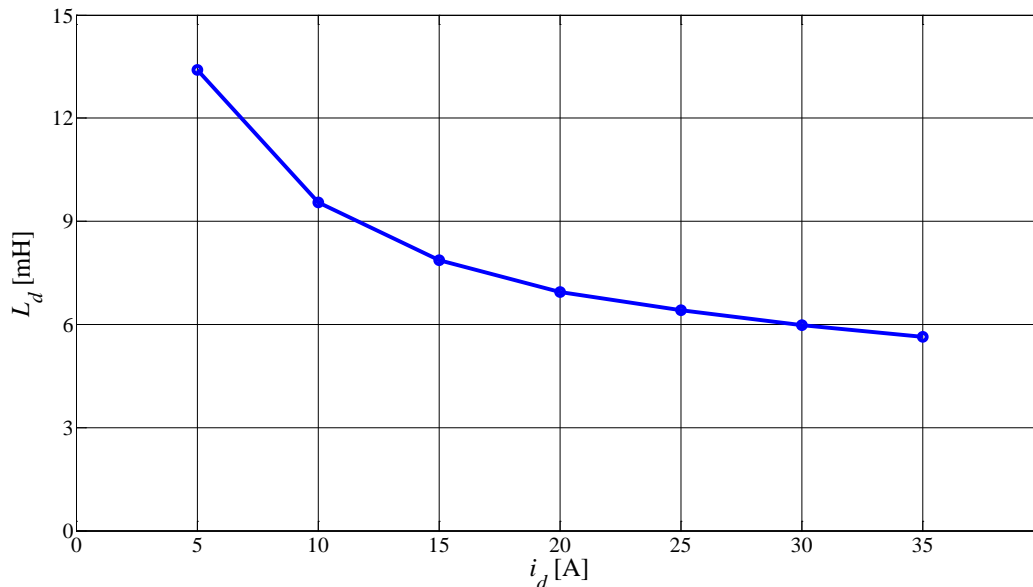
Fig. 4.42: *d*-axis saturation characteristic: inductance decrease with current rise is consistent with Fig. 4.11
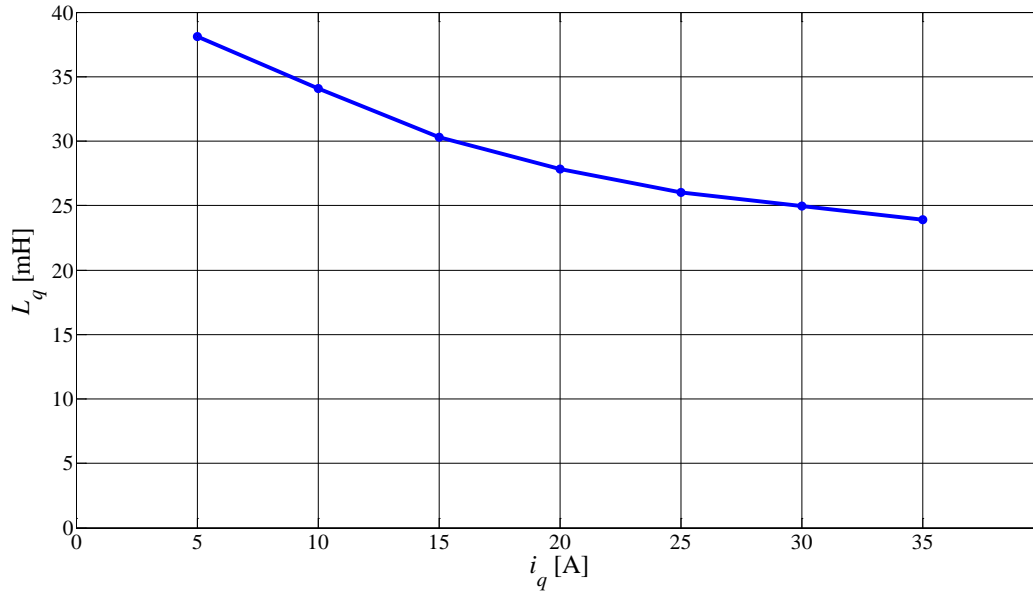
Fig. 4.43: q-axis saturation characteristic

The saturation curve of Fig. 4.42, when compared with the machine magnetic characterization results of Fig. 4.11, shows slight deviations especially at low current levels (Fig. 4.44). As the high-frequency injection is zero-centred, at every cycle the current traces the highly non-linear part of the magnetic curve of the machine shown in Fig. 4.11 and the Fourier series expansion of the controller output voltage integrates the entire cycle of the current and voltage wave, these small deviations are expected. The other reason for this deviation is machine temperature. The machine magnetic characterization tests of Fig. 4.11 are performed by actually loading the machine on the test bench that elevates machine temperature and thus modifies the PM flux (cf. Fig. 4.9). As the PM flux decreases with temperature, the inductance L_d increases according to (4.48). On the contrary, the high-frequency tests are conducted in cold rotor conditions without loading the machine that explains the error in L_d. At higher currents, however, the impact of permanent magnet flux reduces because the saturation is predominantly caused by the d-axis current. This can be seen in Fig. 4.44 as the error between the two inductance values decreases with increasing current in the d-axis.
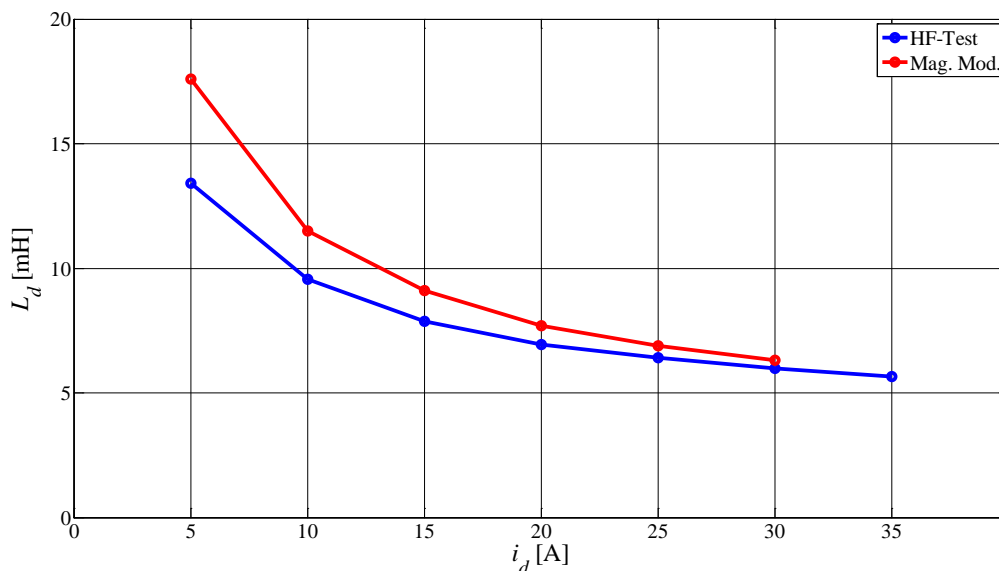
Fig. 4.44: Comparison of d-axis saturation characteristic with magnetic model of Fig. 4.11

In the q-axis, the error between high-frequency tests and magnetic characterization data as seen in Fig. 4.45 is caused by the rotor structure of this particular machine (Fig. 4.24). The magnetic characterization is recorded for constant q-axis currents, in which case once the rotor ribs are saturated, they behave linearly as does air and inductance decreases linearly with current (Fig. 4.45, red curve). However, in the high-frequency tests the q-axis current varies sinusoidally (with zero-crossings) and thus the ribs saturate and desaturate periodically, therefore giving higher average impedance in the q-axis that translates to higher q-axis inductance as observed.
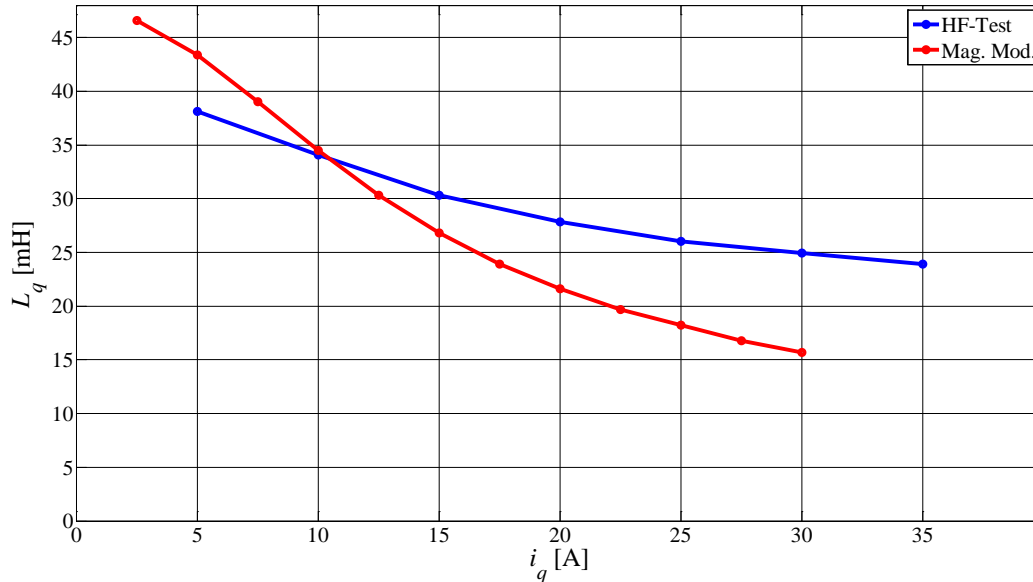
Fig. 4.45: Comparison of q-axis saturation characteristic with magnetic model of Fig. 4.12

The error observed in Fig. 4.45 can be avoided by taking into account only the peak values of the actual machine current. Fig. 4.46 shows the actual q-axis current compared against the fundamental obtained through Fourier analysis. It can be seen that the actual current has sharp positive and negative peaks. If these peak values are used for computing the q-axis impedance and then the inductance, the results closely approach the magnetic characterization data as shown in Fig. 4.47.
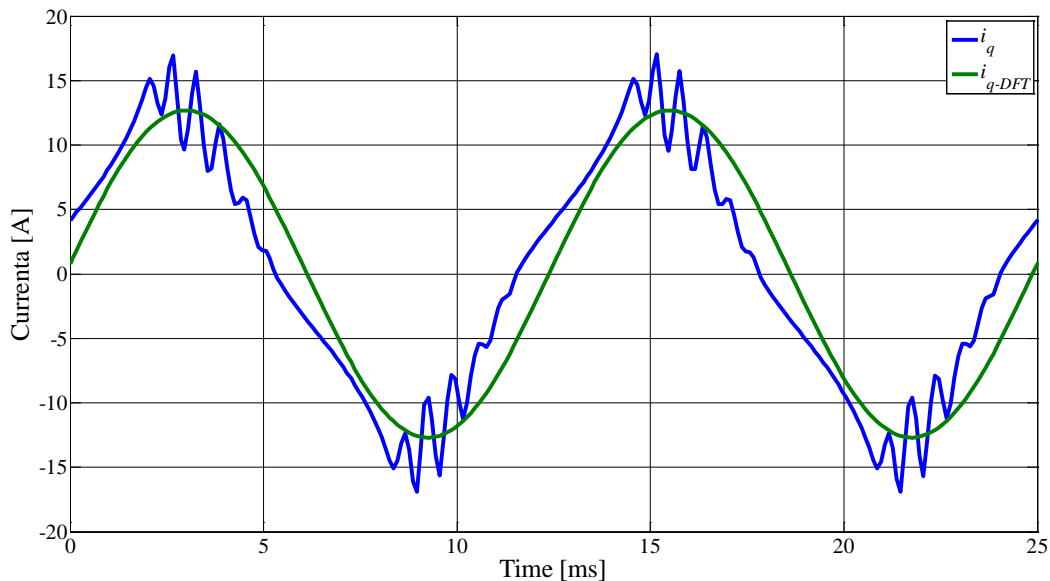
Fig. 4.46: Comparison of q-axis actual current with the fundamental obtained through Fourier analysis
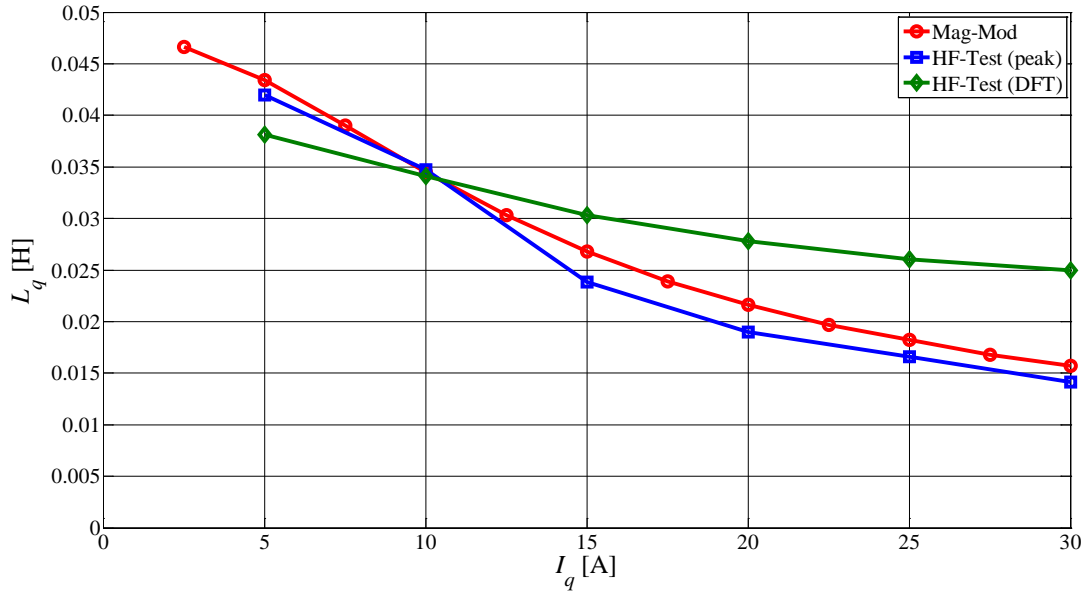
Fig. 4.47: *q*-axis inductances obtained using current peak values and the fundamental waves obtained through DFT compared with the ones computed from the magnetic model of Fig. 4.12

4.8.2. Cross-saturation analysis

Sharing a common ferromagnetic core, the currents in the two orthogonal axes of an ac machine interact in affecting the flux and hence inductance in the perpendicular axis, this effect is explained as the redistribution of flux due to core saturation and is called cross-coupling or cross-saturation effect [140, 154]. As discussed in section 4.3.2 and shown in Fig. 4.11 and Fig. 4.12, the current in *d*-axis modifies magnetic characteristics in *q*-axis and vice versa. These effects must be accounted for during machine identification process. The self-commissioning method proposed here with high-frequency injection must also be capable of considering cross-saturation effects.

In order to verify the effects of current in the cross-axis (e.g. *q*) on the inductance of the self-axis (e.g. *d*), a constant current is applied in the cross-axis through current regulators and high-frequency current of varying amplitude is injected in the self-axis and impedance in the self-axis is estimated. The current in the cross-axis is changed in predetermined steps and inductance in the self-axis is estimated at each value of the cross-axis current and stored. The same is repeated for other axis by changing the role of 'self-axis' and 'cross-axis'.

This approach does not produce electromagnetic torque when the *d*-axis is assumed as cross-axis since *d*-axis current per se does not produce any torque unless there is any *q*-axis current (4.9). However, when the cross-axis is *q* and a non-zero current is injected along it, the machine tends to rotate due to magnet alignment torque (4.31). In the latter case, there are two ways of preventing rotor rotation. First, by cancelling out the alignment torque exploiting the reluctance torque (4.32) by an appropriate constant *d*-axis current superimposed on the applied high-frequency signal. However, a constant *d*-axis current alters machine's magnetization state and thus pollutes the estimation. Second way to keep the rotor at standstill during the tests is to apply a square wave *q*-axis current whose frequency is too high to cause any rotation and too low to interfere with *d*-axis injection.

The effects of *d*-axis current on *q*-axis inductance are first examined by applying constant current in *d*-axis and injected high frequency current in the *q*-axis. Fig. 4.48 shows the results of one such test for one of the test machines.
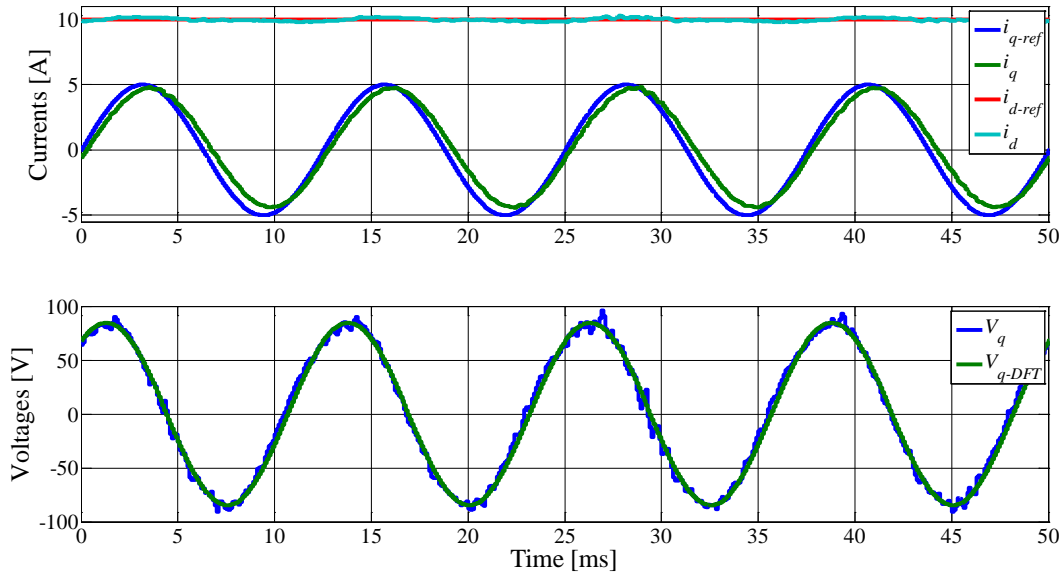
Fig. 4.48: High-frequency test in *q*-axis with constant *d*-axis current

Keeping a constant *d*-axis current, the *q*-axis amplitude is modulated as in the case for saturation tests in the previous section to evaluate variations in *q*-axis inductance due to *d*-axis currents. This is repeated for other constant *d*-axis magnitudes and the curves of Fig. 4.49 are obtained for *q*-axis inductance as a function of *d*-axis current. Fig. 4.49 shows both saturation and cross-saturation effects with inductance varying both with *q*-axis current amplitude as well as *d*-axis current.
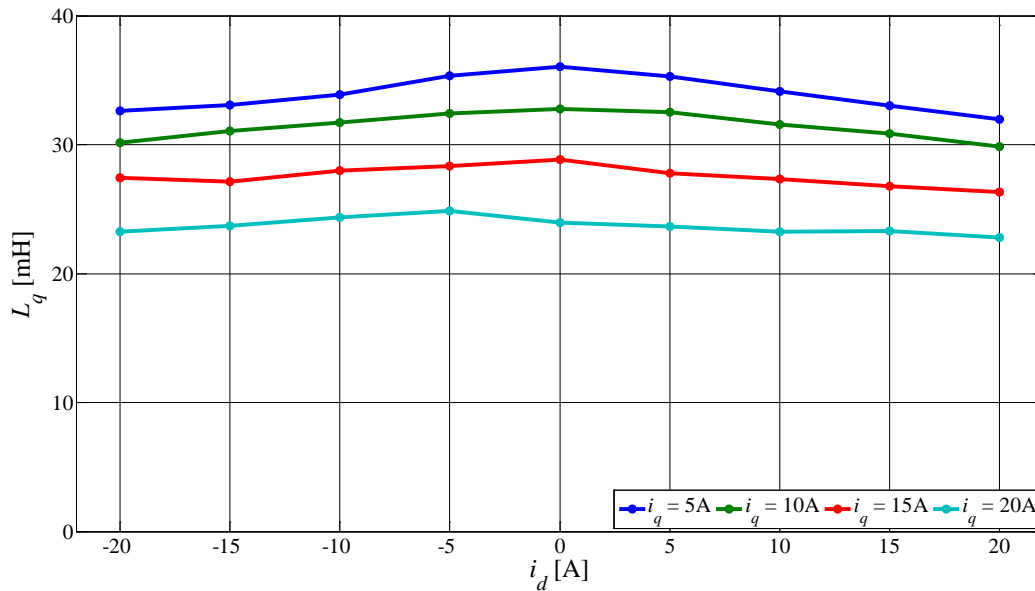
Fig. 4.49: L_q as a function of i_d at various i_q amplitudes

The same procedure is adopted for obtaining *d*-axis inductance at various *q*-axis currents. However, as said before the *q*-axis current applied must be a square-wave with zero average value such that no net torque is generated and the rotor continues to be at rest. Fig. 4.50 gives results for one such test in which the frequency of the *q*-axis current is one-tenth of the injection frequency in *d*-axis so that sufficient periods of injected signal are obtained while the *q*-axis current remains constant.
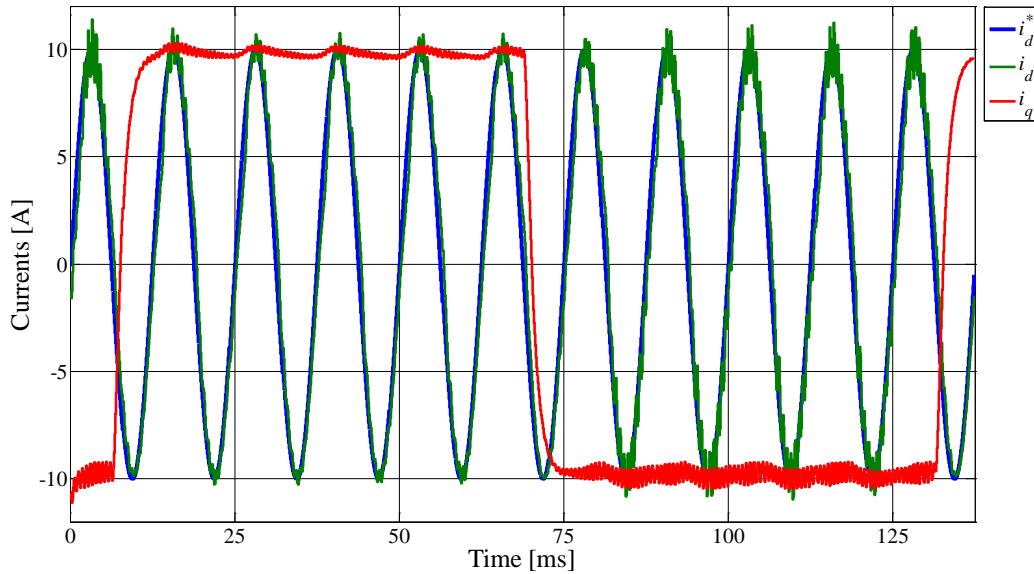
Fig. 4.50: High-frequency test in *d*-axis with square wave *q*-axis current

The *d*-axis inductance is computed during the period through which the current in the orthogonal axis (i.e. *q*-axis) is constant as seen in Fig. 4.50. Inductance variations in *d*-axis due to both positive and negative *q*-axis currents are shown in Fig. 4.51 where the amplitude of the injected signal in *d*-axis is a parameter.
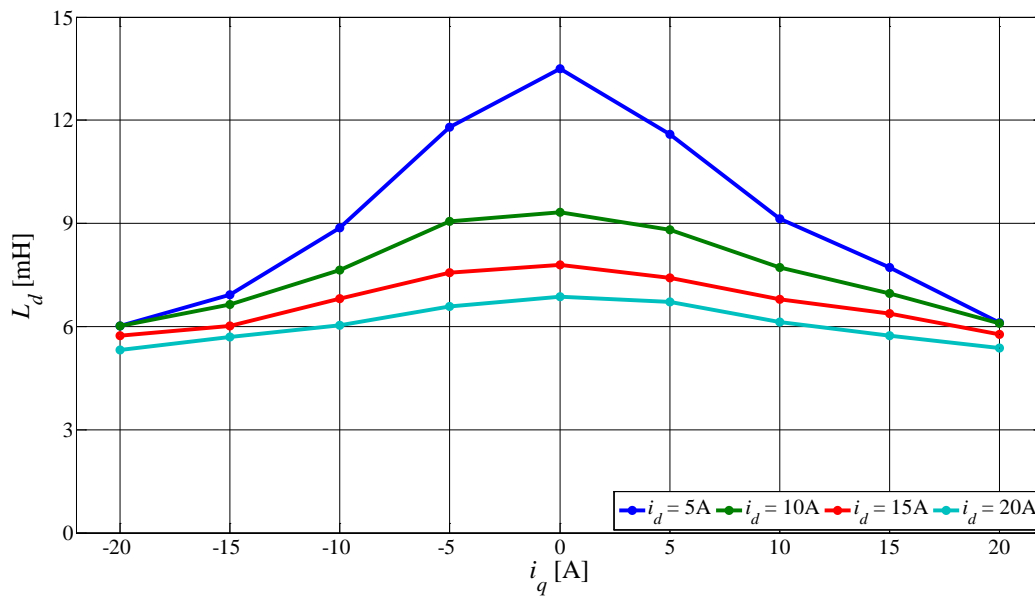
Fig. 4.51: L_d as a function of i_q at various i_d amplitudes

Having known the *d*- and *q*-axis inductances as functions of self-axis and cross-axis currents, the machine's magnetic model on the pattern of Fig. 4.11 and Fig. 4.12 can be constructed. Fig. 4.52 reports the *d*-axis magnetic characteristic for positive i_d values at different current levels in the *q*-axis. The *q*-axis flux as a function of i_q for various i_d values is shown in Fig. 4.53.

$\lambda_d(i_d)$ (parameter i_q)
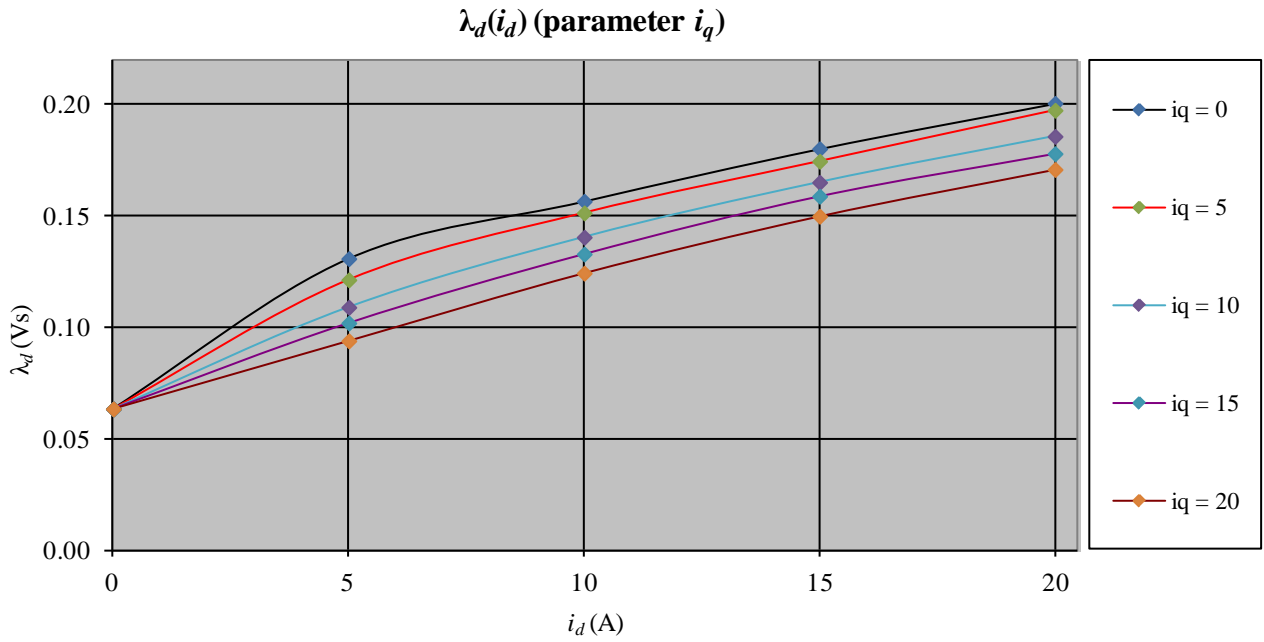
Fig. 4.52: d-axis flux as a function of i_d and i_q (4.30) constructed from data of Fig. 4.51

$\lambda_q(i_q)$ (parameter i_d)
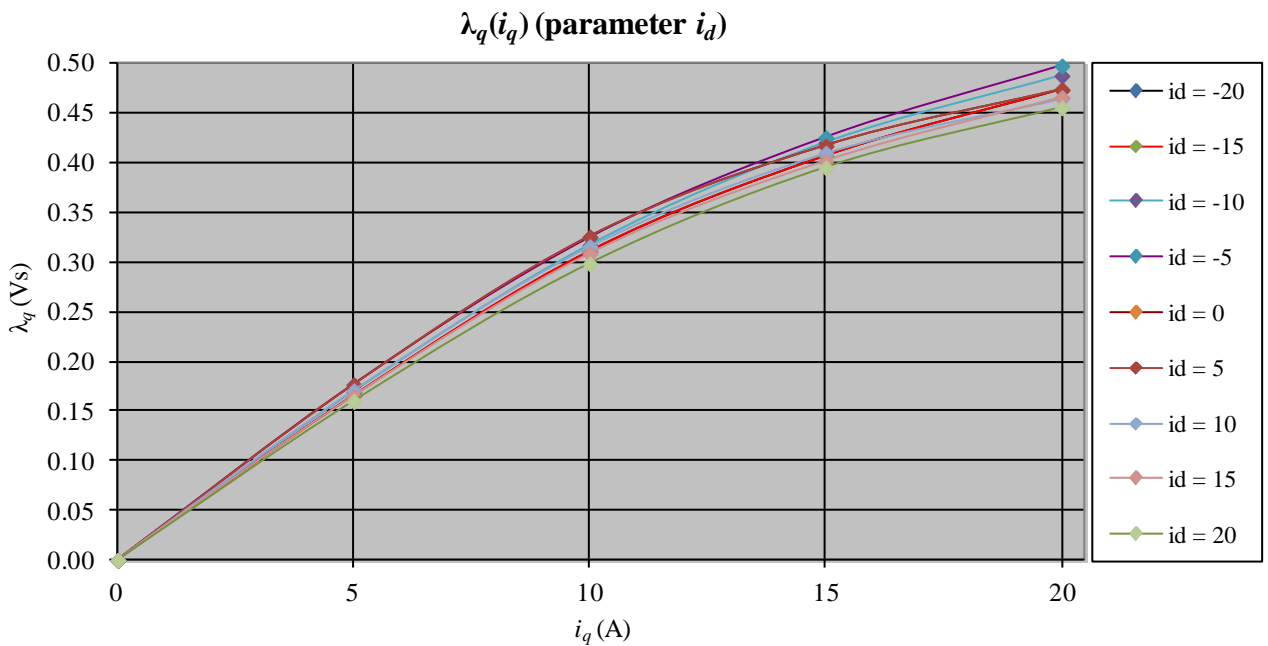
Fig. 4.53: q-axis flux as a function of i_d and i_q (4.30) constructed from data of Fig. 4.50

It is evident from the results presented above that the machine inductances are not constant due to saturation and cross-magnetizing saturation effects, the consequences are seen in the magnetic model. It is always recommendable to have the machine magnetic model directly in terms of flux-linkages as a function of currents (Fig. 4.52 and Fig. 4.53), without passing through the intermediate stage of inductances, for it is the flux that determines control performance and torque estimation accuracy.

4.9.   **Permanent magnet flux estimation**

The impact of permanent magnet flux linkage (λ_m) on machine torque production is significant as seen in Fig. 4.14 and equation (4.9). Its correct value is required for high performance torque/position drives and to operate at higher efficiencies by exploiting maximum torque per ampere profile of the machine (Fig. 4.16). The MTPA operation is only possible through optimum current angle γ that depends also on accurate value of λ_m as in (4.33).

The traditional method of rotating the machine at no-load and analyzing the back-emf induced in stator windings entails (i) mechanical decoupling of machine from its load, (ii) the need of a prime-mover and (iii) terminal voltage measurement instrument(s). Thus, alternatives to this traditional test are required. Whereas the methods proposed in [109, 110] give estimates of permanent magnet flux linkage for a machine in operation, standstill estimation is focused in this thesis, in order to be consistent with the definition of self-commissioning.

The method studied here gives an estimate of permanent magnet flux at standstill that can later on be updated once the normal operation begins through the methods discussed in [109, 110]. The test is carried out through an unconventional closed-loop speed control. The machine torque equation (4.9) is exploited to keep the rotor from moving by applying appropriate d- and q-axis currents. For the rotor to remain stationary, the machine must not produce any torque for which equation (4.9) must be equated to zero i.e.

$$T = \frac{3}{2} p\lambda_m i_q + \frac{3}{2} p\left(L_d - L_q\right) i_d i_q = 0 \tag{4.50}$$

First, a constant q-axis current is applied that would cause rotor movement due to magnet alignment torque given by (4.31). To counter this alignment torque, the reluctance torque of the machine (4.32) can be used. For the reluctance torque to be equal in magnitude and opposite in sign to the alignment torque, an appropriate d-axis current is required. The current angle γ must be negative (Fig. 4.14) for the net torque to be equal to zero. Thus the d-axis current must be positive (cf. Fig. 4.13). More specifically, the d-axis current must numerically be equal to (4.51) after solving (4.50) for i_d.

$$i_d = \frac{-\lambda_m}{L_d - L_q} = \frac{-\lambda_m}{\Delta L} \tag{4.51}$$

so
$$\lambda_m = -i_d\left(L_d - L_q\right) \tag{4.52}$$

In order to implement the procedure described above, an unconventional speed control is employed as shown in Fig. 4.54. Usually, the q-axis current is used to generate torque required for speeding up the machine from zero to a set speed as this gives faster torque response, however, in Fig. 4.54 d-axis current is used for the same that is what makes this control 'unconventional'. This is used only for flux estimation during self-commissioning and not for normal machine operation. Setting speed command to zero, a constant q-axis current is commanded to the current controllers. As soon as the rotor tends to have a slightest of displacement, the d-axis current rises to keep it from turning further. From the output of the PI speed controller i.e. i_d, and already known d- and q-axis inductances estimated as in previous sections, an initial estimate of permanent magnet flux can be obtained from (4.52). The values of L_d and L_q used must correspond to the currents i_d and i_q to render estimate of λ_m accurate.

From (4.51) it is evident that the d-axis current required is theoretically independent of the q-axis current. However, this is true as long as L_d and L_q remain unchanged with i_d and i_q. Fig. 4.19 negates this assumption of constancy of L_d and L_q with current. More specifically, with increasing

i_q, L_q decreases so does the difference ΔL. A reduced ΔL requests more i_d to keep the rotor stationary. On the other hand, a greater i_d means a lower L_d that further lowers ΔL. The system reaches equilibrium thanks to the closed-loop PI control of Fig. 4.54. Therefore, the theoretical constant i_d of (4.51) does not have practical significance and for every i_q there is a unique i_d and hence (4.52) must be used in correspondence to the pair i_d and i_q where the equilibrium is reached.
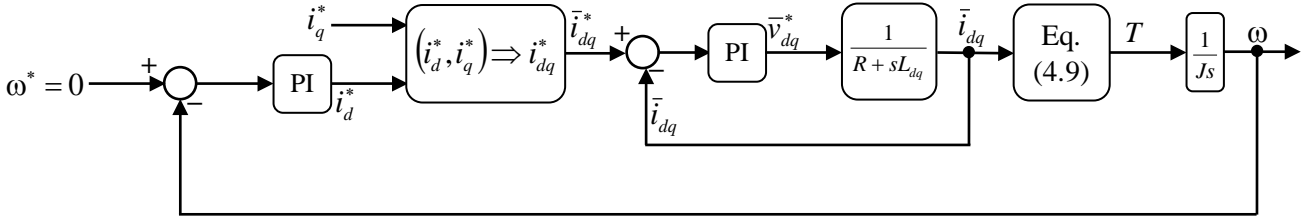
Fig. 4.54: Speed control loop for permanent magnet flux linkage estimation

From the above discussion, it is clear that with increasing i_q the d-axis current required to maintain the torque balance of (4.50) increases. A limit should be placed on applied i_q such that the total phase current does not exceed the maximum permissible current at equilibrium condition in any case. In Fig. 4.14, the angle γ for this particular machine and at that particular phase current is around -40° to give null net torque. A $\gamma = -40°$ means an i_d equal to 0.64 times the total phase current and an i_q equal to 0.77 times. Thus, care must be taken to conduct the test for as smaller i_q as possible. In case a q-axis current close to the rated current is applied, the margin for i_d may not be sufficient to maintain zero torque angle since i_d must be limited to (4.53) at all times, here I_n is the rated machine current or the maximum current allowed by semiconductor switches' ratings (whichever is smaller).

$$i_d \leq \sqrt{I_n^2 - i_q^2} \tag{4.53}$$

It must be mentioned here that the method described above is applicable only to machines having considerable reluctance torque such that, within the machine current limits, there exists a certain angle γ for which the total torque is zero. For instance, Fig. 4.55 shows total torque breakup of one of the test machines at a current equal to 20% of its rated value. It can be seen that even at 20% current, there does not exist an angle γ where the reluctance torque can counter the permanent magnet alignment torque. From the available data of this machine, it is found that the d-axis current required to keep rotor stationary as computed from (4.51) is as high as 4.5 times the rated current of the machine. Therefore it becomes impractical to estimate λ_m using this technique.
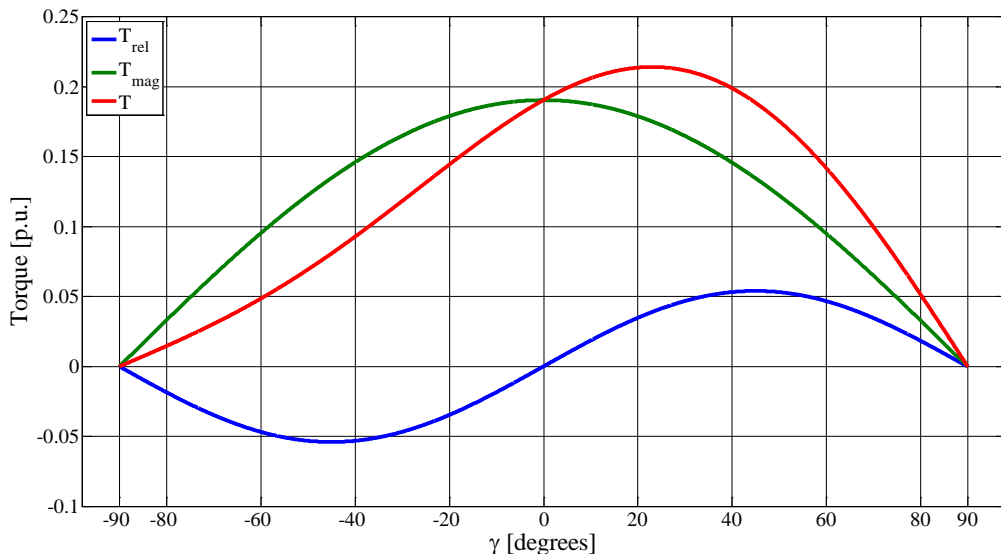
Fig. 4.55: Torque components as a function of γ at 20% rated current – test machine with low reluctance torque

This is typical of IPM machines that are designed with greater PM flux and where the reluctance torque acts just as a useful surplus. These machines are not suitable for flux-weakening too because the saliency is too low to allow flux-weakening to permit high speed operation. Additionally, the high permanent magnet flux increases the characteristic current (4.35) which is an important metric to effectuate flux-weakening operation.

4.10. Machine MTPA table generation

Having estimated the parameters of the IPM, it is necessary to define look-up tables for optimal current vector selection that gives maximum torque at a given phase current magnitude. As it has been shown throughout the previous sections, the machine's magnetic characteristics and therefore the inductances are current dependent. For this reason, the optimum current angle computed through (4.33), that assumes constant inductances, deviates from true optimal angle (as seen in Fig. 4.18, for example).

Although the machine MTPA look-up tables generated on the test bench with torque-sensor are the most accurate for they emulate also the actual on-load operating conditions and temperature rise due to machine loading, determining these tables from offline tests is among the aims of this thesis. The tables are then compared with the test bench results to verify how effective the offline testing method has been and to what extent it can substitute actual commissioning procedures currently in practice.

In order to determine current angle γ that gives maximum torque, the following procedure is adopted:

    i)   Choose a phase current magnitude I (Amps)

    ii)   Set $\gamma = 0°$ (i.e. $i_d = 0$ and $i_q = I$)

    iii)   Read L_d from the characteristics of Fig. 4.51 for the pair (i_d, i_q)

    iv)   Read L_q from the characteristics of Fig. 4.49 for the pair (i_d, i_q)

    v)   Use λ_m as estimated in section 4.9

    vi)   Compute torque using (4.9) γ

    vii)   Increase γ by a certain step and compute new pair of currents (i_d, i_q)

   viii) Repeat steps (iii) through (vii) till $\gamma = 90°$ (i.e. $i_d = I$ and $i_q = 0$)

    ix)   Store γ_{max} for which torque computed in step (vi) is maximum

    x)   Increment phase current I and repeat steps (ii) through (ix)

    xi)   Stop when rated machine current is reached

The flowchart of Fig. 4.56 describes the procedure outlined above. The permanent magnet flux used throughout the generation of MTPA tables is assumed constant since the process takes place offline and the temperature of the permanent magnets and hence their flux is assumed constant.
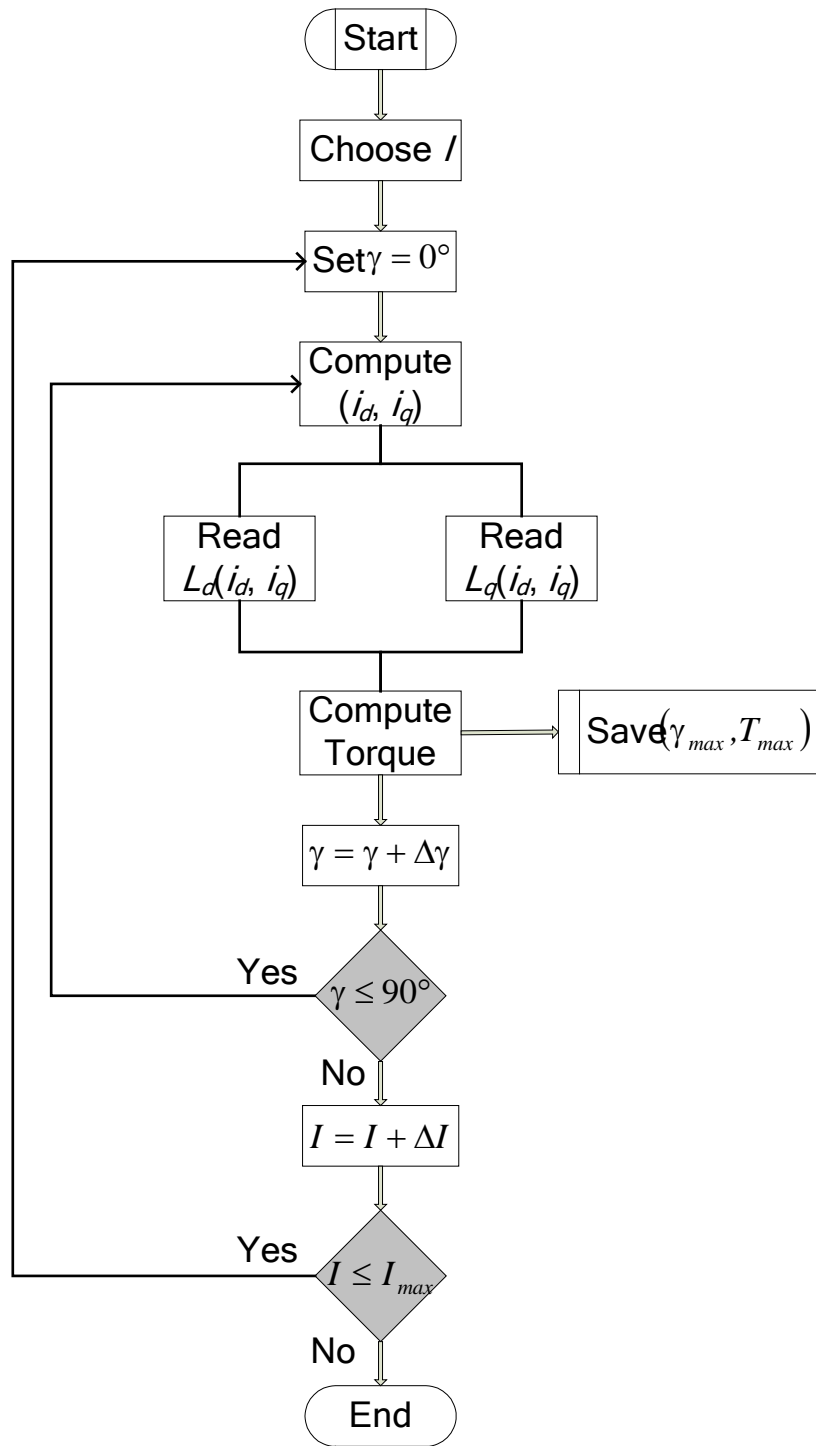
Fig. 4.56: Flowchart for generating MTPA table from identified parameters

In Fig. 4.57, the torque is plotted against optimal d- and q-axis currents as obtained with the self-commissioning process. The curves of Fig. 4.57 compared with the optimum dq-currents obtained from machine's magnetic characterization data are shown in Fig. 4.58. The same conditions are assumed in both the cases in that the machine inductances are obtained at the same magnetization state (cf. Fig. 4.11 and Fig. 4.12) and the permanent magnet flux is considered constant (also for the case of Fig. 4.58).
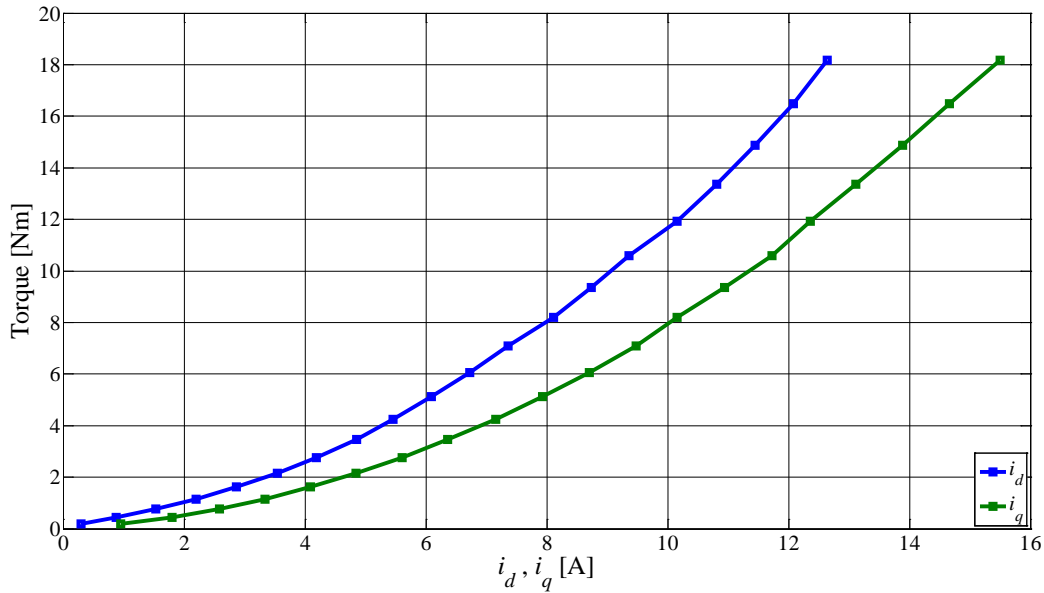
Fig. 4.57: Offline identification of maximum torque per ampere of phase current characteristic – torque as a function of i_d and i_q
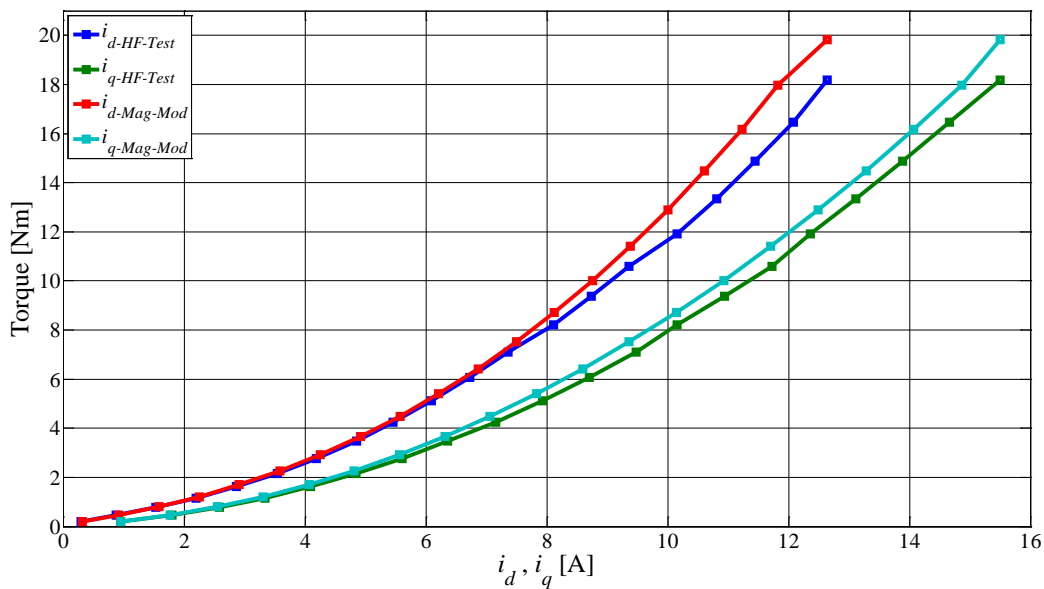
Fig. 4.58: Comparison of offline MTPA curves obtained with self-commissioning process and those obtained from magnetic characterization data of the machine (Fig. 4.11 and Fig. 4.12)

Appendix

This section gives the nameplate and equivalent circuit parameters' data for the machines used in tests.

Machine – 1: 30 kW Traction Motor Prototype

General Data			
Nominal power	30 [kW]	Pole pairs	8
Peak power*	60 [kW]	Rated current	120 [A]
Back-emf	64.5 [V]	Max. speed**	2800 [rpm]
Rated speed	1300 [rpm]		

* Peak power with 25% duty
** With flux-weakening

Equivalent circuit parameters		
Parameter	Value	Unit
R_s	9	mΩ
L_d (unsaturated)	0.4	mH
L_q (unsaturated)	0.5	mH
λ_m	0.0838	Vs

Machine – 2: 7.5 kW Light traction machine

General Data			
Nominal power	7.5 [kW]	Pole pairs	2
Peak power	10 [kW]	Rated current	24 [A]
Back-emf	32.6 [V]	Max. speed*	10000 [rpm]
Rated speed	2450 [rpm]	J	0.0046 [kg m^2]

* With flux-weakening

Equivalent circuit parameters		
Parameter	Value	Unit
R_s	0.3	Ω
L_d (unsaturated)	4	mH
L_q (unsaturated)	40	mH
λ_m	0.0635	Vs

Machine – 3: 700 W CE_PF_R1 – IPM prototype

General Data			
Nominal power	0.7 [kW]	Pole pairs	2
Rated torque	1 [Nm]	Rated current	5 [A]
Back-emf	37 [V]	Max. speed*	15000 [rpm]
Rated speed	3000 [rpm]	J	0.0005 [kg m^2]

* With flux-weakening

Equivalent circuit parameters		
Parameter	Value	Unit
R_s	8	Ω
L_d (unsaturated)	39	mH
L_q (unsaturated)	138	mH
λ_m	0.0589	Vs

<div align="right">

Chapter – 5

</div>

SURFACE MOUNTED PERMANENT MAGNET SYNCHRONOUS MOTOR DRIVE

5.1.   Introduction

This is the third ac machine type studied for parameter identification in this thesis. The machine, being synchronous and having permanent magnets, is similar to an IPM discussed in the previous chapter. However, the disposition of permanent magnets is not 'interior' to the ferromagnetic core as in the IPM that makes this machine different from an IPM. The permanent magnets are placed at the circumferential boundary of the rotor in a surface mounted permanent magnet synchronous motor (SPMSM). If the magnets are embedded inside the grooves of rotor laminations, the structure is called surface-inset permanent magnet and if they are bonded or bound to the rotor surface and are exposed, it makes surface permanent magnet rotor. In both the case, since the magnets remain near the surface of the rotor, therefore the name 'surface mounted' does not change. The electrical and magnetic characteristics do not change significantly with inset or surface, but the mechanical strength against centrifugal forces at high speeds is significantly increased with surface-inset PM rotors as the magnets are braced by rotor laminations that prevents them from 'flying out'. Fig. 5.1 shows the inset (a) and surface (b) permanent magnet rotor structures.

Each magnet forming the pole surface can either be a single-segment structure (as in Fig. 5.1) or consisting of multiple segments bonded together for large machines. Multiple segment solution allows easy machining of magnets and eases their charging to magnetize besides boosting flux-weakening capability [155].

With regards to stator windings, the available options are as many as for an IPM. The most commonly used winding configurations, however, are the distributed and concentrated winding types. In Fig. 5.1, the stator winding shown for both the rotor variants is distributed type; these same rotors can equally be utilized with concentrated winding as in Fig. 5.2. The concentrated winding allows better flux-weakening capability [156] compared to its distributed counterpart.

Compared to an IPM, this machine often has higher torque-per-volume, less cogging torque and the torque ripple is also lower under identical control and operating conditions. The lower cogging torque is due to the fact that the reluctance to the flux path at different rotor positions with respect to stator slots remains constant thus the need for skewing is excluded that simplifies the manufacturing process.

<div align="center">

(a)   (b)

Fig. 5.1: Two SPMSM configurations with different rotor structures: inset (a), surface (b)

</div>

<center>(a)   (b)</center>

<center>Fig. 5.2: Machines with same rotors as those of Fig. 5.1 and concentrated stator windings</center>

The machine's equivalent circuit and characteristics are discussed in section 5.2, while section 5.3 gives a concise description of machine control. Section 5.4 presents an insight into inverter limits and flux-weakening operation. Section 5.5 gives some of the available parameter identification techniques found in literature along with the method proposed in this thesis. Some experimental results for parameter identification are included in section 5.6.

5.2. <u>Machine Equivalent Circuit and Characteristics</u>

Except the structure and position of permanent magnets, the machine is similar to the IPM of previous chapter. The rotor currents are absent in this machine as well and therefore the machine's electrical behaviour is completely described by the stator voltage equations (5.1). Although given for stator's three phases in compact vectorial notation, these equations are equally valid in the two-phase equivalent of machine in αβ stationary reference frame (Fig. 5.3).

$$\overline{v} = R_s \overline{i} + \frac{d\overline{\lambda}}{dt} \tag{5.1}$$

Here, R_s is the stator per-phase resistance. Following the standard convention of permanent magnet machines, Fig. 5.3 describes the dq reference frame where the north pole of the magnets is tied to the d-axis of the synchronously revolving reference frame. The equations (5.1) can then be transformed to this new reference frame as done for other ac machines discussed in previous chapters. The transformation details are not repeated here for brevity. The equations in vectorial form in the new dq frame can be written as in (5.2).

$$\overline{v}_{dq} = R_s \overline{i}_{dq} + \frac{d\overline{\lambda}_{dq}}{dt} + j\omega\overline{\lambda}_{dq} \tag{5.2}$$

Here ω is the speed of the rotating reference frame which is the same as the rotor speed since the machine is synchronous and there is no 'lag' between stator's rotating magnetic field and rotor's magnetic field (produced by magnets). The magnetic equations of the machine give the flux-current relationship as in (5.3) and contain the flux-linkages due to permanent magnets (λ_m) as well.

$$\overline{\lambda}_{dq} = \begin{bmatrix} \lambda_d \\ \lambda_q \end{bmatrix} = \begin{bmatrix} L_d & 0 \\ 0 & L_q \end{bmatrix} \begin{bmatrix} i_d \\ i_q \end{bmatrix} + \begin{bmatrix} \lambda_m \\ 0 \end{bmatrix} \tag{5.3}$$

Here, L_d and L_q are the inductances along d- and q-axis respectively. Unlike an IPM, this time the d- and q-axis inductances are equal for the rotor is isotropic i.e.

$$L_d \approx L_q \tag{5.4}$$
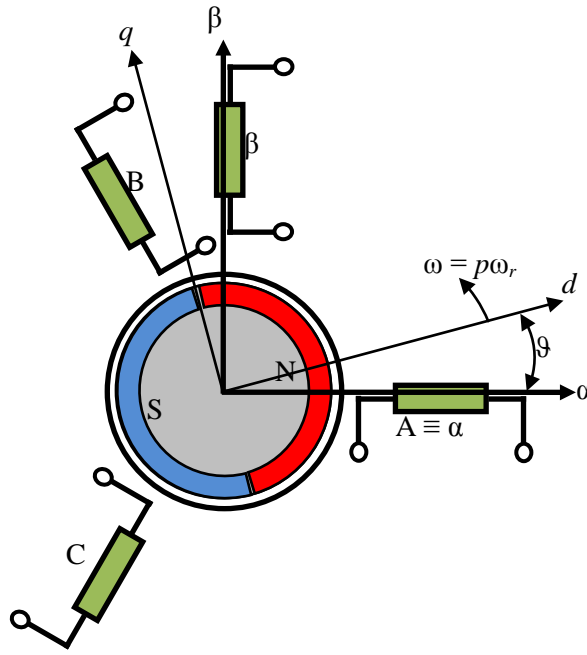
Fig. 5.3: Reference frame definition for SPMSM

The isotropic nature of the rotor allows us to write (5.4) for the flux lines along the *d*-axis cross the same thickness of the permanent magnet material as well as the back iron as do the lines along the *q*-axis, this is illustrated in Fig. 5.4.
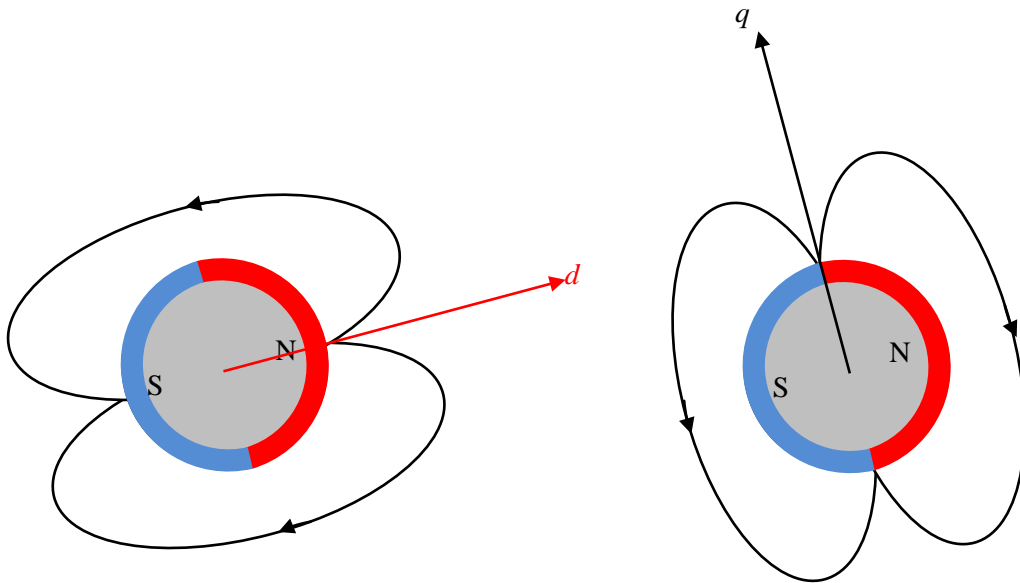
Fig. 5.4: *d*-axis (left) and *q*-axis (right) flux path through the magnets

Substituting (5.3) into (5.2) and writing the *d*- and *q*-axis equations separately, while noting that $\omega = p\omega_r$, as in (5.5) and (5.6).

$$v_d = R_s i_d + L_d \frac{di_d}{dt} - p\omega_r L_q i_q \tag{5.5}$$

$$v_q = R_s i_q + L_q \frac{di_q}{dt} + p\omega_r L_d i_d + p\omega_r \lambda_m \tag{5.6}$$

Fig. 5.5 and Fig. 5.6 show the *d*- and *q*-axis equivalent circuits, respectively.
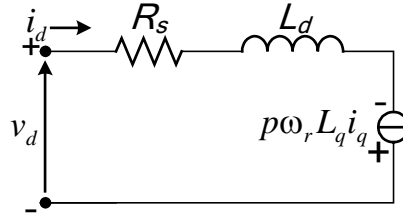
Fig. 5.5: *d*-axis equivalent circuit: eq. (5.5)
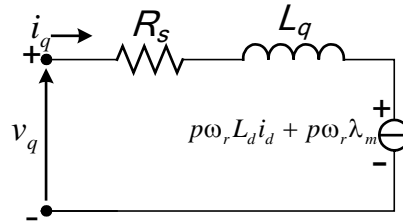
Fig. 5.6: *q*-axis equivalent circuit eq. (5.6)

As for other ac machines, the mechanical torque produced by this machine is also given by the vector product of flux and current vectors (5.7).

$$T = \frac{3}{2} p \left(\overline{\lambda}_{dq} \wedge \overline{i}_{dq} \right) = \frac{3}{2} p \left(\lambda_d i_q - \lambda_q i_d \right) \qquad (5.7)$$

Substituting for λ_d and λ_q from (5.3):

$$T = \frac{3}{2} p \left[\left(L_d i_d + \lambda_m \right) i_q - L_q i_q i_d \right]$$

Noting (5.4) and rearranging:
$$T = \frac{3}{2} p \lambda_m i_q \qquad (5.8)$$

The torque expression (5.8) shows that the developed torque consists of magnet alignment torque only; the reluctance torque is not present due to (5.4) since the reluctance all around the rotor circumference remains essentially constant. Further, the *d*-axis current does not play any role in torque production. Nevertheless, it is useful for flux-weakening.

Although the rotor's uniform cylindrical shape and uniform thickness of magnets would theoretically give same L_d and L_q and hence the machine saliency ratio of 1.0, practically this is not always the case. Since the magnetic operating point for the ferromagnetic core used in machine is set close to saturation during design stage for reasons of obtaining maximum coenergy that translates to maximum energy conversion [118], the core saturation comes into play and modifies L_d and L_q unequally.

In the *d*-axis, the flux is non-zero even at zero i_d (Fig. 5.7) due to the presence of permanent magnets (5.3), any current in the *d*-axis would change the magnetization state of the machine in a different way as it would in the *q*-axis, therefore a small saliency is always there, however, that is not usually exploited for producing reluctance torque for it would reduce the maximum current that can be applied in the *q*-axis given a certain total phase current. Fig. 5.7 and Fig. 5.8 show the magnetic characteristics of one of the test machines in *d*- and *q*-axis, respectively.
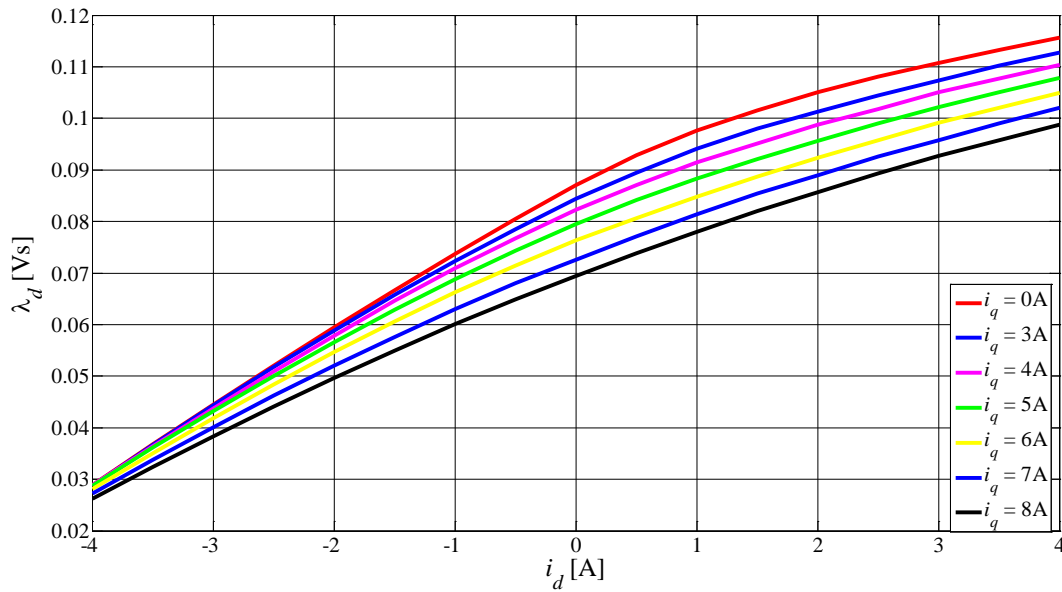
Fig. 5.7: *d*-axis flux versus *d*-axis current: parameter *q*-axis current
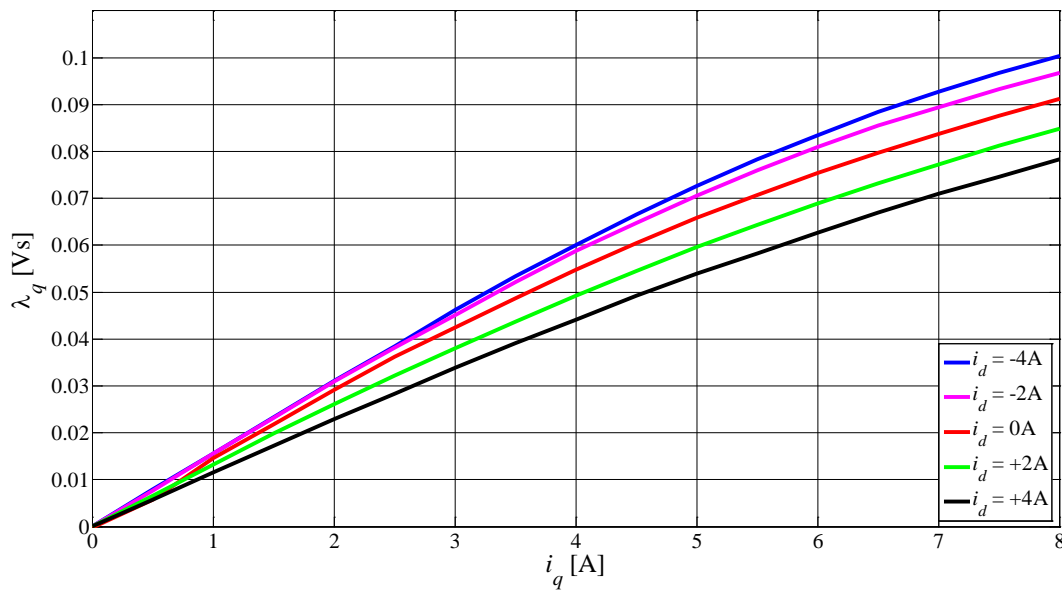
Fig. 5.8: *q*-axis flux versus *q*-axis current: parameter *d*-axis current

Fig. 5.9 shows the saturation characteristics of the two axes in terms of decreasing inductance with increasing current. It can be seen that the *d*-axis inductance experiences steeper negative slope than does the *q*-axis inductance. The machine is designed such that only with the permanent magnet flux in the *d*-axis the core approaches saturation. This is evident in Fig. 5.7 which shows that the knee of flux-current relationship is close to the point where $i_d = 0$. Any positive *d*-axis current drives the core further into saturation to the point that the flux remains essentially constant with further *d*-axis current which can be seen in the upper plot of Fig. 5.9 as inductance being inversely proportional to current and the relationship is close to linear.
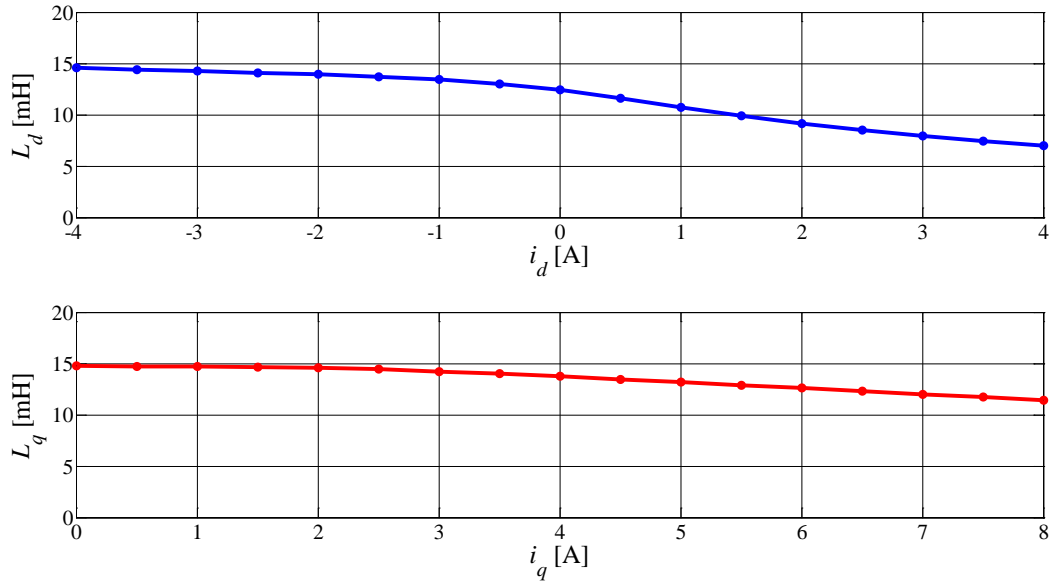
Fig. 5.9: L_d as a function of i_d (upper plot) and L_q as a function of i_q (lower plot)

5.3.   Machine Control

The machine torque expression (5.8) hints at a relatively simpler control of the machine compared to the induction machine or an IPM discussed in previous chapters. The machine torque is a function of permanent magnet flux λ_m, which is a design variable and cannot be varied during operation except undesired decrement due to temperature rise, and the q-axis current. In order to generate the demanded torque, the q-axis current must be controlled accordingly. For continuously injecting the current along the q-axis, it must be continuously identified for which the rotor position information is indispensable, here comes again the concept of vector control for this machine as well.

The vector control is about applying (continuously) a certain current vector in space that gives maximum rotor displacement (torque). As discussed for previous ac machine types, the two vector control strategies, adopted in this thesis, are presented in the following sections for this machine as well.

5.3.1.   Rotor Field Oriented Control

The rotor field oriented control (RFOC) works in the rotor flux frame. The synchronously revolving dq reference frame is fixed with respect to the rotor flux vector. As shown in Fig. 5.3, the d-axis is tied to the north pole of the rotor permanent magnets. The rotor position information is necessary to implement this control to know exactly where the magnetic north pole lies in space. The control then simply keeps track of the demanded torque by appropriately injecting q-axis current. The common control strategy for an SPMSM is zero d-axis control i.e. the field component of the stator current is null and the magnetic field of the rotor permanent magnets is exploited.

From the machine electrical equations in dq reference frame (5.5) and (5.6), the state equations (5.9) can be easily derived. Although the torque is controlled only through q-axis current Fig. 5.10, the d-axis state equation is necessary to control the current $i_d = 0$ as seen in the block diagram of Fig. 5.11. The cross-coupling terms between the two axes can be feed-forward compensated as shown, to increase the controller bandwidth. In case of an IPM, owing to different d- and q-axis inductances, the bandwidth of the current control in the two axes was different; however, here the two current controllers do not need to be tuned separately for the inductances are almost equal (5.4).

$$\frac{d}{dt}\begin{bmatrix} i_d \\ \\ i_q \end{bmatrix} = \begin{bmatrix} -\dfrac{R_s}{L_d} & p\omega_r \dfrac{L_q}{L_d} \\ \\ -p\omega_r \dfrac{L_d}{L_q} & -\dfrac{R_s}{L_q} \end{bmatrix}\begin{bmatrix} i_d \\ \\ i_q \end{bmatrix} + \begin{bmatrix} \dfrac{1}{L_d} \\ \\ \dfrac{1}{L_q} \end{bmatrix}\begin{bmatrix} v_d \\ \\ v_q - p\omega_r\lambda_m \end{bmatrix} \tag{5.9}$$
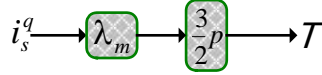
Fig. 5.10: Graphical representation of eq. (5.8)
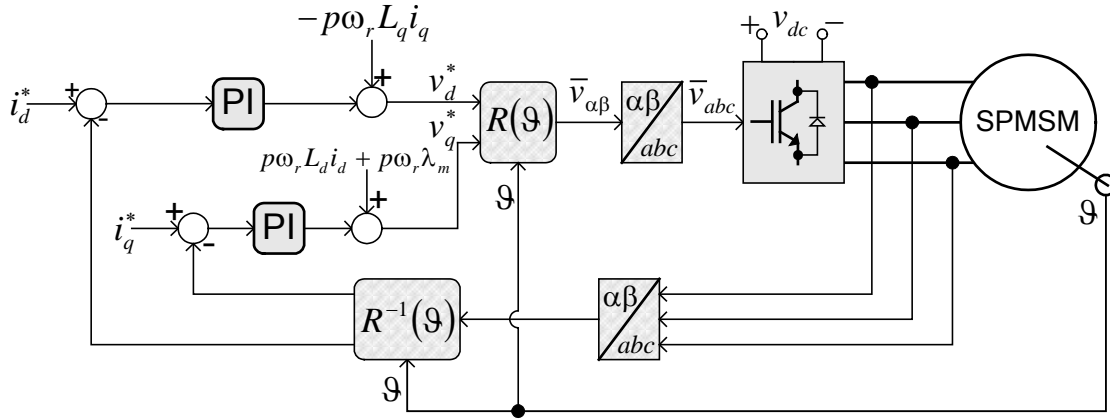
Fig. 5.11: Vector control block diagram

Based on the available system resources and load requirements of specific application at hand and the performance constraints, the control strategy can change. [155] describes as many as seven different control types, they are: (i) constant torque angle control (i.e. $i_d = 0$ control), (ii) unity power factor control, (iii) constant mutual airgap flux-linkages control, (iv) angle control of airgap flux and current phasors, (v) optimum torque per ampere control, (vi) constant loss based maximum torque speed boundary control, and (vii) minimum loss or maximum efficiency control.

5.3.2. *Unified Direct Flux Vector Control*

This control strategy has been presented in previous chapters in detail. Unlike rotor field oriented control of section 5.3.1, this control works in the stator field oriented frame for which the new reference frame $d^s q^s$ is defined as in Fig. 5.12. The speed of the rotor's mechanical reference frame ($d^m q^m$) is the same as ω in (5.2) that means the rotor flux vector remains fixed with respect to magnetic north pole and the slip is zero. The load angle (δ) is the angle between stator and rotor flux vectors, it determines the torque (and hence power) the machine produces at a certain instant and it is this angle that varies in response to varying torque demands.

Since the control is direct-flux type, the stator flux is controlled directly by d^s-axis voltage with no current controllers in the d^s-axis; however, torque control is through current regulator in the q^s-axis as discussed above for rotor field oriented control.

Referring to Fig. 5.12, the machine equations are derived from equations (5.2) in this new reference frame as in (5.10) where the subscripts dq^s signify the quantities in $d^s q^s$ frame.

$$\bar{v}_{dq^s} = R_s\bar{i}_{dq^s} + \frac{d\bar{\lambda}_{dq^s}}{dt} + j\bar{\lambda}_{dq^s}\left(\omega + \frac{d\delta}{dt}\right) \tag{5.10}$$
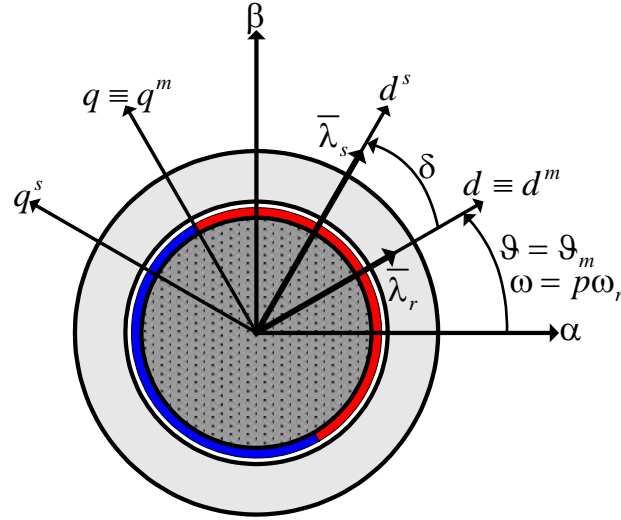
Fig. 5.12: Stator flux oriented reference frame definition

In case of stator flux oriented control, the q^s-axis component of the stator flux must be zero such that

$$\overline{\lambda}_{dq^s} = \lambda_{d^s} + j\lambda_{q^s} = \lambda_{d^s} + j0 = \lambda$$

or
$$\overline{\lambda}_{dq^s} = \lambda \qquad (5.11)$$

Having defined (5.11), the d^s- and q^s-axis equations can individually be written as (5.12) and (5.13), respectively.

d^s-axis:
$$v_{d^s} = R_s i_{d^s} + \frac{d\lambda}{dt} \qquad (5.12)$$

q^s-axis:
$$v_{q^s} = R_s i_{q^s} + \left(\omega + \frac{d\delta}{dt}\right)\lambda \qquad (5.13)$$

Equations (5.12) and (5.13) can be written in state-space notation as in (5.14).

$$\frac{d}{dt}\begin{bmatrix} \lambda \\ \delta \end{bmatrix} = \begin{bmatrix} -R_s & 0 \\ 0 & \dfrac{-R_s}{\lambda} \end{bmatrix}\begin{bmatrix} i_{d^s} \\ i_{q^s} \end{bmatrix} + \begin{bmatrix} 1 \\ \dfrac{1}{\lambda} \end{bmatrix}\begin{bmatrix} v_{d^s} \\ v_{q^s} \end{bmatrix} + \begin{bmatrix} 0 \\ -\omega \end{bmatrix} \qquad (5.14)$$

Machine torque in terms of stator flux oriented quantities, as defined above, can be written as in (5.15) by putting (5.11) in (5.7).

$$T = \frac{3}{2} p \lambda i_{q^s} \qquad (5.15)$$

As the state variable δ of (5.14) does not appear directly in torque expression (5.15), it must be replaced with i_{q^s} to render the control simpler, the mathematical derivation steps are similar to those used in previous chapter for IPM, only results are given here.

The d^s-axis state equation remains the same as in (5.14) while the q^s-axis state equation changes to (5.17) such that the state variable is i_{q^s} rather than δ when i_{q^s} is defined by (5.16).

$$i_{q^s} = \frac{1}{L_d}\left\{\left(\frac{L_d}{L_q}-1\right)\lambda\,\frac{sin\,2\delta}{2}+\lambda_m\,sin\,\delta\right\} \tag{5.16}$$

$$\frac{di_{q^s}}{dt} = -\frac{k}{L_d}\left(v_{d^s}-R_s i_{d^s}\right)+\frac{b}{L_d}\left(v_{q^s}-R_s i_{q^s}-\omega\lambda\right) \tag{5.17}$$

The factors k and b appearing in (5.17) are given by (5.18) and (5.19), respectively.

$$k = \frac{1}{2}\left(1-\frac{L_d}{L_q}\right)sin\,2\delta \tag{5.18}$$

$$b = -\left(1-\frac{L_d}{L_q}\right)cos\,2\delta+\frac{\lambda_m}{\lambda}cos\,\delta \tag{5.19}$$

However, under the condition (5.4) for an SPMSM, the factor k disappears and only b remains, which reduces the cross-coupling effect of d^s-axis on the q^s-axis only to the flux component as seen in the new state equations (5.20) written in terms of new state variables λ and i_{q^s}.

$$\frac{d}{dt}\begin{bmatrix} \lambda \\ i_{q^s} \end{bmatrix} = \begin{bmatrix} -R_s & 0 \\ 0 & \dfrac{-bR_s}{L_d} \end{bmatrix}\begin{bmatrix} i_{d^s} \\ i_{q^s} \end{bmatrix}+\begin{bmatrix} 1 & 0 \\ 0 & \dfrac{b}{L_d} \end{bmatrix}\begin{bmatrix} v_{d^s} \\ v_{q^s} \end{bmatrix}+\begin{bmatrix} 0 \\ -\dfrac{b}{L_d}\omega\lambda \end{bmatrix} \tag{5.20}$$

The developed torque can also be written in terms of load angle δ by substituting for i_{q^s} from (5.16) into (5.15) to get (5.21).

$$T = \frac{3}{2}p\lambda\left[\frac{1}{L_d}\left\{\left(\frac{L_d}{L_q}-1\right)\lambda\,\frac{sin\,2\delta}{2}+\lambda_m\,sin\,\delta\right\}\right]$$

Using (5.4) and rearranging: $\qquad\qquad T = \frac{3}{2}p\frac{1}{L_d}\lambda\lambda_m\,sin\,\delta \tag{5.21}$

Differentiating (5.21) with respect to δ and equating to zero gives the condition for maximum torque as (5.22) which is consistent with the results obtained in previous chapter. Observing (5.4) and substituting (5.22) into (5.19) gives the boundary for control stability as $b = 0$ since the q^s-axis control is stable only with $b > 0$ (5.20). The load angle is limited to (5.22) in all operating conditions especially in flux-weakening region.

$$\delta_{max} = 90° \tag{5.22}$$

Referring to the state equations (5.20), the q^s-axis control is a straightforward current control with the current sensors included in a standard drive hardware providing the necessary feedback for closed-loop control. However, in the d^s-axis, the flux control needs stator flux as feedback which is not always the measured quantity. Stator flux observer of Fig. 5.13 comes in handy here and the

control in d^s-axis depends on how accurate this observer is. As discussed before, this observer is obtained by combining equation (5.12) and the magnetic model of equations (5.3) through the observer gain g (rad/s) as shown in Fig. 5.13. At low speeds, the voltage integration part of the observer based on equation (5.12) does not give accurate flux estimate for the back-emf it needs for integration is insufficient therefore the magnetic model (represented by the block named Mag. Mod.) must be known *a priori* for proper low speed flux estimation. As the machine electrical speed rises above g (rad/s), the observer smoothly switches to back-emf integration estimation mode. In Fig. 5.13, the voltage vector $\overline{v}_{dt}^{\alpha\beta}$ is required for inverter dead-time compensation.

Fig. 5.13: Stator flux observer

Fig. 5.14 shows the overall control scheme for unified direct flux vector control. The block MTPA is not used here for $i_d = 0$ control is maintained at low speeds and this condition is relaxed only in case of flux weakening. Under the flux-weakening regime of operation, the load angle δ is limited to (5.22) through a PI controller that reduces the q^s-axis current [120] as shown on top right of Fig. 5.14.

Fig. 5.14: UDFVC Scheme

5.4.   Inverter limits and flux-weakening

The inverter current and voltage limits impose restrictions on machine control. The current limit caps the maximum torque the machine can produce at start-up or under transients. Even if the machine is capable of momentary overload to cater for the load demands, the power semiconductor switches are not. A more stringent limit is in terms of speed which is imposed by the available dc-link voltage. Above a certain speed, the back-emf induced by rotor magnetic field equals, and subsequently exceeds, the maximum phase voltage that can be applied through the inverter with a fixed available dc-link voltage. With a back-emf approaching maximum applicable stator terminal voltage, driving current into the machine becomes physically impossible (cf. Fig. 5.6). Therefore the machine flux must be reduced with increasing speed to maintain the current direction as shown in Fig. 5.6 and to respect the inverter voltage limit conditions. The current and voltage limits can mathematically be derived from the steady state equations of the machine and graphically analysed as follows.

The inverter current limit in terms of machine d- and q-axis currents can be written as in (5.23) which is the equation of a circle.

$$I_{max}^2 = i_d^2 + i_q^2 \tag{5.23}$$

For determining the voltage limit, machine equations (5.5) and (5.6) in the rotor field oriented frame are used; in steady state the derivative terms of i_d and i_q vanish. Further, noting that $\omega = p\omega_r$ from Fig. 5.12 and by assuming $R_s = 0$ for simplicity and substituting $L_d = L_q = L$ from (5.4), the two equations in the d- and q-axis become (5.24) and (5.25) respectively.

$$v_d = -\omega L i_q \tag{5.24}$$

$$v_q = \omega L i_d + \omega \lambda_m \tag{5.25}$$

The voltage limit can be obtained from (5.24) and (5.25) as follows:

$$V_{max}^2 = v_d^2 + v_q^2 = \left(\omega L i_q\right)^2 + \left(\omega L i_d + \omega \lambda_m\right)^2$$

Factorizing ωL:

$$\left(\frac{V_{max}}{\omega L}\right)^2 = \left(i_d + \frac{\lambda_m}{L}\right)^2 + i_q^2 \tag{5.26}$$

Eq. (5.26) is again the equation of a circle, however, with its centre displaced from origin due to permanent magnet flux. The equations (5.23) and (5.26) are graphically represented in the dq plane in Fig. 5.15. The voltage limit circle is drawn for three different speeds by varying ω in (5.26). It can be seen that for increasing speed ($\omega_3 > \omega_2 > \omega_1$) the voltage limit circle shrinks.

In Fig. 5.15, the centre of all the voltage limit circles is the point where the d-axis current is equal to (5.27). This current is called the characteristic current or critical current. Contrary to what is shown in Fig. 5.15, if the characteristic current lies within the current limit circle, the machine can achieve infinite speed without touching inverter voltage limit.

$$i_{char} = \frac{\lambda_m}{L} \tag{5.27}$$

The machine's magnetic equations (5.3) show that any negative d-axis current would reduce the total flux in the d-axis. Equation (5.25) confirms that a negative d-axis current would reduce the voltage required in the q-axis. Thus flux-weakening is achieved by applying a negative d-axis current. This not only keeps the voltage limit in check, it improves the power factor as well. The phasor diagram of Fig. 5.16 shows that a current vector in the second quadrant of the dq-plane (with negative i_d) reduces the voltage required and the phase angle between the current and voltage vectors. This phasor diagram is drawn for equations (5.5) and (5.6) in steady state (stator resistance is also included).
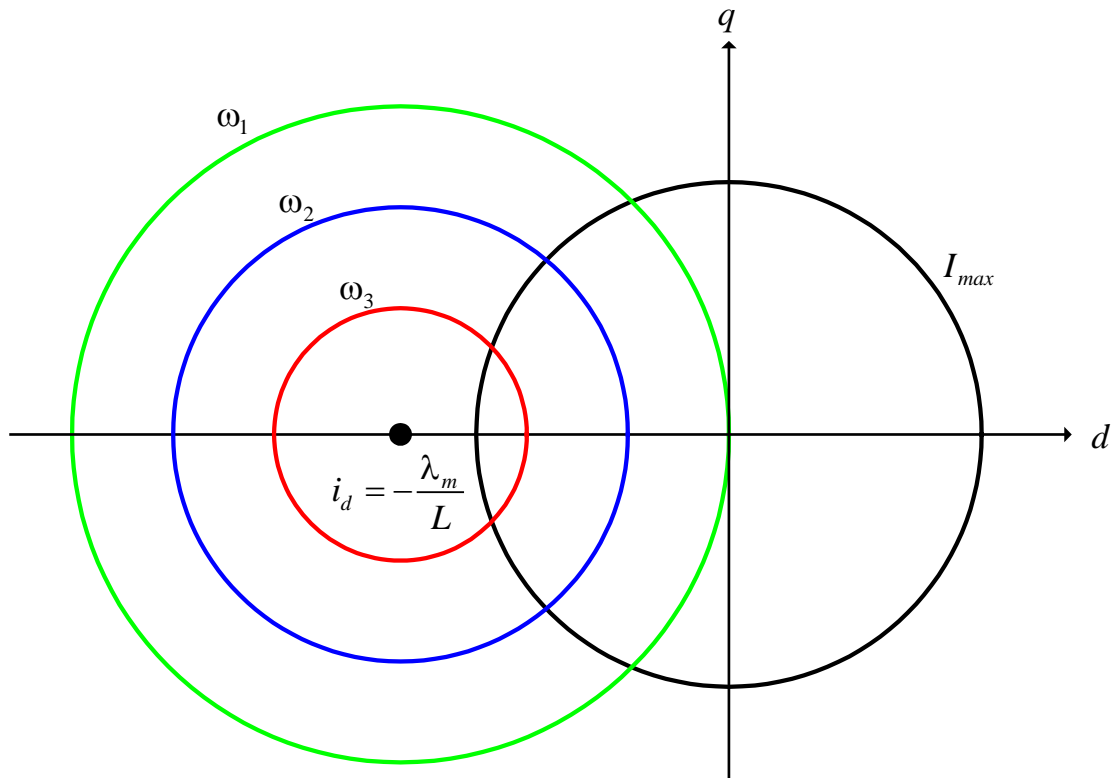
Fig. 5.15: Current and voltage limit circles
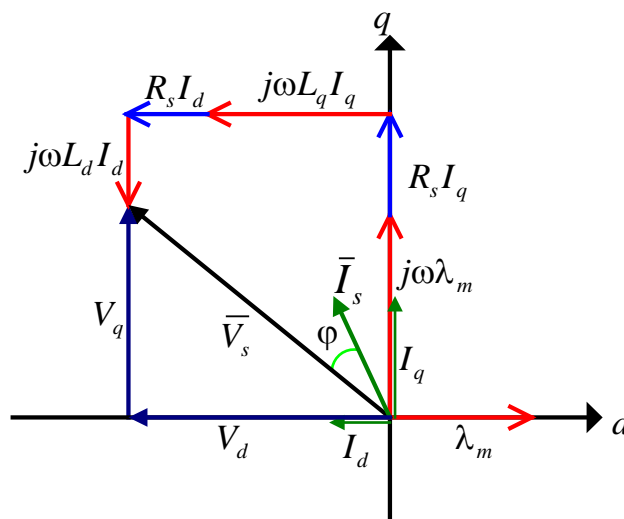
Fig. 5.16: Phasor diagram in steady state conditions with negative i_d

However, unlike an IPM that also has reluctance component of torque, the SPMSM cannot be operated with zero flux (absolute flux-weakening) for there is no torque at this condition, and

thus the maximum speed is limited to the point that also corresponds to minimum torque needed. Therefore, this machine has an upper limit on the speed it can reach while generating a minimum torque.

5.5.   <u>Parameter identification</u>

The parameter identification techniques for this machine presented in literature are no different from those discussed for an IPMSM in the previous chapter. In fact the machine parameter identification methods reviewed for the IPMSM are equally applicable to this machine as well. Apart from the methods discussed in the chapter on IPMSM, other methods for synchronous machine parameters' offline calculation and/or identification include [157-163]. Some online methods are [102, 164]. As commented earlier, the methods proposed for synchronous machines' identification do not completely respect the definition of self-commissioning followed here.

In order to identify machine parameters such that the constraints imposed by the definition of self-commissioning are all respected, a new identification strategy is required. The new method based on high-frequency injection, devised for estimating inductances of an interior permanent magnet synchronous motor and discussed in detail in the previous chapter, can be applied to this machine type as well for identifying the inductances. The details of the method are given in the previous chapter and only experimental results are presented in the following section. Core saturation effects are taken into account by varying the amplitude of injected high-frequency signal while cross-magnetization effects are taken care of through the application of a constant current in the cross-axis during high-frequency injection in the self-axis. The stator resistance is obtained through the dc injection test as described for other ac machines discussed so far. As far as the permanent magnet flux estimation is concerned, it is still a challenge and the method discussed here has its limitations which are described in detail below.

The strategy of balancing magnet alignment torque with reluctance torque poses difficulties in applying to this type of machine due to its isotropic nature. Because of (5.4), the reluctance torque is negligible in normal unsaturated conditions. However, if magnetic saturation in d-axis is exploited through d-axis current, the saturation-induced saliency may help in determining the permanent magnet flux using the torque balancing technique presented in the previous chapter. The d-axis current required may be too high and whether the test can be conducted or not depends on whether the inverter permits applying that current for carrying out the test. The following paragraph numerically and graphically analyses the case of a test machine used in this thesis.

In Fig. 5.18 the torque components of this machine are shown, as a function of current angle γ (defined by Fig. 5.17 below), in unsaturated conditions. The inductances L_d and L_q are obtained from Fig. 5.9 and the total phase current is equal to rated machine current. It can be seen that the reluctance torque is quite small compared to magnet alignment torque. Under heavy d-axis saturation conditions, the reluctance torque component increases as shown in Fig. 5.19 for the same phase current. It can be seen in Fig. 5.19 that even at rated phase current and complete saturation, there does not exist current angle (γ) for which the reluctance torque is equal (and opposite) to the magnet alignment torque to give null net torque. This is because the d-axis current required to make the reluctance torque approach the magnet alignment torque, given by (5.28), is above this machine's rated current (which is 9A).

$$i_d = -\frac{\lambda_m}{L_d - L_q} \tag{5.28}$$
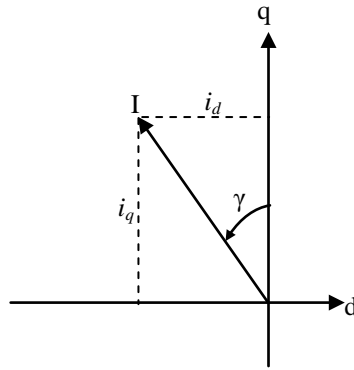
Fig. 5.17: Defining the current angle γ
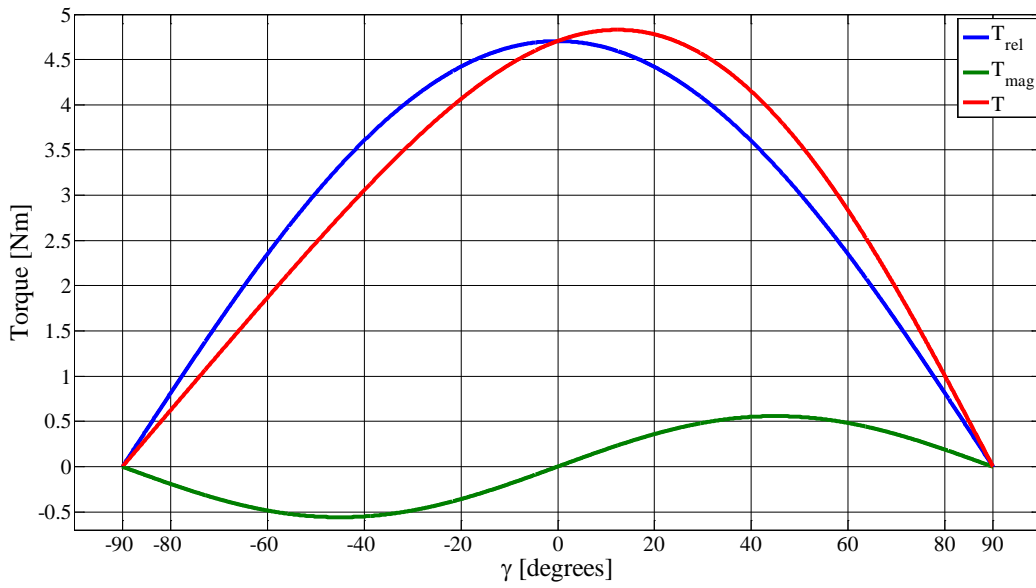
Fig. 5.18: Torque components as a function of current angle (γ) at rated current and unsaturated conditions for which inductances are obtained from Fig. 5.9
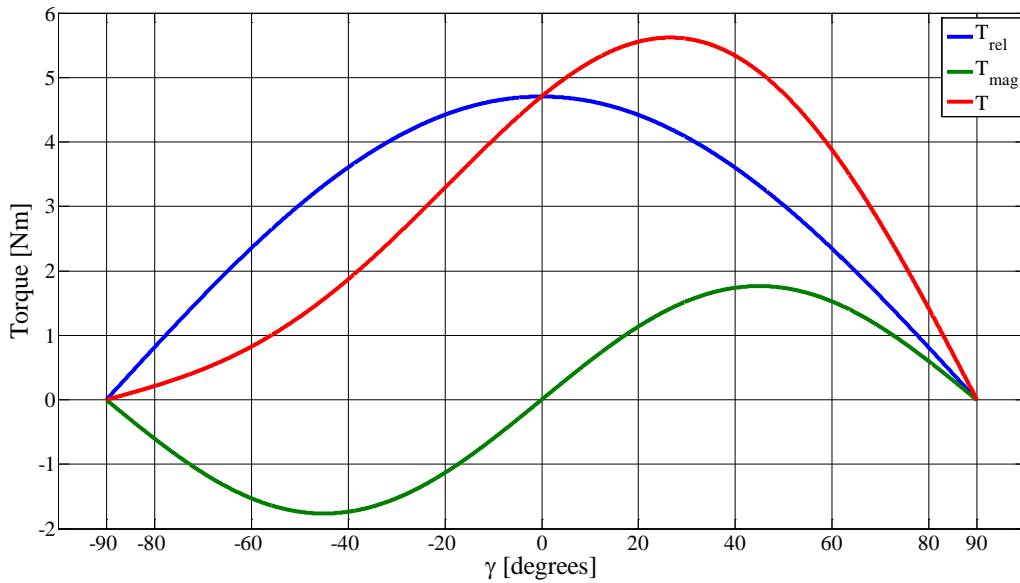
Fig. 5.19: Torque components as a function of current angle (γ) at rated current with saturated d-axis

Reading values for L_d and L_q from Fig. 5.9 at maximum i_d and $i_q = 0$ and substituting λ_m from the machine's test data, we have:

$$i_d = -\frac{0.0871}{6.98 - 14.71} \frac{[Vs]}{[mH]} = 11.3 \, [A]$$

It is evident from Fig. 5.9 (top curve) that the inductance L_d follows a linear downward droop with increasing current beyond the knee of the curve. As can be seen in Fig. 5.7, the design of this machine is such that the permanent magnet flux saturates the core even in the absence of d-axis current, any positive d-axis current does not cause appreciable flux increment and the inductance has a quasi-linear inverse proportionality with current. By extrapolating the curve for d-axis inductance, it is observed that by increasing d-axis current beyond 4A (the maximum value of i_d in Fig. 5.9), L_d reduces further to the extent that a point is reached when the reluctance torque of the machine is comparable to magnet alignment torque as seen in Fig. 5.20. At this point, the saturation-induced saliency allows the use of torque balancing method (through closed-loop speed control of Fig. 5.21) to obtain permanent magnet flux. However, this is applicable only in the condition analysed here and depends on the design of particular machine at hand.
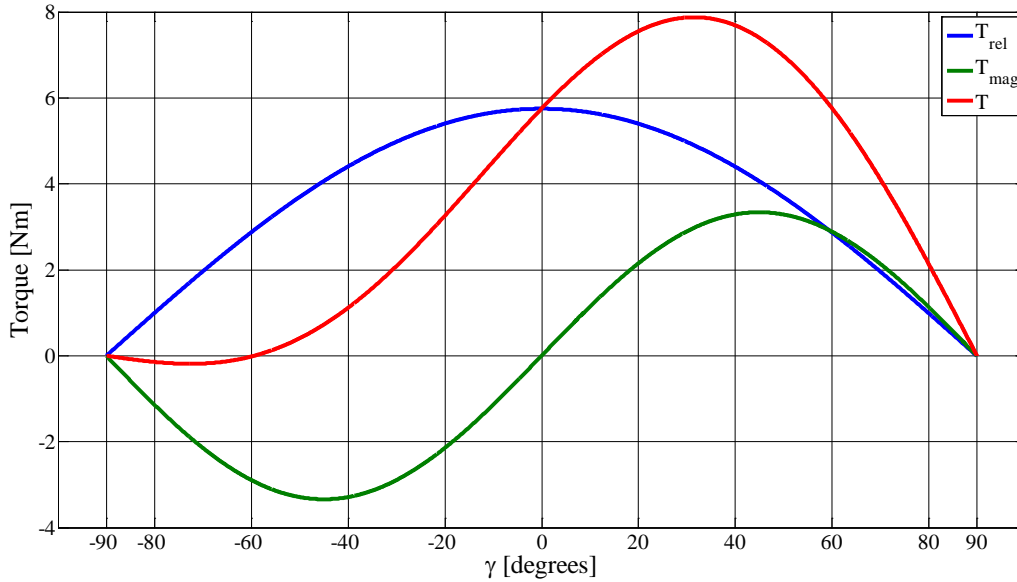
Fig. 5.20: Torque components as a function of current angle (γ) at a current higher than rated machine current and with saturated d-axis
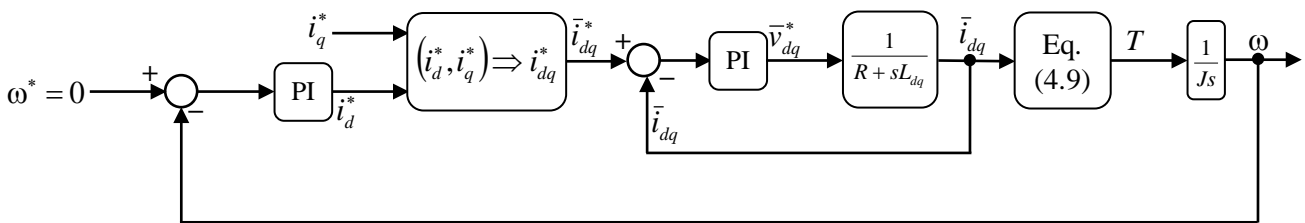
Fig. 5.21: Speed control loop for permanent magnet flux linkage estimation

For the machine under discussion, the torque balance is achieved with maximum $i_q = 3.2$A. Beyond this i_q, the alignment torque outweighs the reluctance torque, as the d-axis current is capped by the phase current limit, and the machine starts to rotate. Under this particular torque balance condition the speed controller (Fig. 5.21) output for d-axis current is noted as $i_d = 7.4$A with total phase current below machine's rated current (in violation of Fig. 5.20). The reason for this deviation is that while drawing Fig. 5.20 the dq inductances are assumed constant throughout the interval of γ

(between -90° and +90°), whereas in actual conditions they vary with i_d and i_q as per Fig. 5.9. Furthermore, (5.28) suggests that the d-axis current is independent of i_q which would mean that regardless of i_q, i_d given by the controller should remain fixed. However, that is true only when L_d and L_q are constant. Actually, L_q decreases with increasing i_q (cf. Fig. 5.9) and as L_q decreases i_d increases due to (5.28) which in turn reduces L_d further leading to more i_d required to maintain the rotor stationary. Therefore, for every i_q there exists a distinct i_d for torque balance.

At the particular dq currents at which torque balance is achieved, L_q is read from Fig. 5.9 (lower curve) and L_d is obtained from interpolation. λ_m is then estimated using (5.29). This estimate of λ_m when compared with known permanent magnet flux gives an error as high as 10%. Although λ_m estimated in this way is not as accurate, nevertheless it gives an initial offline estimate without rotating the machine.

$$\lambda_m = -i_d\left(L_d - L_q\right) \tag{5.29}$$

5.6.   Experimental results

The experiments are conducted on a commercial washing machine motor. The stator resistance estimation is through dc injection method whereas the inductances of the machine are identified with high-frequency current injection tests. The block diagram of Fig. 5.22 shows the system setup for injecting high-frequency current through PI current controllers enhanced with resonant term. The details about the PI-Res controller are given in the previous chapter.
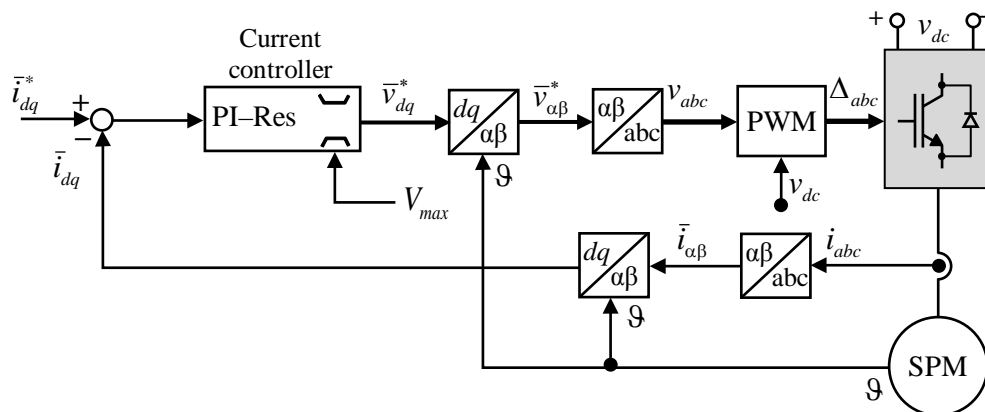
Fig. 5.22: System block diagram for tests with high frequency injection through PI-resonant controllers

Fig. 5.23 shows high-frequency injection in the d-axis while Fig. 5.24 gives the controller output voltage along with the fundamental extracted through Fast Fourier Transform (FFT). The disturbances in the voltage are caused by permanent magnet flux as well as inverter non-linearity effects as can be seen in the bar chart of Fig. 5.25. The harmonic content of the controller output voltage shows odd harmonics due to inverter non-linearity effects and even harmonics are prevalently caused by permanent magnet flux.
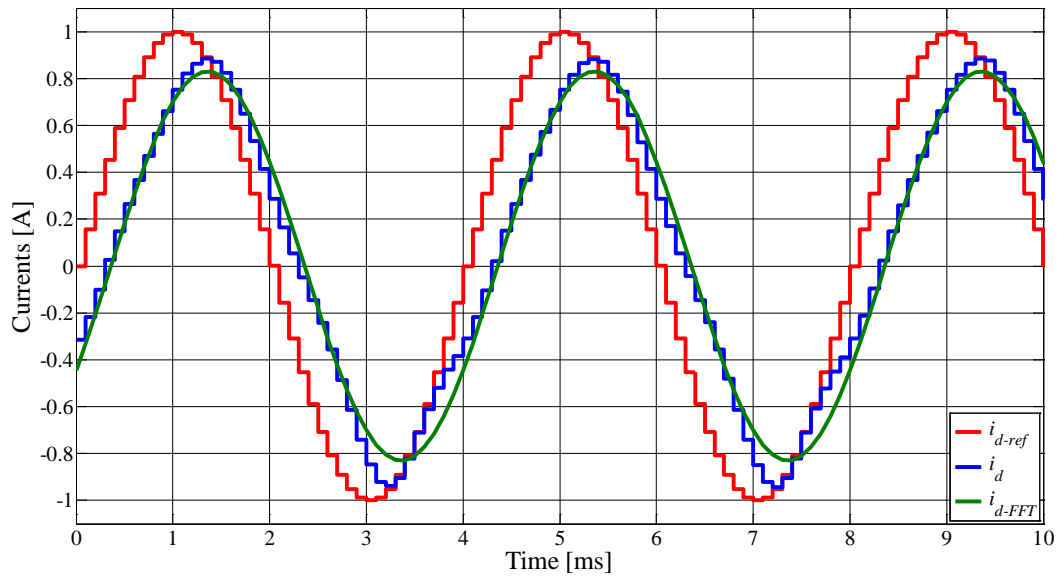
Fig. 5.23: Currents for high-frequency injection in *d*-axis: reference, actual and fundamental of the measured *d*-axis current obtained through FFT
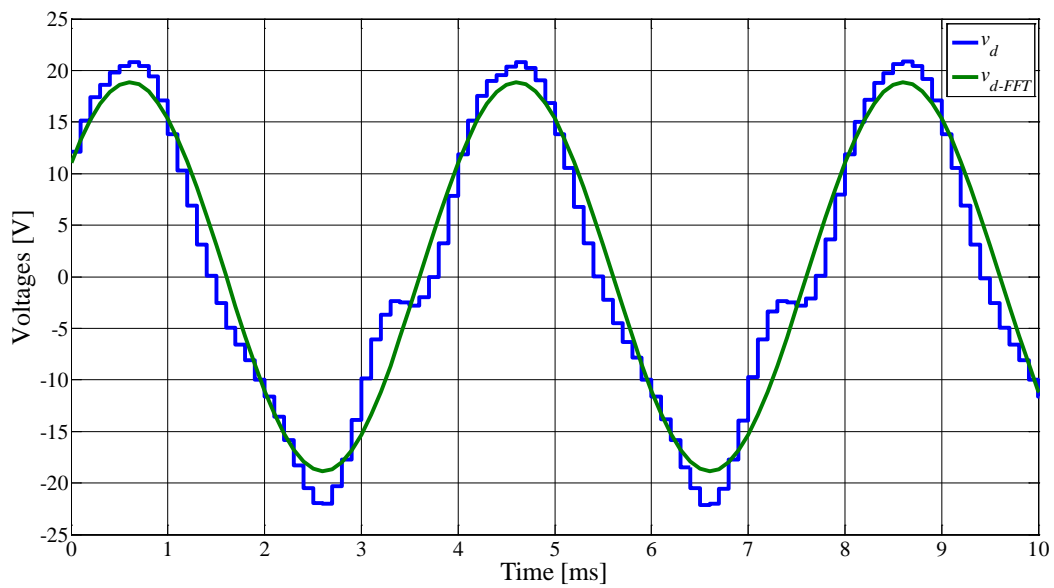
Fig. 5.24: Controller output voltage in *d*-axis and reconstructed fundamental for current injection of Fig. 5.23
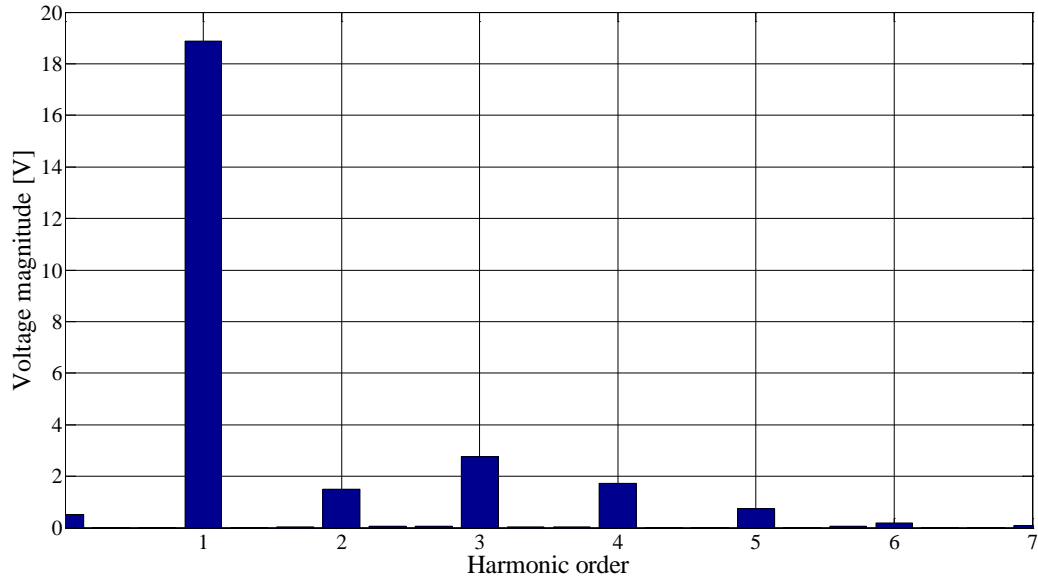
Fig. 5.25: Harmonic content of the controller output voltage for high-frequency injection in *d*-axis – FFT analysis of the voltage wave of Fig. 5.24

Similar results are seen in the *q*-axis where Fig. 5.26 shows the currents for high-frequency injection with Fig. 5.27 showing the controller output voltage. Unlike Fig. 5.24 (for *d*-axis injection) the controller output voltage is much cleaner this time for there are no distortions due permanent magnet flux linkages. The harmonic content bar graph of Fig. 5.28 confirms this fact showing only odd harmonics due to inverter non-linearity effects with no even harmonics.
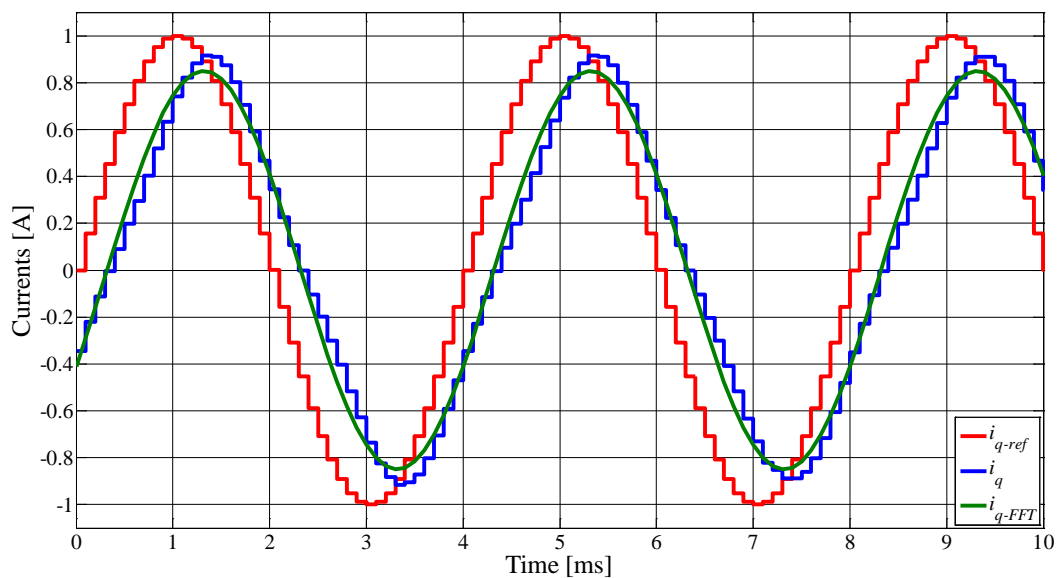
Fig. 5.26: Currents for high-frequency injection in *q*-axis: reference, actual and fundamental of the measured *q*-axis current obtained through FFT
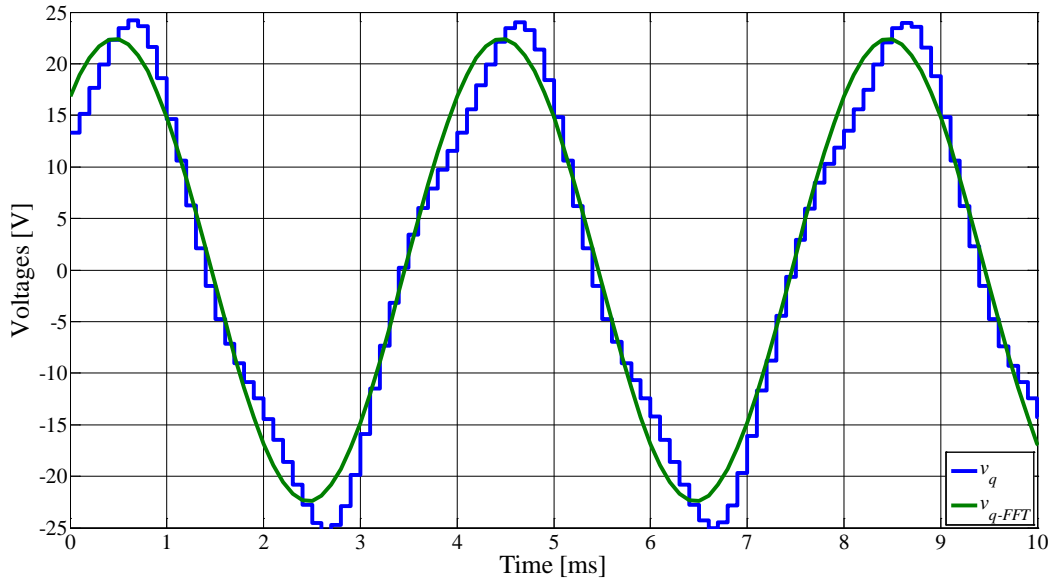
Fig. 5.27: Controller output voltage in *q*-axis and reconstructed fundamental for current injection of Fig. 5.26
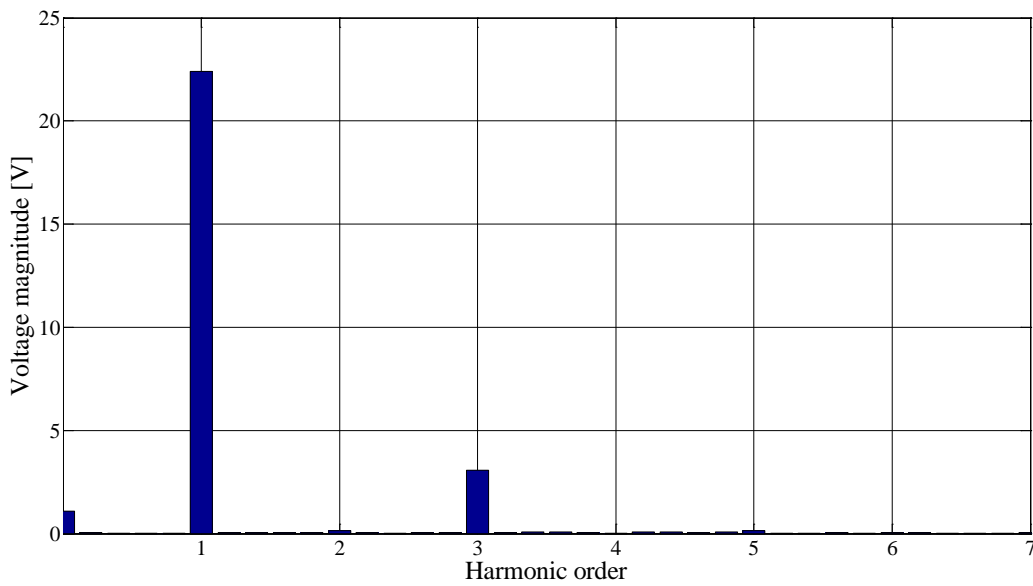
Fig. 5.28: Harmonic content of the controller output voltage for high-frequency injection in *q*-axis – FFT analysis of the voltage wave of Fig. 5.27

The inductance decrease due to saturation is observed by modulating the amplitude of the injected current and estimating the inductances from the peak values. Fig. 5.29 shows how *d*-axis inductance varies with i_d whereas Fig. 5.30 describes the situation in the *q*-axis.
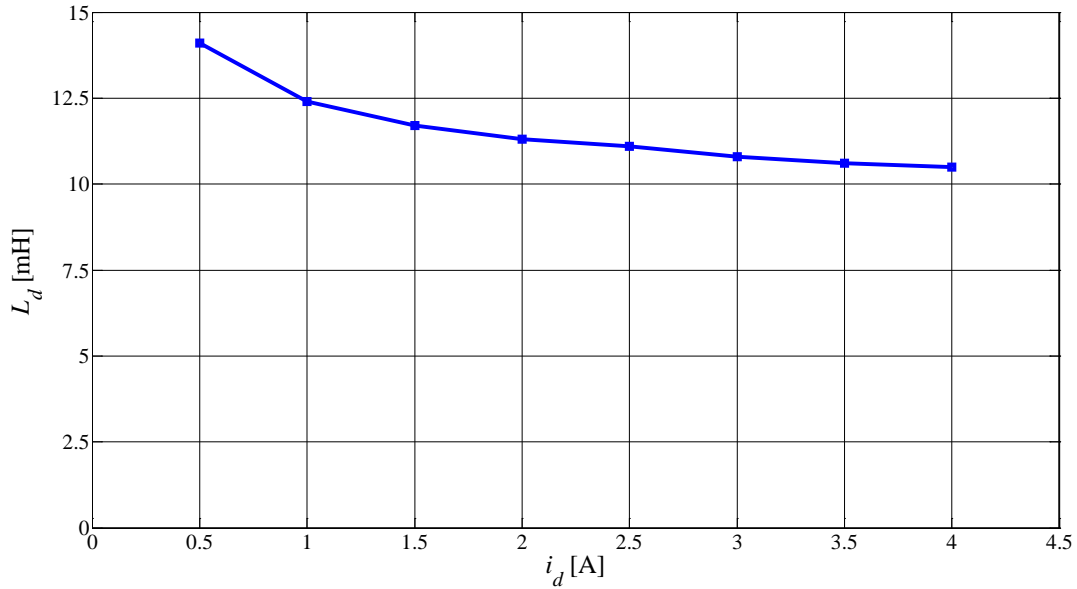
Fig. 5.29: *d*-axis saturation characteristic
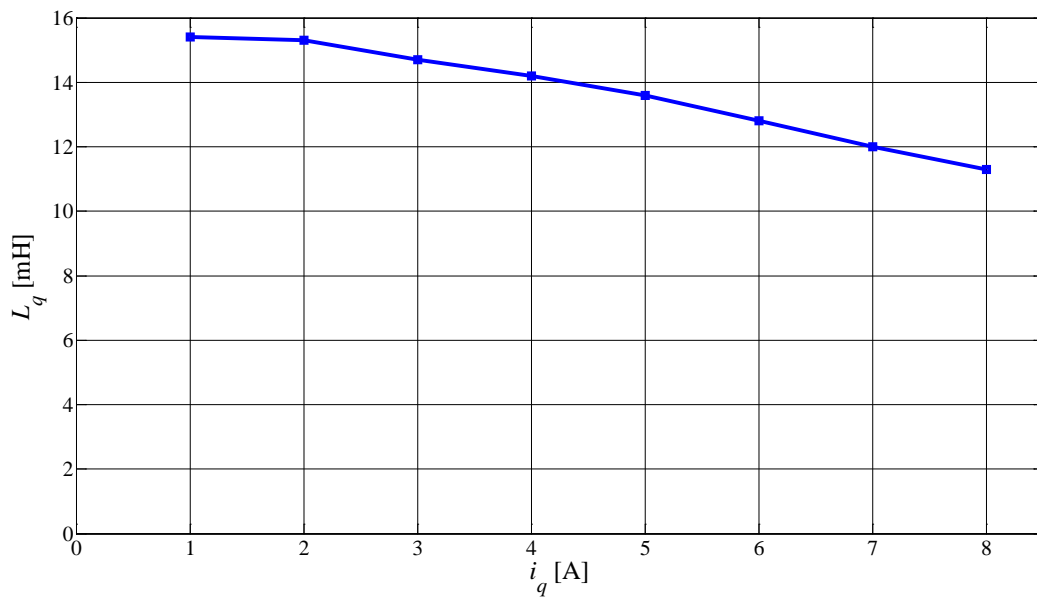
Fig. 5.30: *q*-axis saturation characteristic

Cross-magnetization effects are verified by applying constant current in the cross-axis and high-frequency injection in the self-axis. Fig. 5.31 shows the impact of *q*-axis current on *d*-axis inductance. While the self-axis saturation effects of Fig. 5.29 are evident, the cross-magnetization effects arriving from *q*-axis are also observed. It should be noted that the strategy of square-wave *q*-axis current application at a lower frequency is adopted here to keep the rotor stationary; the details about this strategy are given in the previous chapter. The cross-saturation phenomenon is also noticed in the *q*-axis in Fig. 5.32; however, the impact of positive *d*-axis current is different from the negative *d*-axis current due to the presence of permanent magnets in the *d*-axis.
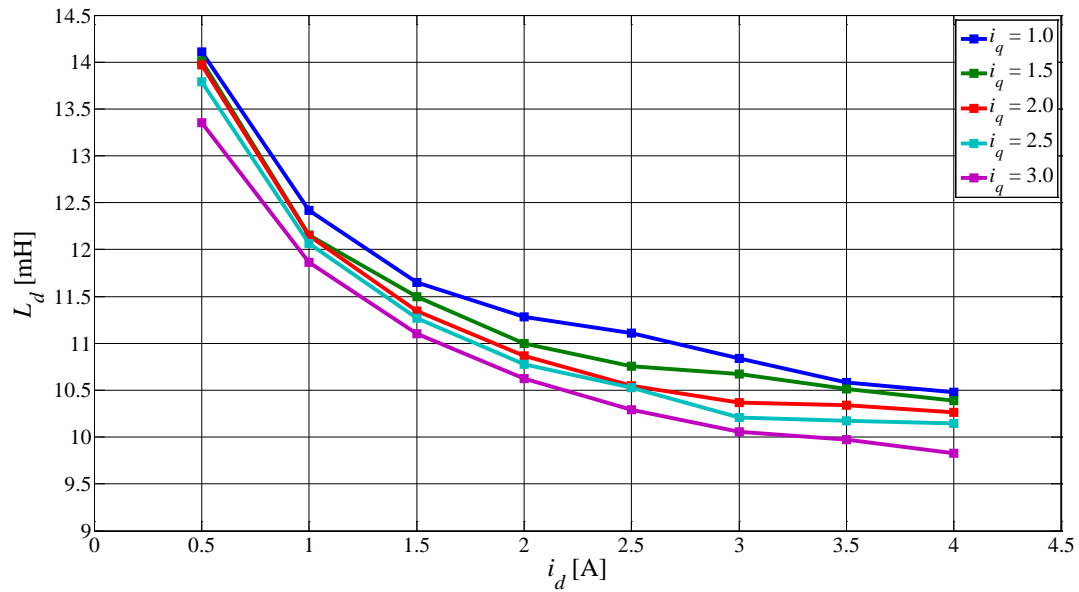
Fig. 5.31: Effects of q-axis current on d-axis inductance
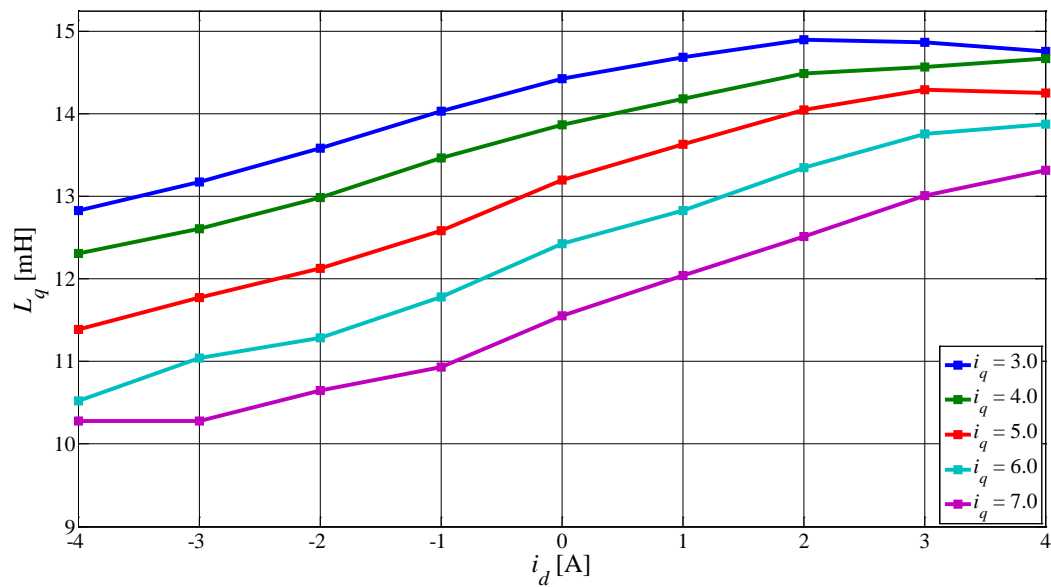
Fig. 5.32: q-axis inductance as a function of d-axis current at various i_q injection current amplitudes

The results obtained for saturation and cross-saturation effects here are useful for implementing as a look-up table for the Mag. Mod. block of Fig. 5.13 for flux estimation at low speeds when the back-emf integration model fails.

Stator resistance estimation results are not given here to avoid repetition, the results are no different from the ones obtained for induction machine and/or the IPM of previous chapters. Permanent magnet flux estimation through exploiting saturation-induced saliency is discussed in the previous section and results are given therein along with the limitations of the method.

Appendix

This section gives the nameplate and equivalent circuit parameters' data of the test machine used here.

Machine – 1: 0.60 kW Washing machine motor

General Data			
Nominal power	0.6 [kW]	Pole pairs	4
Peak power	--	Rated current	9 [A]
Back-emf	-- [V]	Max. speed*	-- [rpm]
Rated speed	-- [rpm]	J	-- [kg m^2]

* With flux-weakening

Equivalent circuit parameters		
Parameter	Value	Unit
R_s	1.32	Ω
L_d (unsaturated)	13	mH
L_q (unsaturated)	15	mH
λ_m	0.0871	Vs

<div align="right">

Chapter – 6

</div>

TORQUE ESTIMATION ACCURACY IMPROVEMENT

6.1.   <u>Importance in Traction Applications</u>

In vehicular traction applications where the internal combustion engine (ICE) reigned for almost a century, the electric motors are getting back into business due to their superior efficiency. There are many factors that contribute towards a growing interest in electrification of vehicles such as: (a) advanced design tools for efficiency and performance optimization, (b) a steady progress in power electronics over the last few decades that allowed devising and implementing better control strategies, (c) developments in storage technology (batteries) and capacity, and (d) growing concerns about environmental implications of internal combustion engines especially in congested urban centres.

The electrification is not just limited to road vehicles, other object/people carriers such as railways, aircraft systems and marine propulsion are among other sectors where electric motors enhanced with intelligent power electronics are finding a greater number of applications. The reasons are simply greater efficiency and ease of control along with minimal atmospheric pollution.

However, the electrification of road vehicles is not 100% yet for the energy density for storage batteries is yet to increase and match that of traditional fuels such as gasoline to give long-range fuel autonomy. Fig. 6.1 shows the specific energy and energy density comparison for different fuels [165]. Even the best available state-of-the-art batteries have specific energies a 100 times as smaller as those of gasoline [166]. This restriction on specific energy and energy density hinders the progress of all electric vehicles however it does pave the way for more efficient hybrid vehicles. In a hybrid electric vehicle, the ICE is reinforced with an electric motor that supplements the engine during power intensive drive cycles, such as while accelerating or on an upward ramp, and absorbs excessive power during braking that otherwise gets wasted as heat. Depending on the power rating of electric motor as a percentage of engine power, the hybrid vehicles are classified as nano- or micro-hybrid (<1%), mild hybrid (≈25%), full hybrid (50%) [165].

In a hybrid electric vehicle (HEV), the electrical machine in its motoring mode boosts the shaft torque by complementing the ICE and recovers the kinetic energy of wheels while braking which the ICE is not capable of. The drive operation selector decides when to call in electric motor to boost the torque and when to let the ICE work on its own. The power train management system called 'hybrid controller' in the context of HEVs optimizes the operation based on input parameters and decision-making algorithms defined inside it. Fig. 6.2 shows various inputs to the hybrid controller (left) and the torque demand as a function of speed (right). It can be observed that the torque demand is a vital input and therefore its estimate at the shaft as well. The torque contributed by the electrical machine can be estimated through its electrical variables and fed to the hybrid controller. It is here that the torque estimation accuracy comes into play in traction applications and affects the drive performance, efficiency and fuel economy directly.
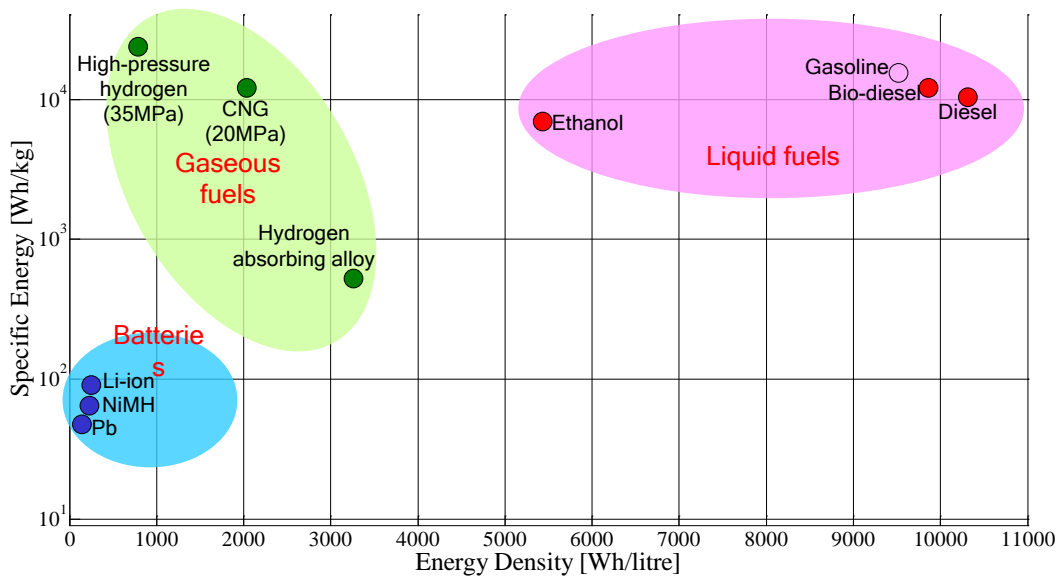
Fig. 6.1: Specific energy and energy density comparison of fuel mix and batteries [165]

ICE: combustion engine   SOC: State Of Charge
EM: Electric Motor   OPS: operation point switch
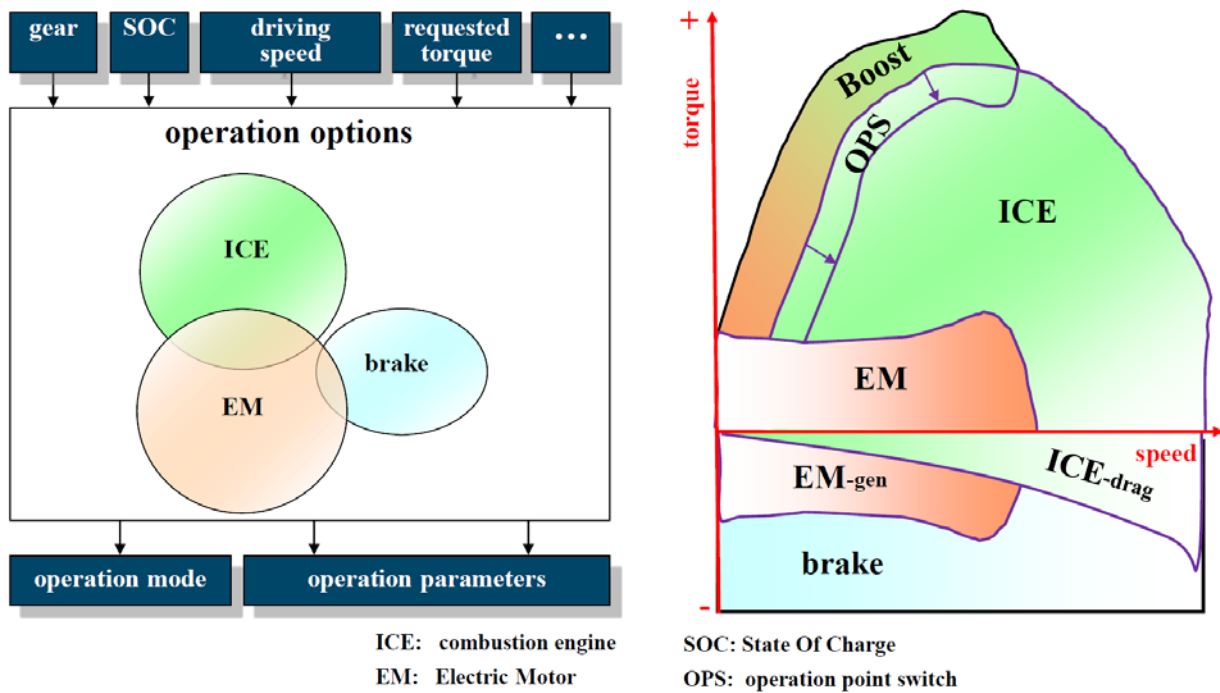
Fig. 6.2: Hybrid controller inputs and operation options (left) and torque-speed curve for a hybrid electric vehicle [165]

For parallel hybrid configurations like the one shown in Fig. 6.3 where the electrical machine is mechanically coupled with the flywheel, the machine may be required to have a 'flying start' and contribute additional torque or regenerate. In motoring mode, the torque produced by the machine must be such that it aids the engine at the rotational speed of the shaft (Fig. 6.2 - right). The torque estimation plays an important role here in that if, due to inaccurate torque computation, the electric motor is not appropriately controlled, its presence may be counterproductive besides causing severe stability problems at the drive train.
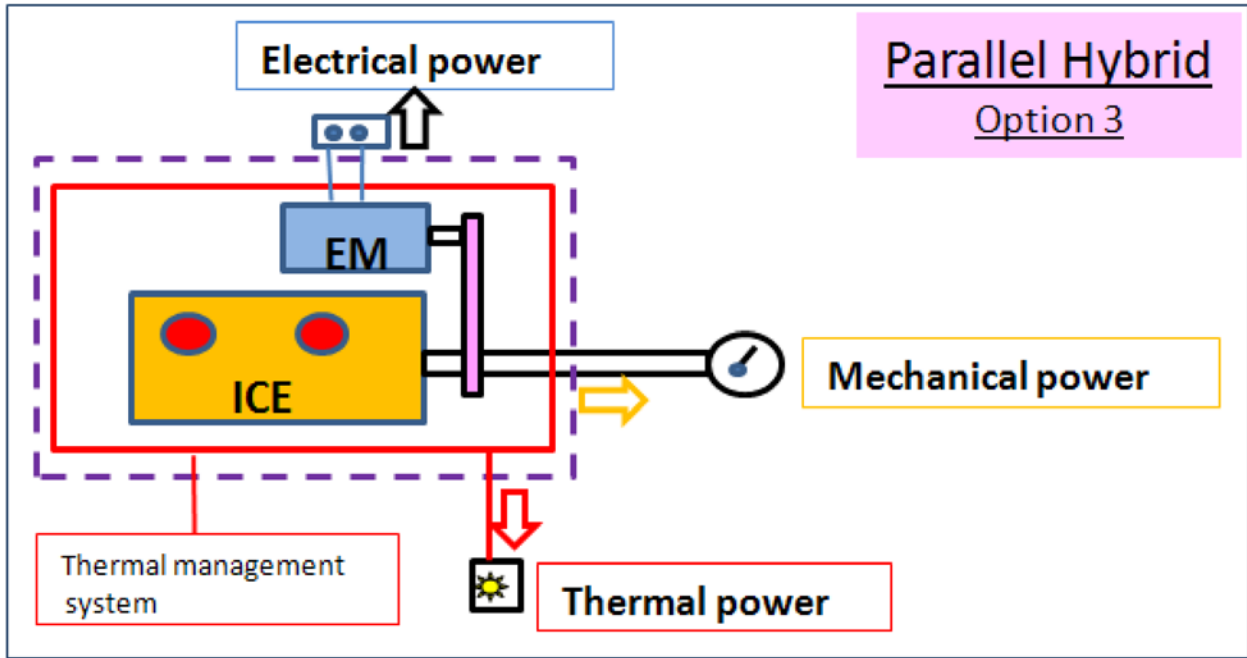
Fig. 6.3: A possible parallel hybrid configuration [165]

Another reason for having accurate measure/estimate of mechanical torque is when the wheel-mounted electric motors are to be controlled such that the functionality of differential gears is to be emulated. Differential gears come into play when the vehicle follows a curve. The individual wheels' torque demands are different on curves and therefore their control.

For the reasons detailed above, in the absence of any torque-sensing instrument, the accuracy of estimated torque is of paramount importance for proper and efficient operation of a traction drive.

6.2.   Dependence on Machine Parameters

Revisiting the torque expressions for the ac machines discussed in previous chapters, it can be observed that the computed torque depends on measurements as well as machine parameters. Various torque expressions for the induction machine derived before are reported in (6.1), while (6.2) and (6.3) give the expressions for IPMSM and SPMSM, respectively. The subscripts 'IM', 'IPM' and 'SPM' refer to induction motor, IPMSM and SPMSM, respectively.

$$T_{IM} = \frac{3}{2} p \begin{Bmatrix} \bar{i}_r \wedge \bar{\lambda}_r \\ L_m \left(\bar{i}_r \wedge \bar{i}_s \right) \\ \bar{\lambda}_s \wedge \bar{i}_s \\ \dfrac{L_m}{L_r} \left(\bar{\lambda}_r \wedge \bar{i}_s \right) \\ \dfrac{1}{\sigma L_s} \left(\bar{\lambda}_r \wedge \bar{\lambda}_s \right) \end{Bmatrix} \tag{6.1}$$

$$T_{IPM} = \frac{3}{2} p \begin{Bmatrix} \bar{\lambda}_{dq} \wedge \bar{i}_{dq} \\ \lambda_m i_q + \left(L_d - L_q \right) i_d i_q \end{Bmatrix} \tag{6.2}$$

$$T_{SPM} = \begin{cases} \dfrac{3}{2} p\left(\overline{\lambda}_{dq} \wedge \overline{i}_{dq}\right) \\ \dfrac{3}{2} p\lambda_m i_q \quad for \ i_d = 0 \end{cases} \tag{6.3}$$

As said earlier, the rotor currents in an induction machine are not directly measurable for the rotor is not 'electrically' accessible especially in case of squirrel cage induction machines. The expressions containing rotor current cannot be used for torque estimation. Other expressions contain either stator or rotor flux linkages or both as the quantities required for torque computation. The stator and rotor flux linkages are not measured quantities in standard drive, only the stator phase currents and dc-link voltage are usually measured and available for control to manipulate commands to inverter switches. In the absence of flux measurement, it must somehow be estimated from the measured quantities. The flux observers discussed throughout previous chapters just do that. However, the accuracy of these flux observers depends heavily on the machine parameter information.

For induction machines, the flux estimation at low speeds takes place using the rotor model i.e. the rotor voltage equations. The estimate is dependent on the known values of magnetizing inductance and the rotor time constant. The rotor time constant itself depends on magnetizing inductance, rotor leakage inductance and rotor resistance. While the magnetizing inductance depends on the saturation level the machine operates at, the rotor resistance varies with temperature. At high speeds the stator model based flux estimation takes over and the flux estimation is quite accurate. The stator resistance may affect the estimation depending on the switchover frequency from rotor model to stator model. This is discussed in detail in the chapter on induction machine and the results are given therein.

In case of permanent magnet machines, the computed torque is given by the vector product of rotor flux and stator current vectors as in (6.2) and (6.3). Whereas the estimated torque depends on permanent magnet flux linkages in both the cases, the reluctance torque component in the case of an IPMSM additionally depends on the d- and q-axis inductances. It can be argued that at higher speeds the torque can be directly obtained from the total d-axis flux and measured q-axis current (for rotor field oriented control) without the necessity of knowing accurately the dq-axes inductances. The argument is valid as far as the speed is high enough to give sufficient back-emf for integration and reliable flux estimation; at low speeds the machine's magnetic model is indispensable for flux, and torque, estimation. The magnetic model can be constructed either through load tests or through knowing machine inductances as a function of current (as estimated in the previous chapters).

The dependence of estimated torque on machine measurements as well as parameters is more than obvious from the discussion above. The available torque estimation methods given in literature also reiterate this fact. For instance, [167] analyses in detail the sensitivity of estimated torque of an induction machine with measurement errors as well as parameter inaccuracies and variations. The fact that the torque estimate is susceptible to parameter variations especially at low speeds is highlighted.

Torque estimation through the stator voltage model of an induction machine is presented in [168] by modifying the flux estimator. Open-loop integration is avoided and a PI regulator is used to maintain perpendicularity between back-emf and flux vectors. It is claimed that the modification improves results however results for low-speed operation are not presented and only rated speed operation is shown. At rated speed, the back-emf flux estimator is known to be quite accurate even without any modification.

Modified stator resistance approach is used to correct estimated torque of an induction machine in [169]. Neural networks based methods are used in [170, 171] while torque estimation through wavelet transforms are presented for sensorless induction motor drives in [172].

Estimation of electromagnetic torque for permanent magnet synchronous machines attracts greater interest due to their ever increasing use in vehicular applications. Model based torque estimation is discussed in [173] where the machine model's parameters are estimated and error in these parameters is minimized through a cost function. From the corrected parameters the electromagnetic torque is obtained.

Online average torque estimation, regardless of whether the phase current is sinusoidal or not, is investigated in [174] through a magnetic energy based scheme. The phase current–flux-linkage loops are determined and instantaneous torque is computed.

An analytical method is reported in [175] for calculating magnet alignment and reluctance torques of an IPMSM without computing inductances. The method constructs the reluctance model of every stator tooth and computes total torque as a summation of individual current–flux-linkage vector products.

A polynomial q-axis flux approximation is used in [176] to estimate the electromagnetic torque online. The coefficients of the polynomial are unique to every machine and hence must be determined through testing before the online torque estimation can effectively be achieved. The polynomial approximation does not cover the entire torque range of the machine.

High-frequency injection based online parameter estimation is used to estimate the stator flux as well as the electromagnetic torque for direct torque and flux control (DTFC) in [177]. A high-frequency current is superimposed on the normal sinusoidal load currents of the machine and appropriate filter and demodulation schemes are used to extract machine response to these injected currents. Machine parameters and electromagnetic torque is then recovered from the high-frequency response of the machine.

A nonlinear electrical torque observer for hybrid electrical vehicle applications is presented in [178]. Although the estimated torque is dependent on the changing machine parameters, the observer ensures that the estimation error converges to zero.

Full order flux observer is used for torque estimation in a synchronous reluctance (SynchRel) machine by [179]. The method is proposed for SynchRel machines but can easily be extended to permanent magnet machine.

A comparison of different torque estimation methods is presented in [180]. Torque estimation through general torque equations (6.2) and (6.3) is shown to be less complex and hence less costly; however, the accuracy and robustness are not as high as those of Model Reference Adaptive System (MRAS) based estimation technique. Other estimation strategies explored in this work are flux estimation with compensation scheme and torque estimation employing Sliding Mode Observer (SMO) with their relative merits and demerits discussed.

6.3.   Improving torque estimation accuracy

In the scope of this thesis, the torque is computed from general torque expressions of the machines given in the previous section. The dependencies of torque estimation accuracy on machine parameters are briefly described and experimental results are presented for torque estimation accuracy improvements by taking care of parameter variations.

For an induction machine, the electromagnetic torque is given by the expressions (6.1) and as seen here the estimation accuracy depends on the flux estimation and machine parameters. It is shown in chapter 3 that the flux estimation at low speeds heavily depends on machine parameters especially magnetizing inductance. It has also been stated that the magnetizing inductance is a

function of magnetizing current of the machine since the core saturation renders the flux-current relationship of the machine nonlinear.

At high speeds, the stator voltage equation model for flux estimation takes over and the saturation effects are inherently taken care of by the back-emf integration. The back-emf in the synchronously rotating reference frame can be estimated from the stator voltage equations of the machine as in (6.4). Since the back-emf is proportional to flux and the flux goes constant in saturation conditions, the back-emf also remains constant. The stator resistance error effect diminishes as the speed increases. The equation (6.4) shows that the back-emf is dependent both on flux and machine speed. In case the machine operates at its rated flux, the speed decides the magnitude of the back-emf that determines the accuracy of the flux estimation through voltage integration (in stationary $\alpha\beta$ reference frame).

$$\overline{E}^{dq} = \overline{v}_s^{dq} - R_s \overline{i}_s^{dq} = jp\omega_r \overline{\lambda}_s^{dq} \tag{6.4}$$

The other quantity appearing in the torque expressions (6.1) is the stator q-axis current which is a measured variable so it is dependent only on the precision of current sensors. Thus, the torque estimation accuracy is majorly affected by machine flux and its equivalent circuit parameters.

Torque estimation accuracy improvement of induction machine through self-commissioning has been partially discussed in chapter 3 (cf. section 3.7, Fig. 3.74 and Fig. 3.75). The better accuracy achieved is a direct result of knowing correct machine parameters at its current operating point. However, the case discussed in chapter 3 relates to torque estimation accuracy improvement under constant flux operation. Here the case of variable flux conditions is evaluated and a strategy for accurate torque estimation under changing flux conditions is presented.

In order to improve flux estimation accuracy at low speeds, the machine's magnetic characteristics must be incorporated into flux observer. Fig. 6.4 shows the variation of magnetizing inductance as a function of main flux for one of the test machines. The inductance is seen to decrease at higher flux levels due to saturation. Fig. 6.5 shows the rotor equation based flux estimation with appropriate modifications made to read magnetizing inductance look-up table based on the magnitude of mutual flux. The magnetizing inductance is no longer considered constant. The main or mutual flux is computed from the stator flux linkage vector using (6.5).
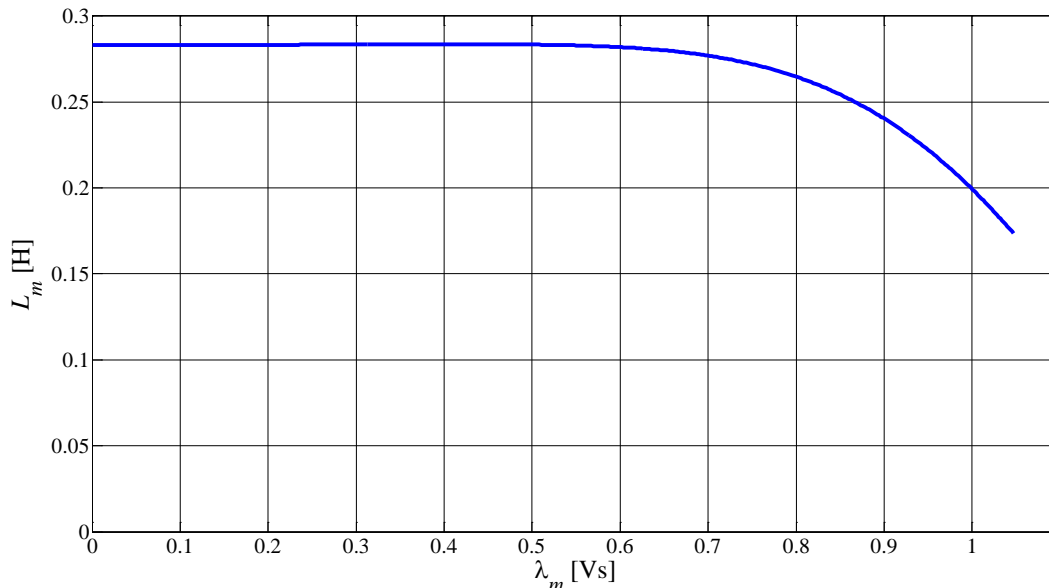
Fig. 6.4: Magnetizing inductance as a function of main flux $L_m = f\left(\left|\overline{\lambda}_m\right|\right)$

$$\overline{\lambda}_m = \overline{\lambda}_s - L_{ls}\overline{i}_s \tag{6.5}$$
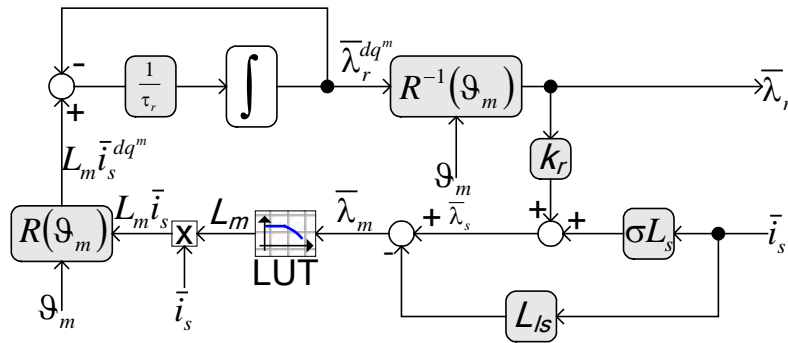
Fig. 6.5: Modified scheme for flux estimation through rotor model taking into account saturation effects of Fig. 6.4

The effects of magnetic saturation on flux and hence torque estimation in permanent magnet machines pose similar problems in that the low-speed flux estimation accuracy is highly dependent on the magnetic model of the machine. The effects of saturation and cross-magnetizing flux saturation on the magnetic model of the PM machines are discussed in detail in the previous chapters. Unlike induction machines, the control algorithm of PM machines contains look-up tables that store the detailed magnetic model of the machine, thus the torque estimation can be improved by appropriately utilizing these tables.

The peculiar problem in PM machines is the permanent magnet flux-linkages' variation with temperature. As the magnet flux varies with operating temperature so does the machine's magnetic map. Hence the magnetic model obtained at a certain temperature becomes invalid unless suitable temperature compensation strategies are adapted.

6.4.   Experimental results and comparison with torque sensor output – Induction Motor

The electromagnetic torque of an induction machine estimated from electrical variables through expressions (6.1) was compared with the output of a high-precision torque sensor. The effects of magnetic saturation on estimation accuracy were verified. Fig. 6.6 shows the torque sensor used for experiments while Table I gives the datasheet information of the torque transducer. The experimental setup used for conducting tests is shown in Fig. 6.7.

Fig. 6.6: Torque transducer Magtrol TM-308 [181]

Table I: Torque sensor datasheet information (source: [181])

Rated Torque		Torsional stiffness		Moment of inertia		Weight	
N.m	lb.ft	N.m/rad	lb.ft/rad	kg.m^2	lb.ft.s^2	kg	lb
20	15	2900	2139	2.66×10^{-5}	1.96×10^{-5}	1.2	2.65

Torque measurement	
Measurement range	0 to ±100% of rated torque
Maximum Dynamic Torque Peak Value (Overload Capacity)	0 to ±200% of rated torque
Maximum Dynamic Torque Without Damage (Overload Limit)	0 to ±400% of rated torque
Combined Error of Linearity and Hysteresis to 100% of rated torque	< ±0.1% of rated torque
Combined Error of Linearity and Hysteresis from 100% to 200% of rated torque	< ±0.1% of measured value
Temperature Influence on the Zero/Sensitivity: • In the Compensated Range +10 °C to +60 °C • In the Compensated Range –25 °C to +80 °C	 < ±0.1% of rated torque/10K < ±0.2% of rated torque/10K
Influence of Speed on the Zero Torque Signal	< ±0.01% of rated torque/1000rpm
Long-term Stability of Sensitivity	< ±0.05% of rated torque/year

Environment	
Storage Temperature Range	–40 °C to +100 °C
Operating Temperature Range	–40 °C to +85 °C
Mechanical Shock	According to IEC 68.2.27 / Class D3
Vibration	According to IEC 68.2.6 / Class D3
Protection Class	IP 44

Input and output signals	
Power Supply (max. voltage / current)	20 to 32 V$_{DC}$ / 100 mA
Torque Output (rated / max.)	±5 / ±10 V$_{DC}$
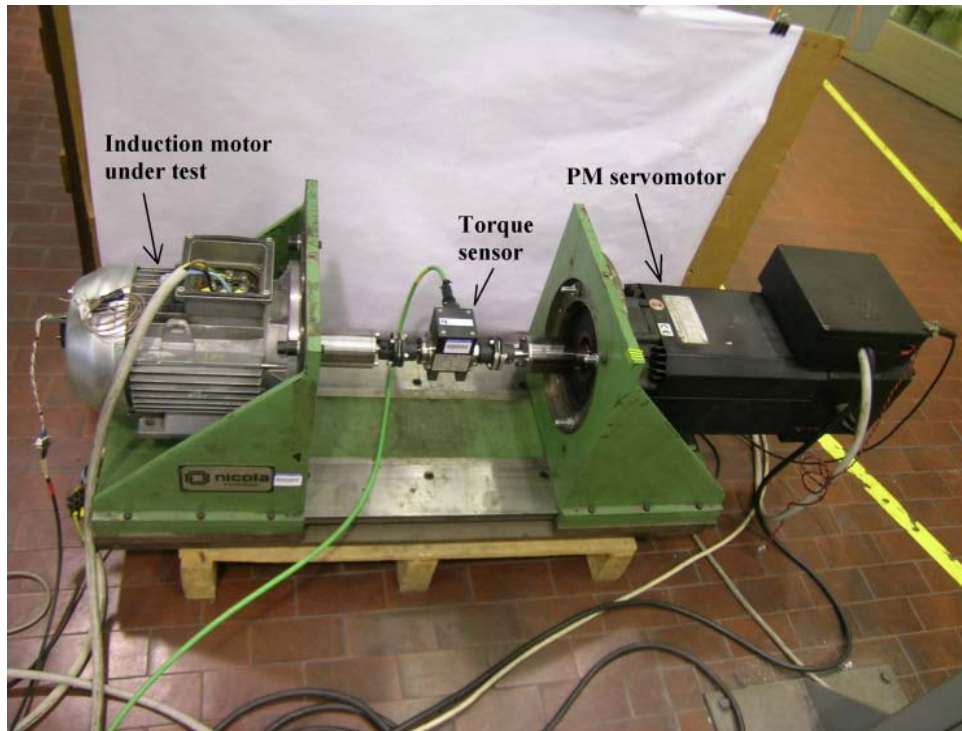
Fig. 6.7: Experimental rig showing induction machine under test, torque sensor and the prime mover

Fig. 6.8 shows estimated and measured torque as a function of machine flux. The shaft speed is set by the prime mover which is a speed controlled synchronous machine with its independent drive (Fig. 6.7). The saturation compensation through look-up table is disabled first up to verify the effects on torque estimation. As seen, at low flux levels the difference between estimated and measured torque is small however at higher flux levels when saturation comes into play the gap increases.
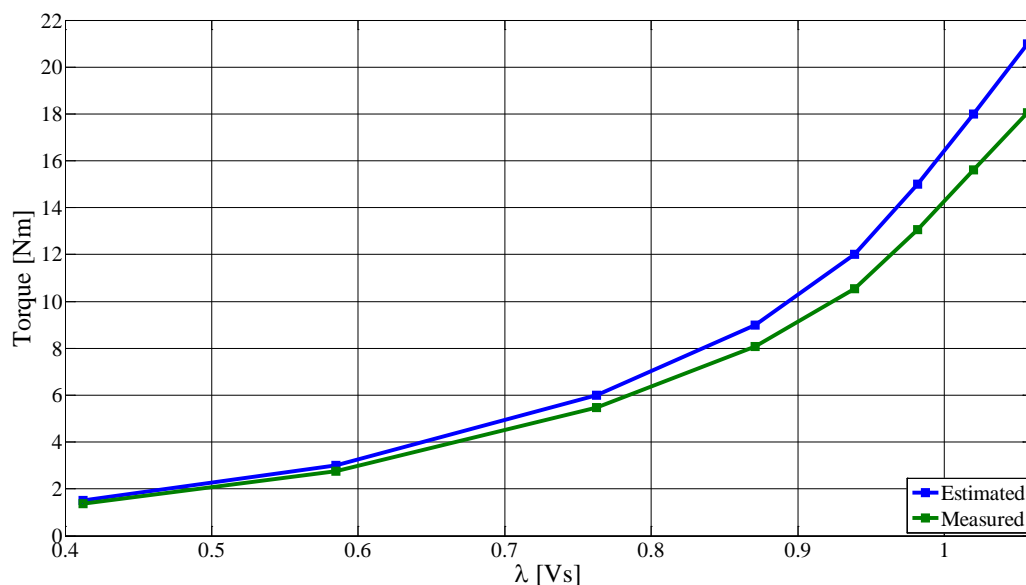
Fig. 6.8: Estimated and measured torque versus machine flux at 200 rpm with constant magnetizing inductance

In Fig. 6.9, the estimated and measured torque is plotted against machine flux with magnetizing inductance look-up table enabled in Fig. 6.5. Fig. 6.10 gives the torque estimation error for the two cases of Fig. 6.8 and Fig. 6.9. As observed, the estimation error reduces from 16% (in case of Fig. 6.8) to below 5% (Fig. 6.9).
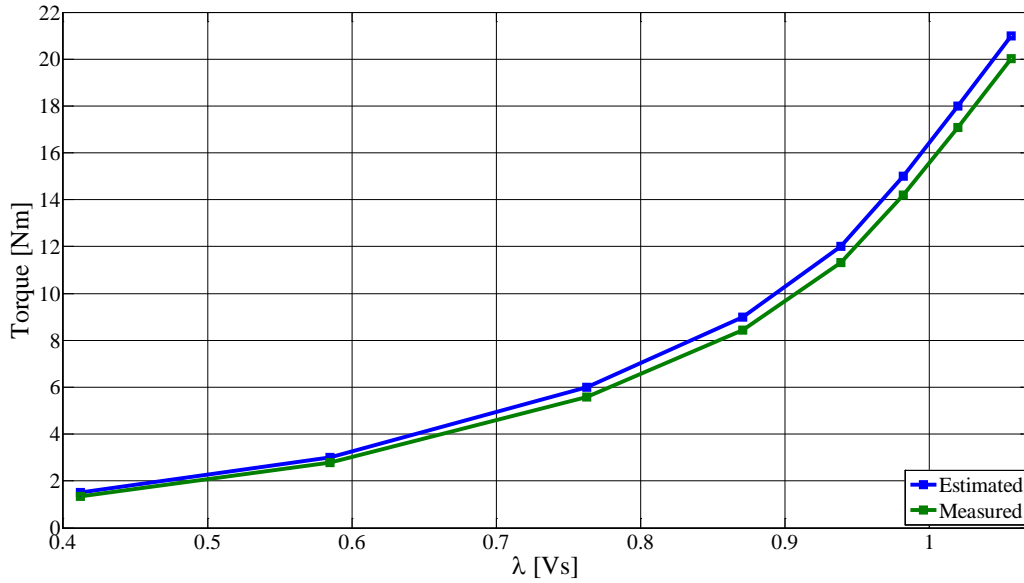
Fig. 6.9: Estimated and measured torque versus machine flux at 200 rpm with saturation compensation in flux estimate
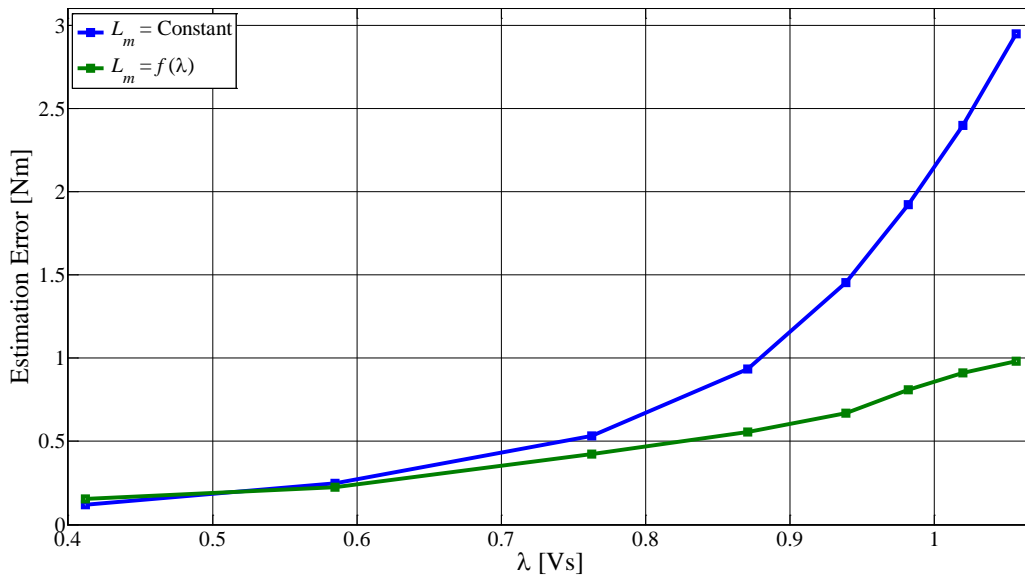
Fig. 6.10: Torque estimation error as a function machine flux at 200 rpm with and without saturation compensation

6.5.   <u>Simulation results – IPMSM</u>

For permanent magnet synchronous machines, the torque estimation through the torque expressions, (6.2) and (6.3), involving machine flux can only be used when the flux is known at all times. The accurate information about machine flux is also important for control. For instance, the direct flux control requires accurate flux magnitude information and the field-orientation, whether stator or rotor, is dependent on the flux vector's angle with respect to stator or rotor reference frame. The inability of the back-emf integration method of flux estimation at low speeds necessitates the availability of the machine's detailed magnetic model (as has been stated in previous chapters). In case the magnetic model is not available and its determination is prevented by operating conditions, the use of back-emf integration is the only solution.

Besides being dependent on speed, the accuracy of back-emf integration for flux estimation is highly influenced by errors due to inverter non-linearity and stator resistance. The effects due to these errors reduce as the speed increases. Specifically, the speed at which the back-emf goes higher in magnitude than the stator resistance and semiconductor switches' voltage drops, the flux estimation becomes immune to these errors.

In order to render the flux, and hence torque, estimation reliable at as low a speed as possible, the voltage used for integration must be refined and purified of errors for which it is necessary that the inverter effects are precisely known and stator resistance estimation is as accurate as possible.

To study the effects of stator resistance errors on torque estimation, a simulation model of an interior permanent magnet synchronous motor drive is built in Matlab Simulink. The machine's magnetic model obtained through load tests is incorporated through look-up tables. Closed-loop speed control is implemented and the machine is loaded with a constant torque. The block-diagram of Fig. 6.11 shows this closed-loop speed control.

Fig. 6.11: Simulation block diagram

The torque is estimated in the stationary αβ-reference frame using the expression (6.6) when the flux estimation is only through the back-emf integration at all speeds.

$$T = \frac{3}{2} p \left(\lambda_\alpha i_\beta - \lambda_\beta i_\alpha \right) \tag{6.6}$$

The machine is first rotated at a certain speed and then it is loaded through applying a constant load torque (T_{load} in Fig. 6.11) as shown in Fig. 6.12. On the application of a step load torque, the PI speed control loop (outer loop in Fig. 6.11) responds to this disturbance and ensures the proper tracking of reference speed signal. Once the steady state is reached after load torque application, the torque estimated through (6.6) is compared with the actual electromagnetic torque computed within the model and torque error is computed. Fig. 6.13 shows the torque estimation error as a function of speed for the three situations: stator resistance used for back-emf computation is (i) underestimated, (ii) exact, and (iii) overestimated.

It can be seen that the torque estimation error decreases considerably with increasing speed because with increasing speed the back-emf increases past the stator resistance drop and the stator resistance estimation error weighs less heavily on flux and hence torque estimation. Since the inverter dead time compensation is disabled in the simulation, the torque estimation error with overestimated R_s is seen smaller than that with correct R_s value in Fig. 6.13. This unusual result is because the overestimated R_s compensates for inverter errors and gives a better estimate at low speeds, however, at higher speeds the overestimated R_s pollutes the torque estimation as expected.

Fig. 6.12: Simulation results: load torque and induced torque (top), reference and actual speed (bottom)

Fig. 6.13: Simulation results: torque estimation error at various speed for underestimated, exact and overestimated stator resistance values

Chapter – 7

CONCLUSIONS

7.1.   Conclusions drawn from this research

The focus of this PhD work is the self-commissioning of ac motor drives. Self-commissioning is defined as the accurate estimation of machine electrical parameters (at standstill) without the necessity of rotor mechanical blocking, additional test equipment and/or commissioning personnel. The focus of the research has been on the ac motors that are most commonly used in motion control, traction applications and other industrial processes. The three ac motor types discussed are: the induction motor, interior permanent magnet synchronous motor, and surface mounted permanent magnet synchronous motor.

The accurate information of motor parameters is important for good control performance. This work has emphasized the adverse effects of inaccurate parameters on control stability, efficiency and performance and these effects are systematically studied through simulations and experiments. The most critical parameters are singled out and their importance is stated. The situations in which standard tests for obtaining machine equivalent circuit parameters are hard to carry out or are particularly inconvenient are identified. The usefulness of having machine parameters corresponding to its operating environment is underlined and that requires machine identification on site.

Among the process benefits of self-commissioning include: shorter pre-commissioning durations, least user-intervention requirements, ability of the drive to self-start, exclusion of inconvenient offline testing requirements, better exploitation of machine and inverter ratings, more accurate torque estimation in the absence of torque sensors, and so on.

The major goal of this research has been the development of automatic test strategies for parameter identification that require minimal user intervention, least data about the machine (preferably working with the nameplate data only), safest testing, no additional hardware or test equipment requirements, and finally, no or minimum disturbance in the motor-load setting.

This research has been divided in the following major areas:

1.   Study and analysis of available identification techniques from the literature and their comparison with the definition of self-commissioning to verify compliance

2.   Self-commissioning of induction motor drives

3.   Self-commissioning of interior permanent magnet synchronous motor drives

4.   Self-commissioning of surface mounted permanent magnet synchronous motor drives

5.   Torque estimation accuracy improvement

In the following, the abovementioned areas are described, emphasizing the PhD work contributions.

1.   Study and analysis of available identification techniques

In chapter 1 of this thesis, a detailed analysis of the methods and test strategies found in the literature is given. The parameter identification techniques are first divided based on the machine type they belong to and then on the basis of methodologies adopted and prerequisites for testing.

The induction machine, being the most widely used in industry due to its robustness and overloadability, has attracted the attention of most of the researchers worldwide. Therefore, the efforts directed towards accurate identification of its parameters constitute a major part of the literature available on the subject. In this thesis more than 70 publications are cited that have to do with the detection of all or some of the parameters of induction machine. The methods qualifying for self-commissioning are grouped under the heading 'offline identification techniques'. The online parameter update strategies are helpful in tracking parameter variation over time during operation; however, these methods do no lie under the definition of self-commissioning and are not discussed in depth in this thesis.

The permanent magnet synchronous machines' parameter identification has drawn interest of late as their use increased in traction applications. However, the methods dealing with standstill identification are rather few and require additional test supplies apart from the standard inverter supplying the machine. Most of the techniques found in literature give machine parameters for a running machine or require machine's isolation from the load so that the testing can be carried out. The load tests proposed for identifying the detailed magnetic model of the Permanent Magnet (PM) machines entail additional complications such as requiring a static or rotating load, torque-sensing devices etc.

Parameter identification techniques proposed in the literature are thoroughly analysed and these methods are compared against the definition of self-commissioning devised here. Some of the most promising identification methods are implemented on test machines and their implementation issues are discussed. The available parameter identification strategies are commented based on the ease of implementation, special precautions to be taken and, most importantly, the effective use of available hardware resources without requiring additional equipment on part of the user.

2.   Self-commissioning of induction motor drives

The induction machine is studied in detail in chapter 3 where its equivalent circuit, equations, and control is discussed in detail. It is shown that the machine's nameplate, although containing essential data about the machine, is not sufficient to establish accurately the numeric values of the equivalent circuit parameters: stator resistance, total leakage inductance, rotor resistance, rotor time constant and magnetizing inductance. The effects of incorrect equivalent circuit parameters on control are studied in detail and results are given for degraded performance.

The available techniques of induction motor parameter identification found in the literature which did not completely comply with the definition of self-commissioning are modified to do so. Some of the already known techniques are refined to improve accuracy and make effective use of the available hardware resources. The drawbacks rendering the tests unsafe for the machine, drive and/or the load are removed by modifying the test strategies. The tests requiring additional sensors (such as stator terminal voltage measurement) are improved such that accurate parameters are obtained also in the absence of these sensors.

The most salient improvements, outcomes and contributions with regards to self-commissioning of induction motor drives are summarized below:

a)   Stator resistance estimation: The stator resistance is estimated through the dc injection tests. Two levels of constant current are applied to the machine and the voltages required for imposing the two current levels are recorded. The resistance is

estimated from the ratio of voltage and current differences. This method is refined to minimize the effect of inverter non-linearities.

b)   Estimation of total leakage inductance:

- Estimation of this parameter through direct connection of machine across high dc-link voltage, as proposed in the literature, exposes the machine to the risk of excessive currents since the applied voltage on the phase under test is 2/3 times the dc-link voltage. Instead of applying the full dc-link voltage, a reduced voltage using PWM is applied for a new test strategy.

- For high-power low-reactance machines, a new method is proposed that uses a fast current ramp generated through current controller. The total leakage inductance is obtained from the required voltage imposed by the current controller and the slope of the reference current. The method is particularly suitable for applications in which the sampling frequency is low and open-loop voltage application may cause high current through power switches before current protection can detect this excessive current. This method is currently in production for a 150 kVA induction motor drive for compressor application.

c)   Rotor resistance estimation: 2 methods have been proposed

- The dc method of rotor resistance estimation, found in the literature, calls for the availability of inverter non-linearity compensation tables to exclude inverter errors from estimation. This dependence is excluded by introducing a new test strategy and by using a slightly modified mathematical expression. This strategy is adopted here to estimate rotor resistance referred to stator.

- Another way of estimating rotor resistance is through ac method, which is reported in the literature. The method requires an open-loop voltage application to the machine and observing the resultant current. This strategy is reversed here in that closed-loop current control is used and controller output voltage is observed. The magnitude of the applied current is limited to respect the machine's and power semiconductor switches' ratings.

d)   Estimating the rotor time constant: the following methods are studied and improved

- The first is an ac method whose theoretical background is studied from the literature but the implementation is completely modified to eliminate the need of stator terminal voltage measurement. The method injects a sinusoidal current through current regulator in one of the machine phases and then changes it to a dc value. A voltage transient appearing in the controller output voltage is observed. While the existing technique requires the iterative change in frequency of the applied signal, in this thesis the amplitude of the injected signal is iteratively changed. The benefits of this modification are: (i) no need to measure stator terminal voltage, (ii) effective use of machine nameplate data, (iii) excluding the skin effects on rotor resistance due to variable frequency.

- Rotor time constant estimation can also be carried through a dc method that uses the I-ω flux observer at standstill and applies a special current waveform through current controller. The effects of incorrect rotor time constant are seen as transients in controller output voltage. The iterative method corrects the rotor time constant value until the transient in voltage is minimum. The following improvements in this method are proposed here: the convergence speed is increased with an underestimated value of time constant to initialize

the iterative process, the magnitude of injected current is selected such that the variations in magnetizing inductance due to saturation are taken care of. The modified and improved version of this method is currently in production for a 150 kVA induction motor drive for compressor application.

All of the above methods are experimentally verified on induction motors of diverse power ranges from 0.7 kW up to 100 kW. Using these methods, a fully automatic induction motor start-up routine is devised that identifies the parameters and readies the drive for normal operation in less than 3.5 seconds. These solutions have also been provided to an industrial partner under a research contract.

e) Single phase tests identify all the induction machine equivalent circuit parameters at once by applying single-phase ac voltage to the machine at two different frequencies. The available methods work in open-loop and require extensive memory and computational power to perform offline Fourier series expansion for computing parameters. The known single-phase tests are conducted through closed-loop current controllers here and offline data elaboration is replaced with online parameter computation. Resonant filters are used here instead of Fourier analysis to establish phase angle between applied current and controller voltage. The controller output voltage is distorted due to inverter non-linearity effects that render the computation of phase angle rather difficult.

3. Self-commissioning of interior permanent magnet synchronous motor drives

In chapter 4 an in-depth analysis of parameter identification of IPMSMs is presented along with the most up-to-date publications available in literature (at the time of compiling this dissertation). The available schemes do not all identify machine's magnetic behaviour at standstill which is the foremost requirement for self-commissioning.

In the scope of self-commissioning of IPMSM drives, following are some highlights of the work presented in this thesis:

a) Estimation of stator resistance is through well-established dc injection strategy as discussed for induction machine above. The inverter non-linearity effects are excluded by applying two-level dc with the difference between them kept a minimum. The resistance is obtained from the ratio of the voltage and current differences.

b) Parameter identification techniques found in literature are studied in detail while classifying them in 'standstill' and 'in-operation' identification schemes. The feasibility and applicability of these methods are discussed and their shortcomings and limitations are pointed out.

c) A detailed study of a test machine's magnetic model is presented. It is shown how the magnetic model not only affects flux estimation but also the maximum torque per ampere characteristic. The drawbacks of using analytical expressions assuming constant inductances instead of true magnetic model for maximum torque angle computation are exposed.

d) A new method for inductances' estimation that complies with the definition of self-commissioning is proposed and its implementation issues are discussed. The method is based on high-frequency current injection. A high-frequency current is injected through current controllers along d- and q-axis and controller output voltage is recorded. The impedance for the injection axis is computed at different current levels and inductances are obtained from known injection frequency. This new method has the following salient features:

- The injected current is zero-centered so there is zero mean torque on the rotor even if the injection axis is the q-axis. The rotor blocking is thus ruled out.

- The closed-loop feedback controlled nature of the method does not compromise machine and inverter safety.

- Magnetic saturation effects are taken care of by modulating the amplitude of the injected current. Saturation is seen as inductance decrement along the axis of injection.

- Cross-saturation effects are also evaluated by this method. These cross-saturation effects are quantified by maintaining a constant current along cross-axis while injecting high-frequency currents in the self-axis.

- During cross-saturation effects analysis, a constant current along d-axis does not produce any torque, however along q-axis it does. To rule out rotor blocking, a square wave current is applied along q-axis whose frequency is lower than d-axis injection and high enough to give zero average torque on the shortest time span possible.

This new method is experimentally verified on two different machines: first, a 30 kW traction motor prototype is tested and results are compared with finite element analysis solution for inductances; secondly, a 7.5 kW light traction prototype is self-commissioned and results are matched with magnetic characterization data of the machine.

e)   A new method for permanent magnet flux-linkages estimation is proposed here. This method adopts the torque balance strategy between magnet alignment torque and reluctance torque. An unconventional speed control is designed that keeps the rotor at rest by controlling the d-axis instead of q-axis current. A constant q-axis current is applied through current regulator which causes alignment torque that tends to turn the rotor. The speed controller issues appropriate d-axis current command to nullify the alignment torque. At the equilibrium condition, the d- and q-axis inductances are used along with d-axis current to compute λ_m. This method is suitable for machines having considerable reluctance torque.

f)   Once the machine's inductances are obtained as function of d- and q-axis currents and PM flux is known, the machine MTPA table is generated completely offline. The results are compared with MTPA curve obtained experimentally.

4.   Self-commissioning of surface mounted permanent magnet synchronous motor drives

Parameter identification strategies for these machines, discussed in chapter 5, are similar to those discussed for IPMSM in the previous section. The high-frequency based method for estimating inductances as a function of current proposed for IPMSM is equally applicable to this machine. However, the method for estimating PM flux linkages discussed above can be applied only to machines that have considerable saturation-induced saliency.

The conclusions given above for self-commissioning of IPMSM are relevant to this machine as well. The following are some additional points to be noted for a SPMSM:

a)   Given that the rotor is isotropic, the d- and q-axis inductances are equal (at least theoretically). However, depending on the design of the machine and the quantity of the permanent magnet material used, the core saturation may cause these inductances to differ a great deal at higher current levels. These effects are presented in the results' section of the chapter on SPMSM where the d- and q-axis inductances given as functions of d- and q-axis currents, respectively, show the impact of saturation along d-axis to be more significant than that in the q-axis.

b)   The torque balance method of PM flux estimation is applied to this machine by exploiting the saturation induced saliency. A positive d-axis current drives the core into saturation along the d-axis thereby reducing the L_d. A reduced L_d with a fixed L_q helps generate enough reluctance torque to facilitate λ_m estimation. However, the method is limited to machines that can experience considerable saturation induced saliency.

The experiments for self-commissioning are conducted on a commercial 900 W washing machine motor and results are compared with known magnetic characterization data of the machine.

5.   Torque estimation accuracy improvement

Influence of motor parameter errors/variations on torque estimation of ac machines and torque estimation improvement are discussed in chapter 6 with a particular reference to traction applications. Available torque estimation methods reported in the literature are studied. From these methods, it is noted that no matter how complicated algorithms are used the best way to improve estimation accuracy is to increase the precision with which the electrical variables and parameters are known.

For the machine types studied in this thesis, following strategies are adapted to improve torque estimation accuracy:

a)   For induction machine, the accuracy of torque estimation depends on the estimated flux. In the absence of flux sensors in standard drive hardware, the machine's flux is estimated from measured electrical quantities and parameters. At high speeds, the voltage integration model gives accurate flux estimation. However, at low speeds the rotor equation model is the only choice to estimate flux with and this model depends highly on machine parameters. One of these parameters being the magnetizing inductance that is saturation level dependent. By incorporating the machine's saturation characteristic in the flux observer, estimation accuracy is improved here. The results are compared with a high-precision torque sensor measurements.

b)   In case of an IPMSM, the magnetic model of the machine is indispensable to accurately determine the torque at low speeds. However, in the absence of magnetic model, the flux and torque estimation takes place through back-emf integration model for which it is important to know stator resistance and inverter non-linearity effects accurately. The simulation results have shown that the minimum speed at which the torque estimation error is small can be lowered by compensating for inverter dead-time effects and determining the stator resistance accurately.

7.2.   <u>**Publications**</u>

Following is a list of research publications produced in the course of this PhD work.

1.   Self-Commissioning of Interior Permanent Magnet Synchronous Motor Drives with High Frequency Current Injection – in IEEE Transactions on Industry Applications [182]

2.   Unified Direct-Flux Vector Control of Induction Motor Self-Commissioning Drive with Analysis of Parameter Detuning Effects [183]

3.   Self-Commissioning of Interior Permanent Magnet Synchronous Motor Drives with High Frequency Current Injection [184]

4.   Unified Direct-Flux Vector Control of Induction Motor Drives with Maximum Torque per Ampere Operation [185]

The following publications were under review at the time this thesis was submitted:

1. S. A. Odhano, R. Bojoi, S. Rosù, A. Tenconi, "Identification of the Magnetic Model of Permanent Magnet Synchronous Machines Using DC-biased Low Frequency AC Signal Injection", under review for ECCE-2014, Pittsburgh, PA, USA

2. S. A. Odhano, R. Bojoi, A. Boglietti, S. Rosù, G. Griva, "Maximum Efficiency per Torque Direct Flux Vector Control of Induction Motor Drives", under review for ECCE-2014, Pittsburgh, PA, USA

7.3.   **Recommendations for future work**

This PhD research has shown that offline standstill parameter identification is a viable solution for industry to reduce pre-commissioning time and outage-time in case of broken motor replacements without changing the drive. The methods for parameter estimation studied, refined and proposed here can be used with no additional hardware requirements. The test algorithms developed can work with maximum autonomy with minimum intervention from the user and without exposing the machine and/or drive to any risk of damage. The closed-loop nature of most of the tests ensures that the system is not exposed to high voltages and currents at any time.

Any future research in the area of self-commissioning may benefit from this study. The test strategies adopted here can be improved and combined with other identification methods to improve results. Following points can be considered, in particular, as the starting point for further research:

a) Inverter self-commissioning algorithms available in literature can be merged with the tests proposed here to render the entire drive capable of automatic parameter identification and user-free start-up

b) Methods and algorithms that combine the offline identification process with online parameter update schemes can be developed. This will help in keeping track of parameter variations with operating conditions and in identifying anomalous system conditions, such as faults.

c) A study can be undertaken to identify and correlate permanent magnet flux with temperature to take care of changing machine operating conditions.

d) The present study can extended to other machine types such as switched-reluctance machines that are finding increasing applications in high-performance drives.

e) Self-commissioning can be helpful in fault-tolerant drives for increased system reliability.

This page was intentionally left blank

Appendices

A1.   Software and hardware tools used in this research

The work presented in this PhD research has been carried out at the Electrical Machines Laboratory of the Dipartimento Energia (previously Dipartimento di Ingegneria Elettrica Industriale) at the Politecnico di Torino (Italy). A part of the experimental work has also been performed at the High Power Machines Laboratory of the Department of Electrical and Electronic Engineering at the University of Nottingham (the United Kingdom). During this research, a number of hardware and software tools have been used which are listed below.

Software:

i)   Matlab® Programming Language

ii)   Matlab Simulink

iii)   C Programming Language

iv)   dSpace's experiment software ControlDesk

v)   Infolytica's MagNet (Finite Element Analysis software)

Hardware:

i)   dSpace PPC (Power PC) Controller Boards (DS1103, DS1104)

ii)   40 kVA ABB Servo Drive Selivector (Fig. A.1)

iii)   Siemens DC Machine Drive

iv)   45 kVA Eurotherm Drive 584SV

v)   27 kVA Sitra Converter (Fig. A.2)

vi)   25 kVA Power Converter E5 (Fig. A.3)

vii)   Analog to Digital and Digital to Analog Converters

viii) Position sensors and torque transducers

Test motors:

i)   CESET 700 W induction motor prototype

ii)   Electro Adda 2.2 kW induction machine (Fig. A.4)

iii)   Electro Adda 4 kW induction machine (Fig. A.5)

iv)   Siemens' 32 kW D-91066 Erlangen Compressor induction motor (Fig. A.6)

v)   Inversys, Brook Crompton 3 kW induction machine

vi)   Interior Permanent Magnet Traction Motor Prototype 30 kW (Fig. A.8)

vii)   Interior Permanent Magnet Light Traction Prototype 7.5 kW (Fig. A.7)

viii) 700 W CE_PF_R1 – IPM prototype

ix)   Aksoll 600 W commercial washing machine motor (Fig. A.9)
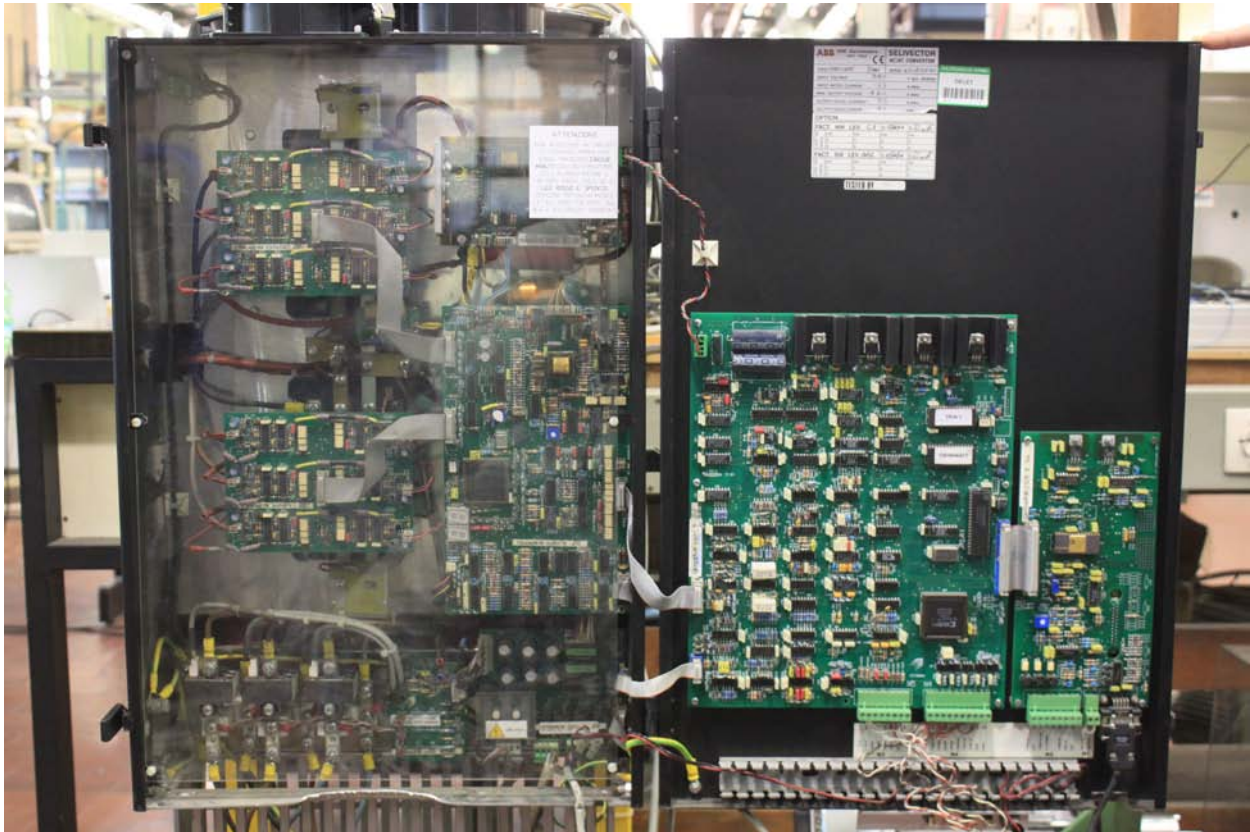
Fig. A.1: 40 kVA ABB Servo Drive Selivector
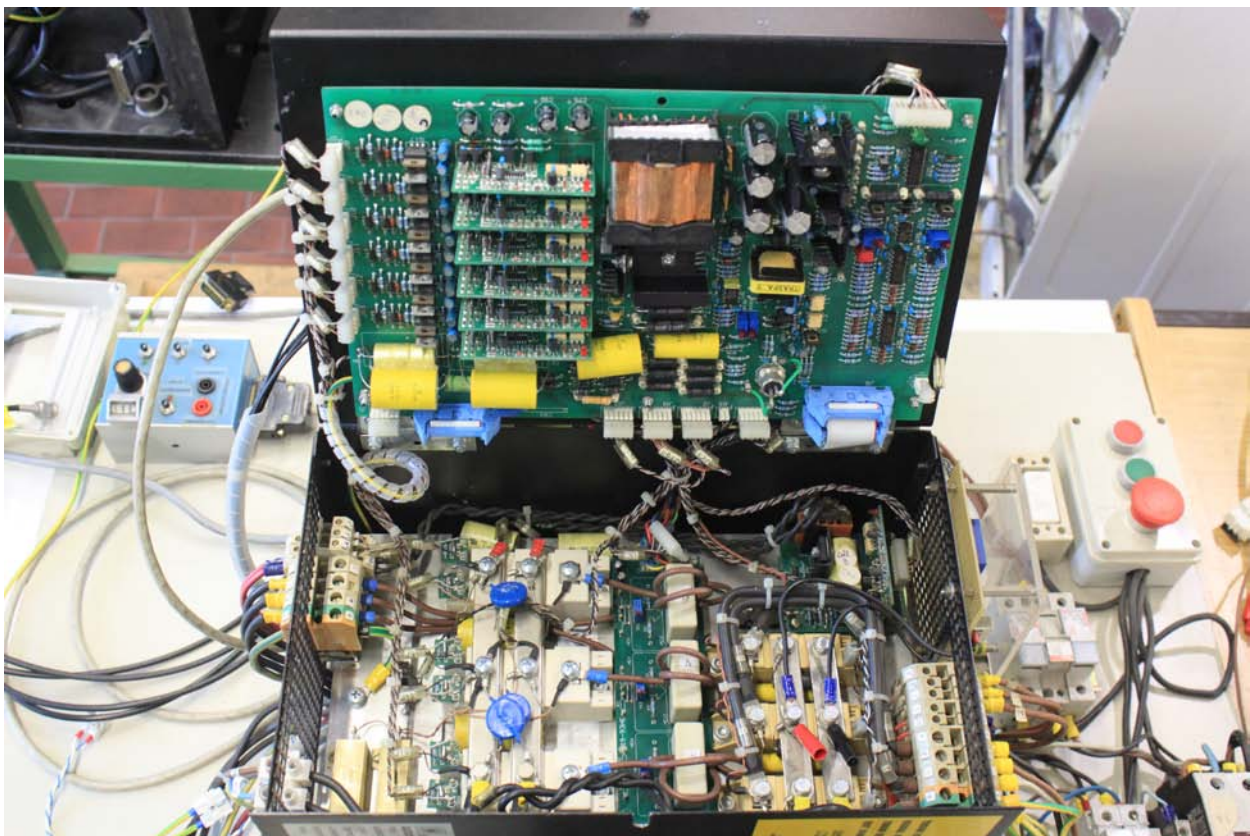
Fig. A.2: 27 kVA Sitra Converter
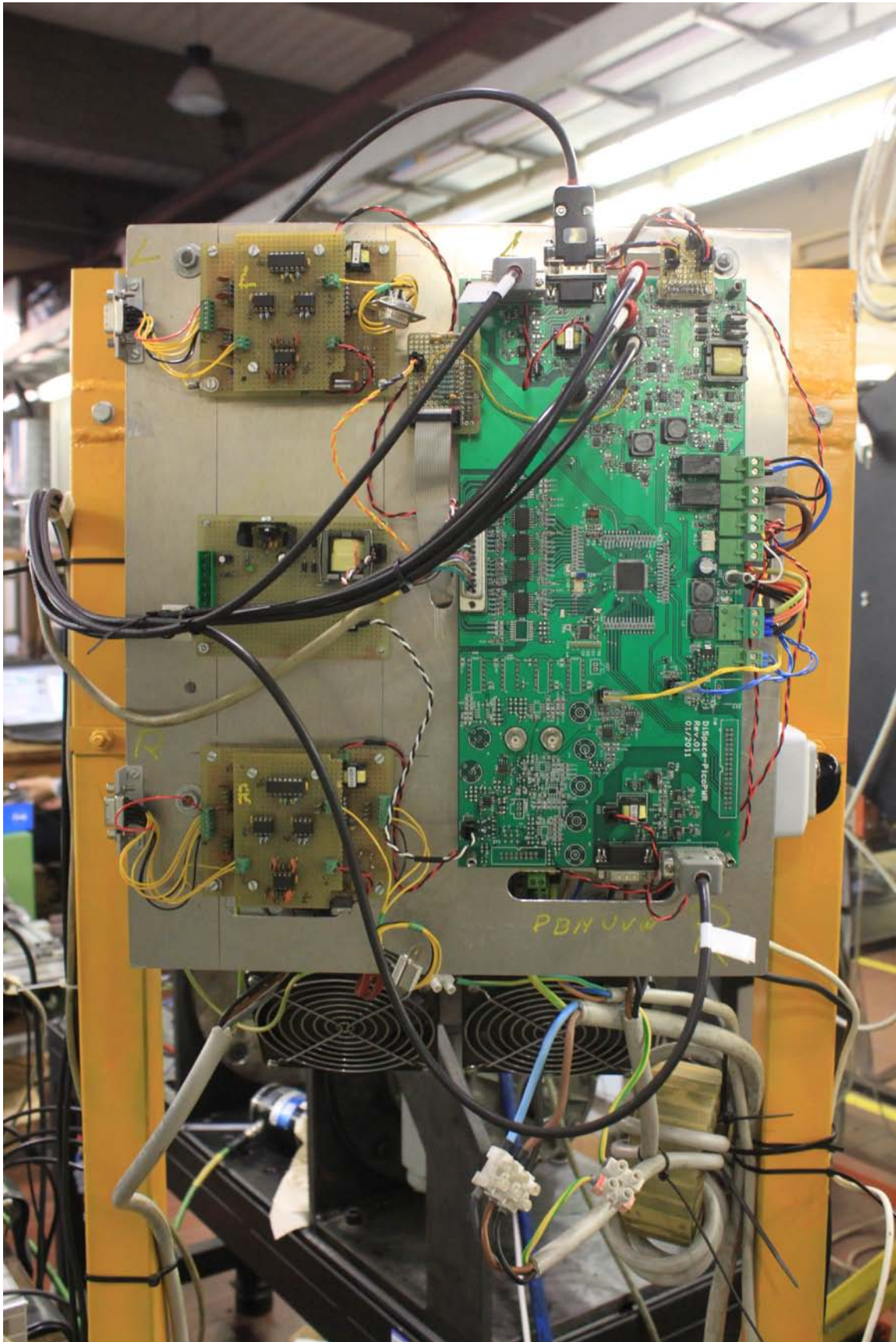
Fig. A.3: 25 kVA Power Converter E5
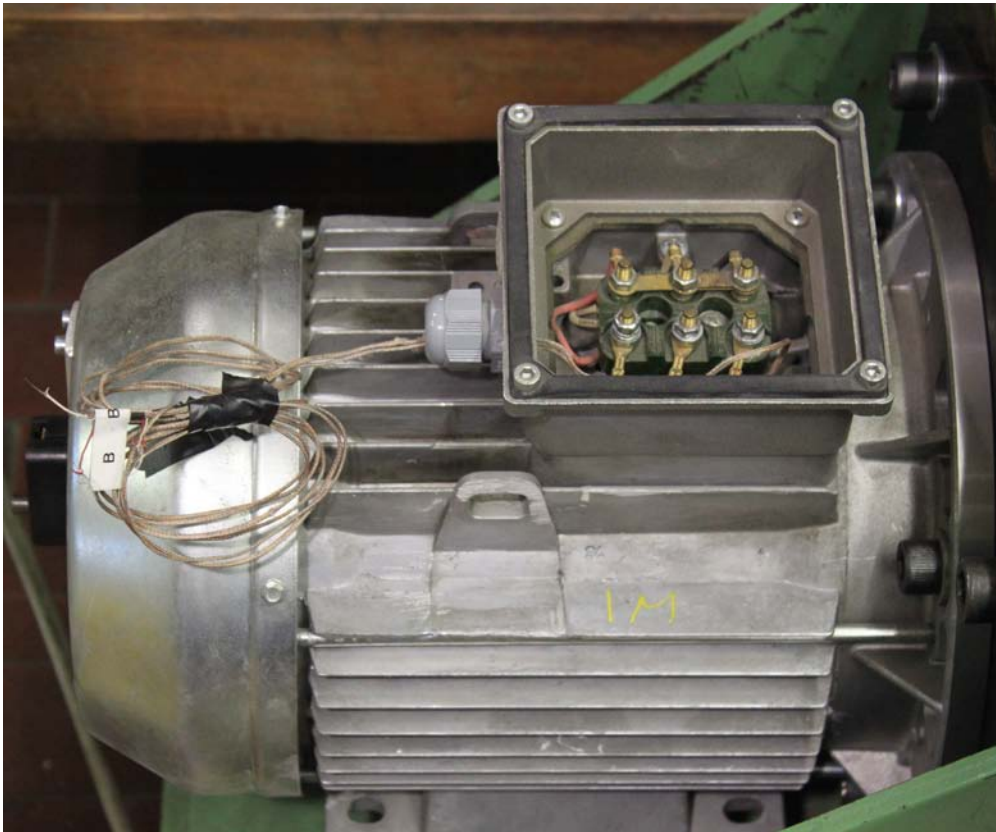
Fig. A.4: Electro Adda 2.2 kW induction machine
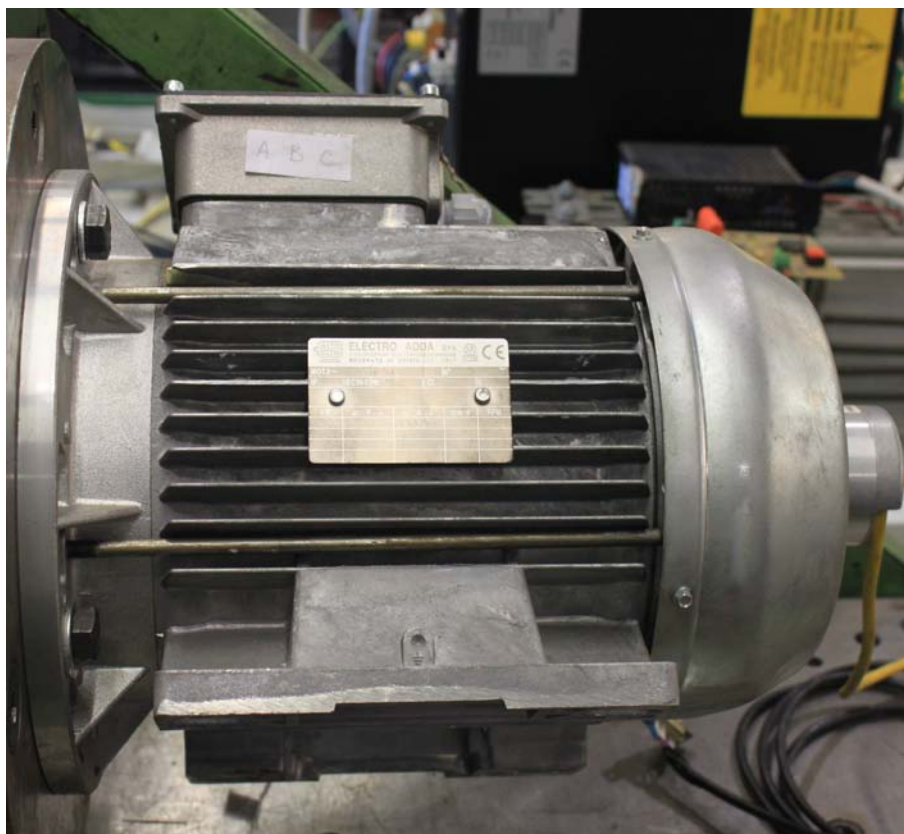
Fig. A.5: Electro Adda 4 kW induction machine

Fig. A.6: Siemens' 32 kW D-91066 Erlangen Compressor induction motor
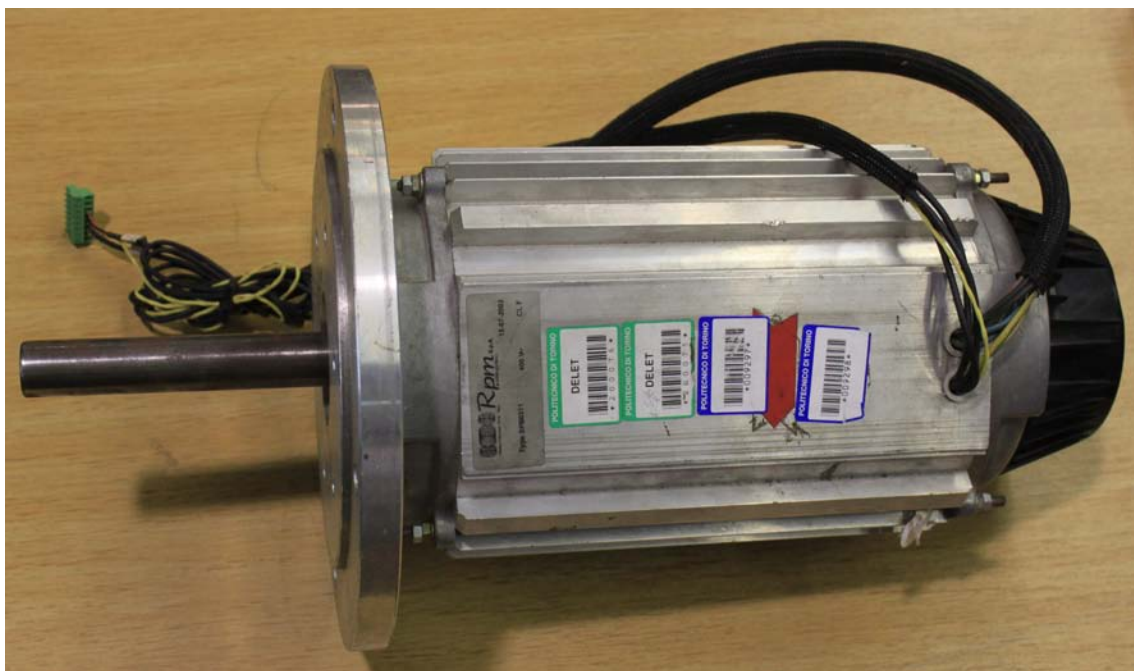
Fig. A.7: 7.5 kW Light Traction Prototype Interior Permanent Magnet Synchronous Motor (IPMSM)
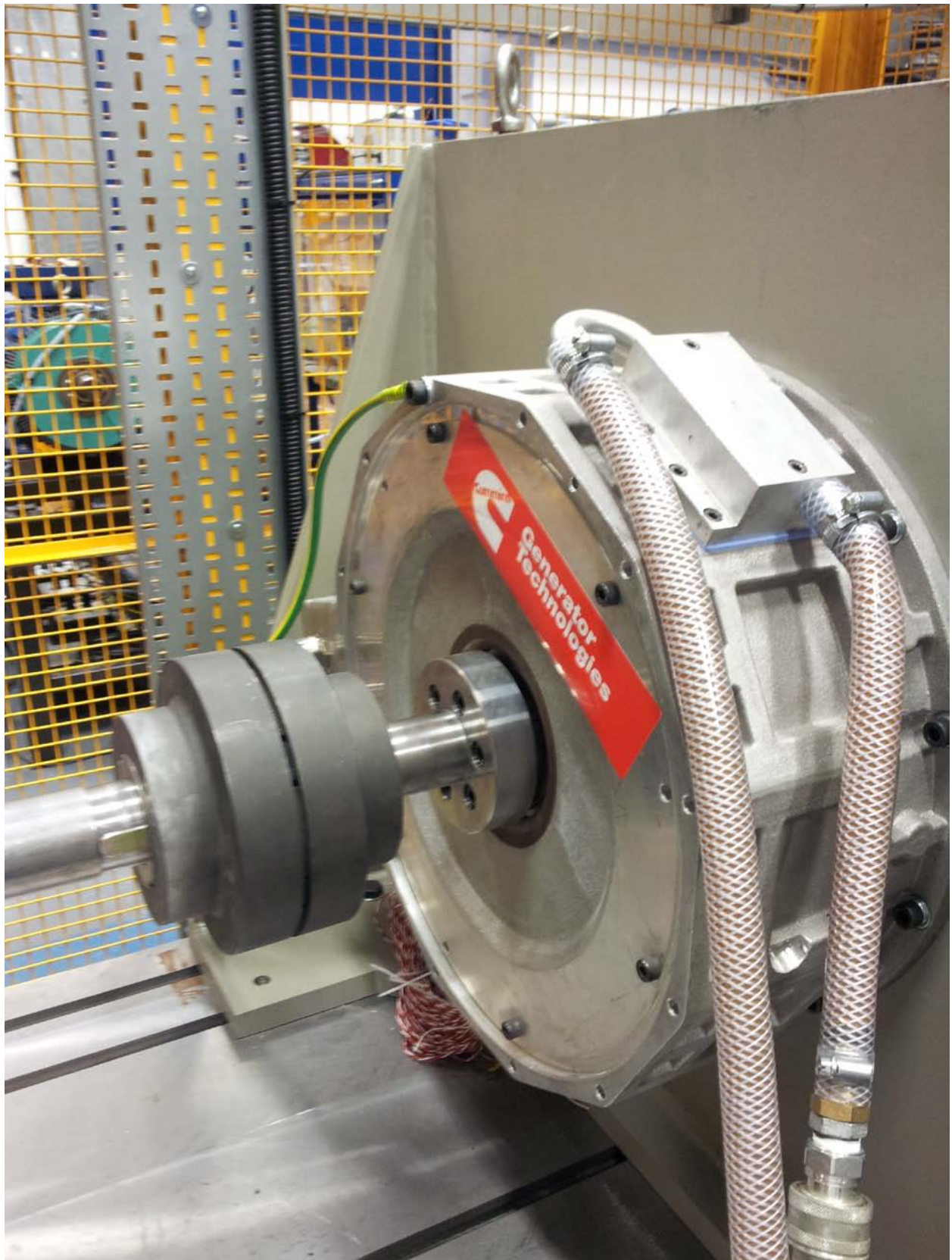
Fig. A.8: Interior Permanent Magnet Traction Motor Prototype 30 kW
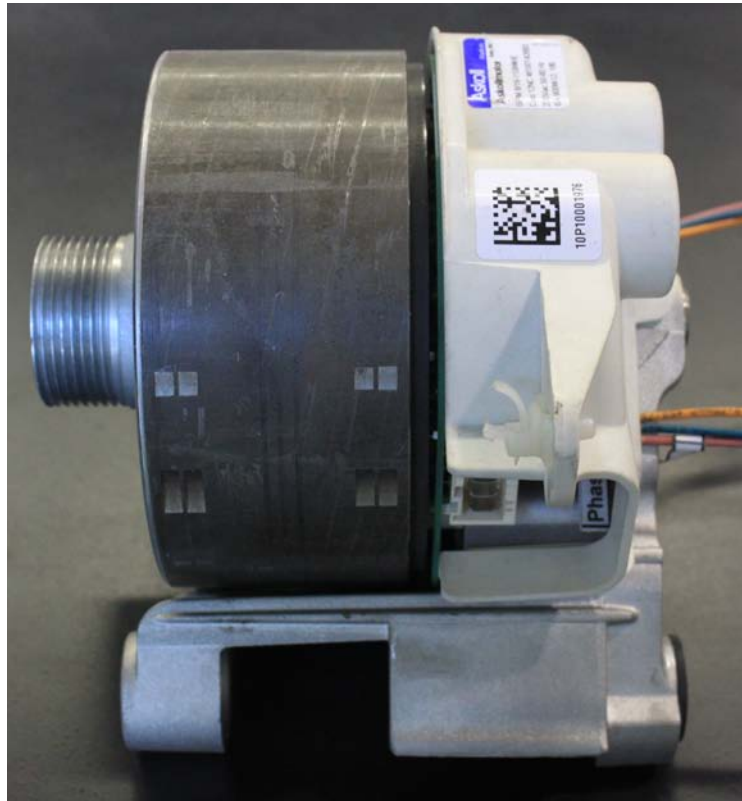
Fig. A.9: A commercial washing machine's Surface Mounted Permanent Magnet Synchronous Motor (SPMSM)

A2. Parameter Identification Algorithms for Induction Machine

A2.1 Instructions for initializing the motor control

```
/*---------------------------------------------------------------------------*/
/* Description:        Parameter identification of induction machine       */
/* Date:              January 19th, 2012                                    */
/* Author:            Shafiq Ahmed Odhano                                   */
/* Status:            Final                                                 */
/*---------------------------------------------------------------------------*/

#define S_FUNCTION_NAME IM_Param_Ident_01
#define S_FUNCTION_LEVEL 2

#include "simstruc.h"
#include <math.h>
#include "Include\MotorData.h"          // if included in a separate file
#include "Include\UserDataTypes.h"      // contains custom data types
#include "Include\UserSetup.h"          // if included in a separate file
#include "Include\Global_variables.h"   // if included in a separate file
#include "Include\dead_time_error.h"    // a separate file is needed
#include "Include\MotorControl.h"       // contains frequently used functions

#define U(element) (*uPtrs[element])     /* Pointer to Input Port0 */


#define NINPUTS     13
#define NOUTPUTS    44
#define NPARAMS     11


//Parameters from the ControlDesk virtual control panel

//Control loops parameters

#define kp_i                (mxGetPr(ssGetSFcnParam(S,0))[0])
/* Proportional constant for current controller          */
```

196

```
#define ki_i                (mxGetPr(ssGetSFcnParam(S,1))[0])
/* Integral constant for current controller              */

#define kp_w                (mxGetPr(ssGetSFcnParam(S,2))[0])
/* Proportional constant for speed controller            */

#define ki_w                (mxGetPr(ssGetSFcnParam(S,3))[0])
/* Integral constant for speed controller                */

#define flag_omega_ref      (mxGetPr(ssGetSFcnParam(S,4))[0])
/* Step/ramp reference speed selection                   */

#define accel               (mxGetPr(ssGetSFcnParam(S,5))[0])
/* Reference acceleration for the drive [rpm/sec]         */

#define fcut_off_w          (mxGetPr(ssGetSFcnParam(S,6))[0])
/* Rotor speed filter cut-off frequency                  */

#define over_speed_limit    (mxGetPr(ssGetSFcnParam(S,7))[0])
/* Trip level for overspeed protection                   */

#define freq1               (mxGetPr(ssGetSFcnParam(S,8))[0])
/* 1-phase signal freq. for two-frequency test           */

#define freq2               (mxGetPr(ssGetSFcnParam(S,9))[0])
/* 1-phase signal freq. for two-frequency test           */

// Inverter non-linear effects

#define enable_dt           (mxGetPr(ssGetSFcnParam(S,10))[0])
/* Dead time compensation (0 = OFF, 1 = ON)              */

// Default commands for all s-functions

static void mdlInitializeSizes(SimStruct *S)
{
    ssSetNumSFcnParams(S, NPARAMS);       // Number of expected parameters
    if (ssGetNumSFcnParams(S) != ssGetSFcnParamsCount(S)) {
    return; // Parameter mismatch will be reported by Simulink
    }

    ssSetNumContStates(S, 0);
    ssSetNumDiscStates(S, 0);

    if (!ssSetNumInputPorts(S, 1)) return;
    ssSetInputPortWidth(S, 0, NINPUTS);
    ssSetInputPortDirectFeedThrough(S, 0, 1);

    if (!ssSetNumOutputPorts(S, 1)) return;
    ssSetOutputPortWidth(S, 0, NOUTPUTS);

    ssSetNumSampleTimes(S, 1);
    ssSetNumRWork(S, 0);
    ssSetNumIWork(S, 0);
    ssSetNumPWork(S, 0);
    ssSetNumModes(S, 0);
    ssSetNumNonsampledZCs(S, 0);

/* Take care when specifying exception free code - see sfuntmpl_doc.c*/
    ssSetOptions(S, SS_OPTION_EXCEPTION_FREE_CODE);
}

static void mdlInitializeSampleTimes(SimStruct *S)
{
    ssSetSampleTime(S, 0, INHERITED_SAMPLE_TIME);/*inherited*/
    ssSetOffsetTime(S, 0, 0.);
}
```

```
/*----------------------------------------------------------------------*/
/*                            Motor Data                                 */
/*----------------------------------------------------------------------*/
// This data must correspond to the nameplate of the machine being tested
#define IsMax             12.445                          // Amps
#define p                 2                               // pole pairs
#define wnom              1410                            // rpm
#define cos_fi            0.82                            // power factor
#define IdRated           (IsMax*sqrt(1-cos_fi*cos_fi))   // Amps


/*----------------------------------------------------------------------*/
/*                          Global Constants                             */
/*----------------------------------------------------------------------*/
#define Ts                (1.0/10000.0)       // Sampling time
#define Ts_inv            10000               // Sampling frequency


// Low Pass Filters (LPF)
#define fcut_off_vDC      20.0
#define fcut_off_volt     20.0
#define fcut_off_torque   500.0
#define f_cutoff_dq_crt   20.0


// MTPV max load angle
#define deltaMax          45.0


// Mathematical constants
#define double_pi         6.2831853
#define pi                3.1415926
#define sqrt2             1.4142135
#define sqrt3             1.7320508
#define sqrt2_inv         0.7071067
#define sqrt3_inv         0.5773502
#define one_over_pi       0.31830988
#define rad2deg           57.295779513
#define deg2rad           0.01745329
#define k_angle           57.29578 // 180/pi - conversion from rad to degrees
#define rpm2rad           (p*pi/30.0) /* p*pi/30.0 – conversion from rpm to
                          electrical rad/sec /*
#define rad2rpm           (30.0/(p*pi)) /* 30/(p*pi) - conversion from
                          electrical rad/sec to rpm */
#define k_omega_ref       (Ts*p*pi/30.0) /* Ts*p*pi/30.0 - conversion from
                          rpm/sec rad/s^2 */


// Modulation index limits
#define DUTY_MIN          0.02
#define DUTY_MAX          0.98


// Stator resistance detect and adaptation mechanism
#define CounterDC         4000
#define Nsamples          32


// Drive states
#define RESET                              -3
#define WAKE_UP                            -2
#define DRIVE_INIT                         -1
#define GO_MOTOR                            0
#define STOP_MOTOR                          1
#define BOOTSTRAP_LOAD                      2
#define ERROR                               3
#define STATOR_RESISTANCE_DETECT1           4
#define STATOR_RESISTANCE_DETECT2           5
#define DC_BRAKE                            6
#define STATOR_TRANSIENT_INDUCTANCE_EST1    7
```

```
#define STATOR_TRANSIENT_INDUCTANCE_EST2    8
#define ROTOR_TIME_CONSTANT_EST             9
#define ROTOR_RESISTANCE_EST               10
#define TWO_FREQ_TEST_1                    11
#define TWO_FREQ_TEST_2                    12


// Threshold values
#define wrated              wnom*rpm2rad
#define VDC_WAKE_UP         250.0
#define VOLT_PROT           450.0
#define CRT_PROT            (1.1*IsMax)
#define OVERSPEED_LIMIT     (2000.0*rpm2rad)
#define Nmax                8000.0


/*------------------------------------------------------------------------------*/
/*                          Frequently Used Functions                           */
/*------------------------------------------------------------------------------*/
// Proportional-Integral Regulator with anti-wind-up
void PIReg(XPIReg *Reg)
{
    double error;

    error=Reg->ref-Reg->actual;
    Reg->prop = error*Reg->kp;

    if (Reg->prop>Reg->lim)
        Reg->prop=Reg->lim;
    if (Reg->prop<(-Reg->lim))
        Reg->prop=-Reg->lim;

    Reg->int_lim=Reg->lim-fabs(Reg->prop);
    Reg->integral+=Ts*Reg->ki*error;

    if (Reg->integral>Reg->int_lim)
        Reg->integral=Reg->int_lim;
    if (Reg->integral<(-Reg->int_lim))
        Reg->integral=-Reg->int_lim;

    Reg->out=Reg->prop+Reg->integral+Reg->vfw;
}

// Inverter non-linearity effects' compensation in function of phase currents
void DeadTimeCompLUT(Xabc *iabcdt,double *Vdc,Xabc *vabcdt)
{
    int dt_index;
    double tmp1,tmp2,tmp3;
// phase a
    if (fabs(iabcdt->a)>=dt_crt_range)
    {
        dt_index=dt_points-1;
        tmp3=dt_error_vector[dt_index]*(*Vdc);
    }
    else
    {
        dt_index=(int)(fabs(iabcdt->a)/dt_crt_step);
        if (dt_index>30)
            dt_index=30;
        if (dt_index<0)
            dt_index=0;

        tmp1=fabs(iabcdt->a)-dt_crt_vector[dt_index];
        tmp2=dt_error_vector[dt_index+1]-dt_error_vector[dt_index];
        tmp3=(dt_error_vector[dt_index]+tmp1*tmp2/dt_crt_step)*(*Vdc);
```

```
    }

    if (iabcdt->a>=0)
        vabcdt->a=-tmp3;
    else
        vabcdt->a= tmp3;


// phase b
    if (fabs(iabcdt->b)>=dt_crt_range)
    {
        dt_index=dt_points-1;
        tmp3=dt_error_vector[dt_index]*(*Vdc);
    }
    else
    {
        dt_index=(int)(fabs(iabcdt->b)/dt_crt_step);
        if (dt_index>30)
            dt_index=30;
        if (dt_index<0)
            dt_index=0;
        tmp1=fabs(iabcdt->b)-dt_crt_vector[dt_index];
        tmp2=dt_error_vector[dt_index+1]-dt_error_vector[dt_index];
        tmp3=(dt_error_vector[dt_index]+tmp1*tmp2/dt_crt_step)*(*Vdc);
    }

    if (iabcdt->b>=0)
        vabcdt->b=-tmp3;
    else
        vabcdt->b= tmp3;

// phase c
    if (fabs(iabcdt->c)>=dt_crt_range)
    {
        dt_index=dt_points-1;
        tmp3=dt_error_vector[dt_index]*(*Vdc);
    }
    else
    {
        dt_index=(int)(fabs(iabcdt->c)/dt_crt_step);
        if (dt_index>30)
            dt_index=30;
        if (dt_index<0)
            dt_index=0;
        tmp1=fabs(iabcdt->c)-dt_crt_vector[dt_index];
        tmp2=dt_error_vector[dt_index+1]-dt_error_vector[dt_index];
        tmp3=(dt_error_vector[dt_index]+tmp1*tmp2/dt_crt_step)*(*Vdc);
    }

    if (iabcdt->c>=0)
        vabcdt->c=-tmp3;
    else
        vabcdt->c= tmp3;
}

// Three-phase to Two-phase transformations
void DirectClarke(Xabc *Abc, Xalphabeta *AlphaBeta)
{
    double tmp;

    tmp=(Abc->a+Abc->b+Abc->c)/3.0;
    AlphaBeta->alpha=Abc->a-tmp;
    AlphaBeta->beta =(Abc->b-Abc->c)*sqrt3_inv;
```

```c
}

// Two-phase to Three-phase transformations
void InvClarke(Xalphabeta *AlphaBeta, Xabc *Abc)
{
    Abc->a=AlphaBeta->alpha;
    Abc->b=-0.5*AlphaBeta->alpha+0.5*sqrt3*AlphaBeta->beta;
    Abc->c=-0.5*AlphaBeta->alpha-0.5*sqrt3*AlphaBeta->beta;
}

// Transformation from stationary frame to rotating frame
void DirectRot(Xalphabeta *AlphaBeta, Xsc *SinCos,Xdq *DQ)
{
    DQ->d= AlphaBeta->alpha*SinCos->cos+AlphaBeta->beta*SinCos->sin;
    DQ->q=-AlphaBeta->alpha*SinCos->sin+AlphaBeta->beta*SinCos->cos;
}

// Transformation from rotating frame to stationary frame
void InvRot(Xdq *DQ,Xsc *SinCos, Xalphabeta *AlphaBeta)
{
    AlphaBeta->alpha=DQ->d*SinCos->cos-DQ->q*SinCos->sin;
    AlphaBeta->beta =DQ->d*SinCos->sin+DQ->q*SinCos->cos;
}

// Function that generates PWM switching commands
void PWMCompute(Xabc *ABC, Xabc *Duty, double *Vdc)
{
    double a,b,c,x1,y1,pwm_zero_seq;
    x1=1.0/(*Vdc);
    a=ABC->a*x1;
    b=ABC->b*x1;
    c=ABC->c*x1;

    if (a>b)
    {
        x1=a;
        y1=b;
    }
    else
    {
        x1=b;
        y1=a;
    }

    if (x1<c)
        pwm_zero_seq=x1;
    else
    {
        if (y1>c)
            pwm_zero_seq=y1;
        else
            pwm_zero_seq=c;
    }
// This duty computation applies to 25kVA SITRA converter only
    Duty->a=0.5-a-0.5*pwm_zero_seq;
    Duty->b=0.5-b-0.5*pwm_zero_seq;
    Duty->c=0.5-c-0.5*pwm_zero_seq;

    if (Duty->a<DUTY_MIN)
        Duty->a=DUTY_MIN;
    if (Duty->a>DUTY_MAX)
        Duty->a=DUTY_MAX;
```

```
    if (Duty->b<DUTY_MIN)
        Duty->b=DUTY_MIN;
    if (Duty->b>DUTY_MAX)
        Duty->b=DUTY_MAX;

    if (Duty->c<DUTY_MIN)
        Duty->c=DUTY_MIN;
    if (Duty->c>DUTY_MAX)
        Duty->c=DUTY_MAX;
}

/*-----------------------------------------------------------------------*/
/*                    Initializations for s-function                     */
/*-----------------------------------------------------------------------*/

#define MDL_INITIALIZE_CONDITIONS
/* Function: mdlInitializeConditions ==================================*/
static void mdlInitializeConditions(SimStruct *S)
/* This routine is called at the start of simulation */
{
    omega_ref          = 0.0;

    wr_                = 0.0;
    theta_enc          = 0.0;
    offset_in.ch0      = 0.0;
    offset_in.ch1      = 0.0;
    offset_in.ch2      = 0.0;
    offset_in.ch3      = 0.0;
    offset_in.ch4      = 0.0;
    offset_in.ch5      = 0.0;
    offset_in.ch6      = 0.0;
    offset_in.ch7      = 0.0;

    counter            = 0.0;
    StateDrive         = RESET;
    pwm_enable         = 1.0;
    duty.a             = 1.0;
    duty.b             = 1.0;
    duty.c             = 1.0;
    counterTask        = 0.0;
    vabcsRef.a         = 0.0;
    vabcsRef.b         = 0.0;
    vabcsRef.c         = 0.0;
    sum                = 0.0;
    vdsRefFilt         = 0.0;
}

#define MDL_START
static void mdlStart(SimStruct *S)
{
}

static void mdlOutputs(SimStruct *S, int_T tid)
/*this routine compute the outputs of S-Function block */
{
    double            *y      = ssGetOutputPortRealSignal(S,0);
    double            *x      = ssGetRealDiscStates(S);
    InputRealPtrsType uPtrs   = ssGetInputPortRealSignalPtrs(S,0);

// Local variables
    double test_type;
```

```
// State command flags and other params
    double              Go_motor;
    double              Stop_motor;
    double              Restart;
    double              StopPWM;
    double              Error;

// Feedback
    Xin                 input;
    Xabc                iabcs;
    double              sat_omega_ref, sat_omega_refAbs;
    double              omega_refAbs;
    double              vdc, idc;
    Xabc                vABC;
    Xabc                vabcs;
    double              theta_encOld;
    double              theta_enc_mec;
    double              ProtFlagIn;

// Two-phase variables
    Xalphabeta          isab;
    Xsc                 SinCosEnc;

    double              k_LPF_speed;
    double              k_LPF_voltage;
    double              k_LPF_vDC;
    double              k_LPF_torque;
    double              k_LPF_dq_current;

// Measured speed
    double              wr_deriv;


// Inverter non-linearity compensation variables
    Xabc                vdt;
    Xalphabeta          vdtab;

// General-purpose temporary variables
    Xabc                tmp123;
    double              tmp1, tmp2, tmp3, tmp4;


/*-----------------------------------------------------------------------------*/
/*                    Control Algorithm Begins Here                            */
/*-----------------------------------------------------------------------------*/
// Get variables and measurements from ControlDesk
    input.ch0       = U(0);             // Phase a current (A)
    input.ch1       = U(1);             // Phase b current (A)
    input.ch2       = U(2);             // Phase c current (A)
    input.ch3       = U(3);             // DC link voltage (V)
    Go_motor        = U(4);
    Stop_motor      = U(5);
    StopPWM         = U(6);
    Restart         = U(7);
    wRefIn          = U(8)*rpm2rad;
    ProtFlagIn      = U(9);
    input.ch4       = U(10);
    tau_est_start   = U(11);            // Starting value of rotor time constant
    test_type       = U(12);

/*=============================================================================*/
/*                               Feedback                                      */
/*=============================================================================*/
    iabcs.a         = input.ch0 - offset_in.ch0;
```

```
    iabcs.b          = input.ch1 - offset_in.ch1;
    iabcs.c          = input.ch2 - offset_in.ch2;
    vdc              = input.ch3;


/*============================================================================*/
/*                   Filters on Various Quantities                          */
/*============================================================================*/
// Coefficient of DC link voltage Low Pass Filter working at Ts sampling time
    tmp1 = Ts*double_pi*fcut_off_volt;
    k_LPF_voltage = tmp1/(1.0+tmp1);
    vdcFilt += k_LPF_voltage*(vdc - vdcFilt);

// Coefficient of speed Low Pass Filter working at Ts sampling time
    tmp1 = Ts*double_pi*fcut_off_w;
    k_LPF_speed = tmp1/(1.0+tmp1);

// Filter on torque
    tmp1=Ts*double_pi*fcut_off_torque;
    k_LPF_torque=tmp1/(1.0+tmp1);

// Filter on dq-axis currents for correct magnetising current identification
    tmp1 = Ts*double_pi*f_cutoff_dq_crt;
    k_LPF_dq_current = tmp1/(1.0 + tmp1);


/*============================================================================*/
/*                          Protection Module                               */
/*============================================================================*/

    if (fabs(iabcs.a)>CRT_PROT)
    {
        StateDrive=ERROR;
        protection_flag=1.0;
    }
    if (fabs(iabcs.b)>CRT_PROT)
    {
        StateDrive=ERROR;
        protection_flag=2.0;
    }
    if (fabs(iabcs.c)>CRT_PROT)
    {
        StateDrive=ERROR;
        protection_flag=3.0;
    }
    if (vdc>VOLT_PROT)
    {
        StateDrive=ERROR;
        protection_flag=4.0;
    }

    if (MotorSpeedAbs>OVERSPEED_LIMIT)
    {
        StateDrive=STOP_MOTOR;
        protection_flag=5.0;
    }

/*============================================================================*/
/*              Clarke Transformation: abc --> alpha, beta                  */
/*============================================================================*/
    DirectClarke(&iabcs,&isab);
    DirectClarke(&vabcsRef, &vsabRef);
    vds_max = 0.9*vdc*sqrt3_inv;
```

```
/*============================================================================*/
/*                      Defining Drive Operation States                       */
/*============================================================================*/

    switch(StateDrive)
    {
      case WAKE_UP:

          ResetVars();

          if (vdc>VDC_WAKE_UP)
          {
              StateDrive=DRIVE_INIT;
              protection_flag=0.0;
          }
          else
          {
              StateDrive=WAKE_UP;
              protection_flag=6.0;
          }

          if (StopPWM>0.5)
              StateDrive=RESET;

      break;

      case DRIVE_INIT:
// Offset computation for feedback quantities

          if (counter<=255)
          {
              offset.ch0+=input.ch0;
              offset.ch1+=input.ch1;
              offset.ch2+=input.ch2;
              offset.ch3+=input.ch3;
              offset.ch4+=input.ch4;
          }
          else
          {
              if (counter==256)
              {
                  offset_in.ch0=offset.ch0/256.0;
                  offset_in.ch1=offset.ch1/256.0;
                  offset_in.ch2=offset.ch2/256.0;
                  offset_in.ch3=offset.ch3/256.0;
                  offset_in.ch4=offset.ch4/256.0;
                  counter=0.0;
                  StateDrive=STOP_MOTOR;
              }
          }

          counter++;

      break;

      case ERROR:
// Impose duty-cycles to 1.0 --> all LOW IGBTs are ON (according to SITRA logic)
          duty.a=1.0;
          duty.b=1.0;
          duty.c=1.0;

          counter=0.0;
          pwm_enable=0.0;
```

```
        if (StopPWM>0.5)
            StateDrive=RESET;

        if (Restart>0.5)
            StateDrive=RESET;

    break;


    case RESET:
// Impose duty-cycles to 1.0 --> all LOW IGBTs are ON (according to SITRA logic)
        duty.a=1.0;
        duty.b=1.0;
        duty.c=1.0;

        counter=0.0;
        pwm_enable=1.0;

        if (Restart>0.5)
            StateDrive = WAKE_UP;
        else
            StateDrive = RESET;

    break;


    case STOP_MOTOR:

        counter=0.0;
        pwm_enable=0.0;
        InitVarsCtrl();

        if (Go_motor>0.5)
            if (test_type <= 0.0)
                StateDrive = GO_MOTOR;
            if (test_type == 1.0 || test_type == 6.0)
                StateDrive = STATOR_RESISTANCE_DETECT1;
    break;
```

A2.2   Stator resistance estimation algorithm

```
/*----------------------------------------------------------------------------*/
/*                        Stator Resistance Estimation                        */
/*----------------------------------------------------------------------------*/
    case STATOR_RESISTANCE_DETECT1:

        counter++;

// Current control
        SinCosRot.sin = 0.0;
        SinCosRot.cos = 1.0;
        DirectRot(&isab,&SinCosRot,&idqs);
        idqsRef.d = 0.5*IsMax;
        idqsRef.q = 0.0;

        CrtRegVars_d.kp          = kp_i;
        CrtRegVars_d.ki          = ki_i;

        CrtRegVars_d.ref         = idqsRef.d;
        CrtRegVars_d.actual      = idqs.d;
```

```
        CrtRegVars_d.lim        = vds_max;
        CrtRegVars_d.vfw        = 0.0;

        PIReg(&CrtRegVars_d);
        vdqsRef.d = CrtRegVars_d.out;

        CrtRegVars_q.kp         = kp_i;
        CrtRegVars_q.ki         = ki_i;

        CrtRegVars_q.ref        = idqsRef.q;
        CrtRegVars_q.actual     = idqs.q;
        tmp3 = vds_max*vds_max-vdqsRef.d*vdqsRef.d;
        if (tmp3 <= 0.001)
            tmp3 = 0.0;
        CrtRegVars_q.lim        = sqrt(tmp3);
        CrtRegVars_q.vfw        = 0.0;

        PIReg(&CrtRegVars_q);
        vdqsRef.q = CrtRegVars_q.out;

        InvRot(&vdqsRef,&SinCosRot,&vsabRef);
        InvClarke(&vsabRef,&vabcsRef);
        PWMCompute(&vabcsRef,&duty,&vdc);

// Filtered voltage on d-axis
        vdsRefFilt+=k_LPF_voltage*(vdqsRef.d-vdsRefFilt);

        if ((counter>=CounterDC-Nsamples)&&(counter<CounterDC))
            sum+=vdsRefFilt;

        if (counter==CounterDC)
        {
            vErrorBuf[0]        = sum/Nsamples;
            counter            = 0;
            sum                = 0.0;
            StateDrive         = STATOR_RESISTANCE_DETECT2;
        }

    break;

    case STATOR_RESISTANCE_DETECT2:

        counter++;

// Current control
        idqsRef.d=IsMax;
        idqsRef.q=0.0;
        DirectRot(&isab,&SinCosRot,&idqs);
        CrtRegVars_d.ref        = idqsRef.d;
        CrtRegVars_d.actual     = idqs.d;
        CrtRegVars_d.lim        = vds_max;
        CrtRegVars_d.vfw        = 0.0;

        PIReg(&CrtRegVars_d);
        vdqsRef.d = CrtRegVars_d.out;

        CrtRegVars_q.ref        = idqsRef.q;
        CrtRegVars_q.actual     = idqs.q;
        tmp4 = vds_max*vds_max-vdqsRef.d*vdqsRef.d;
        if (tmp4 <= 0.001)
            tmp4 = 0.0;
        CrtRegVars_q.lim        = sqrt(tmp4);
        CrtRegVars_q.vfw        = 0.0;
```

```
        PIReg(&CrtRegVars_q);
        vdqsRef.q = CrtRegVars_q.out;

        InvRot(&vdqsRef,&SinCosRot,&vsabRef);
        InvClarke(&vsabRef,&vabcsRef);
        PWMCompute(&vabcsRef,&duty,&vdc);

// Filtered voltage on d-axis
        vdsRefFilt+=k_LPF_voltage*(vdqsRef.d-vdsRefFilt);

        if ((counter>=CounterDC-Nsamples)&&(counter<CounterDC))
            sum+=vdsRefFilt;

        if (counter==CounterDC)
        {
            vErrorBuf[1]            = sum/Nsamples;
            tmp1                   = vErrorBuf[1]-vErrorBuf[0];
            tmp2                   = 0.5*IsMax;
            RsEst                  = fabs(tmp1/tmp2);
            Counter                = 0;
            Sum                    = 0.0;

            StateDrive             = STATOR_TRANSIENT_INDUCTANCE_EST1;
        }

    break;
```

A2.3   Leakage inductances' estimation algorithm

```
/*------------------------------------------------------------------------*/
/*                    Transient Inductances Estimation                    */
/*------------------------------------------------------------------------*/

/*========================================================================*/
/*                        For low power machines                         */
/*========================================================================*/
    case STATOR_TRANSIENT_INDUCTANCE_EST1:

        counter++;

        if (counter <= 0.01*Ts_inv)
        {
            SinCosRot.sin=0.0;
            SinCosRot.cos=1.0;
            DirectRot(&isab,&SinCosRot,&idqs);

            idqsRef.d = 0.0;       // Reduce DC current of Rs detect steps
            idqsRef.q = 0.0;       // to zero to have zero initial flux for
                                   // transient inductance estimation

            CrtRegVars_d.ref       = idqsRef.d;
            CrtRegVars_d.actual    = idqs.d;
            CrtRegVars_d.lim       = vds_max;
            CrtRegVars_d.vfw       = 0.0;
            PIReg(&CrtRegVars_d);
            vdqsRef.d = CrtRegVars_d.out;

            CrtRegVars_q.ref       = idqsRef.q;
            CrtRegVars_q.actual    = idqs.q;
            tmp4 = vds_max*vds_max-vdqsRef.d*vdqsRef.d;
            if (tmp4 <= 0.001)
```

```
            tmp4 = 0.0;
        CrtRegVars_q.lim     = sqrt(tmp4);
        CrtRegVars_q.vfw     = 0.0;

        PIReg(&CrtRegVars_q);
        vdqsRef.q = CrtRegVars_q.out;

        InvRot(&vdqsRef,&SinCosRot,&vsabRef);
        InvClarke(&vsabRef,&vabcsRef);
        PWMCompute(&vabcsRef,&duty,&vdc);
        }

    if (counter > 0.01*Ts_inv)
    {
        duty.a               = 1.0;
        duty.b               = 0.0;
        duty.c               = 0.0;
        InvClarke(&vsabRef,&vabcsRef);
        PWMCompute(&vabcsRef, &duty, &vdc);
        if (iabcs.a >= 0.8*CRT_PROT)
        {
            counter          = 0.0;
            duty.a           = 0.5;
            duty.b           = 0.5;
            duty.c           = 0.5;
            StateDrive       = STATOR_TRANSIENT_INDUCTANCE_EST2;
        }
    }
break;

case STATOR_TRANSIENT_INDUCTANCE_EST2:
    counter++;
    if (iabcs.a >= IdRated)
    {
        iDC_level1           = iabcs.a;
        CounterTmp1          = counter;
    }

    if (iabcs.a < IdRated)
    {
        duty.a               = 0.0;
        duty.b               = 1.0;
        duty.c               = 1.0;

        InvClarke(&vsabRef,&vabcsRef);
        PWMCompute(&vabcsRef, &duty, &vdc);

        if (fabs(iabcs.a) >= 0.8*CRT_PROT)
        {
            iDC_level2       = iabcs.a;
            duty.a           = 0.5;
            duty.b           = 0.5;
            duty.c           = 0.5;
            CounterTmp2      = counter - CounterTmp1;
            tmp1             = iDC_level1 - iDC_level2;
            TrLsEst          = (2./3.)*vdcFilt*(CounterTmp2*Ts)/tmp1;
            Counter          = 0.0;

            StateDrive       = ROTOR_TIME_CONSTANT_EST;
        }
    }
    if (StopPWM > 0.5)
        StateDrive = RESET;
```

```
      break;

/*=============================================================================*/
/*                          For high-power machines                            */
/*=============================================================================*/
      case STATOR_TRANSIENT_INDUCTANCE_EST1:

          counter++;

          CrtRegVars_d.kp          = kp_i;
          CrtRegVars_d.ki          = ki_i;
          CrtRegVars_q.kp          = kp_i;
          CrtRegVars_q.ki          = ki_i;

          if(counter <= 20)
          {
              SinCosRot.sin        = 0.0;
              SinCosRot.cos        = 1.0;
              DirectRot(&isab,&SinCosRot,&idqs);

              iDC_level1           = idqs.d;
              idqsRef.d           += IsMax/20.0;
              idqsRef.q            = 0.0;
              CrtRegVars_d.ref     = idqsRef.d;
              CrtRegVars_d.actual  = idqs.d;
              CrtRegVars_d.lim     = vds_max;
              CrtRegVars_d.vfw     = 0.0;

              PIReg(&CrtRegVars_d);
              vdqsRef.d = CrtRegVars_d.out;

              CrtRegVars_q.ref     = idqsRef.q;
              CrtRegVars_q.actual  = idqs.q;
              tmp4 = vds_max*vds_max-vdqsRef.d*vdqsRef.d;
              if (tmp4 <= 0.001)
                  tmp4 = 0.0;
              CrtRegVars_q.lim     = sqrt(tmp4);
              CrtRegVars_q.vfw     = 0.0;

              PIReg(&CrtRegVars_q);
              vdqsRef.q = CrtRegVars_q.out;

              InvRot(&vdqsRef,&SinCosRot,&vsabRef);
              InvClarke(&vsabRef,&vabcsRef);
              PWMCompute(&vabcsRef,&duty,&vdc);
              iDC_level2           = idqs.d;
              if (fabs(idqs.d)>0.0 && fabs(iDC_level1-iDC_level2)<=0.0)
              {
                  CounterTmp1 += 1.0;
                  DCVoltageLevel1 += vdqsRef.d;
              }
          }
          else
          {
              iDC_level1           = idqs.d;
              DCVoltageLevel2      = DCVoltageLevel1/CounterTmp1;
              tmp1                 = CounterTmp1*Ts;
              TrLsEst              = DCVoltageLevel2/(iDC_level1/tmp1);
              StateDrive           = ROTOR_TIME_CONSTANT_EST;
          }
      break;
```

A2.4 *Rotor time constant estimation algorithm*

```
/*----------------------------------------------------------------------------*/
/*                         Rotor Time Constant Estimation                     */
/*----------------------------------------------------------------------------*/
     case ROTOR_TIME_CONSTANT_EST:
         counter++;

         if (iteration >= 20.0)   // Abandon tests if there is no convergence
         {
             counter = 0.0;
             StateDrive = GO_MOTOR;
         }

// Dead-time compensation using measured phase currents
         DeadTimeCompLUT(&iabcs,&vdc,&vdt);
         DirectClarke(&vdt,&vdtab);
         DirectRot(&vdtab, &SinCosRot, &vdtdq);

         if (counter < 5)
         {
             idqsRef.d             = IdRated;
             idqsRef.q             = 0.0;
             im_est                = IdRated;
             im_actual             = IdRated;
             CounterTmp1           = 0.0;
             CounterTmp2           = 0.0;
             CounterTmp3           = 0.0;
         }

         im0 = -IdRated;
         if(counter == 0.25*Ts_inv && im_est >= -IdRated)
             idqsRef.d = -IsMax;

         if (im_est <= im0)
             idqsRef.d = im0;

         SinCosRot.sin         = 0.0;
         SinCosRot.cos         = 1.0;
         DirectRot(&isab,&SinCosRot,&idqs);
         v0                    = vdqsRef.d;
         CrtRegVars_d.kp       = kp_i;
         CrtRegVars_d.ki       = ki_i;
         CrtRegVars_d.ref      = idqsRef.d;
         CrtRegVars_d.actual   = idqs.d;
         CrtRegVars_d.lim      = vds_max;
         CrtRegVars_d.vfw      = 0.0;
         PIReg(&CrtRegVars_d);
         vdqsRef.d = CrtRegVars_d.out;

         CrtRegVars_q.kp       = kp_i;
         CrtRegVars_q.ki       = ki_i;
         CrtRegVars_q.ref      = idqsRef.q;
         CrtRegVars_q.actual   = idqs.q;
         tmp4 = vds_max*vds_max-vdqsRef.d*vdqsRef.d;
         if (tmp4 <= 0.001)
             tmp4 = 0.0;
         CrtRegVars_q.lim      = sqrt(tmp4);
         CrtRegVars_q.vfw      = 0.0;

         PIReg(&CrtRegVars_q);
         vdqsRef.q = CrtRegVars_q.out;
```

```
    InvRot(&vdqsRef,&SinCosRot,&vsabRef);
    InvClarke(&vsabRef,&vabcsRef);
    PWMCompute(&vabcsRef,&duty,&vdc);

    v1 =                    vdqsRef.d;

    if (idqsRef.d == im0 && fabs(v1-v0) >= 50.0)        // > 50-V spike
        CounterTmp2 = counter;

    tmp2 = CounterTmp2, tmp3 = Ts_inv*8.0*tau_est;

    if (tmp2 > 0.0 && counter > tmp2 && counter <= tmp2 + tmp3)
    {
        integration_time += Ts;
        half_period = 8.0*tau_est/2.0;

        if (integration_time <= half_period)
            S1 += vdqsRef.d - vdtdq.d*enable_dt;
        else
            S2 += vdqsRef.d - vdtdq.d*enable_dt;
    }

    if (counter > CounterTmp2 + Ts_inv*8.0*tau_est && CounterTmp2 > 0.0)
    {
        area_err = 0.001;
        delta_S = (S2 - S1)*Ts;
        if (fabs(delta_S) > area_err)
        {
            k_S = 0.20;
            tau_est = tau_est + k_S * delta_S;
            if (tau_est <= 0.001)
                tau_est = tau_est_start;// avoiding -ve time constant
            counter = 0.0, iteration++;
            S1 = 0.0, S2 = 0.0, integration_time = 0.0;
            StateDrive = ROTOR_TIME_CONSTANT_EST;
        }
        else
        {
            counter = 0.0;
            StateDrive = ROTOR_RESISTANCE_EST;
        }
    }

    if (counter >= 0.25*Ts_inv)
    {
        im_actual += (idqs.d - im_actual)*(1/tau_actual)*Ts;
        im_est += (idqs.d - im_est)*(1/tau_est)*Ts;
    }

    if (StopPWM>0.5)
        StateDrive=RESET;

break;
```

A2.5   *Rotor resistance estimation algorithm*

```
/*------------------------------------------------------------------------*/
/*          Estimation of Rotor Resistance Referred to Stator             */
/*------------------------------------------------------------------------*/

case ROTOR_RESISTANCE_EST:
    counter ++;
```

```
        SinCosRot.sin           = 0.0;
        SinCosRot.cos           = 1.0;
        DirectRot(&isab,&SinCosRot,&idqs);

        if (counter > 0.5*Ts_inv && counter <= 1.0*Ts_inv)
        {
            idqsRef.d           = -0.33*IsMax;
            idqsRef.q           = 0.0;
        }

        if (counter > 1.0*Ts_inv && counter <= 1.5*Ts_inv)
        {
            idqsRef.d           = IsMax;
            idqsRef.q           = 0.0;
            if (counter <= 1.1*Ts_inv)
                sum += vdqsRef.d;
        }

        vds_max                 = 0.9*vdc*sqrt3_inv;
        CrtRegVars_d.kp         = kp_i;
        CrtRegVars_d.ki         = ki_i;

        CrtRegVars_d.ref        = idqsRef.d;
        CrtRegVars_d.actual     = idqs.d;
        CrtRegVars_d.lim        = vds_max;
        CrtRegVars_d.vfw        = 0.0;

        PIReg(&CrtRegVars_d);
        vdqsRef.d = CrtRegVars_d.out;

        CrtRegVars_q.kp         = kp_i;
        CrtRegVars_q.ki         = ki_i;

        CrtRegVars_q.ref        = idqsRef.q;
        CrtRegVars_q.actual     = idqs.q;
        tmp3 = vds_max*vds_max-vdqsRef.d*vdqsRef.d;
        if (tmp3 <= 0.001)
            tmp3 = 0.0;

        CrtRegVars_q.lim        = sqrt(tmp3);
        CrtRegVars_q.vfw        = 0.0;

        PIReg(&CrtRegVars_q);
        vdqsRef.q = CrtRegVars_q.out;

        InvRot(&vdqsRef, &SinCosRot, &vsabRef);
        InvClarke(&vsabRef, &vabcsRef);
        PWMCompute(&vabcsRef, &duty, &vdc);

        if (counter > 1.5*Ts_inv)
        {
            iDC_level1          = -0.33*IsMax;
            iDC_level2          = IsMax;
            vDC_level2          = sum/(0.1*Ts_inv);
            tmp1                = iDC_level2-iDC_level1;
            Rr_ref              = (vDC_level2-Rs*iDC_level2)/tmp1;

// Computing the rest of the equivalent circuit parameters
            Ls_Est              = TrLsEst + tau_est*Rr_ref;
            sigma_Est           = TrLsEst/Ls_Est;
            M_Est               = Ls_Est - 0.5*TrLsEst;
            Lr_Est              = M_Est*M_Est/(tau_est*Rr_ref);
```

```
            Rr_Est                  = Lr_Est/tau_est;

            counter = 0.0;
            sum = 0.0;
            StateDrive = RESET;
        }

    break;

    }
/*------------------------------------------------------------------------*/
/*                          Drive Ready to Start                          */
/*------------------------------------------------------------------------*/
```

A2.6   Two-frequency single phase test algorithm

```
/*------------------------------------------------------------------------*/
/*            Parameter Identification with Single Phase Tests            */
/*          at Two Different Injection Frequencies by Computing           */
/*           Total Impedance Using Sinusoidal Signal Integrators          */
/*------------------------------------------------------------------------*/
// Apply single-phase sinusoid at first frequency
    case TWO_FREQ_TEST_1:

        counter++;

        if (counter <= Ts_inv)                    // Apply test for 1 second
        {
            SinCosRot.sin        = 0.0;
            SinCosRot.cos        = 1.0;
            DirectRot(&isab, &SinCosRot, &idqs);

            vds_max              = 0.9*vdc*sqrt3_inv;

            w1                   = double_pi*freq1;
            ThetaRef            += w1*Ts;
            if (fabs(ThetaRef) >= double_pi)
                ThetaRef         = -fabs(ThetaRef) + double_pi;

            idqsRef.d            = IsTest*sin(ThetaRef);
            idqsRef.q            = 0.0;

            CrtRegVars_d.kp      = kp_i;
            CrtRegVars_d.ki      = ki_i;
            CrtRegVars_d.ref     = idqsRef.d;
            CrtRegVars_d.actual  = idqs.d;
            CrtRegVars_d.lim     = vds_max;
            CrtRegVars_d.vfw     = 0.0;

            PIReg(&CrtRegVars_d);
            vdqsRef.d = CrtRegVars_d.out;

            CrtRegVars_q.kp      = kp_i;
            CrtRegVars_q.ki      = ki_i;
            CrtRegVars_q.ref     = idqsRef.q;
            CrtRegVars_q.actual  = idqs.q;
            tmp3 = vds_max*vds_max - vdqsRef.d*vdqsRef.d;
            if (tmp3 <= 0.001)
                tmp3 = 0.0;

            CrtRegVars_q.lim     = tmp3;
            CrtRegVars_q.vfw     = 0.0;
```

```
            PIReg(&CrtRegVars_q);
            vdqsRef.q = CrtRegVars_q.out;

// Store sum of squares of voltage for r.m.s value computation
            if (counter > 0.4*Ts_inv && counter <= (0.4+1./freq1)*Ts_inv)
                sum += vsabRef.alpha*vsabRef.alpha;

// SSI for phase angle detection
            ki                = 2.*10.; // filter gain
            I_SSI_ab.alpha += (I_SSI_FB + ki*(idqsRef.d - I_SSI_ab.alpha))*Ts;
            I_SSI_FB       += -w1*w1*I_SSI_ab.alpha*Ts;
            I_SSI_ab.beta   = -I_SSI_FB/w1;

            V_SSI_ab.alpha += (SSI_FB + ki*(vdqsRef.d - V_SSI_ab.alpha))*Ts;
            SSI_FB         += -w1*w1*V_SSI_ab.alpha*Ts;
            V_SSI_ab.beta   = -SSI_FB/w1;

// Current vector is the reference
            ThetaSSI               = atan2(I_SSI_ab.beta, I_SSI_ab.alpha);
            SinCosSSI.sin          = sin(ThetaSSI);
            SinCosSSI.cos          = cos(ThetaSSI);

            DirectRot(&V_SSI_ab, &SinCosSSI, &V_SSI_dq);
            phi = atan2(V_SSI_dq.q, V_SSI_dq.d);
        }

        else
        {
            V_ph               = sqrt(sum/(Ts_inv/freq1)); // r.m.s value
            I_ph               = IsTest/sqrt2;
            Req1               = ((V_ph - RsEst*I_ph)/I_ph)*cos(phi);
            Xeq1               = Req1*tan(phi);

            ThetaRef = 0.0, sum = 0.0, ThetaSSI = 0.0;
            counter = 0.0, SSI_FB = 0.0;
            V_SSI_dq.d = 0.0, V_SSI_dq.q = 0.0;
            V_SSI_ab.alpha = 0.0, V_SSI_ab.beta = 0.0;
            I_SSI_ab.alpha = 0.0, I_SSI_ab.beta = 0.0, I_SSI_FB = 0.0;

            StateDrive         = TWO_FREQ_TEST_2;
        }

        InvRot(&vdqsRef, &SinCosRot, &vsabRef);
        InvClarke(&vsabRef, &vabcsRef);
        PWMCompute(&vabcsRef, &duty, &vdc);

    break;

/*==========================================================================*/

// Apply single-phase sinusoid at second frequency

    case TWO_FREQ_TEST_2:
        counter++;
        if (counter <= Ts_inv)                  // Apply test for 1 second
        {
            SinCosRot.sin       = 0.0;
            SinCosRot.cos       = 1.0;
            DirectRot(&isab, &SinCosRot, &idqs);

            w2                  = double_pi*freq2;
            ThetaRef            += w2*Ts;
```

```
                    if (fabs(ThetaRef) >= double_pi)
                        ThetaRef = -fabs(ThetaRef) + double_pi;

                    idqsRef.d            = IsTest*sin(ThetaRef);
                    idqsRef.q            = 0.0;

                    CrtRegVars_d.kp      = kp_i;
                    CrtRegVars_d.ki      = ki_i;
                    CrtRegVars_d.ref     = idqsRef.d;
                    CrtRegVars_d.actual  = idqs.d;
                    CrtRegVars_d.lim     = vds_max;
                    CrtRegVars_d.vfw     = 0.0;

                    PIReg(&CrtRegVars_d);
                    vdqsRef.d = CrtRegVars_d.out;

                    CrtRegVars_q.kp      = kp_i;
                    CrtRegVars_q.ki      = ki_i;
                    CrtRegVars_q.ref     = idqsRef.q;
                    CrtRegVars_q.actual  = idqs.q;
                    tmp3 = vds_max*vds_max - vdqsRef.d*vdqsRef.d;
                    if (tmp3 <= 0.001)
                        tmp3 = 0.0;

                    CrtRegVars_q.lim     = sqrt(tmp3);
                    CrtRegVars_q.vfw     = 0.0;

                    PIReg(&CrtRegVars_q);
                    vdqsRef.q = CrtRegVars_q.out;

// Store sum of squares of voltage for r.m.s value computation
                    if (counter > 0.4*Ts_inv && counter <= (0.4+1./freq1)*Ts_inv)
                        sum += vsabRef.alpha*vsabRef.alpha;

// SSI for phase angle detection
                    ki                   = 2.*10.; // filter gain

                    I_SSI_ab.alpha += (I_SSI_FB + ki*(idqsRef.d - I_SSI_ab.alpha))*Ts;
                    I_SSI_FB       += -w2*w2*I_SSI_ab.alpha*Ts;
                    I_SSI_ab.beta   = -I_SSI_FB/w2;

                    V_SSI_ab.alpha += (SSI_FB + ki*(vdqsRef.d - V_SSI_ab.alpha))*Ts;
                    SSI_FB         += -w2*w2*V_SSI_ab.alpha*Ts;
                    V_SSI_ab.beta   = -SSI_FB/w2;

                    ThetaSSI             = atan2(I_SSI_ab.beta, I_SSI_ab.alpha);
                    SinCosSSI.sin        = sin(ThetaSSI);
                    SinCosSSI.cos        = cos(ThetaSSI);

                    DirectRot(&V_SSI_ab, &SinCosSSI, &V_SSI_dq);
                    phi = atan2(V_SSI_dq.q, V_SSI_dq.d);

                }

                else
                {
                    V_ph                 = sqrt(sum/(Ts_inv/freq2)); // r.m.s value
                    I_ph                 = IsTest/sqrt2;
                    Req2                 = ((V_ph - RsEst*I_ph)/I_ph)*cos(phi);
                    Xeq2                 = Req2*tan(phi);

                    ThetaRef = 0.0, sum = 0.0, counter = 0.0;
                    V_SSI_dq.d = 0.0, V_SSI_dq.q = 0.0;
```

```
                V_SSI_ab.alpha = 0., V_SSI_ab.beta = 0.;
                I_SSI_ab.alpha = 0., I_SSI_ab.beta = 0., I_SSI_FB = 0.;

// Calculate equivalent circuit parameters

                K1 = w1*w1*w2*w2*fabs(Req1 - Req2)/(Req1*Req2*(w1*w1 - w2*w2));
                K2 = sqrt((Req2*w1*w1 - Req1*w2*w2)/fabs(Req1 - Req2))/(w1*w2);

                Lm_est = sqrt(fabs(Xeq1*K1 + Xeq1*K1*K2*K2*w1*w1 + K2*w1*w1*w1) /
                        (K1*K1*K2*w1 + K1*K1*K2*K2*K2*w1*w1*w1));

                R2_est              = K1*Lm_est*Lm_est;
                L3_est              = K2*R2_est;
                L_est               = L3_est - Lm_est;

                StateDrive          = RESET;
            }

        InvRot(&vdqsRef, &SinCosRot, &vsabRef);
        InvClarke(&vsabRef, &vabcsRef);
        PWMCompute(&vabcsRef, &duty, &vdc);

        break;

/*----------------------------------------------------------------------------*/
/*                          Drive Ready to Start                             */
/*----------------------------------------------------------------------------*/
```

A3.   Parameter Identification Algorithms for Permanent Magnet Synchronous Machines

The drive initialization algorithms are the same as give in appendix A2.1 above. In the current section only the algorithms specific to the self-commissioning of an Interior Permanent Magnet Synchronous Machine (IPMSM) are given for the sake of brevity. These algorithms are equally applicable for a Surface-mounted Permanent Magnet Synchronous Machine (SPMSM). The stator resistance estimation strategy is the same as adopted for the induction machine, therefore the instructions remain effectively the same (cf. appendix A2.2).

A3.1   General functions

In addition to the functions defined above, some new functions are necessary for this machine.

```
/*----------------------------------------------------------------------------*/
/*                          Additional Functions                             */
/*----------------------------------------------------------------------------*/
// Finite Impulse Response (FIR) filter
void Filter(double *xk, double *xf_k, double kfilt)
{
    *xf_k=(*xk-*xf_k)*2*two_pi*kfilt*Tsw+*xf_k;
}

// Sign function
double Sign(double V)
{
    double abs_V;
    abs_V = fabs(V);
    if (V != 0)
        return V/abs_V;
    else
        return 0.;
```

```
}

// Resonant Controller
void ResonantCtrlr(XRC *RCVars)
{
    double error, err_sin, err_cos;
    double int_sin, int_cos, out_sin, out_cos;

    error = RCVars->ref - RCVars->actual;

    err_sin = error*RCVars->sin;
    err_cos = error*RCVars->cos;

    int_sin = RCVars->int_sin;
    int_cos = RCVars->int_cos;

// Low-pass filter instead of pure integrator
    Filter(&err_sin, &int_sin, RCVars->fc);
    Filter(&err_cos, &int_cos, RCVars->fc);

    out_sin = int_sin*RCVars->gain;
    out_cos = int_cos*RCVars->gain;

    RCVars->out = 2*(out_cos*RCVars->cos + out_sin*RCVars->sin);

    if (RCVars->out > RCVars->lim)
        RCVars->out = RCVars->lim;

    if (RCVars->out < -RCVars->lim)
        RCVars->out = -RCVars->lim;
}
```

A3.2   *High frequency injection algorithm*

```
/*----------------------------------------------------------------------------*/
/*                Current Controlled High-Frequency Injection                  */
/*----------------------------------------------------------------------------*/

      case HF_Test:
         counter_test++;

         if (counter_test < Fsw)
         {
// High frequency injection in self-axis
            theta_hftest         = two_pi*inj_freq*counter_test*Tsw;

// Low frequency oscillations in cross-axis (when cross axis is q-axis)
            theta_cross          = pi/2 + two_pi*cross_freq*counter_test*Tsw;

            if (inj_axis <= 0.5)
            {
                iRef_comm.d      = id_offset + Itest*sin(theta_hftest);
                tmp2             = sin(theta_cross);
                iRef_comm.q      = Icross*Sign(tmp2); // Square wave in q-axis
            }

            else
            {
                iRef_comm.d      = Icross; // Constant current in d-axis
                iRef_comm.q      = Itest*sin(theta_hftest);
            }
```

```
        }
        else
            iRef_comm.d = 0.0, iRef_comm.q = 0.0;

// Using PI+Resonant Current Controllers
// d-axis PI current control
        CrtReg.kp                = kp_id;
        CrtReg.ki                = ki_id;
        CrtReg.ref               = iRef_comm.d;
        CrtReg.actual            = idq.d;
        CrtReg.lim               = VsMax;
        CrtReg.vfw               = 0;

        PIReg(&CrtReg);
// Take d-axis voltage command from PI regulator
        vdqsRef_PI.d = CrtReg.out;

// q-axis PI current control
        CrtReg.kp                = kp_iq;
        CrtReg.ki                = ki_iq;
        CrtReg.ref               = iRef_comm.q;
        CrtReg.actual            = idq.q;

        tmp1 = VsMax*VsMax - vdqsRef.d*vdqsRef.d;
        if (tmp1<0.001)
            tmp1 = 0.001;
        CrtReg.lim               = sqrt(tmp1);
        CrtReg.vfw               = 0;

        PIReg(&CrtReg);
// Take q-axis voltage command from PI regulator
        vdqsRef_PI.q = CrtReg.out;

// Resonant part of controller
        ResCtrlVars_d.ref        = iRef_comm.d;
        ResCtrlVars_d.actual     = idq.d;
        ResCtrlVars_d.fc         = fc_RC;
        ResCtrlVars_d.gain       = ki_RC_d;
        ResCtrlVars_d.lim        = VsMax;
        ResCtrlVars_d.cos        = cos(theta_hftest);
        ResCtrlVars_d.sin        = sin(theta_hftest);

        ResonantCtrlr(&ResCtrlVars_d);

        vdqsRef_Res.d            = ResCtrlVars_d.out;

        ResCtrlVars_q.ref        = iRef_comm.q;
        ResCtrlVars_q.actual     = idq.q;
        ResCtrlVars_q.fc         = fc_RC;
        ResCtrlVars_q.gain       = ki_RC_q;        // Higher gain in q-axis
        ResCtrlVars_q.lim        = sqrt(fabs(VsMax*VsMax-vdqsRef.d*vdqsRef.d));
        ResCtrlVars_q.cos        = cos(theta_hftest);
        ResCtrlVars_q.sin        = sin(theta_hftest);

        ResonantCtrlr(&ResCtrlVars_q);

        vdqsRef_Res.q            = ResCtrlVars_q.out;

// Combining and limiting the output of PI and resonant controllers

        vdqsRef.d                = vdqsRef_PI.d + vdqsRef_Res.d;

        if (vdqsRef.d > VsMax)
```

```
        vdqsRef.d = VsMax;
    if (vdqsRef.d < -VsMax)
        vdqsRef.d = -VsMax;

    tmp2 = sqrt(fabs(VsMax*VsMax - vdqsRef.d*vdqsRef.d));

    vdqsRef.q                 = vdqsRef_PI.q + vdqsRef_Res.q;

    if (vdqsRef.q > tmp2)
        vdqsRef.q = tmp2;
    if (vdqsRef.q < -tmp2)
        vdqsRef.q = -tmp2;

    InvRot(&vdqsRef, &SinCosRot, &vsabRef);
    InvClarke(&vsabRef, &vabcsRef);
    PWMCompute(&vabcsRef, &duty, &vdc);

break;
```

A3.3   Automatic test routine with Matlab-dSpace library

The programme below gives the interface commands between Matlab environment and dSpace. The *mlib* library functions can be found in the user guide of dSpace. The test algorithm injects different pairs of self- and cross-axis currents and acquires output signals from dSpace. The algorithm performs post-processing on the data and gives *d*- and *q*-axis inductances as a function of *d*- and *q*-axis currents.

```
%--------------------------------------------------------------------------
%                          Automatic Test Routine                         |
%--------------------------------------------------------------------------

%--------------------------------------------------------------------------
% Description:   The file uses dSpace's interface functions with Matlab to |
%                set variables and acquire data from real-time execution of|
%                experiments on the board.                                 |
%                Frequency injection tests are performed and results are   |
%                elaborated in a separate file for d- and q-axis inductance|
%                estimation.                                               |
%                Functions to be observed: mlib (type doc mlib in Matlab   |
%                command window for more information about its sub-functions)|
%                                                                          |
% Date:          04-02-2013                                                |
% Author:        Shafiq Ahmed Odhano                                       |
% Status:        Final                                                     |
%--------------------------------------------------------------------------
%%
clc, clear;

%%      Before running the test, create a new folder and give its name here
%       each time a new test is performed (e.g. Test2, Test3 etc)

Test_Folder = '\Exp_Results\Test3\';

%%

% VARIABLES DEFINITION

Fs         = 10000;               % Sampling frequency
Ts         = 1/Fs;                % Sampling time
inj_freq   = 80;                  % Test frequency [Hz]
cross_freq = inj_freq/10;         % cross axis frequency [Hz]
```

```
I_mag       = 5:5:20;                % Current amplitude
Cross_Crt   = -20:5:20;              % Cross axis current vector
Id_Offset = 0;

Delay       = 1000;                  % Delay for sample collection [no. of samples]

% VARIABLES INIZIALIZZATION

% RUN THIS FILE AFTER:
    % 1 - BUILD THE MODEL
    % 2 - OPEN THE EXPERIMENT
    % 3 - CONTROL DESK IN ANIMATION MODE
    % 4 - Push ON
    % 5 - Allow Precarica state to pass
    % 6 - Press PWM EN
    % 7 - Press GO_CTRL

% Select DS1104 board for use with MLIB
mlib('SelectBoard','DS1104');

% Check if the application the desired application is running
DemoApplName = lower([pwd,'\E5.ppc']);

if mlib('IsApplRunning'),
    ApplInfo = mlib('GetApplInfo');
    if strcmp(DemoApplName,lower(ApplInfo.name)) ~= 1
        err_msg = sprintf('*** This MLIB demo file needs the real-time ...
        processor application\n*** ''%s'' running!', DemoApplName);
        error(err_msg);
    end;
else
        err_msg = sprintf('*** This MLIB demo file needs the real-time ...
        processor application\n*** ''%s'' running!', DemoApplName);
        error(err_msg);
end;

% Specify the variables used by MLIB and get their descriptors

variables =  {'Model Root/Controllo/State';...            % Retrieve system state

            'User Variables/HF Test/Test_Counter';...    % Counter that controls
%                                                          injection

            'User Variables/HF Test/inj_axis';...        % Injection axis
%                                                          selection

            'User Variables/HF Test/id_offset';...       % d-axis offset

            'User Variables/HF Test/Itest';...           % Injection current
%                                                          magnitude

            'User Variables/HF Test/Icross';...          % Cross axis current
%                                                          magnitude

            'User Variables/HF Test/inj_freq';...        % Injection frequency

            'User Variables/HF Test/cross_freq';...      % Cross-axis frequency

            'User Variables/HF Test/id_comm';...         % d-axis current

            'User Variables/HF Test/id_ref_comm';...     % d-axis current
%                                                          reference
```

```matlab
            'User Variables/HF Test/iq_comm';...        % q-axis current

            'User Variables/HF Test/iq_ref_comm';...    % q-axis current
%                                                         reference

            'User Variables/HF Test/Vd_comm';...        % d-axis imposed
%                                                         voltage

            'User Variables/HF Test/Vq_comm';...        % q-axis imposed
%                                                         voltage
            };
[State, Test_Counter, inj_axis, Id_offset, Itest, Icross, Inj_Freq,...
 Cross_Freq, id_comm, id_ref_comm, iq_comm, iq_ref_comm, Vd_comm, Vq_comm]...
= mlib('GetTrcVar', variables);

% Assign to local variable
State_Drive = mlib('Read', State);

% SEFETY OPERATIONS
if (State_Drive ~= 0)
    err_msg = sprintf('*** The Drive must be in START mode for this test! ***');
    error(err_msg);
end

% Set the value of d-axis offset current to 0 PRECAUTION
mlib('Write',Id_offset,'Data',0);

% Set the value of test current to 0 PRECAUTION
mlib('Write',Itest,'Data',0);

% Set the value of cross axis current to 0 PRECAUTION
mlib('Write',Icross,'Data',0);

% Set the value of test frequency to 0 PRECAUTION
mlib('Write',Inj_Freq,'Data',0);


%==============================================================================
%                      High Frequency Injection in d-axis                      |
%==============================================================================
%       Injection in d-axis at fixed freq. and variable amplitude with
%       iq = -20 ÷ 20 A at a lower frequency

for index = 1:1:length(Cross_Crt)
    mlib('Write', inj_axis, 'Data', 0);          % Select d-axis
    mlib('Write',Inj_Freq, 'Data', inj_freq);    % Injection frequency
    mlib('Write',Id_offset,'Data',Id_Offset);    % d-axis superimposed dc
    mlib('Write',Cross_Freq,'Data',cross_freq);

    for amp = 1:1:length(I_mag)
        mlib('Write', Test_Counter, 'Data', 0); % Reset test counter
        HH = num2str(I_mag(amp));                % Determining filename index
        if HH <= 9                               % Add zero for single digits
            HH = ['0' HH];
        end

        II = num2str(Cross_Crt(index));          % Determining filename index

        if II <= 9                               % Add zero for single digits
            II = ['0' II];
        end
```

```
        JJ = num2str(inj_freq);

% Set the option of the data acquisition performed by service number 1 (default)
        mlib('Set','Trigger', 'on',...
             'TriggerLevel', 0.5,...
             'TriggerEdge','rising',...  % Default, can be omitted
             'TriggerVariable',Itest,... % Trigger when Itest is set
             'TraceVars',[id_comm; id_ref_comm; iq_comm; iq_ref_comm;...
              Vd_comm; Vq_comm],...
             'NumSamples',(Fs-delay),...
             'Delay', delay,...
             'TimeStamping','on');

        mlib('StartCapture');          % Start capture on the DS1104, default
%                                        service number 1

        while mlib('TriggerState')~=1 % Wait until trigger is armed; in pre-
        end                           % trigger mode trigger is armed after the
%                                       delay time is run down!

        mlib('Write',Itest,'Data',I_mag(amp));
        mlib('Write',Icross,'Data',Cross_Crt(index));

        while mlib('CaptureState')~=0
        end                           % Wait until data acquisition finishes

% Fetch the data into MATLAB workspace
        capture_data = mlib('FetchData');

        file_name = ['Id_' HH '_Iq_' II '_Freq_' JJ];
        save([pwd Test_Folder file_name], 'capture_data', 'inj_freq',...
        'cross_freq');

% Compute Ld and save vector
        Iq = Cross_Crt(index);
        Ld(index, amp) = Fourier_d(capture_data, Iq, Fs, inj_freq);
        save([pwd Test_Folder 'Ld_Vector'], 'Ld');

% Show inductance value on screen
        disp(['Id = ', num2str(I_mag(amp))...
              'A; Iq = ', num2str(Cross_Crt(index))...
              'A; Freq. = ', num2str(inj_freq)...
              'Hz; Ld = ', num2str(Ld(index, amp))])

        tic
        while toc<0.5                  % Wait 0.5 second before applying new
%                                        magnitude

            mlib('Write', Itest, 'Data', 0);
            mlib('Write',Id_offset,'Data',0);
        end
    end
end


%===============================================================================
%                       High Frequency Injection in q-axis                     |
%===============================================================================
%       Injection in q-axis at fixed freq. and variable amplitude with
%       id = -20 ÷ 20 A (dc)

for index = 1:1:length(Cross_Crt)
    mlib('Write', inj_axis, 'Data', 1);        % Select q-axis
    mlib('Write',Inj_Freq, 'Data', inj_freq);     % Injection frequency
```

```
    mlib('Write',Cross_Freq,'Data',0);                % Constant current in d-axis

    for amp = 1:1:length(I_mag)
        mlib('Write', Test_Counter, 'Data', 0);   % Reset test counter
        HH = num2str(I_mag(amp));                      % Determining filename index
        if HH <= 9                                     % Add zero for single digits
            HH = ['0' HH];
        end

        II = num2str(Cross_Crt(index));           % Determining filename index

        if II <= 9                                     % Add zero for single digits
            II = ['0' II];
        end

        JJ = num2str(inj_freq);

% Set the option of the data acquisition performed by service number 1 (default)
        mlib('Set','Trigger', 'on',...
              'TriggerLevel', 0.5,...
              'TriggerEdge','rising',...  % Default, can be omitted
              'TriggerVariable',Itest,... % Trigger when Itest is set
              'TraceVars',[id_comm; id_ref_comm; iq_comm; iq_ref_comm;...
               Vd_comm; Vq_comm],...
              'NumSamples',(Fs-delay),...
              'Delay', delay,...
              'TimeStamping','on');

        mlib('StartCapture');            % Start capture on the DS1104, default
%                                          service number 1

        while mlib('TriggerState')~=1 % Wait until trigger is armed; in pre-
        end                              % trigger mode trigger is armed after the
%                                          delay time is run down!

        mlib('Write',Itest,'Data',I_mag(amp));
        mlib('Write',Icross,'Data',Cross_Crt(index));

        while mlib('CaptureState')~=0
        end                              % wait until data acquisition finishes

% Fetch the data into MATLAB workspace
        capture_data = mlib('FetchData');

        file_name = ['Iq_' HH '_Id_' II '_Freq_' JJ];
        save([pwd Test_Folder file_name], 'capture_data', 'inj_freq');

% Compute Lq and save vector
        Id = Cross_Crt(index);
        Lq(index, amp) = Fourier_q(capture_data, Fs, inj_freq);
        save([pwd Test_Folder 'Lq_Vector'], 'Lq');

% Show inductance value on screen
        disp(['Iq = ', num2str(I_mag(amp))...
                'A; Id = ', num2str(Cross_Crt(index))...
                'A; Freq. = ', num2str(inj_freq)...
                'Hz; Lq = ', num2str(Ld(index, amp))])

        tic
        while toc<0.5                    % wait 0.5 second before applying new
%                                          magnitude

            mlib('Write', Itest, 'Data', 0);
```

```
        mlib('Write',Id_offset,'Data',0);
    end
end
end


%-------------------------------------------------------------------------
%                          User Defined Functions                        |
%-------------------------------------------------------------------------


%=========================================================================
%                        Extracting d-axis Inductance                    |
%=========================================================================

function [Ld] = Fourier_d(capture_data, Iq, Fs, Inj_Freq)

% Function name: Fourier_d.m
% Description:   This function performs Fourier Analysis on the captured data   |
%                from dSapce environment and determines inductance Ld.          |

    inj_freq        = Inj_Freq;
    Vd_comm         = capture_data(6,:);
    id_comm         = capture_data(2,:);
    iq_comm         = capture_data(4,:);                % For cross coupling effects
    t               = capture_data(1,:);

    N = 3;

% Making sure that Ld is computed for constant iq (either +ve or -ve)
    if Iq < 0
        start_index = find(t > 0.5 & iq_comm < 0, 100, 'first');
    elseif Iq > 0
        start_index = find(t > 0.5 & iq_comm > 0, 100, 'first');
    else
        start_index = find(t > 0.5, 1, 'first');
    end

    t_start = t(start_index(end));

    Time = t_start:1/Fs:t_start+N/inj_freq-1/Fs;  % Time window for FFT analysis

    index = find(t>=min(Time) & t<=max(Time));

%% FFT
    Ns              = length(Time);                 % No. of samples
    d_F             = Fs/Ns;                         % Frequency step
    FFT_Vd          = fft(Vd_comm(index))/(Ns/2);   % Voltage FFT calculation
    FFT_Id          = fft(id_comm(index))/(Ns/2);   % Current FFT calculation

%% Extracting fundamental voltage and current from FFT and obtaining phi
    fund_index      = round(1+inj_freq/d_F);
    Vd_fund         = FFT_Vd(fund_index);
    Id_fund         = FFT_Id(fund_index);
    V_mag           = abs(Vd_fund);
    V_phi           = angle(Vd_fund);
    I_mag           = abs(Id_fund);
    I_phi           = angle(Id_fund);
    phi             = V_phi - I_phi;

    if phi < 0.
        phi = phi + 2*pi;
    end

    if phi > 2*pi
```

```
        phi = phi - 2*pi;
    end

%% Calculating impedance and inductance from fundamental values
    Z               = V_mag/I_mag;

    Xd              = Z*sin(phi);
    R               = Z*cos(phi);
    Ld              = Xd/(2*pi*inj_freq);
end

%==========================================================================
%                       Extracting q-axis Inductance                       |
%==========================================================================

function [Lq] = Fourier_q(capture_data, Fs, Inj_Freq)

% Function name: Fourier_q.m
% Description:   This function performs Fourier Analysis on the captured data |
%                from dSapce environment and determines inductance Lq.        |

    inj_freq        = Inj_Freq;
    Vq_comm         = capture_data(7,:);
    iq_comm         = capture_data(4,:);
    t               = capture_data(1,:);

    N = 3;

    t_start = 0.3;

    Time = t_start:1/Fs:t_start+N/inj_freq-1/Fs;  % Time window for FFT analysis

    index = find(t>=min(Time) & t<=max(Time));

%% FFT
    Ns              = length(Time);               % No. of samples
    d_F             = Fs/Ns;                       % Frequency step
    FFT_Vq          = fft(Vq_comm(index))/(Ns/2); % Voltage FFT calculation
    FFT_Iq          = fft(iq_comm(index))/(Ns/2); % Current FFT calculation

%% Extracting fundamental voltage and current from FFT and obtaining phi
    fund_index      = round(1+inj_freq/d_F);
    Vq_fund         = FFT_Vq(fund_index);
    Iq_fund         = FFT_Iq(fund_index);
    V_mag           = abs(Vq_fund);
    V_phi           = angle(Vq_fund);
    I_mag           = abs(Iq_fund);
    I_phi           = angle(Iq_fund);
    phi             = V_phi - I_phi;

    if phi < 0.
        phi = phi + 2*pi;
    end

    if phi > 2*pi
        phi = phi - 2*pi;
    end

%% Calculating impedance and inductance from fundamental values
    Z               = V_mag/I_mag;

    Xq              = Z*sin(phi);
    R               = Z*cos(phi);
```

```
    Lq              = Xq/(2*pi*inj_freq);
end
```

A3.4   Permanent magnet flux estimation algorithm

```
/*------------------------------------------------------------------------*/
/*              Permanent Magnet Flux Estimation at Standstill            */
/*------------------------------------------------------------------------*/

      case PM_Flux_Test:

         if (PM_Flux_Est > 0.5)
         {
            CrtReg.ref          = idqsRef.q;
            CrtReg.actual       = idq.q;
            CrtReg.lim          = VsMax;
            CrtReg.vfw          = 0.;

            PIReg(&CrtReg);
            vdqsRef.q = CrtReg.out;

// Using an unconventional speed control loop that exploits reluctance torque
            SpeedReg.ref        = 0.;
            SpeedReg.actual     = omega_meas_mecc_L_f;
            SpeedReg.lim        = Id_Max;
            SpeedReg.vfw        = 0;

            PIReg(&SpeedReg);

// Take d-axis current reference command from the speed loop
            if (PM_Flux_Est > 1.5)
                 idqsRef.d       = -SpeedReg.out;

            CrtReg.ref          = idqsRef.d;
            CrtReg.actual       = idq.d;
            CrtReg.lim          = sqrt(fabs(VsMax*VsMax-vdqsRef.q*vdqsRef.q));

            PIReg(&CrtReg);
            vdqsRef.d = CrtReg.out;
         }

         if (PM_Flux_Est < 0.5 && skip_HF > 0.5)
            vdqsRef.d = 0., vdqsRef.q = 0.;

         InvRot(&vdqsRef, &SinCosRot, &vsabRef);
         InvClarke(&vsabRef, &vabcsRef);
         PWMCompute(&vabcsRef, &duty, &vdc);

// Note 1: The PM flux is computed by observing the d-axis current command given
// by the speed loop at which the torque balance is reached. The inductances
// used in computation must correspond to the d- and q-axis currents.

// Note 2: This algorithm works for machines having high saliency ratio such as
//  an IPMSM. It can be applied for an SPMSM provided it demonstrates a
// considerable saturation-induced saliency.

      break;
```

A4.   Induction Motor Torque Estimation

This section gives the programme sections for induction motor control in which the flux observer is modified to take into consideration the saturation effects. The core saturation affects flux estimation that directly influences the torque estimation accuracy.

```
/*----------------------------------------------------------------------------*/
/*                      Look-Up Table Reading Function                        */
/*----------------------------------------------------------------------------*/
// The look-up table contains Lm as a function of magnetizing flux

void Lm_LUT(double *Lambdam, double *LmLUT)
{
    int index;
    double Flux;

    Flux = *Lambdam;

    if (Flux <= 0.0)                // Precautionary
        *LmLUT = Lm_vector[0];

    if (Flux >= Max_Flux)
        index = LUT_points - 1;
    else
        index = (int) (Flux/Flux_step);

    *LmLUT = Lm_vector[index];
}


/*----------------------------------------------------------------------------*/
/*             Flux Observer with Saturation Compensation                     */
/*----------------------------------------------------------------------------*/

// Read Magnetizing Characteristic for Lm
        Lambdam.alpha           = Lambdas.alpha - Lls*isab.alpha;
        Lambdam.beta            = Lambdas.beta  - Lls*isab.beta ;
        tmp1                    = Lambdam.alpha*Lambdam.alpha;
        tmp2                    = Lambdam.beta*Lambdam.beta;
        LambdamMod              = sqrt(tmp1 + tmp2);

        Lm_LUT(&LambdamMod, &LmLUT);

// Compute parameters based on modified magnetizing inductance
        Lm                      = LmLUT;
        Ls                      = Lls + Lm;
        Lr                      = Llr + Lm;
        kr                      = Lm/Lr;
        sigma                   = 1-Lm*Lm/(Ls*Lr);
        tau_r                   = Lr/Rr;

// Flux-observer parameters
        Kobs1                   = Lm/tau_r;
        Kobs2                   = 1.0/tau_r;
        Kobs3                   = sigma*Ls;
        Kobs4                   = 1.0/kr;

// Stator and rotor flux-observer

// Forward estimator
        tmp1                    = kdt*vdtab.alpha*enable_dt; // For dead-time
        tmp2                    = kdt*vdtab.beta *enable_dt; // compensation
```

```
        BackEmf.alpha              = vsabRef.alpha - RsEst*isab.alpha - tmp1;
        BackEmf.beta               = vsabRef.beta - RsEst*isab.beta - tmp2;
        dLambdas.alpha             = BackEmf.alpha+g*ErrorObs.alpha;
        dLambdas.beta              = BackEmf.beta +g*ErrorObs.beta;
        Lambdas.alpha          += Ts*dLambdas.alpha;
        Lambdas.beta           += Ts*dLambdas.beta;
        LambdarFwd.alpha           = (Lambdas.alpha-Kobs3*isab.alpha)*Kobs4;
        LambdarFwd.beta            = (Lambdas.beta -Kobs3*isab.beta )*Kobs4;

// Feedback estimator
        DirectRot(&isab, &SinCosEnc, &idqsRot);

        dLambdarFback_dq.d         = idqsRot.d*Kobs1-LambdarFback_dq.d*Kobs2;
        dLambdarFback_dq.q         = idqsRot.q*Kobs1-LambdarFback_dq.q*Kobs2;
        LambdarFback_dq.d      += Ts*dLambdarFback_dq.d;
        LambdarFback_dq.q      += Ts*dLambdarFback_dq.q;

        InvRot(&LambdarFback_dq, &LambdarFback, &SinCosEnc);

        LambdasFback.alpha         = Kobs3*isab.alpha + kr*LambdarFback.alpha;
        LambdasFback.beta          = Kobs3*isab.beta  + kr*LambdarFback.beta;

// Error computation
        ErrorObs.alpha             = LambdasFback.alpha-Lambdas.alpha;
        ErrorObs.beta              = LambdasFback.beta -Lambdas.beta ;

/*----------------------------------------------------------------------------*/
/*                          Torque Estimation                                 */
/*----------------------------------------------------------------------------*/

        te = 1.5*p*(Lambdas.alpha*isab.beta - Lambdas.beta*isab.alpha);

// Filter at 1 kHz
        Filter(&te, &te_filt, f_cutoff_torque);
```

References

[1]   V. Donescu, A. Charette, Z. Yao and V. Rajagopalan, *Modeling and simulation of saturated induction motors in phase quantities*, IEEE Transactions on Energy Conversion, Vol. 14, No. 3, **1999**, pp. 386-393

[2]   R. Browning, *Evolution of induction motors-the ever-shrinking motor*, IEEE Industry Applications Magazine, Vol. 3, No. 1, **1997**, pp. 16, 18

[3]   T. M. Jahns, G. B. Kliman and T. W. Neumann, *Interior Permanent-Magnet Synchronous Motors for Adjustable-Speed Drives*, IEEE Transactions on Industry Applications, Vol. IA-22, No. 4, **1986**, pp. 738-747

[4]   M. A. Rahman, *History of Interior Permanent Magnet Motors [History]*, IEEE Industry Applications Magazine, Vol. 19, No. 1, **2013**, pp. 10-15

[5]   F. Blaschke, *The principle of Field Orientation as Applied to the New TRANSVEKTOR Closed-Loop Control System for Rotating-Field Machines*, Siemens Review, Vol. 34, No. **1972**, pp. 217 - 220

[6]   IEEE, *IEEE Standard Test Procedure for Polyphase Induction Motors and Generators*, 2004, pp. 1-79

[7]   H. A. Toliyat, E. Levi and M. Raina, *A review of RFO induction motor parameter estimation techniques*, IEEE Transactions on Energy Conversion, Vol. 18, No. 2, **2003**, pp. 271-283

[8]   H. Schierling, *Self-commissioning-a novel feature of modern inverter-fed induction motor drives*, Conf. Proc. Third International Conference on Power Electronics and Variable-Speed Drives, **1988**, pp. 287-290

[9]   H. Schierling, *Fast and reliable commissioning of AC variable speed drives by self-commissioning*, Conf. Proc. IEEE Industry Applications Society Annual Meeting, **1988**, pp. 489-492 vol.481

[10]   P. Vas, *Vector Control of AC Machines*, Clarendon Press - Oxford, **1994**.

[11]   N. P. Quang and J.-A. Dittrich, *Vector Control of Three-Phase AC Machines*, Springer, **2008**.

[12]   M. Globevnik, *Induction motor parameters measurement at stand still*, Conf. Proc. 24th Annual Conference of the IEEE Industrial Electronics Society, IECON '98, **1998**, pp. 280-285 vol.281

[13]   M. Sumner and G. M. Asher, *Self-commissioning for voltage-referenced voltage fed vector controlled induction motor drives*, Conf. Proc. 23rd Annual IEEE Power Electronics Specialists Conference, PESC '92, **1992**, pp. 139-144 vol.131

[14]   M. Bertoluzzo, G. S. Buja and R. Menis, *Inverter voltage drop-free recursive least-squares parameter identification of a PWM inverter-fed induction motor at standstill*, Conf. Proc. IEEE International Symposium on Industrial Electronics, ISIE '97, **1997**, pp. 649-654 vol.642

[15] P. J. Chrzan and H. Klaassen, *Parameter identification of vector-controlled induction machines*, Electrical Engineering, Vol. 79, No. 1, **1996**, pp. 39-46

[16] M. Sumner and G. M. Asher, *Autocommissioning for voltage-referenced voltage-fed vector-controlled induction motor drives*, IEEE Proceedings on Electric Power Applications, Vol. 140, No. 3, **1993**, pp. 187-200

[17] M. Ruff, A. Bunte and H. Grotstollen, *A new self-commissioning scheme for an asynchronous motor drive system*, Conf. Proc. IEEE Industry Applications Society Annual Meeting, **1994**, pp. 616-623 vol.611

[18] G. S. Buja, R. Menis and M. I. Valla, *MRAS identification of the induction motor parameters in PWM inverter drives at standstill*, Conf. Proc. 21st IEEE International Conference on Industrial Electronics, Control, and Instrumentation, IECON, **1995**, pp. 1041-1047 vol.1042

[19] W. H. Kwon, C. H. Lee, K. S. Youn and G. H. Cho, *Measurement of rotor time constant taking into account magnetizing flux in the induction motor*, Conf. Proc. IEEE Industry Applications Society Annual Meeting, **1994**, pp. 88-92 vol.81

[20] A. Bunte and H. Grotstollen, *Parameter identification of an inverter-fed induction motor at standstill with a correlation method*, Conf. Proc. Fifth European Conference on Power Electronics and Applications, **1993**, pp. 97-102 vol.105

[21] H. B. Karayaka, M. N. Marwali and A. Keyhani, *Induction machine parameter tracking from test data via PWM inverters*, Conf. Proc. IEEE Industry Applications Conference, 1997. Thirty-Second IAS Annual Meeting, IAS '97, **1997**, pp. 227-233 vol.221

[22] M. Seung-Ill and A. Keyhani, *Estimation of Induction Machine Parameters from Standstill Time-Domain Data*, IEEE Transactions on Industry Applications, Vol. 30, No. 6, **1994**, pp. 1609

[23] A. Consoli, L. Fortuna and A. Gallo, *Induction Motor Identification by a Microcomputer-Based Structure*, IEEE Transactions on Industrial Electronics, Vol. IE-34, No. 4, **1987**, pp. 422-428

[24] V. Ambrozic, R. Cajhen and J. Nastran, *A step voltage method for determination of an induction motor rotor time constant in a cold state*, Conf. Proc. IEEE International Symposium on Industrial Electronics, ISIE'93, **1993**, pp. 85-89

[25] H. Rasmussen, M. Knudsen and M. Tonnes, *Parameter estimation of inverter and motor model at standstill using measured currents only*, Conf. Proc. IEEE International Symposium on Industrial Electronics, ISIE '96, **1996**, pp. 331-336 vol.331

[26] M. Ruff and H. Grotstollen, *Identification of the saturated mutual inductance of an asynchronous motor at standstill by recursive least squares algorithm*, Conf. Proc. Fifth European Conference on Power Electronics and Applications, **1993**, pp. 103-108 vol.105

[27] S. Shuang, C. Xiaomeng, L. Haifeng, Q. Wenlong and L. Yituo, *An accurate rotor time constant estimation method for self-commissioning of multi-scale induction motor drives*, Conf. Proc. IEEE Energy Conversion Congress and Exposition (ECCE-2011), **2011**, pp. 1700-1707

[28]   A. Gastli, *Identification of induction motor equivalent circuit parameters using the single-phase test*, <u>IEEE Transactions on Energy Conversion</u>, Vol. 14, No. 1, **1999**, pp. 51-56

[29]   C. Wang, D. W. Novotny and T. A. Lipo, *An automated rotor time-constant measurement system for indirect field-oriented drives*, <u>IEEE Transactions on Industry Applications</u>, Vol. 24, No. 1, **1988**, pp. 151-159

[30]   M. Ruff and H. Grotstollen, *Off-line identification of the electrical parameters of an industrial servo drive system*, Conf. Proc. <u>IEEE Industry Applications Conference, 1996. Thirty-First IAS Annual Meeting, IAS '96</u>, **1996**, pp. 213-220 vol.211

[31]   N. M. Cerqueira, J. R. Soares, R. P. de Castro, H. S. Oliveira and R. E. Araujo, *Experimental evaluation on parameter identification of induction motor using continuous-time approaches*, Conf. Proc. <u>International Conference on Power Engineering, Energy and Electrical Drives, POWERENG</u>, **2007**, pp. 162-167

[32]   Z. Jun, W. Yunkuan, Q. Xiaofei and Z. Xin, *An offline parameter identification method of induction motor*, Conf. Proc. <u>7th World Congress on Intelligent Control and Automation, WCICA</u>, **2008**, pp. 8898-8901

[33]   M. Bertoluzzo, G. S. Buja and R. Menis, *Self-commissioning of RFO IM drives: one-test identification of the magnetization characteristic of the motor*, <u>IEEE Transactions on Industry Applications</u>, Vol. 37, No. 6, **2001**, pp. 1801-1806

[34]   R. J. Kerkman, J. D. Thunes, T. M. Rowan and D. W. Schlegel, *A frequency-based determination of transient inductance and rotor resistance for field commissioning purposes*, <u>IEEE Transactions on Industry Applications</u>, Vol. 32, No. 3, **1996**, pp. 577-584

[35]   Z. M. Assis Peixoto and P. F. Seixas, *Electrical parameter estimation considering the saturation effects in induction machines*, Conf. Proc. <u>31st IEEE Annual Power Electronics Specialists Conference, PESC-2000</u>, **2000**, pp. 1563-1568 vol.1563

[36]   N. R. Klaes, *Parameter identification of an induction machine with regard to dependencies on saturation*, <u>IEEE Transactions on Industry Applications</u>, Vol. 29, No. 6, **1993**, pp. 1135-1140

[37]   F. Barrero, J. Perez, R. Millan and L. G. Franquelo, *Self-commissioning for voltage-referenced voltage-fed vector controlled induction motor drives*, Conf. Proc. <u>The 25th Annual Conference of the IEEE Industrial Electronics Society, IECON '99</u>, **1999**, pp. 1033-1038 vol.1033

[38]   C. B. Jacobina, J. E. C. Filho and A. M. N. Lima, *Estimating the parameters of induction machines at standstill*, <u>IEEE Transactions on Energy Conversion</u>, Vol. 17, No. 1, **2002**, pp. 85-89

[39]   J. Godbersen, *A stand-still method for estimating the rotor resistance of induction motors*, Conf. Proc. <u>IEEE Industry Applications Conference, 1999. Thirty-Fourth IAS Annual Meeting</u>, **1999**, pp. 900-905 vol.902

[40]   A. Ganji, P. Guillaume, R. Pintelon and P. Lataire, *Induction motor dynamic and static inductance identification using a broadband excitation technique*, <u>IEEE Transactions on Energy Conversion</u>, Vol. 13, No. 1, **1998**, pp. 15-20

[41] A. Boglietti, P. Ferraris, M. Lazzari and F. Profumo, *Induction motor equivalent circuit parameters determination from standard tests made with inverter supply*, Conf. Proc. <u>Sixth International Conference on Electrical Machines and Drives</u>, **1993**, pp. 271-276

[42] L. Yih-Neng and C.-L. Chen, *Automatic IM parameter measurement under sensorless field-oriented control*, <u>IEEE Transactions on Industrial Electronics</u>, Vol. 46, No. 1, **1999**, pp. 111-118

[43] S.-K. Sul, *Control of Electric Machine Drive Systems*, <u>John Wiley & Sons Inc.</u>, **2011**.

[44] R. D. Doncker, D. W. J. Pulle and A. Veltman, *Advanced Electrical Drives - Analysis, Modeling, Control*, <u>Springer</u>, **2011**.

[45] A. M. Trzynadlowski, *Control of Induction Motors*, <u>Academic Press</u>, **2001**.

[46] A. M. Khambadkone and J. Holtz, *Vector-controlled induction motor drive with a self-commissioning scheme*, <u>IEEE Transactions on Industrial Electronics</u>, Vol. 38, No. 5, **1991**, pp. 322-327

[47] J. A. Cortajarena, J. De Marcos, P. Alvarez and F. J. Vicandi, *Sensorless induction motor parameter identification and control*, Conf. Proc. <u>IEEE International Conference on Industrial Technology (ICIT)</u>, **2010**, pp. 404-409

[48] C. Attaianese, A. Damiano, G. Gatto, I. Marongiu and A. Perfetto, *Induction motor drive parameters identification*, <u>IEEE Transactions on Power Electronics</u>, Vol. 13, No. 6, **1998**, pp. 1112-1122

[49] S. R. Shaw and S. B. Leeb, *Identification of induction motor parameters from transient stator current measurements*, <u>IEEE Transactions on Industrial Electronics</u>, Vol. 46, No. 1, **1999**, pp. 139-149

[50] N. Gassara, M. Chaabene and M. Ben Ali Kamoun, *Smart model for the identification of the induction motor parameters*, Conf. Proc. <u>6th International Multi-Conference on Systems, Signals and Devices, SSD '09</u>, **2009**, pp. 1-5

[51] E. Levi, M. Sokola and S. N. Vukosavic, *A method for magnetizing curve identification in rotor flux oriented induction machines*, <u>IEEE Transactions on Energy Conversion</u>, Vol. 15, No. 2, **2000**, pp. 157-162

[52] E. Levi and S. N. Vukosavic, *Identification of the magnetising curve during commissioning of a rotor flux oriented induction machine*, <u>Electric Power Applications, IEE Proceedings -</u>, Vol. 146, No. 6, **1999**, pp. 685-693

[53] A. Boglietti, P. Ferraris, M. Pastorelli and C. Zimaglia, *Induction motors field oriented control based on averaged parameters*, Conf. Proc. <u>IEEE Industry Applications Society Annual Meeting</u>, **1994**, pp. 81-87 vol.81

[54] T. Kudor, K. Ishihara and H. Naitoh, *Self-commissioning for vector controlled induction motors*, Conf. Proc. <u>IEEE Industry Applications Society Annual Meeting</u>, **1993**, pp. 528-535 vol.521

[55] J. Weissbacher, A. R. Weber, G. Steiner and M. Horn, *A simple method for self-commissioning of industrial AC motor drives without shaft encoder*, Conf. Proc. 15th International Symposium MECHATRONIKA, **2012**, pp. 1-6

[56] S. Jul-Ki and S. Seung-Ki, *Induction motor parameter tuning for high-performance drives*, IEEE Transactions on Industry Applications, Vol. 37, No. 1, **2001**, pp. 35-41

[57] C. Concari, G. Franceschini and C. Tassoni, *Induction Drive Health Assessment in DSP-Based Self-Commissioning Procedures*, IEEE Transactions on Industrial Electronics, Vol. 58, No. 5, **2011**, pp. 1490-1500

[58] D. Y. Ohm, Y. Khersonsky and J. R. Kimzey, *Rotor time constant adaptation method for induction motors using DC link power measurement*, Conf. Proc. IEEE Industry Applications Society Annual Meeting, **1989**, pp. 588-593 vol.581

[59] W. Leonhard, *Control of Electrical Drives*, Springer, **2001**.

[60] M. Koyama, M. Yano, I. Kamiyama and S. Yano, *Microprocessor-Based Vector Control System for Induction Motor Drives with Rotor Time Constant Identification Function*, IEEE Transactions on Industry Applications, Vol. IA-22, No. 3, **1986**, pp. 453-459

[61] T. M. Rowan, R. J. Kerkman and D. Leggate, *A simple on-line adaption for indirect field orientation of an induction machine*, IEEE Transactions on Industry Applications, Vol. 27, No. 4, **1991**, pp. 720-727

[62] S. N. Vukosavic and M. R. Stojic, *On-line tuning of the rotor time constant for vector-controlled induction motor in position control applications*, IEEE Transactions on Industrial Electronics, Vol. 40, No. 1, **1993**, pp. 130-138

[63] R. D. Lorenz and D. B. Lawson, *A simplified approach to continuous, online tuning of field oriented induction machine drives*, Conf. Proc. IEEE Industry Applications Society Annual Meeting, **1988**, pp. 444-449 vol.441

[64] L. Umanand and S. R. Bhat, *Adaptation of the rotor time constant for variations in the rotor resistance of an induction motor*, Conf. Proc. 25th Annual IEEE Power Electronics Specialists Conference, PESC '94, **1994**, pp. 738-743 vol.731

[65] Z. Li-Cheng, C. L. DeMarco and T. A. Lipo, *An extended Kalman filter approach to rotor time constant measurement in PWM induction motor drives*, IEEE Transactions on Industry Applications, Vol. 28, No. 1, **1992**, pp. 96-104

[66] H. Sugimoto and S. Tamai, *Secondary Resistance Identification of an Induction-Motor Applied Model Reference Adaptive System and Its Characteristics*, IEEE Transactions on Industry Applications, Vol. IA-23, No. 2, **1987**, pp. 296-303

[67] J. W. Finch, D. J. Atkinson and P. P. Acarnley, *Full-order estimator for induction motor states and parameters*, IEE Proceedings on Electric Power Applications, Vol. 145, No. 3, **1998**, pp. 169-179

[68] T. Matsuo and T. A. Lipo, *A Rotor Parameter Identification Scheme for Vector-Controlled Induction Motor Drives*, IEEE Transactions on Industry Applications, Vol. IA-21, No. 3, **1985**, pp. 624-632

[69]   T. Saitoh, T. Okuyama and T. Matsui, *An automated secondary resistance identification scheme in vector controlled induction motor drives*, Conf. Proc. IEEE Industry Applications Society Annual Meeting, **1989**, pp. 594-600 vol.591

[70]   K. Tungpimolrut, P. Fang-Zheng and T. Fukao, *A robust rotor time constant estimation method for vector control of induction motor under any operating conditions*, Conf. Proc. 20th International Conference on Industrial Electronics, Control and Instrumentation, IECON '94, **1994**, pp. 275-280 vol.271

[71]   R. Beguenane, C. Ghyselen and H. Schoorens, *A proposed induction motor speed sensor without contact from slots harmonics. Application to rotoric time constant identification*, Conf. Proc. Fifth International Conference on Power Electronics and Variable-Speed Drives, **1994**, pp. 90-95

[72]   J. Holtz and T. Thimm, *Identification of the machine parameters in a vector-controlled induction motor drive*, IEEE Transactions on Industry Applications, Vol. 27, No. 6, **1991**, pp. 1111-1118

[73]   J. Plotkin, M. Stiebler and D. Schuster, *A novel method for online stator resistance estimation of inverter-fed ac-machines without temperature sensors*, Conf. Proc. 11th International Conference on Optimization of Electrical and Electronic Equipment, OPTIM, **2008**, pp. 155-161

[74]   A. O. Di Tommaso and R. M. Ferrigno, *Sensorless low range speed estimation and parameter identification of induction motor drives devoted to lifts automatic rescue devices*, Conf. Proc. XIX International Conference on Electrical Machines (ICEM), **2010**, pp. 1-6

[75]   T. Kataoka, S. Toda and Y. Sato, *On-line estimation of induction motor parameters by extended Kalman filter*, Conf. Proc. Fifth European Conference on Power Electronics and Applications, **1993**, pp. 325-329 vol.324

[76]   R. Krishnan, *Electric Motor Drives - Modeling, Analysis, and Control*, Prentice Hall, **2001**.

[77]   H. A. Toliyat and A. A. G. Hosseiny, *Parameter estimation algorithm using spectral analysis for vector controlled induction motor drives*, Conf. Proc. IEEE International Symposium on Industrial Electronics, ISIE'93, **1993**, pp. 90-95

[78]   H. Chai and P. P. Acarnley, *Induction motor parameter estimation algorithm using spectral analysis*, IEE Proceedings on Electric Power Applications, Vol. 139, No. 3, **1992**, pp. 165-174

[79]   C. Attaianese, G. Tomasso, A. Damiano, I. Marongiu and A. Perfetto, *On line estimation of speed and parameters in induction motor drives*, Conf. Proc. IEEE International Symposium on Industrial Electronics, ISIE '97, **1997**, pp. 1054-1059 vol.1053

[80]   A. Ba-Razzouk, A. Cheriti and P. Sicard, *Implementation of a DSP based real-time estimator of induction motors rotor time constant*, IEEE Transactions on Power Electronics, Vol. 17, No. 4, **2002**, pp. 534-542

[81]   H. A. Toliyat, M. S. Arefeen, K. M. Rahman and D. Figoli, *Rotor time constant updating scheme for a rotor flux-oriented induction motor drive*, IEEE Transactions on Power Electronics, Vol. 14, No. 5, **1999**, pp. 850-857

[82]   C. C. Hwang, S. M. Chang, C. T. Pan and T. Y. Chang, *Estimation of parameters of interior permanent magnet synchronous motors*, Journal of Magnetism and Magnetic Materials, Vol. 239, No. 1–3, **2002**, pp. 600-603

[83]   A. Tessarolo, *Accurate Computation of Multiphase Synchronous Machine Inductances Based on Winding Function Theory*, IEEE Transactions on Energy Conversion, Vol. 27, No. 4, **2012**, pp. 895-904

[84]   S. Weisberger, A. Proca and A. Keyhani, *Estimation of Permanent Magnet Motor Parameters*, Conf. Rec. IEEE Industrial Applications Conference 1997, year **1997**, pp. 29 - 34

[85]   S. Bolognani, L. Peretti, M. Zigliotto and E. Bertotto, *Commissioning of Electromechanical Conversion Models for High Dynamic PMSM Drives*, IEEE Transactions on Industrial Electronics, Vol. 57, No. 3, **2010**, pp. 986-993

[86]   S. Tao, O. K. Soon, L. Jeong-Jong and H. Jung-Pyo, *An improved AC standstill method for testing inductances of interior PM synchronous motor considering cross-magnetizing effect*, Conf. Proc. IEEE Energy Conversion Congress and Exposition, (ECCE-2009), **2009**, pp. 2415-2422

[87]   T. J. Vyncke, F. M. L. L. D. Belie, R. K. Boel, J. A. A. Melkebeek, Y. Cheng and P. Lataire, *Identification of PM synchronous machines in the frequency domain by broadband excitation*, Conf. Rec. International Symposium on Power Electronics, Electrical Drives, Automation and Motion, 2008, year **2008**, pp. 1253 - 1258

[88]   R. Dutta and M. F. Rahman, *A Comparative Analysis of Two Test Methods of Measuring d - and q - Axes Inductances of Interior Permanent-Magnet Machine*, IEEE Transactions on Magnetics, Vol. 42, No. 11, **2006**, pp. 3712-3718

[89]   K. M. Rahman and S. Hiti, *Identification of Machine Parameters of a Synchronous Motor*, IEEE Transactions on Industry Applications, Vol. 41, No. 2, **2005**, pp. 9

[90]   E. Armando, R. I. Bojoi, P. Guglielmi, G. Pellegrino and M. Pastorelli, *Experimental Identification of the Magnetic Model of Synchronous Machines*, IEEE Transactions on Industry Applications, Vol. 49, No. 5, **2013**, pp. 2116-2125

[91]   J. G. Cintron-Rivera, A. S. Babel, E. E. Montalvo-Ortiz, S. N. Foster and E. G. Strangas, *A simplified characterization method including saturation effects for permanent magnet Machines*, Conf. Proc. XXth International Conference on Electrical Machines (ICEM), **2012**, pp. 837-843

[92]   D. Uzel and Z. Peroutka, *Optimal control and identification of model parameters of traction interior permanent magnet synchronous motor drive*, Conf. Proc. 37th Annual Conference on IEEE Industrial Electronics Society - IECON 2011, **2011**, pp. 1960-1965

[93]   B. Stumberger, G. Stumberger, D. Dolinar, A. Hamler and M. Trlep, *Evaluation of saturation and cross-magnetization effects in interior permanent-magnet synchronous motor*, IEEE Transactions on Industry Applications, Vol. 39, No. 5, **2003**, pp. 1264-1271

[94] S. Moreau, R. Kahoul and J.-P. Louis, *Parameter Estimation of Permanent Magnet Synchronous Machine without Adding Extra Signal as Input Excitation*, Conf. Rec. IEEE International Symposium on Industrial Electronics 2004, year **2004**, pp. 371 - 376

[95] M. A. Jabbar, J. Dong and Z. Liu, *Determination of Parameters for Internal Permanent Magnet Synchronous Motors*, Conf. Rec. IEEE International Conference on Electrical Machines and Drives - 2005, year **2005**, pp. 149 - 156

[96] L. Hong, Z. Hongdong and Y. Xin, *The implementation of parameter identification in the control of permanent magnet synchronous motor*, Conf. Proc. 2nd International Conference on Artificial Intelligence, Management Science and Electronic Commerce (AIMSEC), **2011**, pp. 2562-2566

[97] W. Wang and X. Xiao, *Research on predictive control for PMSM based on online parameter identification*, Conf. Proc. 38th Annual Conference on IEEE Industrial Electronics Society IECON 2012, **2012**, pp. 1982-1986

[98] S. Ichikawa, M. Tomita, S. Doki and S. Okuma, *Sensorless control for all types of synchronous motors using an on-line parameter identification*, Conf. Proc. IEEE Industrial Electronics Society, 2004. IECON, **2004**, pp. 975-980 Vol. 971

[99] U. Schaible and B. Szabados, *Dynamic Motor Parameter Identification for High Speed Flux Weakening Operation of Brushless Permanent Magnet Synchronous Machines*, IEEE Transactions on Energy Conversion, Vol. 14, No. 3, **1999**, pp. 7

[100] Y. Inoue, Y. Kawaguchi, S. Morimoto and M. Sanada, *Performance Improvement of Sensorless IPMSM Drives in a Low-Speed Region Using Online Parameter Identification*, IEEE Transactions on Industry Applications, Vol. 47, No. 2, **2011**, pp. 798-804

[101] M. F. Moussa and Y. Gaber, *Sensorless control drive of permanent magnet motor based on a simple on-line parameter identification scheme*, Conf. Proc. 14th European Conference on Power Electronics and Applications (EPE 2011), **2011**, pp. 1-10

[102] A. H. Wijenayake, J. M. Bailey and M. Naidu, *A DSP-based position sensor elimination method with an on-line parameter identification scheme for permanent magnet synchronous motor drives*, Conf. Proc. IEEE Industry Applications Conference. Thirtieth IAS Annual Meeting, IAS '95, **1995**, pp. 207-215 vol.201

[103] S. Morimoto, M. Sanada and Y. Takeda, *Mechanical Sensorless Drives of IPMSM With Online Parameter Identification*, IEEE Transactions on Industry Applications, Vol. 42, No. 5, **2006**, pp. 1241-1248

[104] S. Ichikawa, M. Tomita, S. Doki and S. Okuma, *Sensorless Control of Permanent-Magnet Synchronous Motors Using Online Parameter Identification Based on System Identification Theory*, IEEE Transactions on Industrial Electronics, Vol. 53, No. 2, **2006**, pp. 10

[105] M. Khov, J. Regnier and J. Faucher, *On-Line Parameter Estimation of PMSM in Open Loop and Closed Loop*, Conf. Rec. IEEE International Conference on Industrial Technology ICIT - 2009, year **2009**, pp. 1 - 6

[106] V. Bobek, B. Dobrucky, R. Pavlanin and P. Sevcik, *VHFIM sensorless control of PMSM*, Conf. Proc. IEEE International Symposium on Industrial Electronics, ISIE-2010, **2010**, pp. 1536-1541

[107] C. Chinchul, L. Wootaik, O. K. Soon and H. Jung-Pyo, *Experimental Estimation of Inductance for Interior Permanent Magnet Synchronous Machine Considering Temperature Distribution*, <u>IEEE Transactions on Magnetics</u>, Vol. 49, No. 6, **2013**, pp. 2990-2996

[108] T. Senjyu, Y. Noguchi, N. Urasaki, A. Yona and H. Sekine, *Parameter identification for interior permanent-magnet synchronous motor*, Conf. Proc. <u>International Conference on Electrical Machines and Systems, ICEMS</u>, **2007**, pp. 566-571

[109] R. Krishnan and P. Vijayraghavan, *Fast estimation and compensation of rotor flux linkage in permanent magnet synchronous machines*, Conf. Proc. <u>IEEE International Symposium on Industrial Electronics, ISIE '99</u>, **1999**, pp. 661-666 vol.662

[110] X. Xi, C. Changming and Z. Meng, *Dynamic Permanent Magnet Flux Estimation of Permanent Magnet Synchronous Machines*, <u>IEEE Transactions on Applied Superconductivity</u>, Vol. 20, No. 3, **2010**, pp. 1085-1088

[111] B. K. Bose, *Power Electronics and Motor Drives - Advances and Trends*, <u>Academic Press</u>, **2006**.

[112] G. S. Buja and M. P. Kazmierkowski, *Direct torque control of PWM inverter-fed AC motors - a survey*, <u>IEEE Transactions on Industrial Electronics</u>, Vol. 51, No. 4, **2004**, pp. 744-757

[113] C. Jong-Woo and S. Seung-Ki, *Inverter output voltage synthesis using novel dead time compensation*, <u>IEEE Transactions on Power Electronics</u>, Vol. 11, No. 2, **1996**, pp. 221-227

[114] G. Pellegrino, R. I. Bojoi, P. Guglielmi and F. Cupertino, *Accurate Inverter Error Compensation and Related Self-Commissioning Scheme in Sensorless Induction Motor Drives*, <u>IEEE Transactions on Industry Applications</u>, Vol. 46, No. 5, **2010**, pp. 1970-1978

[115] I. R. Bojoi, E. Armando, G. Pellegrino and S. G. Rosu, *Self-commissioning of inverter nonlinear effects in AC drives*, Conf. Proc. <u>IEEE International Energy Conference and Exhibition (ENERGYCON)</u>, **2012**, pp. 213-218

[116] J. Pyrhonen, T. Jokinen and V. Hrabovcova, *Design of Rotating Electrical Machines*, <u>John Wiley & Sons</u>, **2008**.

[117] H. A. Toliyat and G. B. Kliman, *Handbook of Electric Motors*, <u>CRC Press</u>, **2004**.

[118] A. Cavagnino and M. Lazzari, *Dinamica delle Macchine Elettriche*, Appunti delle lezioni della materia: Macchine Elettriche - II - Parte Dinamica, 2005, pp.

[119] M. Popescu, *Induction Motor Modelling for Vector Control Purposes*, **2000**, pages 143

[120] G. Pellegrino, R. I. Bojoi and P. Guglielmi, *Unified Direct-Flux Vector Control for AC Motor Drives*, <u>IEEE Transactions on Industry Applications</u>, Vol. 47, No. 5, **2011**, pp. 2093-2102

[121] A. Jidin, N. R. N. Idris and A. H. M. Yatim, *Study on Stability and Performances of DTC Due to Stator Resistance Variation*, Conf. Proc. <u>5th Student Conference on Research and Development, SCOReD</u>, **2007**, pp. 1-6

[122] P. J. C. Branco, *A didactic explanation of field oriented systems sensitivity*, Conf. Proc. <u>Fifth European Conference on Power Electronics and Applications</u>, **1993**, pp. 408-412 vol.405

[123] A. Khedher and M. F. Mimouni, *Effects of the rotor time constant and the mutual inductance on the behaviour of a vector controlled induction motor*, Conf. Proc. IEEE International Conference on Systems, Man and Cybernetics, **2002**, pp. 6 pp. vol.5

[124] NEMA, *NEMA MG-1: Motors and Generators*, 2009, pp. 1 - 671

[125] L. J. Garces, *Parameter Adaption for the Speed-Controlled Static AC Drive with a Squirrel-Cage Induction Motor*, IEEE Transactions on Industry Applications, Vol. IA-16, No. 2, **1980**, pp. 173-178

[126] S. Maiti, C. Chakraborty, Y. Hori and M. C. Ta, *Model Reference Adaptive Controller-Based Rotor Resistance and Speed Estimation Techniques for Vector Controlled Induction Motor Drive Utilizing Reactive Power*, Industrial Electronics, IEEE Transactions on, Vol. 55, No. 2, **2008**, pp. 594-601

[127] S. K. Sul, *A novel technique of rotor resistance estimation considering variation of mutual inductance*, IEEE Transactions on Industry Applications, Vol. 25, No. 4, **1989**, pp. 578-587

[128] R. Krishnan and F. C. Doran, *A Method of Sensing Line Voltages for Parameter Adaptation of Inverter-Fed Induction Motor Servo Drives*, IEEE Transactions on Industry Applications, Vol. IA-23, No. 4, **1987**, pp. 617-622

[129] L. Peretti and M. Zigliotto, *Automatic procedure for induction motor parameter estimation at standstill*, IET Electric Power Applications, Vol. 6, No. 4, **2012**, pp. 214-224

[130] D. Chatterjee, *A Simple Leakage Inductance Identification Technique for Three-Phase Induction Machines Under Variable Flux Condition*, IEEE Transactions on Industrial Electronics, Vol. 59, No. 11, **2012**, pp. 4041-4048

[131] E. Levi and S. N. Vukosavic, *Identification of the magnetising curve during commissioning of a rotor flux oriented induction machine*, IEE Proceedings on Electric Power Applications, Vol. 146, No. 6, **1999**, pp. 685-693

[132] G. Shen, K. Wang, W. Yao, K. Lee and Z. Lu, *DC Biased Stimulation Method for Induction Motor Parameters Identification at Standstill without Inverter Nonlinearity Compensation*, Conf. Proc. IEEE Energy Conversion Congress and Exposition (ECCE-2013), **2013**, pp. 5123-5130

[133] J. Kania, T. H. Panchal, V. Patel and K. Patel, *Self commissioning: A unique feature of inverter-fed induction motor drives*, Conf. Proc. Nirma University International Conference on Engineering (NUiCONE), **2011**, pp. 1-6

[134] R. I. Bojoi, G. Griva, V. Bostan, M. Guerriero, F. Farina and F. Profumo, *Current control strategy for power conditioners using sinusoidal signal integrators in synchronous reference frame*, IEEE Transactions on Power Electronics, Vol. 20, No. 6, **2005**, pp. 1402-1412

[135] L. R. Limongi, R. Bojoi, G. Griva and A. Tenconi, *New Control Strategy for Hybrid Power Filters Using Sinusoidal Signal Integrators for Current Reference Generation*, Conf. Proc. IEEE Industry Applications Conference, 2007. 42nd IAS Annual Meeting, **2007**, pp. 1636-1643

[136] Y. Xiaoming, W. Merk, H. Stemmler and J. Allmeling, *Stationary-frame generalized integrators for current control of active power filters with zero steady-state error for current harmonics of concern under unbalanced and distorted operating conditions*, <u>IEEE Transactions on Industry Applications</u>, Vol. 38, No. 2, **2002**, pp. 523-532

[137] P. B. Reddy, A. M. El-Refaie, H. Kum-Kang, J. K. Tangudu and T. M. Jahns, *Comparison of Interior and Surface PM Machines Equipped With Fractional-Slot Concentrated Windings for Hybrid Traction Applications*, <u>IEEE Transactions on Energy Conversion</u>, Vol. 27, No. 3, **2012**, pp. 593-602

[138] J. K. Tangudu and T. M. Jahns, *Comparison of interior PM machines with concentrated and distributed stator windings for traction applications*, Conf. Proc. <u>IEEE Vehicle Power and Propulsion Conference (VPPC - 2011)</u>, **2011**, pp. 1-8

[139] Arnold Magnetic Technologies, *Sintered Neodymium-Iron-Boron Magnets*, **2011**, Rochester, UK

[140] P. Vas, K. E. Hallenius and J. E. Brown, *Cross-Saturation in Smooth-Air-Gap Electrical Machines*, <u>IEEE Transactions on Energy Conversion</u>, Vol. EC-1, No. 1, **1986**, pp. 103-112

[141] P. Vas, *Sensorless Vector and Direct Torque Control*, <u>Oxford University Press</u>, **1998**.

[142] L. Alberti, M. Barcaro, Pre, x, M. D., A. Faggion, L. Sgarbossa, N. Bianchi and S. Bolognani, *IPM Machine Drive Design and Tests for an Integrated Starter Alternator Application*, <u>Industry Applications, IEEE Transactions on</u>, Vol. 46, No. 3, **2010**, pp. 993-1001

[143] Z. Q. Zhu, S. Ruangsinchaiwanich, N. Schofield and D. Howe, *Reduction of cogging torque in interior-magnet brushless machines*, <u>Magnetics, IEEE Transactions on</u>, Vol. 39, No. 5, **2003**, pp. 3238-3240

[144] W. L. Soong and N. Ertugrul, *Field-weakening performance of interior permanent-magnet motors*, <u>IEEE Transactions on Industry Applications</u>, Vol. 38, No. 5, **2002**, pp. 1251-1258

[145] P. Guglielmi, M. Pastorelli and A. Vagati, *Cross-Saturation Effects in IPM Motors and Related Impact on Sensorless Control*, <u>IEEE Transactions on Industry Applications</u>, Vol. 42, No. 6, **2006**, pp. 1516-1522

[146] B. A. Welchko, T. M. Jahns, W. L. Soong and J. M. Nagashima, *IPM synchronous machine drive response to symmetrical and asymmetrical short circuit faults*, <u>IEEE Transactions on Energy Conversion</u>, Vol. 18, No. 2, **2003**, pp. 291-298

[147] T. M. Jahns and V. Caliskan, *Uncontrolled generator operation of interior PM synchronous machines following high-speed inverter shutdown*, <u>IEEE Transactions on Industry Applications</u>, Vol. 35, No. 6, **1999**, pp. 1347-1357

[148] G. Pellegrino, E. Armando and P. Guglielmi, *Direct Flux Field-Oriented Control of IPM Drives With Variable DC Link in the Field-Weakening Region*, <u>IEEE Transactions on Industry Applications</u>, Vol. 45, No. 5, **2009**, pp. 1619-1627

[149] M. Carraro, F. Tinazzi and M. Zigliotto, *Estimation of the direct-axis inductance in PM synchronous motor drives at standstill*, Conf. Proc. <u>IEEE International Conference on Industrial Technology, ICIT'13</u>, **2013**, pp. 313-318

[150] J. Arellano-Padilla, M. Sumner, C. Gerada and G. Buckley, *Evaluation of the Machine Non-Linearities as an Aid to Develop Self-Commissioning in Sensorless Drives*, Conf. Rec. <u>14th European Conference on Power Electronics and Applications (EPE-2011)</u>, year **2011**, pp. 1 - 9

[151] G. Wang, R. Yang, Y. Wang, Y. Yu and D. Xu, *Initial Rotor Position Estimation for Sensorless Interior PMSM with Signal Injection*, Conf. Rec. <u>International Power Electronics Conference 2010</u>, year **2010**, pp. 2748 - 2752

[152] K. Sungmin, Y. Young-Doo, S. Seung-Ki and K. Ide, *Maximum Torque per Ampere (MTPA) Control of an IPM Machine Based on Signal Injection Considering Inductance Saturation*, <u>IEEE Transactions on Power Electronics</u>, Vol. 28, No. 1, **2013**, pp. 488-497

[153] K. Hyunbae and R. D. Lorenz, *Carrier signal injection based sensorless control methods for IPM synchronous machine drives*, Conf. Proc. <u>Conference Record of the 39th IAS Annual Meeting and IEEE Industry Applications Conference - 2004</u>, **2004**, pp. 977-984 vol.972

[154] B. Sneyers, D. W. Novotny and T. A. Lipo, *Field Weakening in Buried Permanent Magnet AC Motor Drives*, <u>IEEE Transactions on Industry Applications</u>, Vol. IA-21, No. 2, **1985**, pp. 398-407

[155] R. Krishnan, *Permanent Magnet Synchronous and Brushless DC Motor Drives*, <u>CRC Press - Taylor & Francis Group</u>, **2010**.

[156] A. M. El-Refaie and T. M. Jahns, *Optimal flux weakening in surface PM machines using fractional-slot concentrated windings*, <u>IEEE Transactions on Industry Applications</u>, Vol. 41, No. 3, **2005**, pp. 790-800

[157] E. S. Boje, J. C. Balda, R. G. Harley and R. C. Beck, *Time-domain identification of synchronous machine parameters from simple standstill tests*, <u>IEEE Transactions on Energy Conversion</u>, Vol. 5, No. 1, **1990**, pp. 164-175

[158] I. Kamwa, P. Viarouge and E. J. Dickinson, *Identification of generalized models of synchronous machines from time-domain tests*, <u>IEE Proceedings on Generation, Transmission and Distribution</u>, Vol. 138, No. 6, **1991**, pp. 485-498

[159] Y. S. Chen, Z. Q. Zhu and D. Howe, *Calculation of d- and q-axis inductances of PM brushless ac machines accounting for skew*, <u>IEEE Transactions on Magnetics</u>, Vol. 41, No. 10, **2005**, pp. 3940-3942

[160] H. P. Nee, L. Lefevre, P. Thelin and J. Soulard, *Determination of d and q reactances of permanent-magnet synchronous motors without measurements of the rotor position*, <u>IEEE Transactions on Industry Applications</u>, Vol. 36, No. 5, **2000**, pp. 1330-1335

[161] J. F. Gieras, E. Santini and M. Wing, *Calculation of synchronous reactances of small permanent-magnet alternating-current motors: comparison of analytical approach and finite element method with measurements*, <u>IEEE Transactions on Magnetics</u>, Vol. 34, No. 5, **1998**, pp. 3712-3720

[162] B. Stumberger, B. Kreca and B. Hribernik, *Determination of parameters of synchronous motor with permanent magnets from measurement of load conditions*, <u>IEEE Transactions on Energy Conversion</u>, Vol. 14, No. 4, **1999**, pp. 1413-1416

[163]   K. J. Meessen, P. Thelin, J. Soulard and E. A. Lomonova, *Inductance Calculations of Permanent-Magnet Synchronous Machines Including Flux Change and Self- and Cross-Saturations*, IEEE Transactions on Magnetics, Vol. 44, No. 10, **2008**, pp. 2324-2331

[164]   S. Bolognani, M. Zigliotto and K. Unterkofler, *On-line parameter commissioning in sensorless PMSM drives*, Conf. Proc. IEEE International Symposium on Industrial Electronics, ISIE '97, **1997**, pp. 480-484 vol.482

[165]   G. Cipolla, *Hybrid Propulsion Systems for Automotive Applications*, Lecture Notes, 2011, pp.

[166]   *www.energyandclimate.org*, page title: *Batteries Characteristics: energy and power*, accessed in **2013**

[167]   C. Bastiaensen, W. Deprez, W. Symens and J. Driesen, *Parameter Sensitivity and Measurement Error Propagation in Torque Estimation Algorithms for Induction Machines*, Conf. Proc. Proceedings of the IEEE Instrumentation and Measurement Technology Conference, IMTC '06, **2006**, pp. 2289-2293

[168]   D. A. Andrade, A. W. F. V. Silveira, P. B. Severino and T. S. Tavares, *DSP Based Torque Estimation in Three-phase Cage Induction Motors*, Conf. Proc. IEEE International Electric Machines & Drives Conference, IEMDC '07, **2007**, pp. 1726-1731

[169]   C. P. Salomon, W. C. Santana, L. E. B. da Silva, E. L. Bonaldi, L. E. L. de Oliveira, J. G. B. da Silva, G. Lambert-Torres and A. R. Donadon, *A stator flux synthesis approach for torque estimation of induction motors using a modified stator resistance considering the losses effect*, Conf. Proc. IEEE International Electric Machines & Drives Conference IEMDC '13, **2013**, pp. 1369-1375

[170]   A. Goedtel, M. Suetake, I. N. da Silva, C. F. Do Nascimento, P. Serni and S. da Silva, *Torque and speed estimator for induction motor using parallel neural networks and sensorless technology*, Conf. Proc. 35th Annual Conference of IEEE Industrial Electronics, IECON '09, **2009**, pp. 1362-1367

[171]   D. D. Neema, R. N. Patel and A. S. Thoke, *Rotor flux and torque estimator for vector controlled induction drive using ANN*, Conf. Proc. International Joint Conference on Neural Networks, IJCNN 2009, **2009**, pp. 2215-2220

[172]   P. Pang and G. Ding, *An improved flux and torque estimation strategy of speed sensorless induction motor*, Conf. Proc. Chinese Control and Decision Conference, CCDC '09, **2009**, pp. 1144-1147

[173]   A. Zentai and T. Daboczi, *Model based torque estimation of Permanent Magnet Synchronous Machines*, Conf. Proc. IEEE International Symposium on Diagnostics for Electric Machines, Power Electronics and Drives, SDEMPED'07, **2007**, pp. 178-181

[174]   C. Cossar, M. Popescu, T. J. E. Miller, M. McGilp and M. Olaru, *A General Magnetic-Energy-Based Torque Estimator: Validation via a Permanent-Magnet Motor Drive*, IEEE Transactions on Industry Applications, Vol. 44, No. 4, **2008**, pp. 1210-1217

[175]   L. Seong-Taek and L. M. Tolbert, *Analytical method of torque calculation for interior permanent magnet synchronous machines*, Conf. Proc. IEEE Energy Conversion Congress and Exposition, ECCE'09, **2009**, pp. 173-177

[176] M. Carraro, F. Tinazzi and M. Zigliotto, *A novel approach to torque estimation in IPM synchronous motor drives*, Conf. Proc. 38th Annual Conference on IEEE Industrial Electronics Society, IECON'12, **2012**, pp. 4637-4641

[177] X. Wei and R. D. Lorenz, *High frequency injection-based stator flux linkage and torque estimation for DB-DTFC implementation on IPMSMs considering cross-saturation effects*, Conf. Proc. IEEE Energy Conversion Congress and Exposition, ECCE'13, **2013**, pp. 844-851

[178] Y. Fang, S. Yuanzhang and S. Tielong, *Nonlinear Torque Estimation for Vehicular Electrical Machines and Its Application in Engine Speed Control*, Conf. Proc. IEEE International Conference on Control Applications, CCA'07, **2007**, pp. 1382-1387

[179] A. Shinke, M. Hasegawa and K. Matsui, *Torque estimation for synchronous reluctance motors using robust flux observer to magnetic saturation*, Conf. Proc. IEEE International Symposium on Industrial Electronics, ISIE'09, **2009**, pp. 1569-1574

[180] Y. Kheng Cher, G. Heins and F. De Boer, *Comparison of torque estimators for PMSM*, Conf. Proc. Australasian Universities Power Engineering Conference, AUPEC '08, **2008**, pp. 1-6

[181] Magtrol, *Magtrol TM 301-308 In-Line Torque Transducers*, **2013**, New York, USA

[182] S. Odhano, P. Giangrande, R. Bojoi and C. Gerada, *Self-commissioning of Interior Permanent Magnet Synchronous Motor Drives With High-Frequency Current Injection*, IEEE Transactions on Industry Applications, Vol. PP, No. 99, **2014**, pp. 1-1

[183] S. A. Odhano, A. Boglietti, R. Bojoi and E. Armando, *Unified direct-flux vector control of induction motor self-commissioning drive with analysis of parameter detuning effects*, Conf. Proc. IEEE Energy Conversion Congress and Exposition (ECCE-2013), **2013**, pp. 2071-2078

[184] S. A. Odhano, P. Giangrande, R. Bojoi and C. Gerada, *Self-commissioning of interior permanent magnet synchronous motor drives with high-frequency current injection*, Conf. Proc. IEEE Energy Conversion Congress and Exposition (ECCE-2013), **2013**, pp. 3852-3859

[185] R. Bojoi, Z. Li, S. A. Odhano, G. Griva and A. Tenconi, *Unified direct-flux vector control of induction motor drives with maximum torque per ampere operation*, Conf. Proc. IEEE Energy Conversion Congress and Exposition (ECCE-2013), **2013**, pp. 3888-3895